Dissertations, Theses, and Masters Projects   Theses, Dissertations, & Master Projects

2007

Fluorescence imaging study of free and impinging supersonic jets: Jet structure and turbulent transition

Jennifer Ann Inman
College of William & Mary - Arts & Sciences

FLUORESCENCE IMAGING STUDY OF FREE AND IMPINGING

SUPERSONIC JETS:

Jet Structure and Turbulent Transition

A Dissertation

Presented to

The Faculty of the Department of Physics

The College of William and Mary in Virginia

In Partial Fulfillment

Of the Requirements for the Degree of

Doctor of Philosophy

by

Jennifer Ann Inman

2007

APPROVAL SHEET

This dissertation is submitted in partial fulfillment of
the requirements for the degree of

Doctor of Philosophy
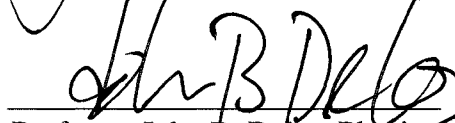
Jennifer Ann Inman

Approved by the Committee, March 2007

Committee Chair
Dr. Paul M. Danehy, NASA Langley Research Center
Adjunct Assistant Professor of Physics, The College of William & Mary

Assistant Professor Jan L. Chaloupka, Physics
The College of William & Mary

Professor John B. Delos, Physics
The College of William & Mary

Professor George M. Vahala, Physics
The College of William & Mary

Dr. J. Philip Drummond
NASA Langley Research Center

ABSTRACT

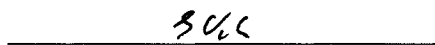A series of experiments into the behavior of underexpanded jet flows has been conducted at NASA Langley Research Center. This work was conducted in support of the Return to Flight effort following the loss of the Columbia. The tests involved simulating flow through a hypothetical breach in the leading edge of the Space Shuttle Orbiter along its reentry trajectory, with the goal of generating a data set with which other researchers can test and validate computational modeling tools. Two nozzles supplied with high-pressure gas were used to generate axisymmetric underexpanded jets exhausting into a low-pressure chamber. These nozzles had exit Mach numbers of 1 and 2.6. Reynolds numbers based on nozzle exit conditions ranged from about 200 to 35,000, and nozzle exit-to-ambient jet pressure ratios ranged from about 1 to 37. Both free and impinging jets were studied, with impingement distances ranging from 10 to 40 nozzle diameters, and impingement angles of 45°, 60°, and 90°. For the majority of cases, the jet fluid was a mixture of 99.5% nitrogen seeded with 0.5% nitric oxide (NO).

Planar laser-induced fluorescence (PLIF) of NO was used to non-intrusively visualize the flow with a temporal resolution on the order of 1μs. PLIF images were used to identify and measure the location and size of flow structures. PLIF images were further used to identify unsteady jet behavior in order to quantify the conditions governing the transition to turbulent flow. This dissertation will explain the motivation behind the work, provide details of the laser system and test hardware components, discuss the theoretical aspects of laser-induced fluorescence, give an overview of the spectroscopy of nitric oxide, and summarize the governing fluid mechanical concepts. It will present measurements of the size and location of flow structures, describe the basic mechanisms and origins of unsteady behavior in these flows, and discuss the dependence of such behavior on particular flow structures. Finally, correlations describing the relationship between flow conditions and the degree of flow unsteadiness at a given location along the jet axis will be presented.

TABLE OF CONTENTS

viii

For Kalpana, David, Michael, Rick, Laurel, Ilan, and William

ACKNOWLEDGMENTS

I would like to thank the Return to Flight team, including Chuck Campbell at Johnson Space Center, Don Picetti at Boeing, and Tom Horvath at Langley Research Center, for providing me with tremendous opportunities and committing to me responsibilities not normally entrusted to graduate student. I would also like to thank James Reuther at Ames Research Center; through our sporadic conversations, you have never ceased to inspire and encourage me, to reaffirm the value of dedicating one's career to the advancement of science. A special thank you is due to Bob Nowak at Langley. Thank you, Bob, for recognizing the value of our work all the way back at that practice talk in 2003. Not only were you instrumental in getting us involved with Return to Flight, you have overseen all of the experiments presented in this dissertation, have challenged me to be rigorous in my methodology, and have fought many of the planning, procurement, and paperwork battles so that I could have fun in the lab. I am a better researcher for having worked with you. Thank you, Chris Glass, for performing CFD against which we could compare our experiments. Thank you, Bala, for setting me on the right track in trying to understand turbulent modes. Aiyana, thanks for all the image processing; it was a huge help. Thank you to all the wind tunnel staff—Tony, Paul, Kevin, Sheila, Johnny, Fitz, Bert, Foretich, Tim, and Rhonda—not only for making things work and obliging my every request, but also for making me look forward to the days we got to be over in 1251 (especially Wednesdays!). A special thank you to Paul Tucker for the long nights and sacrificed family time that went into getting the data that became the backbone of this dissertation.

Dave and Steve, thank you for all the hard work you've put in over the years in helping me with whatever I needed, from dye changes to oil changes and everything in between. You two are a big part of the reason that I look forward to coming to work every day. You've taught me so many things that can't be learned from a book, and hopefully, if they grant me this Ph.D., I won't forget it all! David, I owe you an especially big thank you for the long hours you spent helping me take this data. These results are yours too; I hope you are proud of what we have accomplished. Sadie, your friendship and kindness has been a great encouragement to me; thank you. And how can I thank you, Paul? In a book given to me by my friend Elaine (thank you Elaine!), it says, "In an ideal world, your advisor would be a mentor, an expert in your field, a coach, an editor, and a career counselor; someone to guide, teach, and encourage you from the first glimmer you have of 'the Right Topic' to your happy acceptance of a job at the institution of your choice. There are, however, few human beings who can fill that entire job description." I am incredibly blessed to have had an advisor like you, for you have not only filled this job description, but have been a good friend to me as well.

Lisa Jean—I mean, *Dr.* Lisa Jean, thank you for your love and friendship through these trying years. There is no one else who has been so perfectly able to understand,

x

commiserate, empathize, and support me through all the challenges that grad school (and life!) has thrown our way. Thank you for always believing in me. Mrs. Roberson, thank you for teaching me to love school and to love learning, right from the beginning. Mrs. Allbeck, thank you for teaching me to love math, for treating me with such respect, and for making me believe that I was smart and could accomplish whatever I set out to do. Dr. Walecka, thank you for being a phenomenal teacher, and for your encouragement and support; you gave me the courage to stick with physics. Dad, thank you for teaching me to question the world around me and the things that I am told, to reason, to think, and to wonder "why?". Mom, you have helped me find my path in life. You have helped me to figure out who I am, and have personified God's faithfulness and lovingkindness to me. And Matt, my support and my friend—I don't know how I would have made it through without you. Thank you.

FLUORESCENCE IMAGING STUDY OF FREE AND IMPINGING

SUPERSONIC JETS: JET STRUCTURE AND TURBULENT

TRANSITION

CHAPTER 1

Introduction and Motivation

1.1 Background

1.1.1 Loss of the Columbia

On 1 February 2003, the Columbia Orbiter disintegrated upon reentry to Earth's atmosphere, resulting in the loss of all seven of her crew. Debris recovery teams combed more than one million acres of Texas and Louisiana, and ultimately recovered more than 84,900 lbs of debris, 38% of the dry weight of the Orbiter (Gehman et al. 2003). Reconstruction of the recovered debris was combined with the telemetric stream of data from the Orbiter avionics system (recorded on the ground) and some of the data recorded onboard the Orbiter that was recovered from the debris field. It was ultimately determined that the failure of the vehicle originated from a breach in the leading edge of the wing (Horvath 2004). This breach was caused by impact from foam that separated from the external tank on ascent. Upon reentry, gas, heated by the shock wave in front of the vehicle, entered through this breach in the heat shield, impinging on internal wing

2

structures. They melted and burned, until ultimately, the structural integrity of the wing was critically compromised (Gehman et al. 2003).

1.1.2 The Return-to-Flight (RTF) effort

In addition to debris striking the shuttle on ascent, the possibility of damage on-orbit is very real. Orbiters on past shuttle missions have been struck by MMOD (micrometeorite/on-orbit debris), resulting in damage to the vehicle. In fact, the shuttle mission STS-115 that flew in September of 2006 sustained the second largest impact from an MMOD in the history of the shuttle program (Malik 2006). A schematic and photograph of the damage site are shown in Figure 1.1.
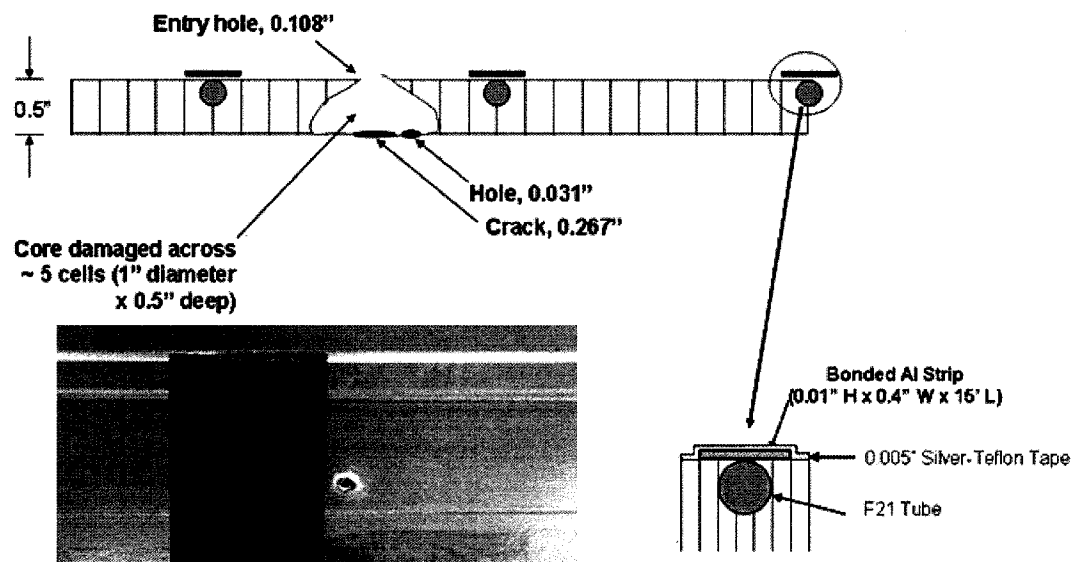
Figure 1.1: Damage to the Atlantis Space Shuttle Orbiter due to an impact from micrometeoroid orbital debris (MMOD) on the STS-115 mission in September 2006. The photograph shows the actual damage site, while the schematic shows a cross section of the right hand payload bay door radiator, the MMOD entry hole, and the geometry of the internal damage. This schematic and the inset photograph are publicly available from NASA and can be found on the following website: http://www.nasa.gov/mission_pages/shuttle/multimedia/sts115/MMOD_impact.html

3

Fortunately, this damage was on the leeward side of the Orbiter, on the right-hand payload bay door radiator, an area not subject to high heating loads on reentry. Similar damage to the heat shield or leading edge surfaces could potentially pose a much more grave danger. A penetration to a wing leading edge, in particular, could cause a breach similar to that which led to the loss of Columbia. Figure 1.2 shows a cutaway view of one of the panels of the wing leading edge, taken from Ritzert (2005). During flight, the interior cavity of the wing is vented to the ambient static pressure, resulting in a large pressure gradient across the RCC (reinforced carbon-carbon) panel.
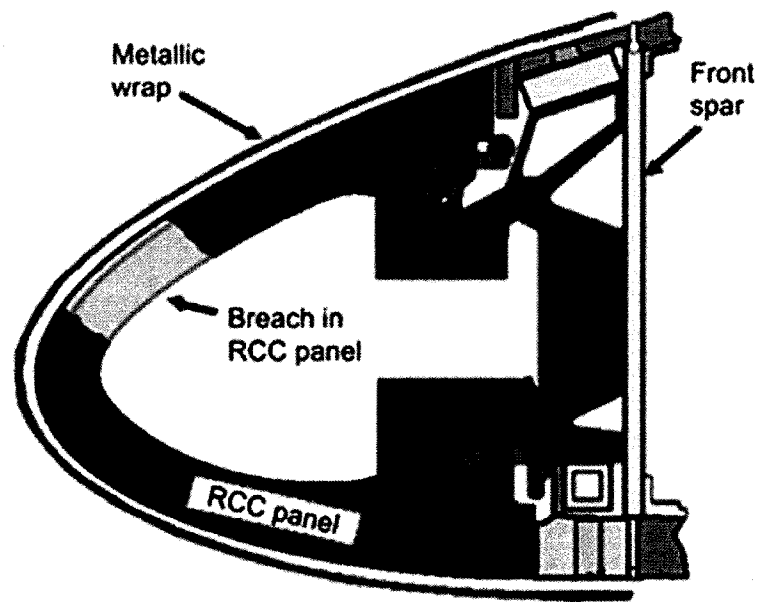
Figure 1.2: Cutaway view of a section of the wing leading edge of the Orbiter including internal structures inside the wing. This schematic of an Orbiter RCC (reinforced carbon-carbon) panel was taken from Ritzert (2005) and shows a metallic wrap repair concept as presented in that paper. A small breach in such a panel could result in a supersonic jet of gas through the hole, with the potential for impingement on internal wing structures.

Following the loss of Columbia, the ensuing accident investigation concluded that future missions needed to have on-orbit vehicle inspection and repair capabilities. The

4

problem is that the inspection and repair activities are high-risk, especially repair activities, since they require a spacewalk by an astronaut. If an inspection were to reveal a breach or crack in the thermal protection system (TPS), or a missing or damaged tile in the heat shield, the question becomes one of relative risk: which is greater—the risk associated with a repair spacewalk, or the risk associated with reentering Earth's orbit with the damage unrepaired?

Ideally, there would exist a computational tool capable of accepting as input the precise geometry of the actual damage. This tool would then run through a simulation that would be able to predict the consequences of reentry with the observed damage configuration. Obviously, if the damage is a sufficiently large hole in the wing, no such simulation is needed to predict the outcome. Alternately, a sufficiently small hole in a non-critical location might not result in loss of the vehicle. Additional damage scenarios include the loss or penetration of heat shield tiles and cracks or penetrations resulting from MMOD impacts. The risk associated with each of these scenarios is less clear and underscores the need for reliable computational tools to inform the decision of whether on-orbit repairs should be attempted. In fact, such a suite of computational tools has been (and is being) developed in accordance with the recommendations of the Columbia Accident Investigation Board (CAIB)(Cockrell et al. 2005).

Experimental investigations are warranted because computational tools need to be validated against real data in order to quantify their capabilities and limitations. A series of experiments was designed with a simple geometry and well-defined boundary conditions in order to acquire data suitable for validating these computational tools. Of particular interest was the determination of which experimental conditions resulted in

5

laminar flows and which resulted in turbulent flows. Current analytical and computation tools cannot confidently predict transition in these flows and the existing experimental database is incomplete for the type of flow of interest in the present investigation, as discussed in greater detail in section 1.3. These experiments were conducted as part of the NASA Space Shuttle Return-to-Flight (RTF) effort, in support of the Breaches Task Group (the collaboration charged with the investigation into the effects of flow through breaches in the surface of reentry vehicles).

1.2 Goals of the Experimental Investigation

The underlying thinking behind the studies presented in this work is that damage to the Orbiter that falls above a certain threshold will require repair, but below that threshold will be safe. Two nozzles were designed to simulate flow through a hypothetical breach in the wing of the Orbiter for two different damage scenarios. The type of flow that is generated when high pressure gas exhausts into a near-vacuum through theses nozzles is known as an *underexpanded jet*. The actual flow conditions encountered in flight would, of course, be much more complicated than our idealized experiment; a real hole would not be perfectly round, the internal structures in the wing have a complicated geometry, the flow conditions are continuously varying, and the geometry itself might evolve – heat transfer could erode and enlarge the hole, etc. But the initial goal is code validation. If the computational tools can be fine-tuned until they do a good job predicting the simple geometries, we can have more confidence in the results of simulations involving more realistic geometries. On the other hand, if discrepancies are noted for even the simple cases, the code will obviously need to be improved before it is considered a reliable tool.

6

1.2.1 Determining Laminar-to-Turbulent Transition Criteria

One issue in particular that arises with using computer models is the issue of the laminar/turbulent state of the flow. If an impinging flow is laminar, it will in general exhibit lower rates of heat transfer to the surface of impingement than would a similar flow that was turbulent. In fact, the impingement heating rates of turbulent flows can be many times larger than those of laminar flows for otherwise similar conditions. For instance, Horvath et al. (2006) found up to a five-fold increase in heat transfer to the windward surface of an Orbiter configuration when the boundary layer flow was tripped from laminar to turbulent.

The approach to modeling a given problem is relatively clear if the flow is known to be steady and laminar. For such flows, a less computationally-intensive laminar code may be used. The methodology is less straightforward for turbulent flows. There exist different computational methods for modeling turbulence—RANS (Reynolds Averaged Navier-Stokes), LES (large eddy simulation), and DNS (direct numerical simulation), to name a few. (See the Glossary for a brief description of each of these computational turbulence modeling techniques.) In practice, more sophisticated models—e.g. LES and DNS—are significantly more computationally intensive than lower fidelity codes—e.g. RANS. Additionally, DNS is suited to low Reynolds number flows and may not extend to realistically high Reynolds numbers due to being prohibitively computationally intensive. The particular choice of model is usually a compromise between answering the question at hand and the resources available. Several of the most common approaches to modeling turbulent flows are compared in Figure 1.3. In addition to considering the

7

computational and monetary resources required, shuttle flights are constrained by the time

between the discovery of a damage location and the time at which a repair/no-repair

decision must be made.
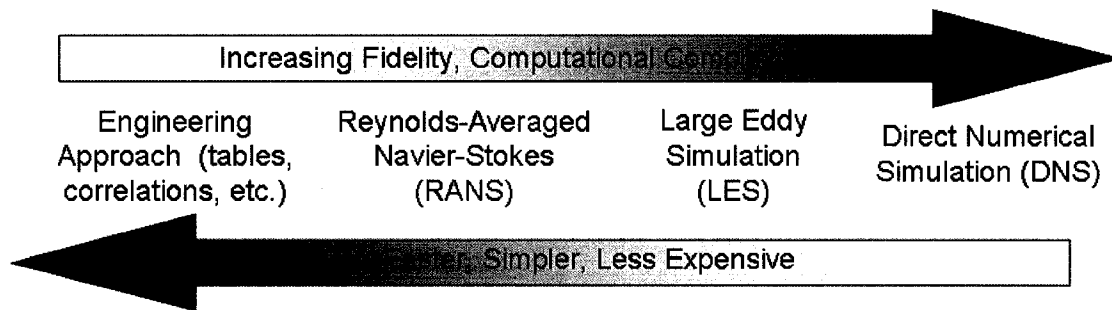
Figure 1.3: Comparison of computational approaches to modeling turbulent flows. The techniques listed towards the left can be used when a quick, approximate answer is needed. When details of the flow or more precise answers are required, the techniques listed to the right may be more appropriate.

The problem arises when the state of the flow is unknown or uncertain. In these

cases, it is unclear how to model the problem. In other words, no reliable code yet exists

that can reliably *predict* whether a flow will be laminar or turbulent, at least within a

certain range of conditions. For low enough Reynolds number flows, the flow will be

laminar, and for very high Reynolds number flows, it will be turbulent; the uncertainty is

in the mid-ranges. The Reynolds number is a ratio of the inertial forces to the viscous

forces in a flow and will be defined more thoroughly in Chapter 4. Without knowing

whether a given flow will be laminar or turbulent, one approach would be to model the

flow as turbulent in order to provide conservative estimates of heat transfer rates.

Turbulence modeling, however, is time consuming and resource intensive. If the actual

flow were laminar, this seemingly conservative approach would not only consume

8

unnecessary resources, it would also overpredict heat transfer rates. Such results could lead to a decision to repair a damage site unnecessarily. Because on-orbit repair activities are dangerous themselves, they should ideally not be attempted unless truly necessary. It is therefore critical to improve the understanding of factors affecting the laminar or turbulent state of jet flows.

When this work was begun, the range of uncertainty in the Reynolds number associated with turbulent flows was large (approximately an order of magnitude, from about 1,000 to 10,000) within the expected conditions that would be encountered along the reentry profile of the Orbiter. The primary goal of the experiments we conducted was to narrow that range of uncertainty, to gain a better understanding of the characteristics of such flows, and to provide a clear set of criteria for the conditions leading to laminar flows versus those resulting in turbulent flows. While the literature contains extensive studies of the transition to turbulence in boundary layers of flat plate flows, the literature containing experimental studies of transition in highly underexpanded axisymmetric free jets is considerably more sparse. Chapters 3-6 provide brief reviews of the relevant literature for laminar free jets, jet turbulence, and impinging jet flows.

1.2.2 Understanding Underexpanded Jet Structure

Highly underexpanded axisymmetric free jets are important flows of interest, for both fundamental fluid mechanics studies and for practical applications. Such jets have been investigated extensively in the study of propulsive jets, rocket exhaust plumes, and vehicle control jets (Love et al. 1958; Love et al. 1959; Crist et al. 1966; Donaldson and Snedeker 1971; Donaldson et al. 1971; Matsuda et al. 1987; Birkby and Page 2001;

9

Danehy et al. 2006). As discussed above, understanding the development of instabilities in these flows is of particular importance to the current study. It was therefore desirable to be able to see the structures in the flow and to see fluctuations and instabilities as they progress from minor to dominant. Being able to see what the flow looks like in the intermediate stages between the region where it is steady and laminar and the region where it has either diffused or become fully turbulent was necessary in order to further the current state of understanding about how and why and when these flows become turbulent.

1.3 Previous Studies

The pioneering work into the experimental study of underexpanded jets was reported by Love et al. (1959) and involved schlieren flow visualization of jets exhausting into atmospheric pressure. Impinging jet flows were studied extensively by Donaldson et al. (1971), including pitot pressure surveys and surface pressure measurements. But the motivation behind these studies is almost universally cited as the study of rocket plumes impinging on the ground, or exhaust from the engine of a V/STOL (vertical/short takeoff and landing) vehicle. As a result of the pressures involved in such flows, such studies were almost all conducted at high Reynolds numbers (over 30,000) where the flows were fully turbulent. Much of the available literature did not apply directly to the kind of problem and flow regimes which were of interest in the present investigation—transitional flow through a hole in the heatshield of the Orbiter along a hypersonic-to-subsonic and rarefied-to-atmospheric flight trajectory. Table 1.1 presents a comparison of several of the relevant operating conditions covered by previous studies. The subscript

10

e indicates conditions at the nozzle exit, while *a* indicates ambient conditions and *imp* indicates quantities associated with impingement. See Henderson (2002) for a more exhaustive list of impinging jet studies.

	M_e	Re_{exit}	JPR (p_e/p_a)	p_a *(atm)*	D_{imp}/D_e	θ_{imp} *(deg)*	Type(s) of measurements
Alvi & Iyer (1999)	1	1.9E6	2.6	1	1.6-2	90	PIV, shadowgraph, acoustic, surface pressure
Donaldson & Snedeker (1971)	0.57,1	1.9E5-1.3E6	1-3.57	1	1.96-39.1	15-90	Pitot & surface pressure, grease streak, heat transfer
Kim et al. (2003)	1	9.7E5-2.7E6	1.1-3.7	1	1.6-2	90	Computational (3D unsteady NS)
Lamont & Hunt (1980)	2.2	4.0E6-6.7E6	1.2,2	1	0.75-15	30-90	Shadowgraph, surface pressure
Love & Lee (1958)	1-3	1.7E5-5.7E7	0.25-19, 60-41,820	1, 5e-5	NA	NA	Schlieren, method of characteristics calculations
Stitt (1961)	1-9.85	3.7E4-2.7E7	545-1.5E5	4.7E-4	0.4-40	90	Schlieren, surface pressure, surface erosion
Present work	1, 2.6	170-3.6E4	1-37	1.3E-3 -0.094	10.5-39.5	90, 60, 45	PLIF, surface pressure

Table 1.1: Comparison of previous underexpanded jet studies with the present investigation. The quantities compared here are, from left to right: nozzle exit Mach number, Reynolds number based on nozzle exit conditions, jet (nozzle-exit-to-ambient) pressure ratio, ambient pressure of test section, impingement angle in nozzle diameters, impingement angle, and type of study and/or measurements.

The absolute pressures, Reynolds numbers, and pressure ratios that we would expect in the Orbiter breach problem described above differ from the impinging jet flows in the literature in the following ways. The absolute pressures in the current investigation are lower, the Reynolds numbers are generally lower, the pressure ratios are generally higher, and the impingement distances (in terms of the number of nozzle diameters) are larger.

11

This is because the flows of interest in the literature generally were at atmospheric pressures, were modeled after the flow through engines that were designed to have relatively low exit pressure ratios, and had rocket-to-ground impingement distances of a few nozzle diameters. Although a rocket taking off has a virtually infinite range of impingement distances, the investigations in the literature were only concerned with the near-field impingement flow within a few nozzle diameters, where the surface heating, ground erosion, and effects on overall thrust or lift would be greatest. Additionally, the angle of impingement is an important variable in the present experiment but only normal impingement is useful in rocket launch studies.

1.3.1 Transition and Turbulence in Free or Impinging Jets

The previous studies—both experimental and computational—of transition and turbulence in these flows were performed almost exclusively with the aim of understanding the acoustic phenomena (i.e., jet noise) associated with such flows. The measurements of turbulence are generally made using hotwire anemometry, and the data are in the form of inferred velocity oscillations as a function of time. These data are then Fourier transformed to extract the frequency spectrum of the pressure oscillations. Truly turbulent flows are characterized by broadband spectra, or nearly broadband: all modes of oscillation are present in the flow, from the spatial scale of the flow itself down to the molecular dissipation scale (also called the "Kolmogorov scale"). Such data were often obtained at points in a single plane, such as the plane of an impingement target, or at points along a single line, such as the centerline of the flow. Because of this, the state of the jet upstream of or between measurement locations was either unknown or had to be

12

inferred. This is a limitation of any single-point measurement approach. Flow visualization data have been sparse, and are almost exclusively path-averaged. Thus, limited direct observation of spatial jet structures had been made prior to the current studies. Understanding the stability characteristics of such flows was a primary motivation behind this work.

1.3.2 Flow Visualization Studies of Jet Structure

Past studies have used flow visualization to examine underexpanded jet structure in the near field (that is, the flow field in close proximity to the nozzle exit). The vast majority of the flow visualization used in these studies was schlieren, a path-averaged technique that is sensitive to strong density gradients in the flow. A series of studies by Lamont and Hunt (1980) examined the relationship between flow structures and characteristics of pressure profiles on an impingement target at various angles. They acquired extensive sets of schlieren images showing great detail of the complicated shock structures associated with the impingement process. They were able to show that the minimum and maximum surface pressures corresponded to specific impinging flow structures. Lamont and Hunt (1980) used shadowgraph to identify shock structures in free and impinging jet flows. Schlieren and shadowgraph, however, would not be adequate in the present investigation for several reasons. These techniques rely on changes in the refractive index of the gas due to density gradients in the flow to produce contrasts in intensity. This makes them poorly suited for low pressure/low density environments such as those expected in the current experiments. Figure 1.4 shows schlieren and PLIF images of jet flows at similar conditions.

13

Schlieren images   NO PLIF images

◄──────── 25 mm ────────►
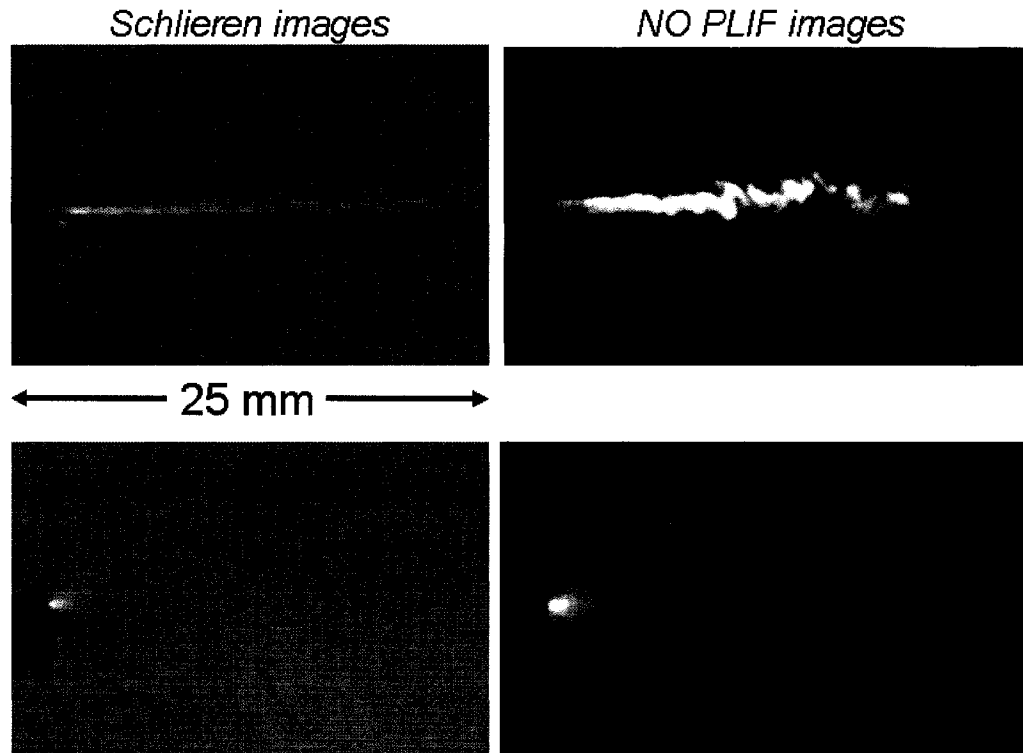
Figure 1.4: Schlieren vs. PLIF imaging at low pressure. The flows here were through a tube with an inside diameter of 0.83 mm. The stagnation pressure was approximately 550 kPa for both cases. The PLIF images were taken of flows with a 1% NO / 99% N_2 gas mixture. The jets exhausted into an ambient pressure of 7.2 kPa in the top images and 0.8 kPa in the bottom images. Exposure times are approximately 3µs for the schlieren images and 1µs for the PLIF images.

The contrast in schlieren images at these conditions is minimal compared to the crisp, high-contrast schlieren images of atmospheric-pressure flows seen in, for example, the work of Lamont and Hunt (1980). An additional limitation of these techniques in light of the goals of the present investigation is that these techniques are path-averaged. For instance, schlieren images are generated by passing collimated light through a measurement region where the trajectory of the light is altered by changes in the refractive index of the fluid. A focusing lens and spatial filtering at the focal point

14

selectively block some of the light that has passed through the measurement region. Intensity variations in the resulting images are thus due to the net variations in refractive index experienced along the path of each light ray, rather than local variations in a measurement plane. Turbulent flow structures are averaged out and indistinct in such path-averaged images, as seen in Figure 1.4.

1.4 Suitability of PLIF

In order to study both the instability and flow structure characteristics of underexpanded jets, spatially and temporally resolved flow visualization was required for these tests. The flow environments encountered in these tests include regions of low static pressure, turbulent and/or three-dimensional flow structures, and regions with both strong and weak density gradients. Planar laser-induced fluorescence (PLIF) of nitric oxide (NO) was selected as the flow-visualization technique for these experiments.

For two-dimensional flows (in this case, for truly axisymmetric flows), path-averaged techniques are often adequate, and can be far more simple and less costly to implement. These techniques are, however, poorly suited to visualizing flow structures in regions of constant density or very low pressure; such regions were expected in our experiments.

For more complex flows, namely, those with three-dimensional structure, measurements must be able to isolate specific volume elements. Since these studies sought to visualize turbulent flow structures, a technique capable of spatially-resolved (as opposed to path-averaged) measurements was needed. Rayleigh scattering can be used to visualize planar slices of a flow in regions of sufficiently high density, but we expected

15

some low pressure, low density regions in these flows and we estimated that Rayleigh imaging would not provide good signal-to-noise images. Particle imaging velocimetry (PIV) uses cross-correlation of two images, taken with a small time delay between them, to make two dimensional maps of velocity which could have been advantageous in the present study. However, this technique requires the seeding of small particles into the flow. These particles may not faithfully track the actual flow, especially in regions of large velocity gradients, such as shock structures, which were anticipated in the present experiments. Doppler global velocimetry (DGV) does not require that seed particles be large enough to be imaged individually, but it still requires some form of seeding such as a fog. For molecular size seed particles, DGV is essentially a form of filtered Rayleigh scattering (FRS), and thus suffers the same limitations in regions of low density. Where a fog is used, the flow may be visualized only in the shear layer (Thurow et al. 2002). PLIF, on the other hand, is capable of providing flow visualization throughout the flowfield.

PLIF is a well-established technique, and others have demonstrated its usefulness in studying combustion in flame environments (see Seitzman et al. 1985, and Eckbreth 1996), mapping temperature and velocity in laminar hypersonic flows in shock tunnels (O'Byrne et al. 2002), and studying separated flow regions in supersonic wind tunnels (Lachney and Clemens 1998; Exton et al. 1999). McMillin et al. (1993) did simultaneous two-line PLIF thermometry in a turbulent supersonic combustor, for both NO and OH as well as simultaneous flow visualization of NO and OH. Laser-induced fluorescence (LIF) provides capabilities favorable for use in the current experiment. LIF does not involve particle seeding but rather uses molecular flow tracers that can be expected to truly follow the flow (if the molecular weight of the tracer molecule nearly matches that of the carrier

16

gas). LIF is most convenient when the fluorescent species is naturally occurring in the flow, but can also be employed if a means exists for seeding the species into the flow. In choosing a resonant species for LIF, the following characteristics are desirable:

1) spectroscopically accessible with existing lasers (the less-expensive, less-complex, and more-robust the laser system, the better)

2) high fluorescence signal intensity

3) gas phase (makes seeding easier) and non-condensing at test conditions

4) naturally occurring in testing environment

5) non-toxic

6) inert

7) inexpensive

The most commonly used fluorescent LIF tracer species are acetone ($(CH_3)_2CO$), the hydroxyl radical (OH), iodine (I_2), and nitric oxide (NO). Each of these species has some of the desirable characteristics listed above, but no one species has them all. A brief and cursory introduction to some of the first demonstrations of LIF using these and other species is given below. For a more comprehensive review of laser-spectroscopic techniques, including applications of LIF, see McKenzie (1991), Hanson (1996), Eckbreth (1996), and Kohse-Höinghaus and Jeffries (2002).

Miles et al. demonstrated LIF of sodium (Na) in helium (He) in 1978. Sodium was made accessible as a fluorescent species because its absorption spectrum overlaps with the wavelengths generated by early narrow linewidth tunable dye lasers. It exhibits strong fluorescence, requiring low seeding levels of a few parts per million (ppm) and is most readily seeded into flames. Disadvantages include the difficulty of seeding Na into non-

17

combustion environments and the difficulty of making quantitative measurements with an atomic (as opposed to molecular) species. McKenzie et al. used biacetyl ($C_4H_6O_2$, also known as *diacetyl*) vapor to measure density fluctuations in unsteady Mach 3 channel flows in 1979.

Grieser and Barnes made LIF measurements of nitric oxide (NO) in flames in 1980. NO is common in environments hot enough to thermally dissociate N_2 and O_2, including most combustion environments. Its density is nearly identical to that of air, and it is chemically stable, so it can be stored in bottles for seeding into flows where it is not naturally present. The primary disadvantages of NO for LIF applications is that it is toxic in sufficient concentrations (the OSHA standard is a time-weighted average of 25 ppm for 8 hours per day), is corrosive in the presence of water, and is strongly quenched (a loss mechanism whereby the net fluorescence is reduced due to inelastic collisions) by oxygen and by self-collisions.

Two-dimensional (i.e., planar) imaging of the hydroxyl radical (OH) was performed by Alden et al., Dyer and Crosley, and Kychakoff et al. in 1982 (also see Carter and Laurendeau 1994). OH is a common intermediary product in combustion reactions of hydrogen and hydrocarbon fuels and is therefore an ideal fluorescent species in many reacting flows. Its main disadvantage is that it is chemically unstable and therefore is unsuitable for seeding into flows in which it is not naturally present.

In 1983, Cheng et al. imaged sodium (Na) in nitrogen (N_2), McDaniel et al. imaged iodine (I_2) in nitrogen (N_2), and Gross and McKenzie demonstrated temperature measurements using NO in N_2. Paul et al. (1989) measured one component of velocity using Doppler-shift effects in a Mach 7 supersonic jet seeded with NO. Donohue and

18

McDaniel (1996) measured several flow parameters using iodine in compressible flowfields. Iodine is a solid at room temperature and pressure, which presents some challenges in seeding large-volume gas flows. Past investigations at NASA Langley have involved painting a small amount of iodine onto an aerospace model, allowing the iodine to be entrained into the flow (Exton et al. 1999).

In 1984, Kychakoff et al. demonstrated NO flow visualization, and Massey and Lemon used a homemade ArF laser to excite fluorescence in oxygen (O_2). In 1987, Miles et al. performed flow-tagging velocimetry of oxygen and Fletcher and McDaniel excited iodine in air. Thurber et al. (1997) used acetone as the resonant species in a heated jet mixing with air. Acetone, however, is a liquid at room temperature and pressure. It does have a high vapor pressure, but, as with iodine, seeding acetone into a large-volume gas flow can be challenging.

Nitric oxide, in contrast, is a gas at room temperature and can be seeded locally or globally into a gas flow. It can also be naturally present in high-temperature or combusting flows. Because its molecular weight is nearly identical to air, NO molecules serve as reliable tracers of flow structures in air and nitrogen flows.

We elected to use planar laser-induced fluorescence (PLIF) because it can non-intrusively measure the challenging flow regimes of these experiments with sub-millimeter spatial resolution and flow-stopping temporal resolution (meaning that the flow evolves a negligible amount during the short exposure time). We opted to use nitric oxide because it is accessible with existing lasers appropriate for NO excitation, is easily seeded into the flow, and because it has favorable spectroscopic characteristics over the anticipated range of flow conditions in these experiments.

19

The primary mechanism working to decrease NO fluorescence signal in air, namely quenching by molecular oxygen, depends linearly on pressure, and is therefore less efficient at low pressures. Consequently, NO fluorescence maintains sufficient intensity even at low pressures whereas many other techniques, such as schlieren, shadowgraph, and Rayleigh scattering, do not.

1.5 Summary of goals of the present investigation

The experimental studies reported herein were designed with several goals in mind. The first is to gain a better understanding of the structure of underexpanded jet flows at conditions relevant to atmospheric reentry flight conditions. The second is to characterize the process of transition to turbulence and to determine the boundaries between those flow conditions that result in steady laminar flow and those that result in unsteady, transitional, and turbulent flows. The third is to characterize the jet impingement process for this same range of flow conditions, including the effect of impingement distance and angle on the resulting flow structures. These data will potentially inform future computational fluid dynamics (CFD) simulations and provide a means of validating and/or improving computational predictions. Finally, these tests had the secondary goal of extending PLIF measurement capabilities at NASA Langley.

The PLIF system and experimental facilities are described in greater detail in Chapter 2. An overview of the spectroscopy of nitric oxide and the theoretical background governing laser-induced fluorescence is presented in Chapter 3. The jet flows that were studied in these tests can be broadly divided into free jet cases and impinging jet cases. They can be further divided into steady and unsteady flows. Chapter 4 contains fluid

20

mechanical descriptions of steady jet flow structures. The location and size of several flow structures are measured using PLIF images and are then compared with computations. Additionally, a simplified method of simulating PLIF images from computational results is presented for the purpose of more direct comparisons with experimental PLIF images. Unsteady jet behavior is covered in Chapter 5, both theoretical aspects of unsteadiness and quantitative measurements using PLIF images of the downstream distance at which jet flows exhibited unsteady behavior. Quantitative correlations are found which can predict the location of the onset of transitional and turbulent jet behavior. Impinging jet flows, both steady and unsteady cases, are presented in Chapter 6. The location and angle of the impingement target is shown to affect the onset of flow unsteadiness as well as impingement surface pressure profiles. Impinging flow structures and pressure profiles are found to exhibit large sensitivity to small changes in particular flow conditions. Finally, Chapter 7 summarizes the results of these studies, discusses the impact of the results to date, and suggests improvements for further studies.

21

CHAPTER 2

Experimental Apparatus

Planar laser-induced fluorescence (PLIF) is a powerful tool that can be applied to the study of supersonic and hypersonic flows. Measurements using PLIF are two-dimensional, have sub-millimeter spatial resolution, and temporal resolution as high as 10 ns. Depending on the specifics of a given experiment, PLIF can be used for flow visualization, species mole fraction imaging, temperature mapping, or velocimetry. PLIF may also be able to provide data in regions of low pressure where other techniques cannot. An advantage of probing nitric oxide is that its spectroscopy is very well understood and that it is a sensitive method, generally yielding high signal levels which produce clear flow images, over a wide range of pressures relevant to ground-based simulation of hypersonic flight. See Chapter 1 for a more detailed discussion of the merits of NO PLIF.

In order to use PLIF to make measurements in wind tunnel facilities, the entire system must be moved from the laboratory to the wind tunnel for the duration of the test, and then moved to another facility or back to the laboratory upon completion of the test.

22
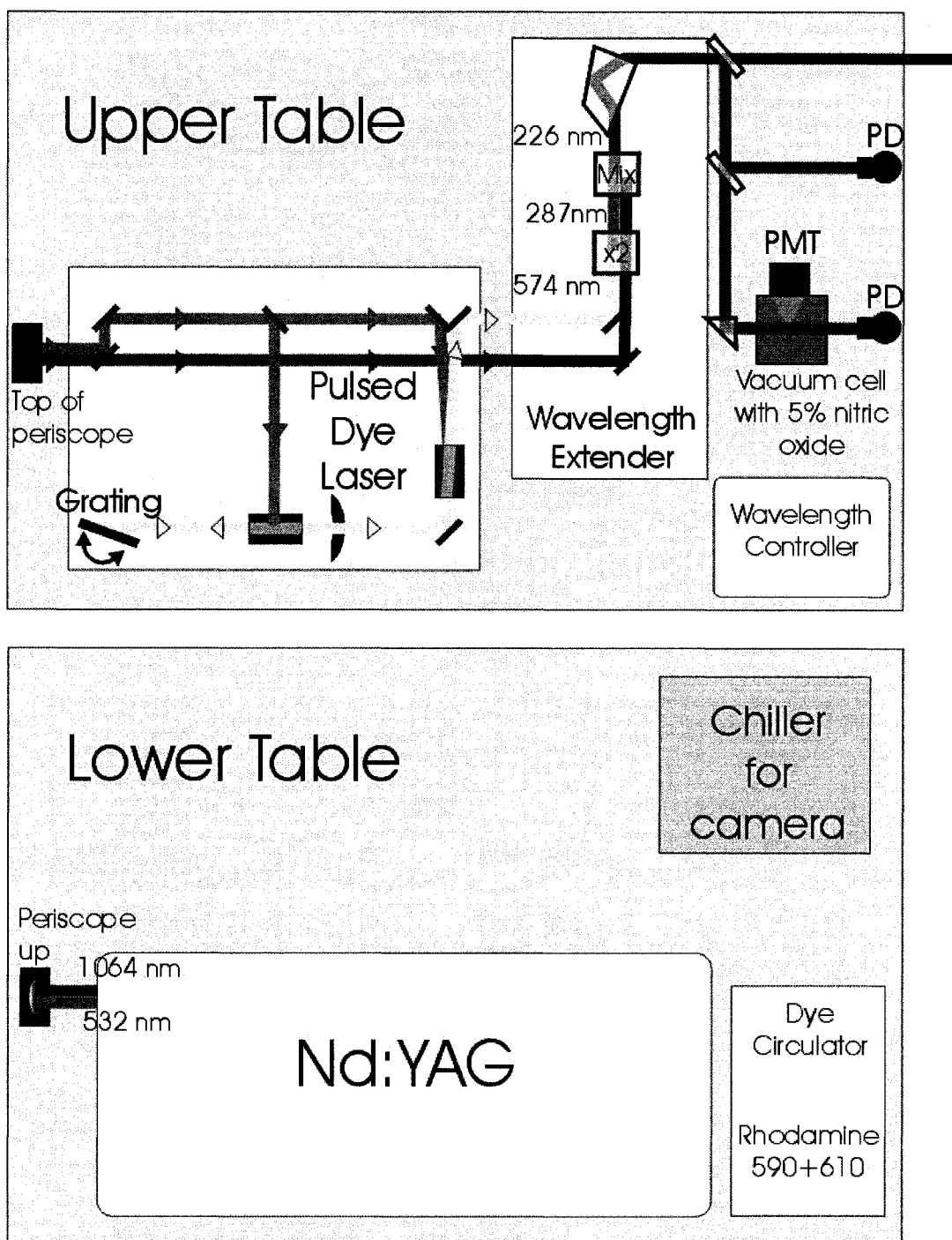
Figure 2.1: Schematic of upper and lower table of mobile PLIF cart. The bottom table houses the Nd:YAG laser and dye reservoirs for the pulsed dye laser (PDL), while the top table has the PDL and wavelength extender (WEX), along with the frequency-monitoring gas cell. The Nd:YAG produces an infrared beam at 1064 nm, along with a frequency-doubled green beam at 532 nm. This green beam pumps the PDL, which produces a tunable yellow beam between 567 and 577 nm. In the WEX, this yellow beam is frequency-doubled to the ultraviolet (between 283.5 and 288.5 nm)

23

In the past, a disadvantage of the PLIF technique has been the large amount of time and effort involved in moving and aligning all of the laser system components. In the present investigation, we have attempted to make the technique more functional by building a mobile PLIF system. The mobile system comprises two 4 ft by 6 ft optical tables. A schematic of the mobile cart is presented in Fig. 2.1, and a photograph of the cart follows in Fig. 2.2.
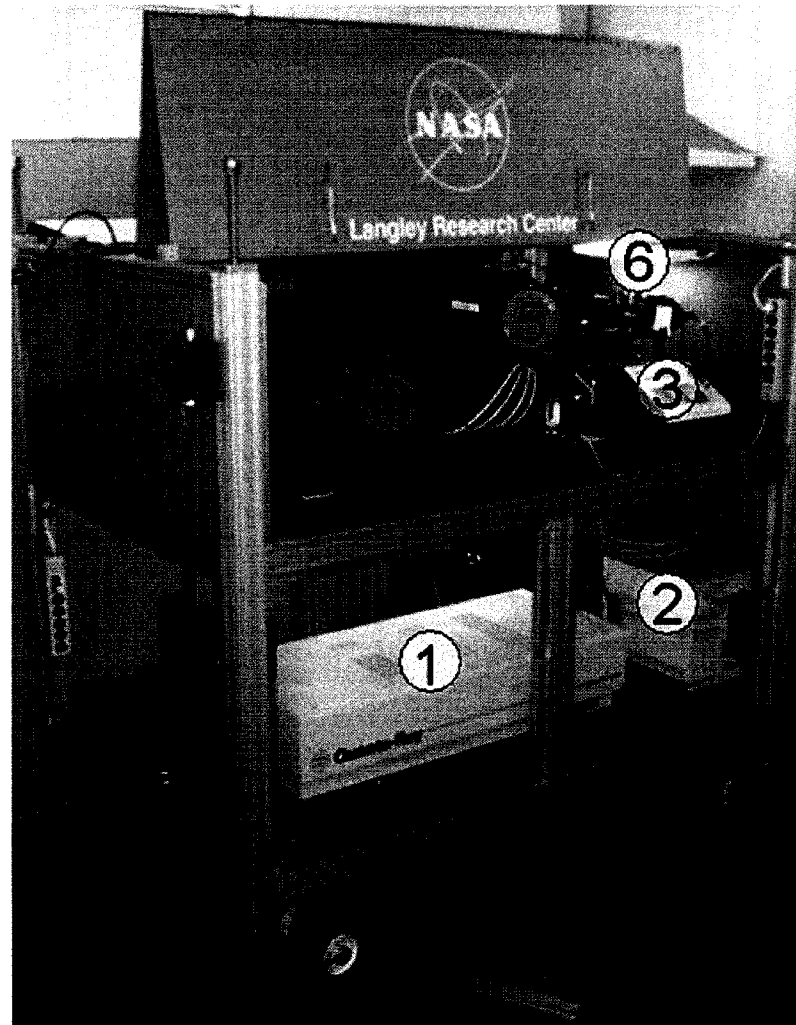
Figure 2.2 The mobile PLIF cart, shown with panels removed. Components include: (1) Nd:YAG laser; (2) dye circulators with Rhodamine 590 and Rhodamine 610 laser dyes in a methanol solvent; (3) wavelength controller for the (4) pulsed dye laser; (5) wavelength extender; and (6) low- pressure monitoring gas cell.

24

2.1 Laser System Components

The following sections give details about the hardware we have used to produce laser pulses appropriate for performing NO PLIF. Table 2.1 summarizes some of the spectral and energy characteristics at each stage leading to the final ultraviolet output. The net result is about 1.2 mJ/pulse at a wavelength of around 226 nm.

	Energy per pulse	λ	υ	$\Delta\upsilon_{unseeded}$			$\Delta\upsilon_{seeded}$		
	mJ	*nm*	*cm⁻¹*	*cm⁻¹*	*nm*	*GHz*	*cm⁻¹*	*nm*	*GHz*
Nd:YAG	1000	1064	9398	1.0 [M]	0.11	30	3 x10⁻³ [M]	3 x10⁻⁴	0.09
Doubled Nd:YAG (Type I)	400	532	18797	1.4 [E]	0.04	42	4 x10⁻³ [E]	1 x10⁻⁴	0.12
Nd:YVO₄ (injection seeder)	3 mW (CW) [S]	1064	18797	3 x10⁻⁷ [S]	3 x10⁻⁸	9 x10⁻⁶	NA	NA	NA
PDL	90	567-577	17637-17331	0.16 [M]	5 x10⁻³	4.8	NA	NA	NA
WEX doubling	5	283.5-288.5	35273-34662	0.23 [E]	2 x10⁻³	6.7	NA	NA	NA
WEX doubling + mixing	1.2	223.85-226.96	44672-44061	1.5 [M]	8 x10⁻³	45	0.8 [M]	4 x10⁻³	24

Table 2.1: Laser system characteristics. Linewidths are labeled according to whether the value was measured [M], estimated [E], or specified by the manufacturer [S]. Measured values have an uncertainty of $\pm$ 0.025 cm-1. Estimated linewidths were calculated by adding the constituent linewidths in quadrature (for doubling, this results in multiplying the undoubled linewidth by the square root of 2).

25

2.1.1 Nd:YAG

The first component of the laser system is an injection-seeded pulsed Nd:YAG laser [Spectra-Physics Quanta-Ray Pro-230-10; injection seeder Model 6350]. The Nd:YAG operates at 10 Hz and produces 1050 mJ per pulse at 1064 nm (9398 cm^{-1}). This infrared beam is then Type I frequency-doubled to produce 390 mJ of 532 nm (18797 cm^{-1}) in 10 ns pulses. When injection seeded, the spectral linewidth of the 1064 nm beam is approximately 3.4 x 10^{-4} nm (3 x 10^{-3} cm^{-1}). The residual 1064 nm pulses (that is, the infrared light that remains after the frequency-doubling process) and the 532 nm pulses exit the Nd:YAG as collinear beams, which are then directed vertically through a beam pipe and through a hole in the upper table.

2.1.2 Pulsed Dye Laser (PDL)

Once on the upper table, the green and infrared beams from the Nd:YAG laser enter a pulsed dye laser, or PDL [Spectra-Physics Quanta-Ray PDL-3]. Inside the laser, a dichroic mirror first separates the two beams. The 1064 nm beam passes straight through the PDL. The 532 nm beam pumps amplifier and oscillator dye cells. The lower table has dye circulators with a mixture of laser dyes [Rhodamine 590 and Rhodamine 610] in a methanol solvent. The laser dye circulating through the dye cells serves as the lasing medium for the PDL. An adjustable grating in the oscillator, controlled by an analog controller [QUESTEK 5220B] also located on the upper table, selects the lasing wavelength. The lasing wavelength of the PDL is broadly tunable over a range of about 10 nm for the dyes used in these tests. This range can be extended further by changing laser dyes if other wavelengths are desired. For the mixture of laser dyes used in this

26

experiment and for output pulse energies greater than or equal to 90% of peak performance, this range is from 567nm to 577nm (17,637-17,331 cm^{-1}). In the present experiments, the fifth order of the grating was used. This resulted in a measured spectral linewidth of 5 x 10^{-3} nm ± 8 x 10^{-4} nm (0.16 cm^{-1} ± 0.025 cm^{-1}).

2.1.3 Wavelength Extender

After exiting the PDL, the 1064 nm beam and the yellow (~574 nm) beam enter a wavelength extender [Spectra-Physics Quanta-Ray WEX-1C]. The yellow beam is frequency-doubled to a wavelength between 283.5 nm and 288.5 nm (35,273-34,662 cm^{-1}) in the first crystal. This wavelength is appropriate for exciting some of the A←X(1,0) lines of hydroxyl (OH) that fall between about 280 nm and 285 nm (35,077-35,714 cm^{-1}). In fact, there are alternate ways to generate UV light for probing NO. However, this method of doubling and then mixing (see below), along with this particular choice of dyes, conveniently generates this intermediate wavelength. This extends the capability of the system to include OH PLIF, for combustion studies where OH is a more logical choice than NO as the probed species.

For excitation of NO, the ~287 nm beam is mixed with the 1064 nm beam in the second crystal of the WEX. The resulting output is normally tuned to a wavelength of 226.256 nm, chosen to excite the strongly fluorescing spectral lines of NO near the Q_1 branch head. A detailed discussion of line-selection criteria is given in Chapter 3. In this notation, Q indicates that the rotational quantum number J is the same for both the upper and lower states of the transition (i.e., $\Delta J=0$). The subscript 1 indicates that, in both the upper and lower states involved in the transition, J is related to N by $J=N+1/2$, where N is

27

the quantum number for total angular momentum, excluding electronic and nuclear spin. See section 3.1 for a more thorough explanation of the molecular spectroscopic notation used to describe the nitric oxide transitions probed in these experiments.

The efficiency of doubling and mixing in the crystals of the WEX is a function of wavelength, temperature, and crystal angle (as well as irradiance). Consequently, the crystals must be rotated when the angle of the grating in the PDL (and therefore, its output wavelength) is changed, or if the temperature of the crystals change. Although this angle can be adjusted manually, the WEX has an electronic tracking feature, which uses a feedback loop to optimize the crystal angles to produce maximum beam intensity as the wavelength is scanned. The resulting beam has a central wavelength that is tunable from 224 nm to 227 nm (44,672 cm^{-1} to 44,061 cm^{-1}) with a measured spectral linewidth of 2 x 10^{-3} nm (0.4 cm^{-1}) and an energy of 0.8-1.5 mJ per pulse.

2.1.4 Frequency-Monitoring Gas Cell

Figure 2.1 contains a diagram of the upper table of the mobile PLIF cart. A gas cell used for monitoring the frequency of the laser is located next to the WEX. After exiting the WEX, a fraction of the beam is picked off by a quartz [UV-grade fused silica] window, creating a weak beam. A second such window directs a portion of this weak beam onto a white card (not shown), which fluoresces in the visible when illuminated with the ultraviolet beam. This card is viewed by a photodiode [Thorlabs, Inc. DET210], hereafter referred to as the laser photodiode. The laser photodiode is used to monitor changes in the laser's energy and correct data for any shot-to-shot fluctuations during wavelength scans.

28

It is also desirable to monitor the level of laser beam transmission through the gas cell, which will decrease when the laser frequency is tuned to a resonance in nitric oxide and photons are being absorbed by the gas. In order to measure this transmission, the beam created by the first quartz window and transmitted through the second window is directed into the low-pressure gas cell. This gas cell has been evacuated and filled to 6 kPa with a 5% NO, 95% N_2 mixture. After passing through the gas cell, the beam terminates on a card (not shown), where it is viewed by a second photodiode, hereafter referred to as the absorption photodiode, which measures the intensity of light transmitted through the gas cell. Additionally, a photomultiplier tube, or PMT [Thorn EMI 9781B], is mounted to the gas cell at 90° to the beam propagation direction. A filter [Schott UG5 Filter Glass] in front of the PMT blocks out scatter at the laser's wavelength. In addition, a neutral density filter [ND 1] in front of the PMT reduces the incident light intensity by 90% so that the voltage supplied to the PMT (in the present work, −600 V) can be of sufficient magnitude so as to ensure that it is operating in a linear response regime.

When the laser is tuned to an allowed optical transition in NO, the beam is partially absorbed and then reemitted as broadband fluorescence by the NO in the cell. The absorption photodiode then measures a corresponding decrease in the light transmitted through the gas cell, while the PMT measures the relative intensity of the resulting fluorescence. If the laser wavelength is then detuned from the absorptive transition, the NO in the cell no longer absorbs the beam, the absorption photodiode will register an increase in transmitted intensity, and the PMT will register a decrease in fluorescence intensity. These data can be recorded and normalized for fluctuations in laser intensity by the readings from the laser photodiode. In this manner, the laser can be scanned over a

29

range of wavelengths and NO fluorescence and transmission spectra can be recorded. Chapter 3 contains further details on the spectrum of NO. This gas cell monitoring system allows the system operator to ensure that the laser is initially tuned to the selected transition in NO, and that it remains tuned to that transition during the course of a measurement. Additionally, a wavemeter [High Finesse WS6-UV Pulsed Laser Wavelength Meter] was sometimes available to verify the laser's frequency and linewidth.

2.1.5 Spectral Scans

In order to ensure that the laser was tuned to the correct wavelength, spectral scans were obtained using the gas cell monitoring system described above. The spectra that result from these scans allow a determination of the particular transition of nitric oxide that is being excited for a given wavelength setpoint (the wavelength indicated on the scan controller of the PDL is not accurate enough to ensure that the laser is tuned to the center of a specific spectral line). When acquiring data during a spectral scan, both the fluorescence signal from the PMT and the transmitted intensity through the gas cell are normalized by a simultaneous measurement of the laser intensity prior to the gas cell to correct for shot-to-shot variations in laser intensity. The resulting spectra are displayed in Fig. 2.3 and Fig. 2.4. Note that the peak measured signal occurs at a wavelength of 226.256 nm. This spectral line was chosen for flow visualization, primarily because it gave the maximum overall fluorescence signal.

30

Measured
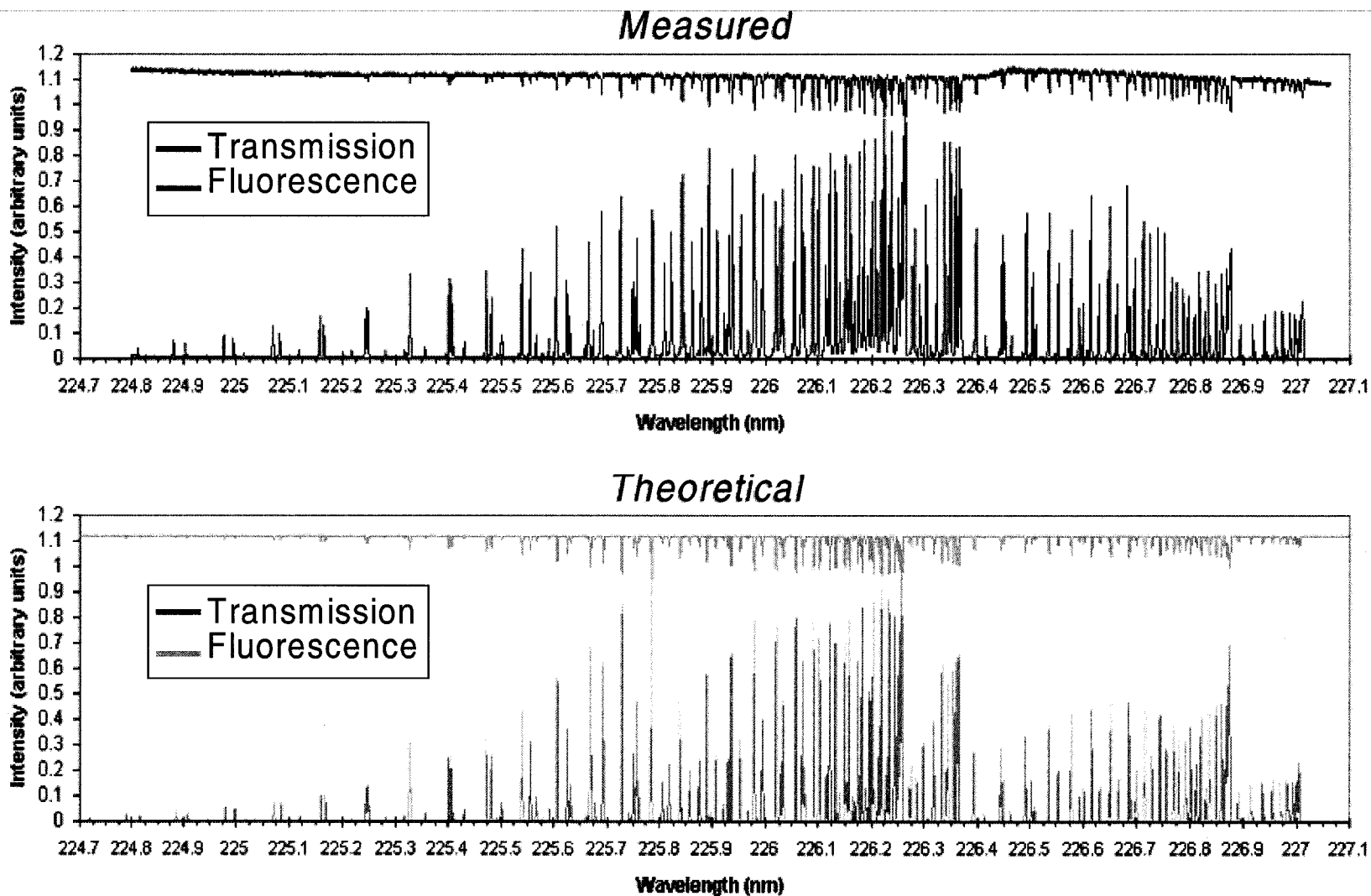
Theoretical

Figure 2.3: Measured and theoretical nitric oxide PLIF excitation spectra. Relative intensity (normalized by the maximum fluorescence intensity) is plotted versus the UV excitation wavelength of the laser. Dips in transmission intensity indicate photon absorption by the gas for laser frequencies that coincide with molecular resonances in NO.

31

In Fig. 2.3, the top graph shows the *measured* normalized fluorescence (red) and

transmission (dark blue) spectra. The bottom graph shows *calculated* theoretical

fluorescence (orange) and transmission (light blue) spectra. In Fig. 2.4, measured and

calculated spectra are plotted together on the same graph and displayed for two smaller

regions of the spectrum. The upper graph shows portions of the R_1+R_{21}, S_{21}, Q_1+Q_{21}, and

R_2 bands (also called *branches*) while the lower graph shows the O_{12} band head.

Rotational quantum numbers label the individual spectral lines. This notation is

explained in greater detail in section 3.1.
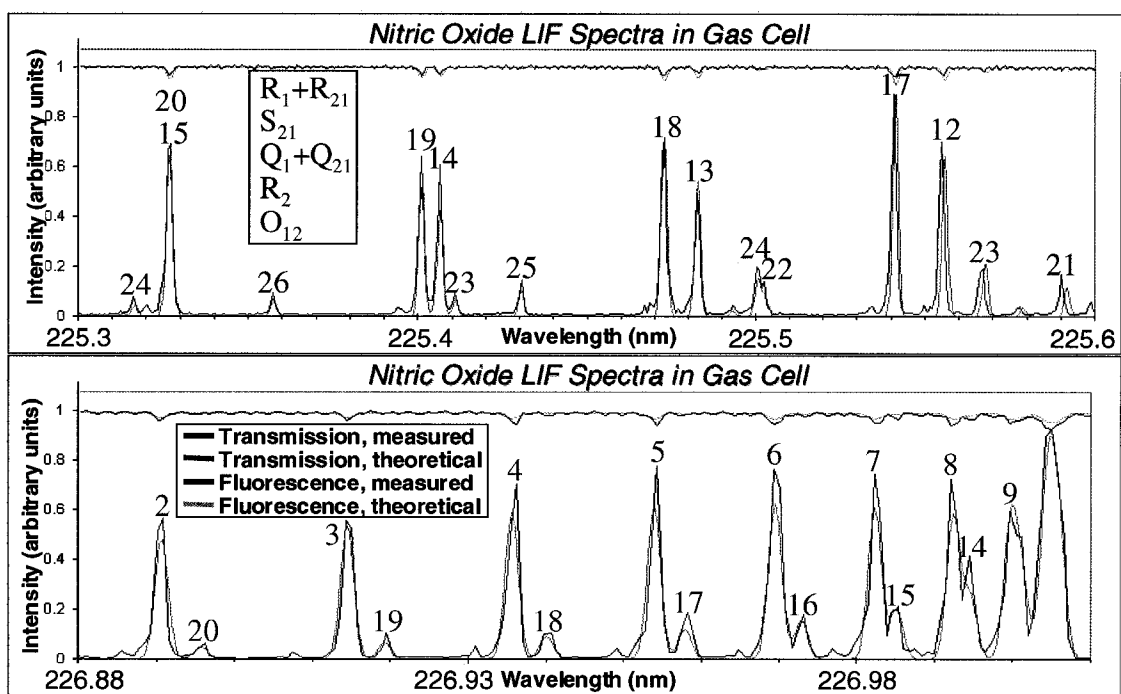
Figure 2.4: Two smaller regions of the nitric oxide spectrum. Rotational quantum
numbers label the individual spectral lines.

The theoretical fluorescence spectra in Fig. 2.3 and Fig. 2.4 were calculated using

LIFBASE, a spectral simulation software program developed by Jorge Luque and Dave

Crosley (Luque and Crosley 1999). These spectra were generated for room temperature

(295 K), with the theoretical laser linewidth fitted to the spectral linewidth measured from the experimental spectrum (2×10^{-3} nm). A qualitative (meaning only relative intensities are significant) theoretical absorption spectrum was generated by using the calculated theoretical fluorescence spectrum and the Beer-Lambert law:

$$I = I_0 e^{-\alpha cL} \tag{2.1}$$

Here, I is the calculated transmitted intensity, $\alpha = \alpha(\lambda_{laser})$ is the effective absorption coefficient of NO as a function of the laser's wavelength λ_{laser}, c is the effective concentration, and L is the measured path length through the gas cell. The value of the intensity of the calculated fluorescence spectrum was substituted for $\alpha(\lambda_{laser})$ at each value of the laser's wavelength. This assumes that the transition is not being saturated by excessive laser power, but rather, that fluorescence and absorption are related linearly. Finally, I_0 and c were fitted to match the magnitude of the measured absorption spectrum.

2.1.6 Sheet-Forming and Positioning Optics

The majority of the UV beam leaving the WEX passes through a hole in the end panel of the enclosed laser cart. Upon exiting the laser cart, the beam is directed through sheet-forming lenses and into the test section by a series of turning prisms. Anti-reflection coated prisms were selected instead of mirrors to allow transmission of laser beams in the range of 220-300 nm so that one set of optics could be used for both NO and OH fluorescence experiments. A schematic depicting two sheet-forming lens arrangements is presented in Fig. 2.5.

33

Plano-convex cylindrical lens + spherical lens
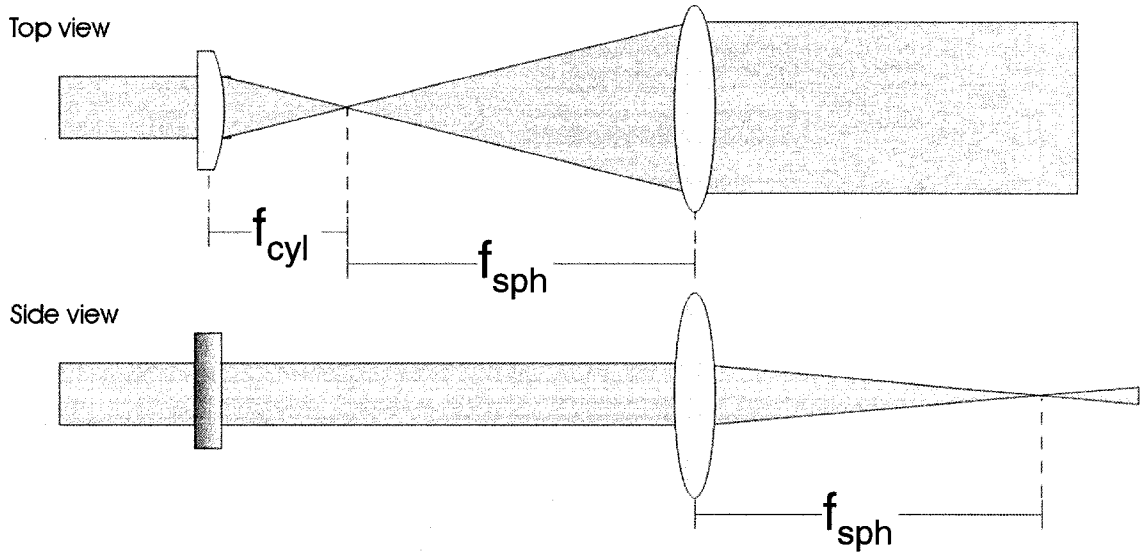
Plano-concave cylindrical lens + spherical lens
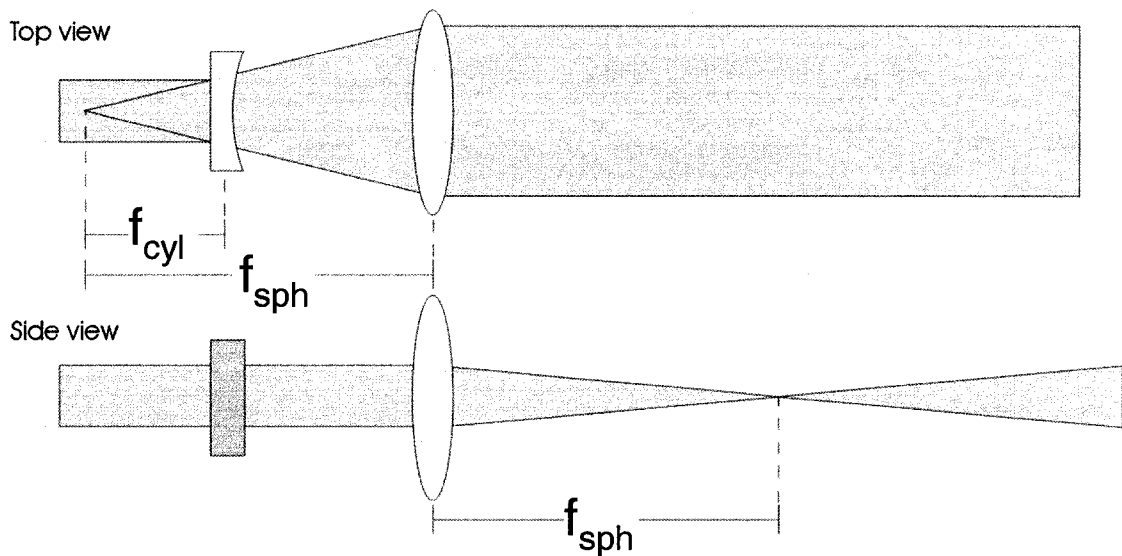
Figure 2.5: Laser sheet forming optics. A cylindrical lens with focal length f_{cyl} focuses the beam in one dimension. A spherical lens with focal length f_{sph} collimates the beam in this dimension and focuses it in the other dimension. The arrangement shown in the upper figure was used in the present experiments

34

The first lens is a plano-convex cylindrical lens, which causes the beam to focus and then diverge in one dimension. In these experiments, the focal length of this cylindrical lens was either 36 mm or 72 mm, depending on the desired width of the laser sheet. The second lens is a spherical lens, which collimates the beam in the first dimension and loosely focuses it in the other dimension. The focal length of the spherical lens was either 1 m or 0.5 m, depending on the desired field of view and the choice of cylindrical lens. Because the spherical lenses were 4 inches in diameter, the maximum field of view with a collimated laser sheet was 4 inches. For some cases, where a field of view greater than 4 inches was desired, the distance between the sheet-forming optics was reduced, resulting in a slightly diverging laser sheet and a larger probed region. The resulting laser sheet was between 76 mm (3 in.) and 178 mm (7 in.) wide with a measured FWHM (full width, half maximum) of 0.2 mm thick in the measurement region. The thickness of the laser sheet is the limiting factor in determining the system's spanwise (out-of-plane) spatial resolution. A motorized translation stage [Velmex single axis BISLIDE Tandem Positioning System] translates one prism and both focusing lenses, allowing the spanwise position of the laser sheet to be adjusted in increments of 0.005 mm. The scan rates and scan distances can be programmed and started using an external, hand-pressed trigger, allowing the motion of the translation stage to be coordinated with the acquisition of images. By translating the measurement plane through the flow, three-dimensional volumetric data can be obtained.

35

2.1.7 Fluorescence Imaging System

Broadband fluorescence from the measurement region is imaged by an intensified charge-coupled device (CCD) [Princeton Instruments PI-MAX® model 7483-0008]. An intensifier is especially important in UV imaging applications, as the CCD itself has a low sensitivity in the UV, but the phosphor coatings used in an intensifier generally result in conversion of incoming photons to visible wavelengths. A UG5 Schott Glass filter placed in front of the camera blocks out most of the light at the laser's wavelength. The camera has a thermoelectric cooler, which cools the detector to -20°C in order to reduce the amount of dark charge and thus improve the signal-to-noise ratio. Data acquisition and storage is controlled via software [Roper Scientific WinView32, Version 2.5.15.5]. A recessed window on the side of the test section allows the camera to be as close as possible (67 cm) to the imaged region when necessary.

2.1.7.1 Image intensifier

The image intensifier has four primary components: a photocathode, microchannel plate, phosphor-coated fluorescent screen, and fiberoptic bundle. Fluorescence captured by the imaging optics falls on the photocathode at the input to the image intensifier, and a percentage of the incident photons are converted into electrons. Gating is achieved by controlling the electric potential of the photocathode relative to the grounded (0 V) input of the microchannel plate (MCP). When the intensifier is gated *on*, the photocathode is at a relatively negative potential (-200 V), and so the electrons generated by incoming photons are accelerated toward the MCP. The output of the MCP is at a positive potential (between +800 and +1100 V, depending on the gain setting) relative to the grounded

36

input of the MCP, and so electrons are further accelerated as they pass through the MCP. The MCP introduces electron gain, as additional electrons are generated when electrons strike the walls of the MCP channels. As the electrons exit the MCP channels, they are accelerated by a constant ~8 kV potential toward the face of the fluorescent screen. When they strike the phosphor coating on the surface of the screen, photons are released. These photons are then transmitted to the surface of the CCD array through a fiberoptic bundle (Princeton Instruments, 2006).

2.1.7.2 Spatial resolution

Two different camera lenses were used to image a region of the flow onto a 512 pixel x 512 pixel CCD array. The first was a 105 mm focal length UV-Nikkor lens. With this lens, the imaged region was between 69 mm x 69 mm (2.7 in. x 2.7 in.) and 101 mm x 101 mm (4.0 in. x 4.0 in.), depending on the distance between the camera and the imaged region. This resulted in spatial resolutions ranging from 5.1 to 7.4 pixels/mm (129 to 188 pixels/inch). The second lens was a 45.5 mm focal length Cerco model 2073 UV lens. With this lens, the imaged region was between 169 mm x 169 mm (6.7 in. x 6.7 in.) and 175 mm x 175 mm (6.9 in. x 6.9 in.), resulting in a spatial resolution of 2.9 to 3.0 pixels/mm (74 to 77 pixels/inch). At high gain settings, the intensifier introduces blurring that may reduce the spatial resolution by up to a factor of two. Together, the combination of the imaging optics, the distance between the imaged region and the CCD, the size of the CCD array, and intensifier blurring represent the limiting factors in determining the in-plane spatial resolution of the imaging system. The out-of-plane resolution is

37

determined by the 0.2 mm FWHM measured thickness of the laser sheet, as previously mentioned.

2.1.7.3 Temporal resolution

The camera controller [Princeton Instruments ST-133 Controller model 7501-0030] houses some of the camera gating and timing electronics, along with the camera power supply, and user input/output connectors. The controller contains an integrated programmable timing generator (PTG) which supplies the high-voltage pulses to the intensifier and controls the timing and width of the gating pulse. Gate widths as fast as 50 ns are possible with this system, although we observed attenuation of the captured intensity for gate durations of less than about 200 ns, even when observing a 10 ns event like scattered laser light. This is likely due to the finite resistance of the photocathode in response to the applied gating voltage, resulting in a trapezoidal (rather than "top-hat") temporal response. For the present work, the gate width was normally set to 1000 ns in order to capture the maximum fluorescence possible. The 1/e fluorescence lifetime of nitric oxide under the conditions of these tests had a maximum of about 220 ns. For long exposure times, this lifetime determines the temporal resolution of the technique. Higher temporal resolutions are limited by the intensifier gate width. Even with the large flow velocities encountered in theses experiments (on the order of 1 km/sec), the flow was essentially frozen in each image, with minimal (2 or 3 pixel) blurring due to motion of the flow during the exposure time. This temporal resolution, together with the spatial resolution of the system, was sufficient to resolve flow structures of interest.

38

2.1.8 Electronic Components

Electronic components for controlling data acquisition and coordinating the timing of other components of the PLIF system are mounted on a mobile rack, located near the laser cart. Outputs from the laser photodiode, absorption photodiode, and PMT are passed through a gated integrator and boxcar averager [SRS Model 280]. A LabVIEW program running on a rack-mounted computer allows fluorescence and transmission spectra to be acquired. The program sends signals to the wavelength controller of the PDL to vary the wavelength of the laser and records the outputs of the photodiodes and PMT through the integrator for wavelength scans. Firing of the laser flash lamps, laser Q-switch and the CCD intensifier gate all must be coordinated. Timing of trigger pulses for each of these components is controlled through a LabSmith LC880 Programmable Experiment Controller [Trigger™ software, version 5.02]. The rack also houses the camera controller and the high-voltage power supply for the PMT attached to the frequency-monitoring gas cell.

2.2 Facility Overview

The results presented herein were obtained after installing the mobile PLIF system in the 15-inch Mach 6 wind tunnel facility at the NASA Langley Research Center. The wind tunnel was not operated as such; instead, the test section of the wind tunnel served as a long-duration sub-atmospheric pressure chamber. The data acquisition system of the tunnel was also used to record temperatures, pressures, and flow rates. Using a combination of the tunnel vacuum pumps and steam ejector, constant test chamber pressures as low as 1 Torr (133 Pa, 0.02 psi, 0.0013 atm) were achievable. In practice,

39

pressures of 2 Torr (267 Pa, 0.04 psi 0.0026 atm) were routinely attained, while pressures close to 1 Torr were only attainable on days when all system components were functioning optimally, and the outside temperature was relatively cool. Tests were run with chamber pressures as high as 72 Torr (1.4 psi, 9.6 kPa, 0.1 atm), although 90% of runs required a chamber pressure under 10 Torr (0.2 psi, 1.3 kPa, 0.013 atm).

Two entries into this facility were made. The first entry was from 1 September through 15 November 2004; the second phase of testing was conducted between 18 October 2005 and 8 February 2006. A schematic of the experimental layout is presented in Fig. 2.6 and a photograph of the system as installed in the wind tunnel facility is presented in Fig. 2.7. The enclosed laser cart is positioned to allow tunnel operators to open and close the door to the test section as required. The laser sheet enters the test section through a window on the top of the test section. The motorized translation stage mounted above the tunnel allows the laser sheet to be scanned spanwise across the test section. This can be done either between tunnel runs or during a run, depending on the region of interest within the flow. Recessed windows on the side of the test section allow the intensified CCD camera to be as close as possible to the measurement region, as discussed in section 2.1.7.2 above.
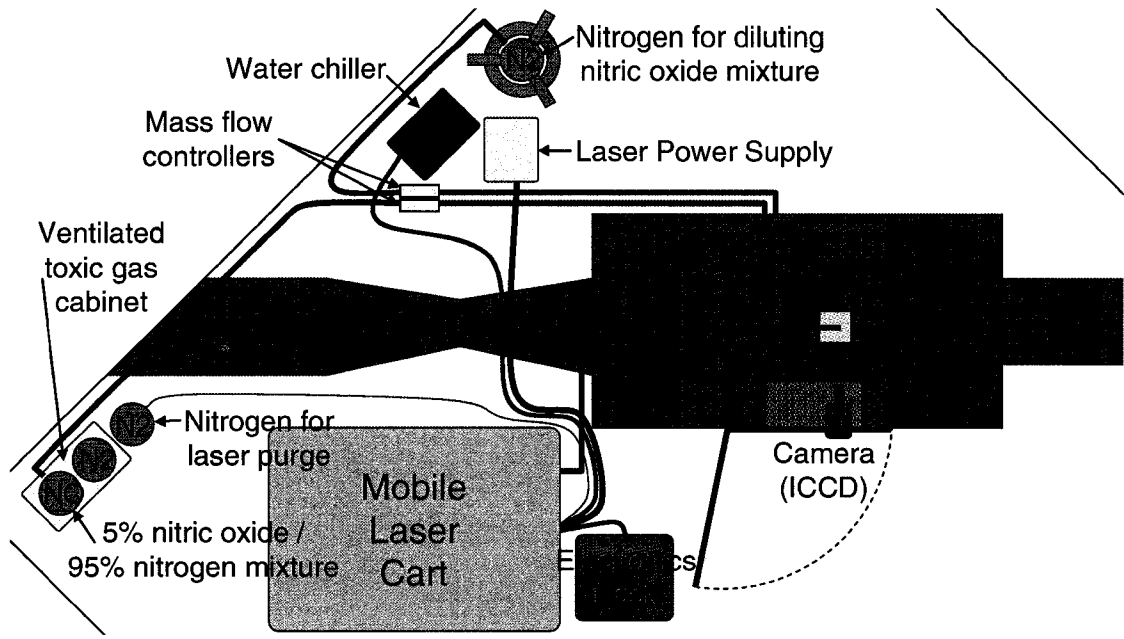
Figure 2.6: Overhead view of PLIF system as installed for underexpanded jet tests. The path of the laser is depicted with a purple line. Stainless steel gas plumbing lines connect gas bottles in the gas cabinet and behind the test section to mass flow controllers. The gas is then plumbed into the back of the test section.
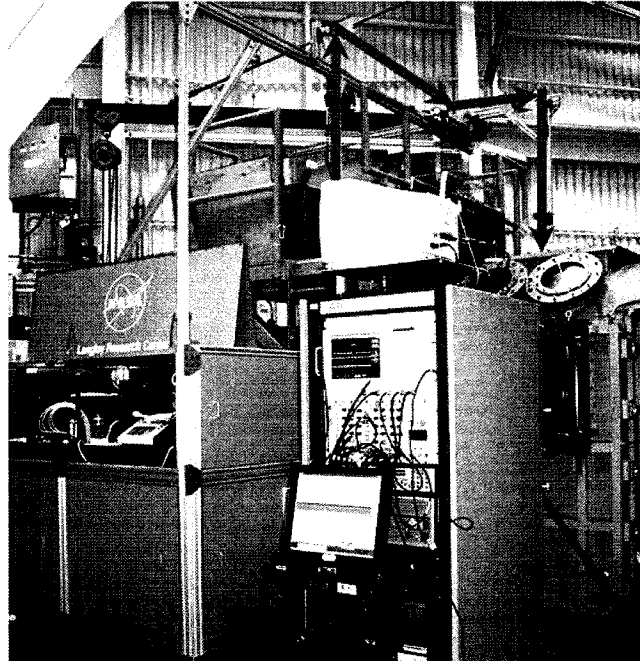
Figure 2.7: Mobile PLIF system installed in 15-inch Mach 6 Air Wind Tunnel. Arrows indicate the path of the laser. The mobile laser cart is shown with the upper panel open. The blue cart in the foreground is the electronics rack.

41

2.2.1 Gas Seeding System

Nitric oxide was chosen as the probe species for the reasons described in section 1.4. Because NO is not naturally present in this facility, it must be seeded into the flow either locally or globally. The main disadvantage of using NO is that it is toxic and corrosive, and many safety precautions had to be incorporated into the NO plumbing system. A forced-ventilation gas cabinet [Matheson Tri-Gas] houses a bottle with a 5% NO gas mixture (see discussion below). Toxic gas detectors [Crowcon Detection Instruments, Ltd.] located in the gas cabinet and on the side of the laser cart set off audible and visible alarms when NO concentrations above 25 ppm are detected (25 ppm is the time-weighted average maximum permissible exposure level for an 8 hour work day determined to be safe by OSHA standards). The gas cabinet includes a pneumatic valve designed to shut off the NO supply if either detector measures 25 ppm, if the ventilation for the gas cabinet fails, or if an excessive flow rate of NO is measured. The gas cabinet also houses a bottle of nitrogen, which can be used both to dilute the NO mixture being seeded into the test section, and to purge all plumbing lines of NO at the end of a test. In these tests, this bottle of nitrogen was used for purging purposes, and a second bottle of nitrogen, located behind the test section, was used to dilute the NO mixture.

Five different mass flow controllers [Teledyne Hastings, models HFC-202, HFC-203 and HFC-302] were used in these tests. Their maximum flow rates were 1, 3, 10, 50, and 100 slpm (standard liters per minute). Gas flow rates were controlled by two of these mass flow controllers. The first mass flow controller was housed inside the gas cabinet. It controlled the flow rate of the gas from the bottle containing nitric oxide. The second

42

mass flow controller was located behind the test section and controlled the rate of nitrogen dilution. Gas from the two mass flow controllers was combined inside the test section, to minimize the number of potential leak sources for toxic gas in the work space.

Between the two test entries, the bottle containing a 5% NO / 95% N_2 mixture had been moved to an outdoor storage area for safety reasons. When the second test entry began, a mistake resulted in a bottle containing a 5% NO / 95% He (helium) mixture being installed, rather than the 95% N_2 bottle. This did not have a large impact on the results of the experiments, as the mixture containing nitric oxide was diluted by nitrogen from the second bottle in the cabinet, resulting in a 0.5% NO / 9.5% He / 90% N_2 mixture in the plenum. However, it did require correcting measured mass flow rate data by a gas correction factor, as well as accounting for the effects of helium in gas dynamic calculations (e.g. the calculation of exit Reynolds number). The viscosity of a gas with this mixture is approximately 1% higher than the viscosity of a gas with a 0.5% NO / 99.5% N_2 mixture. While this is unlikely to have a large effect on our determination of transition criteria, it is a detail that should be taken into consideration in future comparisons with computational results.

2.2.2 Test Hardware

The hardware in these tests was designed to have a simple geometry for modeling in computations. The dimensions of the test hardware and the test cases that were studied were designed to be scalable to the range of conditions expected in a space shuttle orbiter re-entry profile. Test hardware consisted of an insulated, heated stainless steel plenum and nozzle, housed inside a vacuum chamber test section. Inside the test section, gas

43

from the 5% NO bottle and the 100% N_2 bottle was combined. The gas mixture was introduced into the plenum where it was convectively heated to approximately 500 K by the surrounding metal. The gas was heated to attain flows with Reynolds numbers lower than could be achieved with unheated gas (see section 4.2.4 for a definition of *Reynolds number*). The steel of the plenum was itself heated by electrical heat tape wrapped around the exterior of the model and covered with insulation. Due to the large thermal mass of the model, preheat times of approximately four hours were required and fine-tuning of the gas temperature was not feasible.
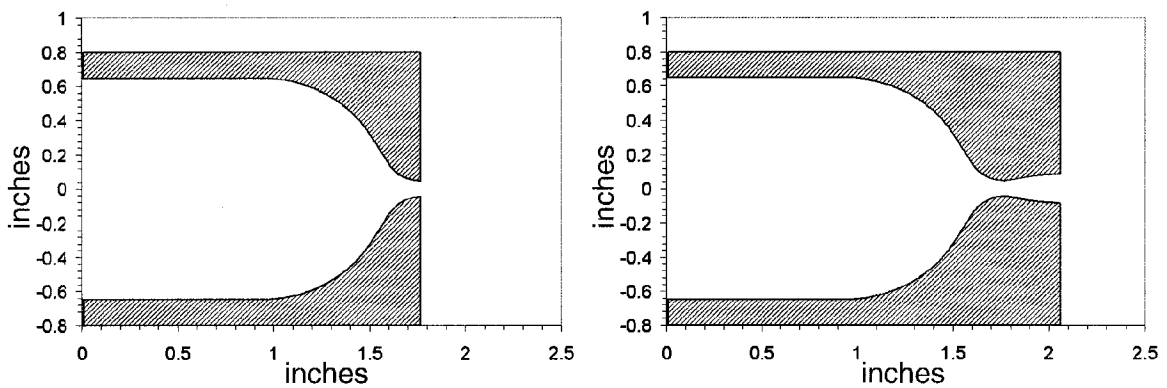
Figure 2.8: Sonic and supersonic nozzle geometries. Given a sufficient pressure difference between the nozzle plenum and ambient conditions, the Mach number at the exit of the converging nozzle (left) will be 1. Similarly, the Mach number at the narrowest part (the throat) of the converging-diverging nozzle (right) will also be 1; the designed exit Mach number of this nozzle is 2.6. The exit diameters of these nozzles are 0.095 in. (2.4 mm) and 0.164 in. (4.2 mm).

After passing through the plenum, the heated gas exhausted through a nozzle and into the vacuum chamber. Two different nozzle geometries were used in these tests. The first was a converging "sonic" nozzle (so called because the Mach number of the flow at the nozzle exit is 1). It had an exit diameter of 2.4 mm (0.095 in.). The second was a converging-diverging supersonic nozzle, with a design exit Mach number of 2.6 and an

44

exit diameter of 4.2 mm (0.165 in.). The converging portion of the supersonic nozzle was identical to that of the sonic nozzle. See section 4.2 for an explanation of flow through both types of nozzles. Diagrams of both nozzle geometries are illustrated in Fig. 2.8. Mass flow controllers adjusted the flow rates, which determined the plenum pressure and nozzle exit Reynolds number. A schematic including these elements of the test apparatus is shown in Fig. 2.9.
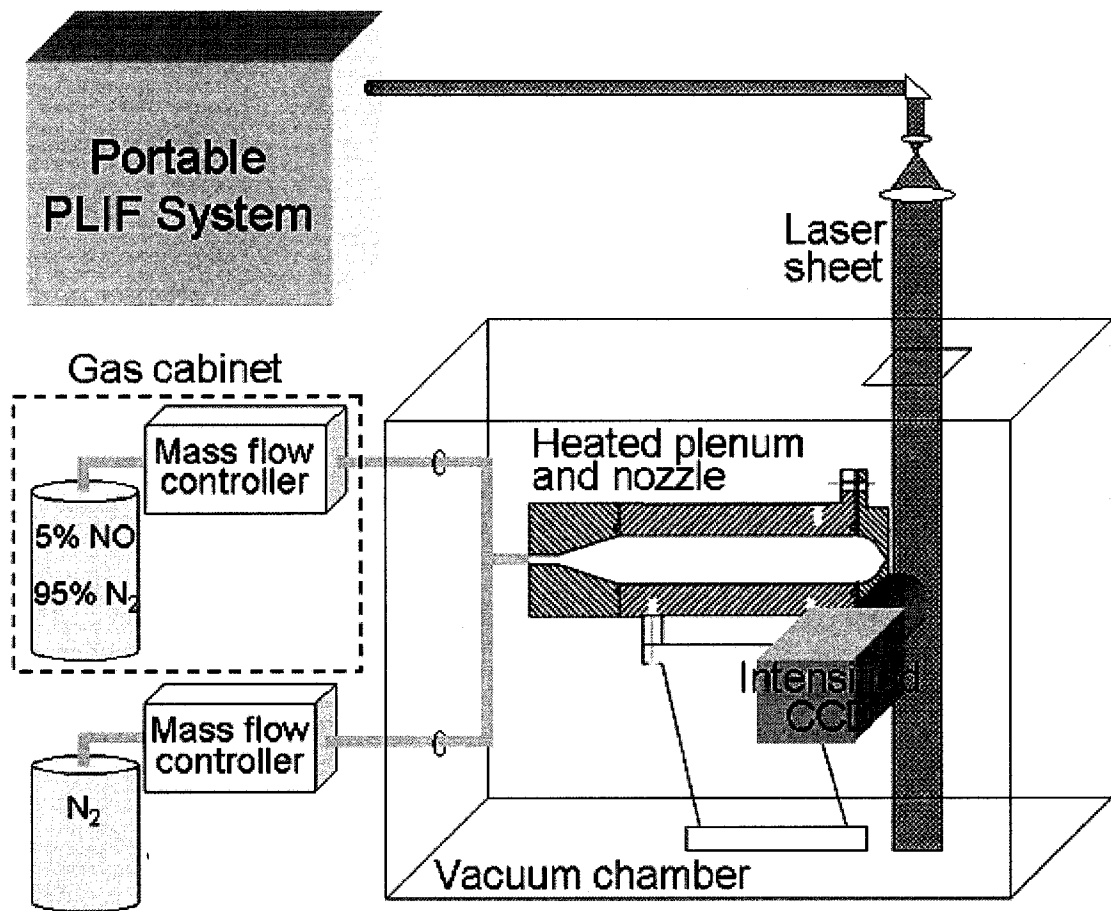
Figure 2.9: PLIF system and experimental hardware. Gas is plumbed through a heated plenum and nozzle into a vacuum chamber. A laser sheet enters the top of the vacuum chamber and excites nitric oxide molecules in the flow. An intensified CCD camera positioned at right angles to the laser sheet images the fluorescence.

45

A subset of test cases investigated the impingement of a jet on a flat plate. The impingement target used for this purpose was a 4 inch (101.6 mm) diameter stainless steel disk. Figure 2.10 shows a diagram and Fig. 2.11 shows a photograph of the impingement target and the plenum/nozzle hardware.
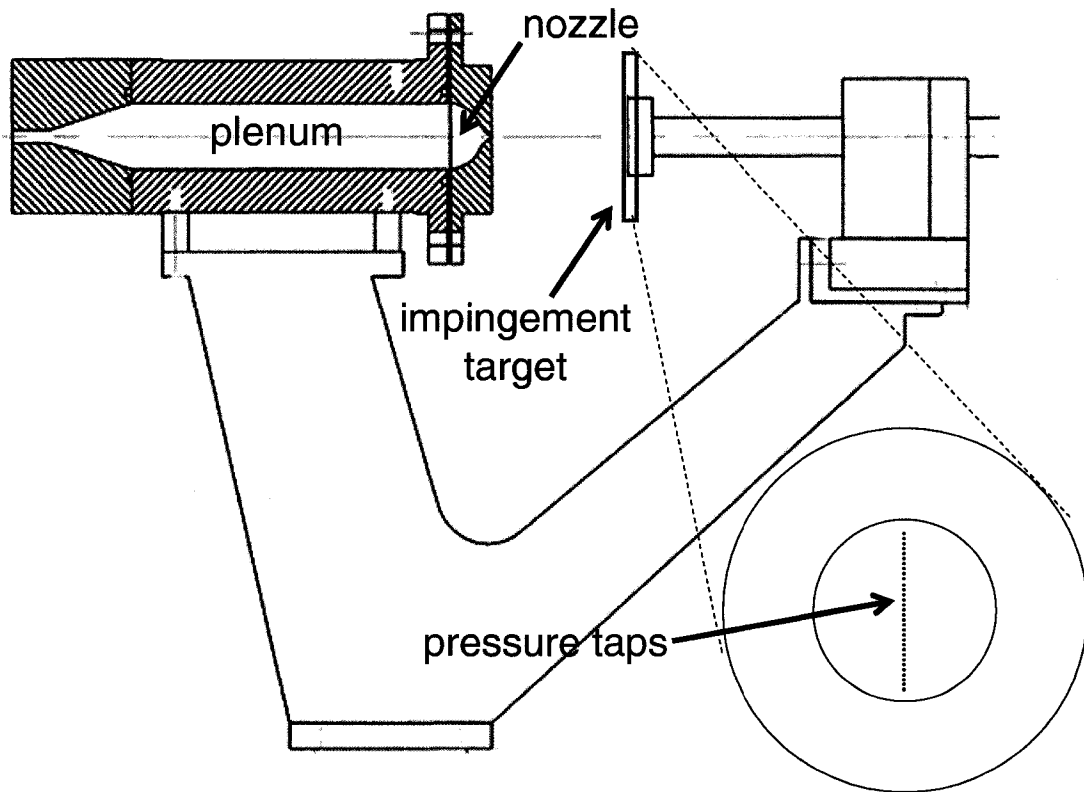
Figure 2.10: Plenum and nozzle hardware with impingement target. The impingement disk includes 2-inch diameter central disk instrumented with 32 pressure taps, which appear almost as a continuous line down the center of the disk in the expanded view of the target surface. The additional collar around the disk brings the impingement target size to 4 inches in diameter. The actual hardware includes a hinge (not shown) that allows the impingement angle to be varied.

For the majority of cases, the impingement disk was oriented normal to the jet axis (which is defined to be a 90° impingement angle). Two configurations included non-normal impingement angles of 45° and 60°. (For these cases, the target was rotated

46

clockwise, as viewed from the camera viewing angle, about the horizontal axis perpendicular to the jet axis.) The impingement distance (the distance between the nozzle exit and the plate) was varied between 1 in. (25.4 mm) and 5 in. (127 mm). In practice, changing impingement distance or angle required approximately a half day of down time, and so the data taken for a given configuration were generally acquired on the same day. The disk was composed of two parts—a central 2 inch (50.8 mm) diameter disk surrounded by a 1-inch wide collar, as shown in Fig. 2.10.
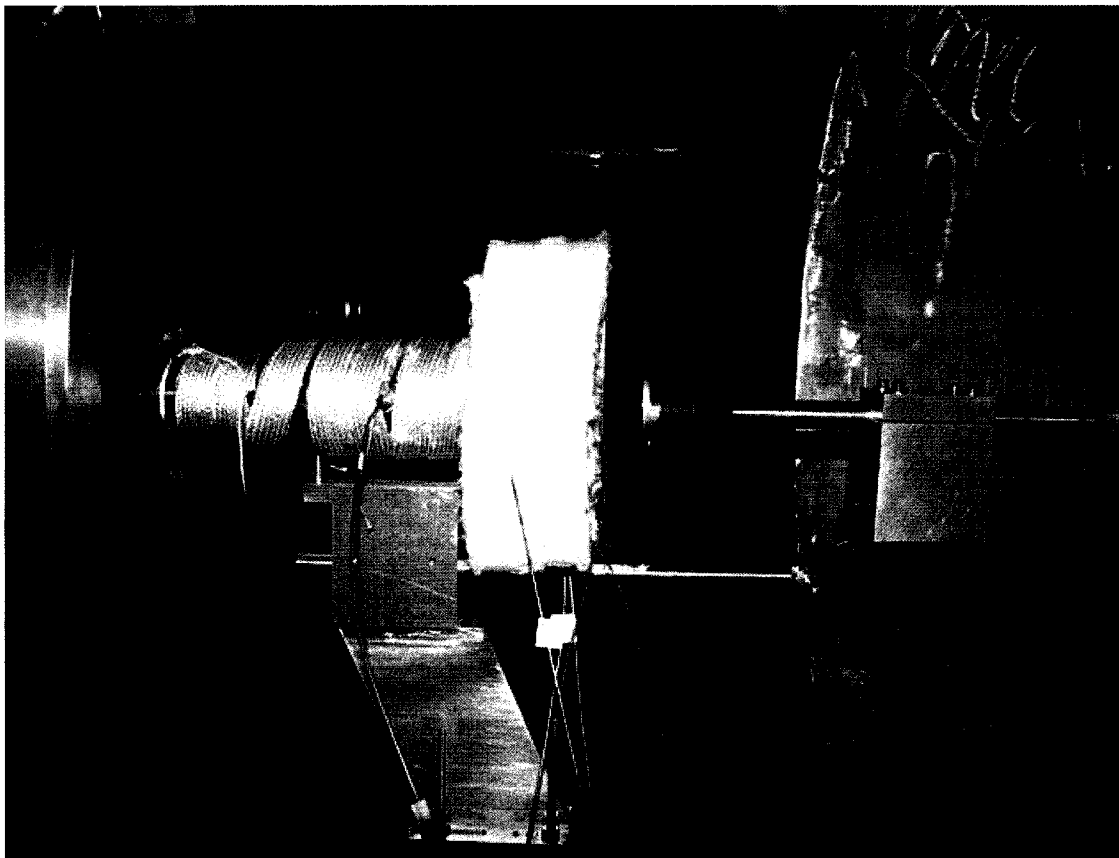
Figure 2.11: Photograph of plenum, nozzle, and impingement disk hardware installed in test section. Some insulation has been removed to reveal the plenum and heat tape underneath. Protruding wires are instrumentation from thermocouples and pressure transducers.

47

2.2.3 Instrumentation and Data Acquisition

As seen in Fig. 2.10, the central disk of the impingement target was instrumented with 32 pressure taps down the center. They had internal diameters of 0.5 mm (0.021 in.) and were spaced ~1.1 mm (0.045 in.) apart. The taps were oriented in a vertical plane coincident with the plane of the laser sheet, on the jet centerline.

In order to stabilize the temperature of the test gas, the sides of the heated stainless steel plenum were covered with insulation. The nozzle exit plane was not insulated. A thermocouple under the insulation and against the model surface measured the metal temperature. Two thermocouples and one pressure transducer were inserted through feed-through holes in the model. They measured the gas temperature, T_0, and pressure, p_0, in the plenum, upstream of the converging nozzle. Measuring these quantities made it possible to calculate conditions at the nozzle exit, and therefore the exit Reynolds number, as described in detail in section 4.2.4. For the supersonic nozzle, an additional pressure transducer measured the pressure inside the nozzle, close to the nozzle exit.

48

CHAPTER 3

Theoretical Aspects of Laser-Induced Fluorescence Imaging

This chapter summarizes the factors governing the fluorescence of nitric oxide. The aim of this chapter is to provide a context for interpreting PLIF images and understanding the trends governing changes in intensity. First, the relevant aspects of diatomic spectroscopy will be introduced. This spectroscopic background will help to elucidate the features of NO excitation spectra. A detailed inspection of the fluorescence equation will then help to identify candidate spectral lines for flow visualization and for scalar-sensitive imaging, that is, imaging for which the fluorescence signal is proportional to scalar flow quantities (e.g. pressure, density, mole fraction). Finally, a brief introduction to flow-tagging velocimetry methodology will be presented.

3.1 Diatomic Molecular Spectroscopy

The laser system that has been used in this work is tunable over a range of wavelengths which excite the $A \leftarrow X(0,0)$ electronic transition of nitric oxide. The

49

numbers in parentheses are the *vibrational* quantum numbers of the (upper, lower) states of the transition. "X" refers to the ground *electronic* state; "A" refers to the first excited electronic state. All of the transitions considered herein involve exciting molecules from the ground electronic, ground vibrational state $X(v''=0)$ to the first excited electronic, ground vibrational state $A(v'=0)$ via single photon absorption. Note that single apostrophes label quantities associated with the upper state, double apostrophes label those associated with the lower state. This convention is derived from emission spectroscopy terminology, since the upper level is taken to be the initial state, and the lower level, the end state. These transitions are indicated by the notation: $A \leftarrow X(0,0)$. The more specific notation for these transitions is given by $A^2\Sigma^+ \leftarrow X^2\Pi_\Omega(0,0)$. See Palma (1999) and Herzberg (1950) for a more thorough explanation of the spectroscopic notation of nitric oxide.

Once molecules are electronically excited, fluorescence can occur at the same wavelength as the excitation, returning molecules to the state they occupied prior to excitation, or it can occur at longer, less energetic wavelengths. It is also possible that higher energy levels may be populated through collisions, resulting in fluorescence at shorter wavelengths than that of the laser. The temperatures (less than 600 K) and pressures (less than 16 psi, 110 kPa, 1.1 atm) that exist in the jet flows of this investigation are low enough that such collisions may populate higher rotational levels, but non-quenching vibrational excitation of the electronically-excited state is rare. However, vibrational excitation of the electronic ground state may result from fluorescence at wavelengths longer than the excitation wavelength. This type of fluorescence occurs when molecules relax to states with less energy than the excited state,

50

but more energy than the probed state. The ground and first excited electronic energy levels of nitric oxide are separated by approximately 5.5 eV, whereas the ground and first excited vibrational levels differ by about 0.3 eV. The vibrational quantum number of the lower level in the fluorescence transition may be non-zero, and so the observed fluorescence will occur via the A$\rightarrow$X(0,0-5) transitions. As discussed in Chapter 2, the fact that a large part of the fluorescence is spectrally distinct from the frequency of the laser allows a filter to be used that transmits fluorescence but blocks elastic scatter at the frequency of the laser. Such a filter blocks the majority of the fluorescence from the A$\rightarrow$X(0,0) transition.

Rotational quantum numbers of the states are also involved. As the frequency of the laser is varied, so is the *rotational quantum number* of the state that is being probed. The rotational quantum number of the ground state is not being varied directly, but rather, the energy difference between the upper and lower states is the variable quantity. If one considers all pairs of rotational quantum numbers in the upper (J') and lower (J") state and sorts all such allowed transitions by the energy difference between them, one finds that transitions with the same ΔJ tend to have similar energies. Transitions are seen to form groups based on their associated ΔJ. These groups (or *bands*) are labeled P, Q, and R, corresponding to ΔJ = -1, 0, +1, respectively.

But it is, of course, more complicated than this. The effect of electronic spin parity, that is, whether the spin of the electron is aligned or antialigned with the total angular momentum (excluding electronic and nuclear spin) of the molecule, also plays a role in splitting these transitions into groups. After the capital letter indicating the value of ΔJ for the transition, two subscripts—α and β—indicate the parity of the upper (α) and

51

lower (β) states involved in the transition. States with positive parity are labeled with a subscript of 1. Positive parity states are those in which the spin of the electron is aligned with the total angular momentum of the molecule N (excluding electronic and nuclear spin), such that J=N+1/2. Those with *negative parity*—where the spin of the electron is antialigned with the total angular momentum such that J=N-1/2—are labeled with a subscript of 2. By convention, repeated indices are dropped (e.g., Q_{22} becomes simply Q_2) (Herzberg 1950).

There exist four classes of transitions as distinguished by the spin parity of the upper and lower states: those in which the parity is *positive* in both the upper and lower state (and so the subscripts $\alpha\beta=11\rightarrow1$), those in which it is *negative* in both the upper and lower state ($\alpha\beta=22\rightarrow2$), those in which it is positive in the upper but negative in the lower state ($\alpha\beta=12$), and those in which it is negative in the upper but positive in the lower state ($\alpha\beta=21$).

Transitions with the same parity in the upper and lower state (i.e., with $\alpha = \beta$) are considered to be the main branches in the spectrum of the molecule, while those involving a parity flip are considered satellite branches. The primary selection rule for these transitions is $\Delta J =0,\pm1$. For every value of J'' (the rotational quantum number of the lower state), there are 3 possible values of ΔJ and 4 possible parity cases, resulting in 12 possible branches—6 main branches (P_1, P_2, Q_1, Q_2, R_1, R_2) and 6 satellite branches (P_{12}, P_{21}, Q_{12}, Q_{21}, R_{12}, R_{21}) (Palma 1999). Table 3.1 summarizes the notation most commonly seen in the literature. In the present text, the $\Delta N_{\alpha\beta}(N'')$ notation is used.

52

ΔJ	ΔN	α	β	$\Delta J_{\alpha\beta}\,(N'')$	$\Delta N_{\alpha\beta}\,(N'')$	$^{\Delta N}\Delta J_{\alpha\beta}\,(J'')$
-1	-2	1	2	P_{12}	O_{12}	$^{O}P_{12}$
	-1		1	P_1	P_1	P_1
	-1	2	2	P_2	P_2	P_2
	0		1	P_{21}	Q_{21}	$^{Q}P_{21}$
0	-1	1	2	Q_{12}	P_{12}	$^{P}Q_{12}$
	0		1	Q_1	Q_1	Q_1
	0	2	2	Q_2	Q_2	Q_2
	+1		1	Q_{21}	R_{21}	$^{R}Q_{21}$
1	0	1	2	R_{12}	Q_{12}	$^{Q}R_{12}$
	1		1	R_1	R_1	R_1
	1	2	2	R_2	R_2	R_2
	+2		1	R_{21}	S_{21}	$^{S}R_{21}$

Table 3.1: Different notations for the branches of the NO $A^2\Sigma^+ \leftarrow X^2\Pi$ transition. The first two columns list the change in rotational quantum number between the upper state and the lower state of each transition, where the Js are half-integer valued and the Ns are integer valued. The next two columns list the spin parity of the upper (α) and lower (β) state of the transition, with 1 corresponding to positive parity and 2 corresponding to negative parity. The notations listed in the last three columns denote entire branches, where the rotational quantum number would need to be specified to refer to a particular spectral line. This text uses the $\Delta N_{\alpha\beta}(N'')$ notation listed in the center of these three columns.

Alternative notations involve a change of basis and use the quantum number N to label states instead of J. This is sometimes more convenient, as J values are half-integers, whereas N values are integers. For the selection rule-allowed values of $\Delta J = 0, \pm 1$, possible values of ΔN are $0, \pm 1, \pm 2$. For branches labeled in this manner, O corresponds to $\Delta N = -2$ and S corresponds to $\Delta N = +2$. The six main branches are labeled the same as in the ΔJ notation, but the six satellite branches are labeled O_{12}, P_{12}, Q_{12}, Q_{21}, R_{21}, S_{21}. Of course, in order to fully specify a selected transition, one must define not only the *changes* in the quantum numbers, but also the specific quantum number of either the upper or lower level. It is conventional to use the quantum number of the lower level— either J'' or N''—for this purpose.

3.2 Laser-Induced Fluorescence

3.2.1 Two-level model

Laser-induced fluorescence can be divided into three main processes by considering a simple two-level model. Figure 3.1 shows a simple diagram of a two-level model. First, a molecule in energy level 1 absorbs a photon from the laser and moves to level 2; this is the excitation process. Second, the excited molecule may undergo collisions, relaxing back down to energy level 1 without emitting a photon; this will be called the energy transfer process. Third, the molecule may instead relax to the lower energy state by emitting a photon; this is the fluorescence process. The following sections describe each of these processes in more detail.

54

excited state

$$g_i EB_{12} \qquad A \lessgtr \qquad Q$$

$$\rho \chi_{NO} f_B \qquad\qquad\qquad \boxed{\;}\; 1$$

ground state
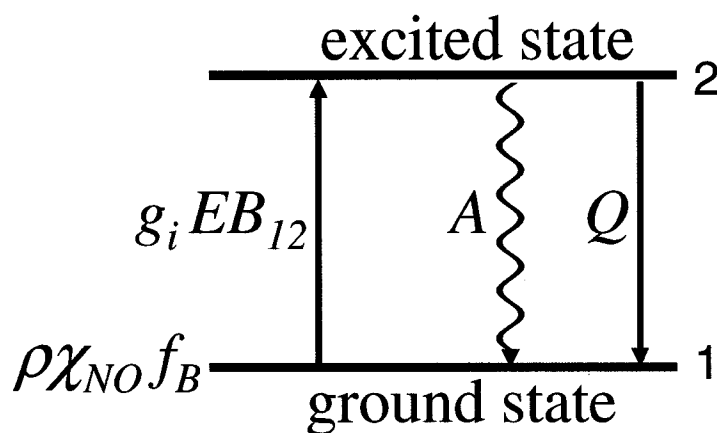
Figure 3.1: The two-level model. The number of molecules in level 1 depends on ρ, the gas density, χ_{NO}, the mole fraction of nitric oxide and f_B, the Boltzmann fraction. The fraction of molecules that are excited depends on g_i, the spectral overlap integral between the laser and the molecular transition, E, the energy in a laser pulse, and B_{12}, the Einstein transition probability for stimulated absorption. The amount of fluorescence depends on the relative rates of spontaneous emission and quenching. These rates are characterized by A, the Einstein transition probability for spontaneous emission, and Q, the collisional quenching rate.

3.2.1.1 Excitation

In order for the excitation process to occur, the laser must be tuned to a particular transition in the resonant species (nitric oxide in these experiments). The amount of light that is actually absorbed will depend on several factors. First, it will depend on the number of absorbers present, which is a function of gas density, species mole fraction, and the population of the probed state (or states, in the case of spectrally coincident transitions). The relative population of the probed state is governed by the Boltzmann fraction, and is a function of the rotational quantum number of the probed state and the temperature of the gas. Second, fluorescence will tend to increase with laser energy unless the laser energy is sufficiently high so as to deplete the probed state, in which case the transition is said to be saturated. Third, it will depend on the amount of overlap

55

between the spectral profile of the laser and the molecular absorption profile. The absorption profile can be broadened and shifted by several means, some of which are functions of temperature and pressure, as will be discussed in greater detail below. Finally, the amount of absorption depends upon the quantum mechanical probability of the absorption transition occurring, a rate which is characterized by the Einstein B coefficient for stimulated absorption.

3.2.1.2 Energy transfer

Once a molecule of the absorbing species has been excited to a higher electronic state, collisions may alter the energy of or depopulate the excited state. Collision processes that change the rotational (J or N) or vibrational (v) quantum number of the excited molecule are known as rotational energy transfer (RET) and vibrational energy transfer (VET), respectively. For the conditions encountered in our tests, VET is slow as compared to the fluorescence lifetime (Stephenson 1974). RET rates were calculated using LINUS (Palma 1998) over a range of conditions expected in the present experiments. They were calculated to be between a factor of 5 and 1,600 times faster than the spontaneous emission rate. The fluorescence lifetime expected in these tests is on the order of 200 ns. Molecules having undergone RET may still be in an electronically excited state, and so may still fluoresce.

An additional collisional process exists in which the excited molecule transfers energy to another molecule, and returns to the electronic ground state without emitting a photon. This process is known as *collisional quenching*. It serves as a loss mechanism because the excited state is depopulated non-radiatively, reducing the net amount of

56

fluorescence. In addition, quenching collisions have a tendency to excite vibrational modes of the NO molecule at the same time that they de-excite electronic modes, populating $X^2\Pi(v'' \neq 0)$ states (Paul et al. 1994). In some flows, this could reduce the overall fluorescence because it serves to depopulate the probed $X^2\Pi(v''=0)$ state. In the present experiments, this mechanism was not a factor because laser pulses were separated by 0.1 s, and the flow velocities were large. Together, these two factors ensured that the molecules tagged by each laser pulse moved well out of the measurement region prior to the next laser pulse.

The calculations of fluorescence intensity carried out for the present experiments have included the effects of quenching collisions by nitrogen, oxygen, and other nitric oxide molecules. Of these three species, the quenching cross section is largest for nitric oxide self-quenching. However, the low mole-fraction of NO results in self-quenching having a small effect on the overall fluorescence signal. Nitric oxide is strongly quenched by molecular oxygen (O_2). The effect of quenching by oxygen is readily apparent in the diffusion and mixing regions of these flows. The collisional quenching cross-section for molecular nitrogen (N_2) is approximately four orders of magnitude smaller than that for either NO or O_2, so at the temperatures encountered in the flows of the present investigation, N_2-NO collisions have a small effect on the overall fluorescence, despite the high percentage of nitrogen in the flow.

3.2.1.3 Fluorescence

Once molecules have been promoted to an excited state, molecules may dissipate the energy they absorbed through a variety of means. Some will relax radiatively; that is,

they will emit a photon as fluorescence. As mentioned previously, excited molecules may emit photons with the same amount of energy (and therefore, the same wavelength) as those that they absorbed, but they may also emit photons of different energies. The net amount of fluorescence can be calculated by integrating the amount of fluorescence from each allowed radiative relaxation pathway. For each pathway, the amount of fluorescence will depend on the population of the excited state and the probability of the relaxation transition. This probability is captured in the Einstein A coefficient for spontaneous emission. The following sections examine each of these parameters in more detail.

3.2.2 PLIF equation

The absolute intensity at any given pixel in a PLIF image has a functional dependence on many local flow parameters as given by the following equation (Danehy et al. 1996):

$$S_f = C \, \rho \, \chi_{NO} E \Phi \left[\sum f_B \, B_{12} \, g_i \right] \tag{3.1}$$

Here, S_f is the fluorescence signal; C is a constant related to the collection solid angle and the efficiency of the detector; ρ is the local gas density (kg/m^3); χ_{NO} is the local mole fraction of NO; E is the energy in a single laser pulse (J); Φ is the fluorescence yield; f_B is the Boltzmann fraction; B_{12} is the Einstein stimulated absorption coefficient for the probed transition; g_i is the spectral overlap integral; and the sum is over all probed (lower) states. Table 3.2 lists many of the constants that will be referenced in the following equations.

58

Speed of light	c	2.998×10^8 m/s
Planck's constant	h	6.63×10^{-34} J·s
Avogadro's number	N_A	6.02×10^{23}
atomic mass: nitrogen	m_N	2.33×10^{-26} kg
atomic mass: oxygen	m_O	2.66×10^{-26} kg
vib-rot interaction constant	α_e	1.64×10^{-2} m^{-1}
Equilibrium radius of NO	r_e	1.0637×10^{-10} m
Boltzmann's constant	k	1.38×10^{-23} J/K
adiabatic index: diatomic gases (NO, O_2, N_2, air)	γ	$7/5 = 1.4$
adiabatic index: monatomic gases (e.g. helium)	γ	$5/3 \approx 1.7$
standard density (273.15 K and 101.325 kPa): nitrogen	$\rho_{N2,standard}$	1.2506 g/L
standard density (273.15 K and 101.325 kPa): helium	$\rho_{He,standard}$	0.178 g/L
universal gas constant	$\mathcal{R}$	8.314 J/(K·mol)
specific gas constant: air	R	287 J/(kg·K)
specific gas constant: N_2	R_{N2}	297 J/(kg·K)
specific gas constant: O_2	R_{O2}	260 J/(kg·K)
specific gas constant: NO	R_{NO}	277 J/(kg·K)
specific gas constant: He	R_{He}	2077 J/(kg·K)
reference temperature	T_{ref}	300 K
Reference dynamic viscosity: N_2	$\mu_{N2,ref}$	1.66×10^{-5} Pa·s
Reference dynamic viscosity: NO	$\mu_{NO,ref}$	1.86×10^{-5} Pa·s
Reference dynamic viscosity: He	$\mu_{He,ref}$	1.80×10^{-5} Pa·s
Exponent in viscosity equation: N_2	n	0.67
Exponent in viscosity equation: NO	n	0.78
Exponent in viscosity equation: He	n	0.666
Collisional cross-section: NO	$<<\sigma_{NO}>>$	4.30×10^{-19} m^2
Collisional cross-section: O_2	$<<\sigma_{O2}>>$	2.51×10^{-19} m^2
specific heat, constant pressure: air	c_p	1004.5 J/(kg·K)

Table 3.2: Values of commonly-used constants, taken from *CRC Handbook of Chemistry and Physics* (1970), *Viscous Fluid Flow* (White 1991), and *Physics for Scientists and Engineers* (Tipler 1990).

Here, it is assumed that the laser intensity is below the saturation intensity, and that absorption along the path of the laser through the imaged region is negligible. Radiative trapping (whereby an emitted fluorescence photon is reabsorbed by the medium) is neglected, primarily because fluorescence at the same frequency of the laser is rejected by a filter in front of the detector. Stimulated emission is also considered to be negligible due to the relatively small population of the upper state prior to excitation at the temperatures encountered in these experiments.

The fluorescence yield (Φ), Boltzmann fraction (f_B) and spectral overlap integral (g_i) are all functions of the local temperature; Φ also depends on the local pressure and mole fractions of each species, while g_i also depends on pressure and velocity. The density ρ is simply calculated from the perfect gas law: $\rho = p/RT$, where R is the *specific gas constant*, rather than the universal gas constant. Since the fluorescence intensity depends on so many local flow parameters, variations in any one of these parameters will affect the resulting intensity in a PLIF image. While this means that the interpretation of PLIF images is not always straightforward, it also means that PLIF images are well suited to detecting fluctuations within a flowfield, and detecting fluctuations is one of the primary goals of this work.

3.2.2.1 Laser Energy and Saturation

Equation 3.1 indicates that the fluorescence signal is proportional to the energy of each laser pulse. This is true in regimes where saturation is not a concern and absorption across the measurement region can be neglected. Saturation is a concern if the laser irradiance is high, resulting in a large percentage of resonant molecules being promoted to

60

the excited state. As molecules are excited, the population of potential absorbers is diminished. The experiment is said to be in the saturated regime if increases in laser energy result in ever-lessening or insignificant increases in fluorescence signal. If, however, the laser pulse energy is sufficiently low, this depletion effect is negligible; under these conditions, the experiment is said to be in the linear regime with regard to saturation.

Calculations performed using LINUS (Palma 1998) over the expected range of conditions for the present experiments indicate that the ratio of the laser irradiance I relative to the saturating irradiance I_{sat} should fall between 0.15 (near the nozzle exit) and 10 (in the lowest pressure regions of highly expanded flows). While having limited regions where the transition is saturated is not of great concern for flow visualization studies, the effect of saturation will need to be considered for any quantitative measurements. If necessary, the laser irradiance could be reduced slightly, either by reducing the laser energy or by focusing the sheet more loosely, or even by imaging a region away from the focal point of the laser sheet, where the laser sheet is thicker.

Absorption is a concern where the concentration of the absorbing species is high. As the laser sheet passes through the gas, photons are absorbed and the laser energy decreases. The transmitted irradiance is related to the incident irradiance by the Beer-Lambert law, given in Chapter 2 and repeated here for convenience:

$$I = I_0 e^{-\alpha c L} \tag{3.2}$$

(I is the calculated transmitted intensity, $\alpha = \alpha(\lambda_{laser})$ is the effective absorption coefficient of NO as a function of the laser's wavelength λ_{laser}, c is the effective concentration, and L

61

is the measured path length through the gas cell.) However, for weak enough absorption and high enough laser energy, the difference in laser irradiance across the imaged region can be neglected. In these experiments, the concentration of nitric oxide has been deliberately limited in order to reduce the attenuation of the laser sheet by absorption.

If neither saturation nor absorption is problematic, ideally laser energy would be uniformly distributed across the imaged region. In practice, the laser has a spatial intensity profile that sometimes can be approximated as Gaussian, being more intense toward the center and less intense along the edges. In the present investigation, the beam-forming optics were chosen in such a way so as to slightly overfill the spherical lens, effectively masking the less-intense edges of the laser profile and creating a laser sheet which with a slightly more "top-hat" profile. Even so, in order to remove the dependency on laser energy from PLIF images, they must be corrected for the remaining spatial variations in laser intensity. Section 5.5.1.1 describes the image processing procedure in which PLIF images can be corrected for mean variations in laser sheet intensity.

3.2.2.2 Fluorescence yield, quenching and the Einstein A coefficient

The *fluorescence yield* parameter Φ effectively parameterizes the efficiency with which fluorescence results from excited molecules. In the absence of quenching and other loss mechanisms (described below), the fluorescence yield is unity, indicating that all excited molecules will eventually relax radiatively. In the presence of quenching, the fluorescence yield is less than one, indicating that not all excited molecules will contribute to the fluorescence. The fluorescence yield is defined to be (Palma 1999):

$$\Phi = \frac{A_{eff}}{A_{total} + Q} \qquad (3.3)$$

A_{eff} and A_{total} are Einstein coefficients of spontaneous emission from a given excited state to a given lower state (the subscripts are explained below). The units of A and Q are inverse time, so they are *rates*. Because NO fluorescence is broadband, a rigorous treatment would require considering every electronic transition that results in fluorescence, the relative populations of their excited states, and the Einstein A coefficient for each transition. The relative populations of the excited states do depend on the particular transition that is excited by the laser. However, A and Q have been found to be relatively independent of rotational level (Paul et al. 1994). Instead, A can be treated as the constant, A_{total}, which is the sum of the coefficients between the excited state and the possible lower states. The numerator, A_{eff}, is an effective emission rate that takes into account the spectrally selective elements (i.e. filters) in the collection optics (Palma 1999). In the absence of quenching, the inverse of A would give the fluorescence lifetime, τ_{LIF}. With the effect of quenching, Q, the fluorescence lifetime becomes (Paul et al. 1994):

$$\tau_{LIF} = \frac{1}{A + Q} \qquad (3.4)$$

Quenching is a means by which excited molecules can lose their energy non-radiatively. Instead of returning to a lower energy level by emitting a photon, the molecule transfers its electronic energy to another molecule through inelastic collisions. Quenching will thus have a larger effect in thermodynamic conditions under which the

63

collision rate is high, namely, at high densities. The quenching rate is species, temperature, and pressure dependent, as it is governed by the physics of molecular collisions. It is calculated via the relation:

$$Q = \langle v_{NO} \rangle \langle\langle \sigma(\chi_p, T) \rangle\rangle \frac{p}{kT} \tag{3.5}$$

Here, p is the local pressure, k is Boltzmann's constant, and T is the local temperature. The average velocity of NO due to thermal motions of the gas is given by:

$$\langle v_{NO} \rangle = \sqrt{\frac{8kT}{\pi m_{NO}}} \tag{3.6}$$

where m_{NO} is the molecular mass of NO, and the total effective collisional cross section is given by:

$$\langle\langle \sigma(\chi_p, T) \rangle\rangle = \sum_p \chi_p \left(1 + \frac{m_{NO}}{m_p}\right)^{0.5} \langle\langle \sigma_p(T) \rangle\rangle \tag{3.7}$$

The summation in this expression is over all perturbative species (m_p is the mass of each perturbative species). Attempting to model mechanisms for the quenching process has proven to be complex. Paul et al. (1994) measured quenching cross sections for many of the common quenching species of NO. They divided the different species into five classes, based on their chemical structure. They postulated a model for the quenching process in each of these five cases and then fit the constants in their model to experimental data obtained in shock tube experiments. In the flows we have studied, the important quenching species are NO (self-quenching), O_2, and N_2, in that order. For NO and O_2, they observe temperature-independent values for the collisional cross sections:

$$\langle\langle\sigma_{NO}(T)\rangle\rangle \approx \langle\langle\sigma_{NO}\rangle\rangle = 4.30 \times 10^{-15} \ cm^2 \tag{3.8}$$

$$\langle\langle\sigma_{O2}(T)\rangle\rangle \approx \langle\langle\sigma_{O2}\rangle\rangle = 2.51 \times 10^{-15} \ cm^2 \tag{3.9}$$

For nitrogen, their empirical formula depends on temperature:

$$\langle\langle\sigma_{N2}(T)\rangle\rangle = \left(0.88e^{-4.8T_{ref}/T} + 3.1e^{-16.0T_{ref}/T}\right) \times 10^{-16} cm^2 \tag{3.10}$$

where $T_{ref} = 300$ K.

3.2.2.3 Mole fraction

As indicated in Equation 3.1, fluorescence is linearly dependent on the mole fraction of the resonant species, nitric oxide (neglecting the contribution of nitric oxide to the quenching). In the jet flows studied in these tests, the mole fraction of nitric oxide can be treated as constant in regions where mixing and/or diffusion with the ambient gas is minimal. As previously discussed, this assumption is most valid in the core of the jet. As the flow moves downstream, diffusion and mixing effects become important. As turbulent structures arise, turbulent transport mechanisms accelerate the rate of mixing and diffusion, and the mole fraction of nitric oxide approaches its fully-mixed value.

For most of our experiments, χ_{NO} was 0.5% in the plenum. For some cases with low Reynolds numbers (and correspondingly low flow rates), we increased the relative flow rate of NO, increasing χ_{NO} in order to increase the overall signal. In these cases, χ_{NO} was between 1% and 5%.

3.2.2.4 Boltzmann fraction

The rotational state of the molecule before and after excitation varies as a function of the wavelength of the laser, and so the fluorescence equation depends on the rotational quantum number, J (or N, depending on the basis that is chosen). If the chosen absorption transition involves exciting molecules from a state with a low value of J, the resulting fluorescence will be found to decrease as the temperature of the gas increases. This is because the Boltzmann fraction of molecules in lower energy states is large when the temperature is low. As temperature increases, molecules begin to occupy the excited states. Thus, if the chosen absorption transition involves exciting molecules from a state with a higher value of J, the fluorescence will exhibit an increase with temperature over a certain range of temperatures. If the gas is very cold, then states with very high values of J are unlikely to be populated, but as the temperature of the gas increases, these upper states will begin to be populated. Figure 3.2 graphically depicts this temperature dependence for rotational quantum numbers up to 19.5, where the following expression (Eq. 7.50 from Eckbreth, 1996) has been used to calculate the Boltzmann fraction:

$$ f_B(T, J'') = hc \frac{B_v}{kT} (2J''+1)\, e^{-hc\frac{B_v}{kT}J''(J''+1)} \tag{3.11} $$

In this expression, B_v is the effective rotational constant for nitric oxide which includes the effects of the vibration/rotation interaction and is taken from Eq. 2.88 in Eckbreth (1996):

$$ B_v = B_e - \alpha_e \left(v + \frac{1}{2} \right) \tag{3.12} $$

66

Here, α_e is the vibration-rotation interaction constant, v is the vibrational quantum number and B_e is the NO equilibrium rotational constant [Eq. (III, 16), Herzberg 1950]:

$$B_e = \frac{h}{8\pi^2 c I_e}.$$ (3.13)

h is Planck's constant, c is the speed of light, and I_e is the equilibrium moment of inertia for NO [Eq. (III, 4) Herzberg 1950]:

$$I_e = \frac{m_N m_O}{m_N + m_O} r_e^2$$ (3.14)

Here, m_N is the mass of the nitrogen atom, m_O the mass of the oxygen atom, and r_e is the equilibrium radius between the two atoms when they are bonded together as NO. A
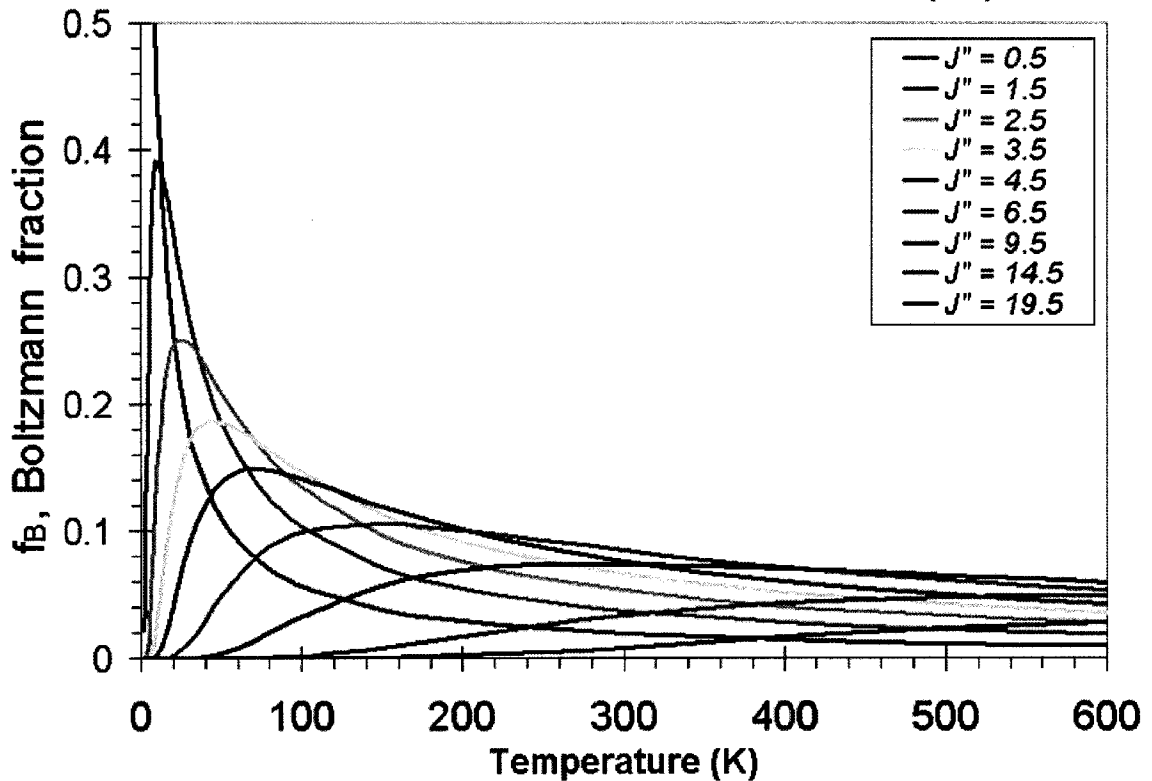
Figure 3.2: Temperature dependence of Boltzmann fraction. At low temperatures, states with low values of the rotational quantum number, J'', are highly populated. As temperature increases, states with higher values of J'' become populated.

67

means of exploiting the different temperature dependencies of the Boltzmann fraction in high and low rotational states for scalar-sensitive imaging will be described in section 3.4.2. Note that probing low-J lines results in fluorescence signal over a wide range of temperatures.

3.2.2.5 Einstein B coefficient

The Einstein B coefficients, B_{21} and B_{12}, give the probabilistic rates of stimulated emission and stimulated absorption, respectively. (The subscripts denote the initial and final states, with the upper level labeled 2 and the lower level, 1.) Since the population of the upper state of the laser-coupled transition is relatively small compared with that of the lower, probed state at the temperatures and low laser intensities used in our experiments, B_{21} can be neglected. The B coefficients are rotational-level dependent. Specifically, $B_{12}(J'')$ is the Einstein coefficient of stimulated absorption for the lower level, denoted by its rotational quantum number, J''. It has units of $cm^2 cm^{-1}/J$. The units involving cm are left in this manner deliberately because the laser frequency is usually given in wavenumbers (cm^{-1}), also called *Kaisers*. We used the LINUS code (v3.0.0) developed by P.C. Palma during his Ph.D. work at the Australian National University (Palma 1999) to calculate $B_{12}(J'')$ for the available rotational levels that could be probed within the spectral envelope of our laser. Table 3.3 contains values of B_{12} for the candidate line groupings.

68

	Transitions: $\Delta N_{\alpha\beta}(N'')$	λ_{laser} (nm)	$B_{12}(N')$	Primary sensitivity
1	$S_{21}(10), Q_1(21), Q_{21}(21)$	225.693	73.37, 296.57, 42.88	pressure (1)
2	$S_{21}(5), R_1(9), R_{21}(9)$	225.979	89.70, 126.31, 141.97	
3	$P_1(17), Q_1(4), Q_{21}(4)$	226.25	140.36, 222.74, 72.03	
4	$Q_1(1), Q_1(2), Q_1(3),$ $Q_{21}(1), Q_{21}(2), Q_{21}(3)$	226.256	216.08, 214.93, 218.27, 59.36, 69.08, 71.72	flow visualization
5	$P_1(1), P_1(16)$	226.275	70.37, 138.21	
6	$P_1(2), P_1(15)$	226.298	86.67, 135.96	
7	$P_1(3), P_1(14)$	226.317	95.22, 133.61	
8	$P_1(4), P_1(13), R_2(11)$	226.333	101.17, 131.16, 115.80	density (1)
9	$P_1(5), P_1(12)$	226.346	105.92, 128.60	density (2)
10	$P_1(6), P_1(11)$	226.355	110.00, 125.92	mole fraction
11	$P_1(7), P_1(10)$	226.361	113.65, 123.11	
12	$R_2(10), Q_2(15), Q_{12}(15)$	226.393	112.39, 274.34, 53.21	pressure (2)

Table 3.3: Twelve spectrally-coincident line groupings. Wavelengths listed are vacuum wavelengths. The coincidental overlap in frequency of transitions which probe states with different values of the rotational quantum number were considered as candidates for scalar-sensitive imaging. Line grouping #10 was identified as a good candidate for mole fraction imaging, while pairs 1 and 8 are good pressure and density candidates, respectively. Pairs 12 and 9 were identified as alternate pressure- and density-sensitive transitions, respectively.

These laser wavelengths were chosen because multiple electronic transitions coincidentally occur at these wavelengths. As discussed further in section 3.4.2, this allows for the possibility that the overall temperature dependence of the fluorescence signal, as given by equation 3.1, would be greatly reduced or eliminated. Instead, the fluorescence signal would depend most strongly on some other flow parameter of interest, such as the pressure, density, or mole fraction of nitric oxide.

69

3.2.2.6 Spectral overlap integral

The laser used in PLIF must be tuned to a frequency that overlaps a transition or transitions in nitric oxide. In general, we desire to have a laser spectral profile with a spectral width similar to that of the spectral width of the absorption lines of NO in our test. If the laser linewidth is greater than the molecular absorption linewidth, then laser energy will be wasted, as only the photons with energy within the absorption linewidth can be absorbed. On the other hand, if the spectral width of the laser is much narrower than the absorption spectrum, the laser will only interact with those molecules having a Doppler shift matching the frequency of the laser. Thus, the ideal spectral linewidth for the laser is one that is similar to that of the absorption transition.

The spectral overlap integral in Equation 3.15 is a convolution of the spectral profile of the laser (g_L) and the molecular absorption lineshape (g_a) and is given by the expression:

$$g_i = \int_0^\infty g_L g_a dv \qquad (3.15)$$

Here, g_L and g_a are both normalized such that their integral over all space is equal to unity. The absorption linewidth depends on the flow parameters and is subject to both *homogeneous* and *inhomogeneous* broadening mechanisms. Homogeneous phenomena are so called because they affect all molecules in the gas equally, and the overall broadening of the lineshape is equivalent to the individual broadening experienced by all molecules. Inhomogenous phenomena, by contrast, affect different groups of molecules differently, and the overall line broadening is a convolution of the individually broadened

70

lines. Collisional broadening is an example of the former. At extremely low pressures, the spectral lines would be very narrow, broadened only by the Heisenberg uncertainty principle. In non-vacuum environments, collisions with other atoms and molecules lead to *collisional broadening*, also called *pressure broadening*, the spectral width of which is Δv_P. Collisional broadening, in general, leads to a Lorentzian lineshape. Collisions can also act to shift the central vacuum frequency, v_{ai0}, by an amount δv_P. We have used the empirically determined relations of Chang et al. (1992) and used in the thesis by DiRosa (1996) given below:

$$\Delta v_P = 0.585 p \left(\frac{295}{T} \right)^{0.75} \tag{3.16}$$

$$\delta v_P = -0.180 p \left(\frac{295}{T} \right)^{0.56} \tag{3.17}$$

where the pressures are in *atm*, the temperatures are in *K*, and the frequency width and shift have units of cm^{-1}. These relations are for N_2 broadening of NO. Because the flows in our experiments were between 90% and 99.5% nitrogen, and because the relations for NO self-broadening and O_2 broadening are similar to those for N_2, we have elected to use the relations given above in our computations. DiRosa's thesis contains extensive additional information on modeling and measuring the collisional lineshape broadening and shift components for nitric oxide from various other gas species.

The other primary broadening mechanism is an inhomogeneous one: Doppler broadening. It arises from the average Doppler shift based on the average velocity component (due to the thermal motion of the molecules) relative to the direction of the

71

propagation of the laser photons and is therefore a function of temperature. Doppler broadening leads to a Gaussian lineshape.

When treated rigorously, the convolution of the Lorentzian lineshape due to collisional processes and the Gaussian lineshape due to Doppler broadening results in a Voigt profile (Siegman 1986). However, we have elected to use the expression of Danehy et al. (1996), which uses the approximation of Gaussian lineshapes for both broadening processes and for the laser lineshape. This significantly reduces the mathematical complexity of the computations involved, allowing an analytic calculation of the overlap integral. Their expression is given by:

$$g_i = \sqrt{\frac{4\ln(2)}{\pi\left(\Delta v_{ai0}^2 + \Delta v_L^2\right)}}\exp\left(-4\ln(2)\frac{\left(v_{ai0} + \delta v_D + \delta v_P - v_L\right)^2}{\Delta v_{ai0}^2 + \Delta v_L^2}\right) \qquad (3.18)$$

where

$$\Delta v_{ai0} \approx \sqrt{\Delta v_D^2 + \Delta v_P^2} . \qquad (3.19)$$

and where δv_D is the Doppler shift, which was set to zero for the calculation shown herein.

3.3 Excitation Spectra

All of the transitions that we will consider involve the ground vibrational state, and the ground and first excited electronic states of nitric oxide. This means that before a laser photon is absorbed, the nitric oxide molecule is in the ground electronic state and the ground vibrational state. After absorbing a laser photon, the molecule will be in the first excited electronic state, but will still be in the ground vibrational state.

The frequency of the selected excitation lines must be accessible by an available laser system and compatible with the optical access of a given experiment (this generally includes the requirement that air be transparent at the excitation frequency). In many applications, this limits the range of useful frequencies to be from the near infrared (around 2 μm) to the ultraviolet frequencies transmitted by UV-grade fused silica optics (down to about 180 nm). The use of magnesium fluoride (MgF_2) and calcium fluoride (CaF_2) optics extends this range down to about 130 nm and 150 nm, respectively, while zinc selenide (ZnSe) and germanium (Ge) are transmissive much further into the infrared, up to about 20 μm

The spectroscopy of nitric oxide has transitions at frequencies that coincide with those achievable by commercially available lasers. Air is generally transparent at NO excitation frequencies, allowing the probe laser to pass freely without absorption. This color also transmits through UV-grad fused silica optics with high efficiency. Additionally, the fluorescence of nitric oxide occurs at wavelengths that are readily imaged by intensified CCDs.

Nitric oxide also has a relatively large number of lines from which to choose within a fairly narrow frequency range. This allows a single tunable laser system to selectively probe many different states. Figure 2.3 in the previous chapter showed measured and calculated excitation spectra for nitric oxide. The theoretical excitation spectrum was calculated using LIFBASE (Luque and Crosley 1999). The experimental spectra were acquired using the gas cell monitoring system, as described in Chapter 2, by varying the frequency of the laser slowly and recording the resulting fluorescence, as well as the transmitted laser intensity through the cell.

The frequency of the laser is controlled by changing the angle of the diffraction grating inside the dye laser. As the grating angle is scanned, the spectral overlap between the laser and the molecule changes. When the laser is tuned to the central frequency of a transition, the spectral overlap integral is large and a (relatively) large amount of fluorescence is generated. As the laser becomes slightly detuned, the value of the spectral overlap integral is reduced and the fluorescence intensity decreases. If the detuning is great enough, no fluorescence results until the overlap begins with the next transition. Slight drifts in the baseline of the experimental spectra probably occur because of geometrical misalignment of the laser beams as the laser frequency is scanned (a known limitation of the PDL-3 / WEX combination).

3.4 Line Selection Criteria

Nitric oxide has favorable spectroscopic characteristics for PLIF. As a diatomic molecule, it has vibrational and rotational modes not present in atomic species. As a heterogeneous diatomic molecule, it exhibits further splitting in its energy levels. This means that many different states can serve as the probed state. Because LIF signal depends on so many spectroscopic and flow parameters, a great deal of information can be extracted from LIF measurements if lines are carefully selected and/or if certain simplifying assumptions or corrections can be applied to a given problem.

As previously indicated, the net amount of fluorescence is dependent upon not only temperature, but also pressure, species mole fraction, and quenching (which also depends on pressure, temperature, and the mole fraction of each quenching species). As a result, interpreting PLIF images is non-trivial. In fact, PLIF images of the same flowfield may

74

look very different depending on which spectral line was excited by the selected laser frequency. It is therefore prudent to consider the flow conditions of a particular test as well as the desired information to be extracted from that test before choosing the excitation frequency of the laser. In this section, line selection criteria are discussed and several candidate excitation lines are suggested for a few specialized applications.

In selecting which molecular transition to excite, many parameters warrant consideration. A line with strong fluorescence is almost always desired; the greater the overall fluorescence, the greater the signal-to-noise ratio in the resulting PLIF images. Lines with strong fluorescence are generally strongly absorbing. Quantitative measurements usually seek to operate in regimes where the fluorescence is linearly proportional to laser energy, and so if the flow conditions and laser energy are such that saturation is possible, a transition with lower absorption may be desirable. Quenching characteristics may also be important in line selection. Generally, low quenching is desirable for the greatest signal levels. In certain applications, however, quenching may be exploited. For instance, the effects of quenching may allow the measurement of the mole fraction of a particular quenching species, as in some mixing and diffusion studies (Fox et al. 2001).

For quantitative imaging, lines may be selected because the temperature dependence of the Boltzmann fraction of that particular line cancels or enhances other temperature dependencies in the PLIF equation. For instance, the Boltzmann fraction of low-J lines tends to decrease with temperature, whereas that of high-J lines tends to increase with temperature. The desired result in such a case would be to have the resulting fluorescence signal be proportional to pressure, temperature, density, or mole fraction.

75

3.4.1 Flow visualization lines

For the majority of the cases studied in this work, visualizing flow structures was the primary goal. Lines that gave strong signal overall, as well as signal throughout the flow were therefore desired. We chose the strongly-absorbing, low-J spectral lines of the coincident Q_1 main branch and Q_{21} satellite branch because it gave strong fluorescence across the field of view. In particular, the laser was tuned to a vacuum wavelength of 226.256 nm with a linewidth of 0.004 nm (0.8 cm^{-1}). In non-vacuum environments, the wavelength λ is modified by the refractive index, n, of the medium such that $\lambda = \lambda_0/n$, where λ_0 is the vacuum wavelength). Three spectrally coincident lines (transitions) are excited at this frequency. Their rotational quantum numbers are all low: $N''=1$, 2, and 3 ($J''=3/2$, 5/2, and 7/2). As a result, the fluorescence signal *decreases* with increasing temperature for this choice of excitation line (see section 3.2.2.4 on Boltzmann fraction for a more detailed explanation). The effects of quenching increase with pressure, and so signal also tends to *decrease* with pressure, everything else being held constant. However, signal tends to *increase* with density, at least in regions where the mole fractions of NO and O_2 are constant. The net effect is that where the mole fraction of nitric oxide is relatively constant, signals are present over a wide range of temperatures and pressures, making these lines appropriate choices for the purposes of flow visualization.

3.4.1.1 Expected signal intensity for jet imaging

The features of underexpanded jet flows encountered in this work will be described in Chapter 4. The upper image in Fig. 3.3 shows a typical PLIF image resulting from

76

exciting the flow visualization transitions at 226.256 nm. In order to understand the trends governing fluorescence intensity in images of these flows, there are two main flow categories to consider. The first will be called the *jet core*. The approximate boundaries of the jet core are indicated by a dashed black line in Fig. 3.3. In this region, mixing of the jet fluid with the ambient is negligible, so the mole fraction can be treated as constant. The jet core is often characterized by large gradients in pressure, temperature, velocity, and the related variables of density and Mach number. Because mole fraction is constant in the jet core, PLIF intensity varies primarily as a function of changes in temperature and pressure.

Figure 3.3: Jet core and mixing regions. The black dashed line indicates the approximate boundary of the jet core, in which the mole fraction of nitric oxide, χ_{NO}, is nearly constant. White dashed lines indicate mixing regions, where χ_{NO} is varying but pressure is nearly constant. The upper image was taken with the laser tuned to the "flow visualization" lines at 226.256 nm. The lower image was taken with the laser tuned to the "pressure-sensitive" lines at 225.693 nm. Both images are the average of 100 uncorrected single-shot images.

77

The second primary flow category comprises regions of constant pressure and includes the shear layer along the jet boundary and the downstream mixing region of the jet. These regions are marked by a dashed white line in Fig. 3.3. In these regions, diffusion and, in some cases, turbulent mixing result in varying mole fractions. Because pressure and temperature are relatively constant in these mixing regions, PLIF intensity varies primarily as a function of the relative mole fractions of NO and its quenching agent, O_2.

In the supersonic expansion region of this flow, the temperature, pressure, and density are all *decreasing* as the gas expands and moves downstream (see Chapter 4 for an overview of the equations governing supersonic flow). The decrease in density leads to a decrease in fluorescence signal, but this trend is somewhat mitigated by the increase in signal due to the corresponding decrease in temperature. These trends are reversed as the flow crosses the *Mach disk* (a shock wave perpendicular to the direction of the gas velocity, to be described in detail in Chapter 4); the gas crossing this shock wave experiences a sudden *increase* in temperature, density, and pressure. While the increase in temperature leads to a decrease in fluorescence, the increase in density leads to an increase in fluorescence intensity.

As a result of all these competing effects, the overall signal intensity is actually relatively constant across many regions of this flow where strong gradients in flow parameters are present. This is not true in general for an arbitrary choice of excitation wavelength, as will be discussed further in the section on *Scalar-Sensitive Imaging*. To illustrate this point, Fig. 3.3 presents a PLIF image taken at conditions similar to those of the upper image, but with the laser tuned to what will be called *pressure-sensitive* lines.

With the temperature dependence largely negated, notice the large increase in intensity as the flow crosses the Mach disk.

3.4.1.2 Computational flow imaging

As discussed in the earlier section on PLIF flow visualization, the relative intensity in a PLIF image depends on many local flow parameters. Most significant among these are the local mole fraction of NO and the local temperature and pressure. Thus, maps of computational results showing individual flow parameters (e.g. maps of Mach number, density, pressure, temperature, etc.) qualitatively bear little resemblance to PLIF images of flows at similar conditions. Others have employed a method known as computational flow imaging (CFI), which uses CFD maps of temperature, pressure, and other flow properties, as input to calculations of fluorescence signal. CFI is thus able to generate theoretical PLIF images (Ruyten et al. 1994).

As a first approximation, we have employed an elementary form of the CFI methodology. This formulation approximates the Voigt profile as a Gaussian function, allowing the overlap integral to be evaluated analytically (Danehy et al. 1996). It assumes the laser wavelength is tuned to the center of the absorption line shape at the Q_1 band head (226.256 nm), that the laser has a spectral line width of 0.5 cm^{-1}, and that the gas is composed of nitrogen (with $\chi_{N2} = 99.5\%$) and nitric oxide (with $\chi_{NO} = 0.5\%$). This last assumption is valid in the core of the jet where little mixing with the ambient gas has occurred; it breaks down along the outer edges of the jet and sufficiently far downstream, where the jet fluid has mixed with ambient air and quenching by oxygen reduces the fluorescence yield. In these calculations, the effect of Doppler shifts on the absorption

79

lineshape has been neglected, an effect which reduces the intensity of the experimental images anywhere the gas has radial velocity components. This approximation is appropriate for the conditions of these tests everywhere but near edges of the jet close to the nozzle exit. The major component of velocity everywhere else was in the axial direction, perpendicular to the laser sheet, resulting in no Doppler shift.

In this formulation, theoretical fluorescence intensity was first calculated for a range of static temperatures (100 K to 500 K, the approximate range of temperatures expected in these tests) and pressures (2 Pa to 30,000 Pa, a range somewhat greater than that expected in these tests) using the equations in this chapter. Next, these calculated relative intensities were plotted versus pressure for five different temperatures, as shown in Fig. 3.4.
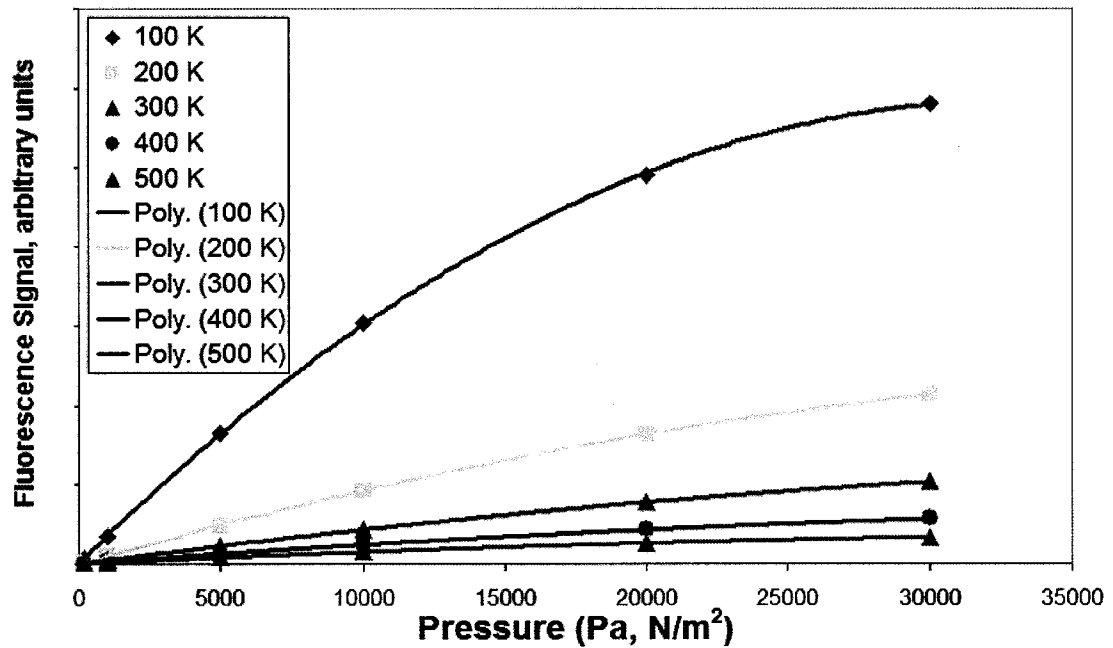
Figure 3.4: Calculated dependence of fluorescence signal on temperature and pressure. Fluorescence signal (arbitrary units) is plotted versus pressure for five temperatures covering the range anticipated in the present study for the flow visualization transitions (line grouping #4 in Table 3.3).

80

The calculations presented in this graph and those that follow are for a gas mixture of 0.5% nitric oxide and 99.5% nitrogen. Second-order polynomials—functions of pressure—were found to give good fits to these data points. The *coefficients* of these polynomials were then plotted as a function of temperature and fitted with power law fits. The result was a simplified equation for fluorescence intensity as a function of temperature, pressure, and mole fraction with semi-empirically determined coefficients which are valid for the excitation wavelength, NO and N_2 mole fraction, and pressure and temperature ranges stated above:

$$S_f \propto \chi_{NO}\left(-0.0018\ T^{-2.12}p^2 + 46\ T^{-1.9}p\right) \qquad (3.20)$$

Here, S_f is the fluorescence intensity, p is the pressure in pascals ($Pa=N/m^2$) and T is the temperature in Kelvin (K). Images were generated in Tecplot by merging variables according to the above equation. Note that, while the PLIF equations here have been formulated in terms of the *mole fractions* of the constituent gas species, GASP gave species *mass fractions* as an output variable. Since the molecular mass of NO, N_2, and air are so similar, mass fraction was simply used in place of mole fraction in these calculations. The results of these computations are presented in Chapter 4.

3.4.2 Scalar-Sensitive Imaging

In the underexpanded jet flows in these experiments, significant regions of the flow exist where mixing and diffusion are negligible (e.g. the jet core), as evidenced by the strong fluorescence signal in these regions (see Fig. 3.3). By contrast, the fluorescence signal decreases markedly in other regions (e.g. the outer shear layer along the jet

81

boundary) where mixing and diffusion are significant. If it is possible to correct for variations in laser intensity in the regions where mixing and diffusion are negligible, then the remaining dependencies in the fluorescence equation can be reduced to primarily functions of pressure and temperature, as previously stated. We have identified several candidate lines that depend approximately linearly on either pressure, density, or mole fraction of nitric oxide. Others have used PLIF to quantitatively measure temperature. These temperature measurements typically involve taking two images of the same flow, using two different excitation frequencies, and taking the ratio of the images (see, for example, McMillin et al. 1993 or Seitzman et al. 1991). Thus, all other dependencies (e.g. pressure, quenching, overlap integral) cancel in the ratio. For this technique, the two lines are chosen such that their relative intensities are a strong function of temperature; usually this means one high-J and one low-J line. The criteria are different when designing a single-image technique, as we have attempted to do here. For the single-image technique, lines are needed which are insensitive to variations in all parameters except the parameter of interest.

Our experiments were conducted in relatively low-pressure and low-temperature regimes where the spectral lines are narrow compared to, for example, combustion environments (see McMillin et al. 1992). As a result, most of the spectral excitation lines of NO are relatively isolated. However, coincidental frequency overlap of two distinct transitions does occur for several line groupings. Twelve such pairings were investigated in the present study. The goal was to find a pair with one low-J and one high-J line, such that the temperature dependence of the two lines would cancel the other temperature dependencies in the PLIF equation across the range of conditions anticipated in the flows

82

of interest to minimize the temperature dependence while maximizing the dependence on mole fraction, density, or pressure. Table 3.3 above lists the twelve candidate line groupings. Note that line grouping #4 consists of three low-J lines (the lines are actually listed using the integer-valued N'' rotational quantum number, rather than half-integer-valued J'' rotational quantum number). While this combination is expected to have a strong temperature dependence, it is also likely to produce good signal, since the lower rotational levels are generally well-populated. In fact, this is the line grouping chosen for general flow-visualization purposes in the present investigation. Figure 3.5 shows the temperature dependence for each of the twelve candidate pairs.

Our target plenum temperature was generally around 500 K, although on some tests it was as high as 608 K. If the gas in the jet were to expand all the way to Mach 7, the temperature would be approximately a factor of 10 less than the stagnation temperature, neglecting heat transfer in the nozzle. The nozzle exit static temperatures are expected to be a factor of 1.2 less than the stagnation temperature for the sonic nozzle and a factor of 2.4 less for the supersonic ($M_e = 2.6$) nozzle. The gas that passes through a normal shock (the Mach disk) is expected to nearly recover the stagnation temperature. Thus, the expected range of temperatures in these jets is approximately 50-500 K. We sought line groupings for which the sum of their Boltzmann fractions had the desired temperature dependence (or independence) over this range of temperatures. The desired temperature-independence is most evident above temperatures of about 100 or 200 K. In Fig. 3.5 it is seen that for the twelve line groupings from Table 3.3, the temperature dependence of the combined Boltzmann fraction increases for some groupings, decreases for others, and is

83

relatively constant over a large range for others. This allows one to choose a line grouping as needed to achieve the desired dependence on temperature.
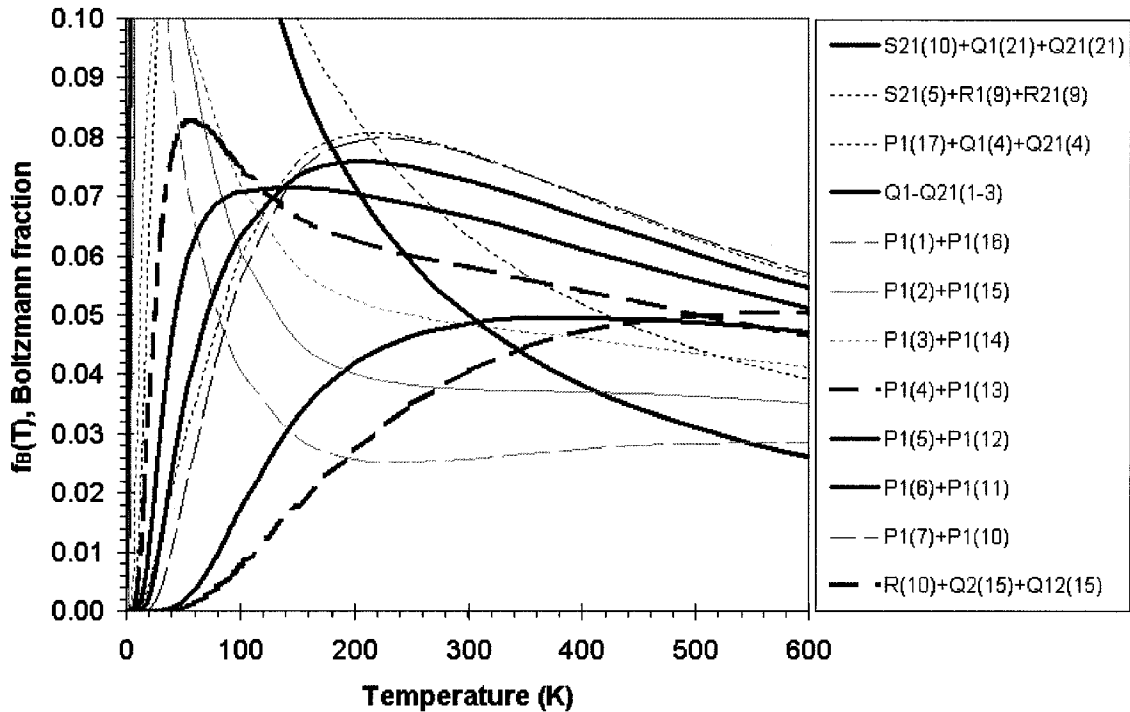
Figure 3.5: Calculated temperature dependence of the 12 spectrally-coincident rotational (N'') line groupings, listed in Table 3.3. Bold lines mark the transitions used in the present investigation. Bold dashed lines mark potential alternate transitions. Colors indicate the primary sensitivity of the transition pair. Blue=flow visualization; Red=mole-fraction-sensitive; Green=density-sensitive; Purple=pressure-sensitive.

Measured plenum pressures ranged from 0.4 psi (23 Torr, 3 kPa) to 16.3 psi (845 Torr, 113 kPa). The pressure at the exit of the sonic nozzle is calculated to be a factor of 1.89 lower than the plenum pressure. For the supersonic nozzle with $M_e = 2.6$, the exit pressure is calculated to be a factor of 20.0 lower than the plenum pressure. The following sections highlight the line groupings that were found to have the strongest dependency on pressure, density, and mole-fraction.

3.4.2.1 Pressure-sensitive lines

Candidate line groupings #1 and #12 were identified as the most monotonic with pressure. Figure 3.6 shows a graph of calculated fluorescence signal from the $S_{21}(10)+Q_1(21)+Q_{21}(21)$ (line grouping #1) transitions at $\lambda_{laser} = 225.693$ nm versus pressure for 6 different temperatures. From a measured fluorescence intensity, one could use this graph to infer a specific pressure. In practice, this will result in relative temperature measurements, with a calibration point or calibration condition needed in order to make the measurement quantitative.
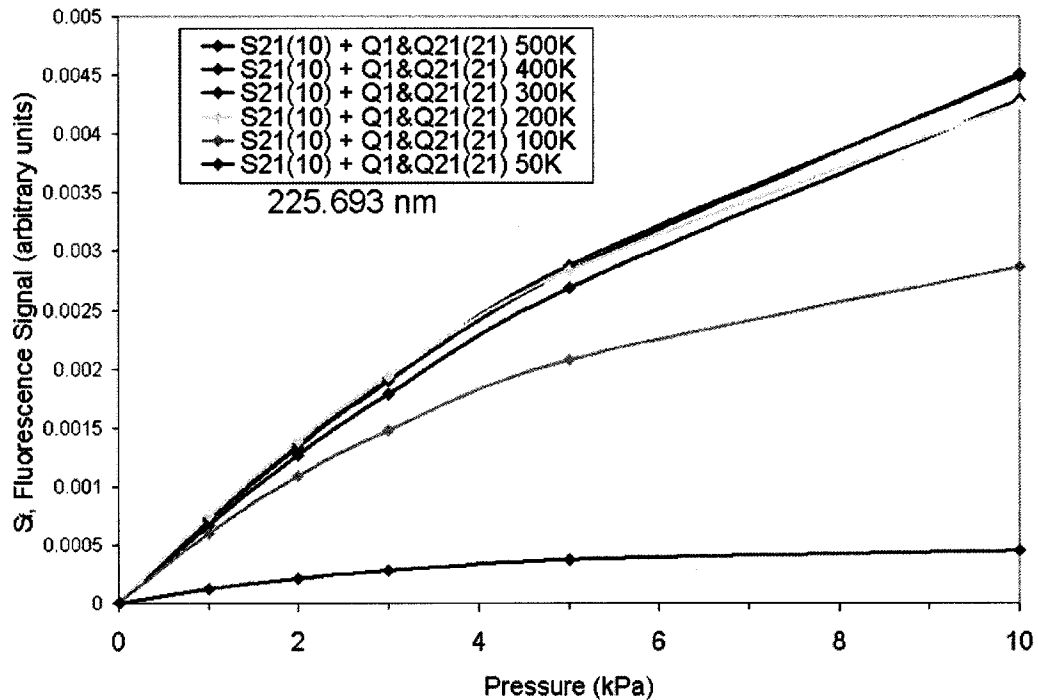
Figure 3.6: Fluorescence signal vs. pressure for line grouping #1. Above temperatures of about 150 K, the signal is relatively independent of temperature, making this line grouping a good candidate for pressure-sensitive imaging. These results and those that follow are for a gas mixture of 0.5% nitric oxide and 99.5% nitrogen.

85

As seen in Fig. 3.6, the fluorescence signal is most monotonic with pressure for temperatures above about 150 K, with a large decrease in signal for lower temperatures. The flow conditions in the present experiments have regions of high pressure/high temperature and low pressure/low temperature, but the combination of high pressure/low temperature does not exist. Therefore, for the temperature and pressure combinations encountered in these jet flows, this line combination is fairly monotonic with pressure, independent of temperature, and is even fairly linear up to a pressure of about 4 kPa. Figure 3.4 shows the pressure dependence of the flow visualization transitions (line grouping #4) used for the majority of this work. Note that the signal strongly depends on temperature as well as pressure, which makes it unsuitable for quantitative scalar-sensitive imaging.

3.4.2.2 Density-sensitive lines

Two candidate line groupings were identified that have a nearly monotonic dependence on density for the conditions of these tests. Figures 3.7 through 3.10 show the calculated fluorescence intensity as a function of density for 6 pressures spanning the range of expected pressures in the present experiments. The first two figures show that line groupings #8 and #9 are both good candidates for density-sensitive imaging as both are nearly monotonic functions of density over the entire range of expected densities. Figures 3.9 and 3.10 show the dependence on density for the flow visualization lines and the leading candidate for pressure-sensitive imaging, respectively. In Fig. 3.10, note how a given level of fluorescence signal corresponds strongly with a given pressure, but with a comparatively large range of densities.
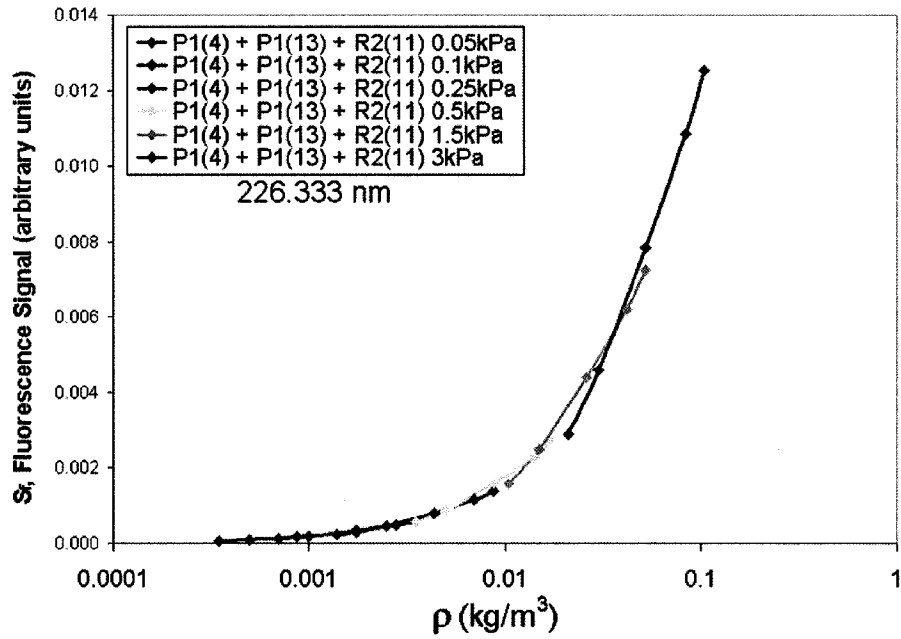
Figure 3.7: Fluorescence signal vs. density for line grouping #8. This pair of transitions is a good candidate for density-sensitive imaging due to the nearly monotonic dependence of signal intensity on density.
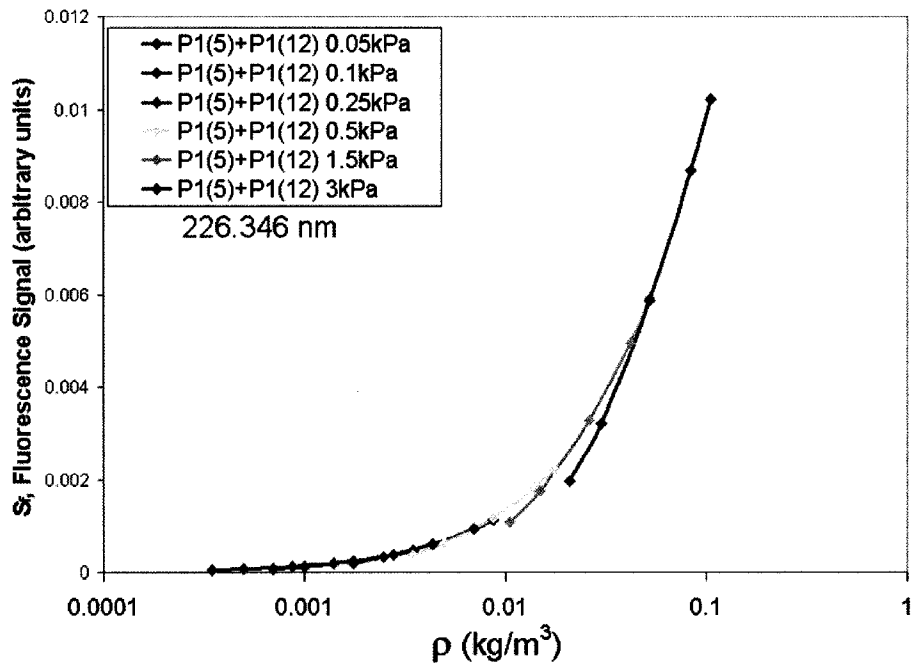
Figure 3.8: Fluorescence signal vs. density for line grouping #9. This pair of transitions is also a good candidate for density-sensitive imaging.

87
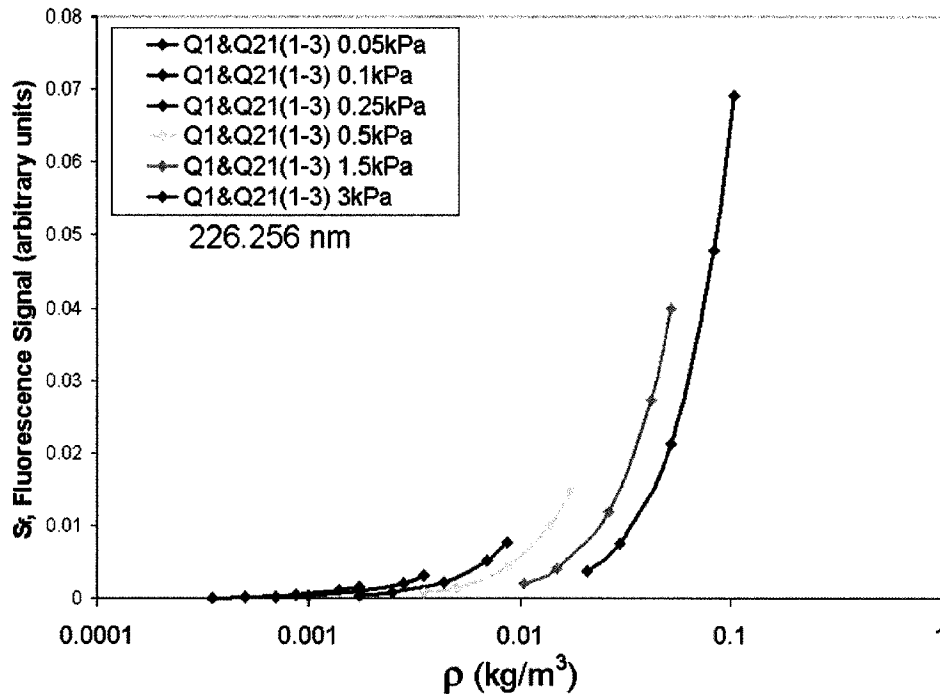
Figure 3.9: Fluorescence signal vs. density for line grouping #4, the transitions used for flow visualization in the majority of the present experiments.
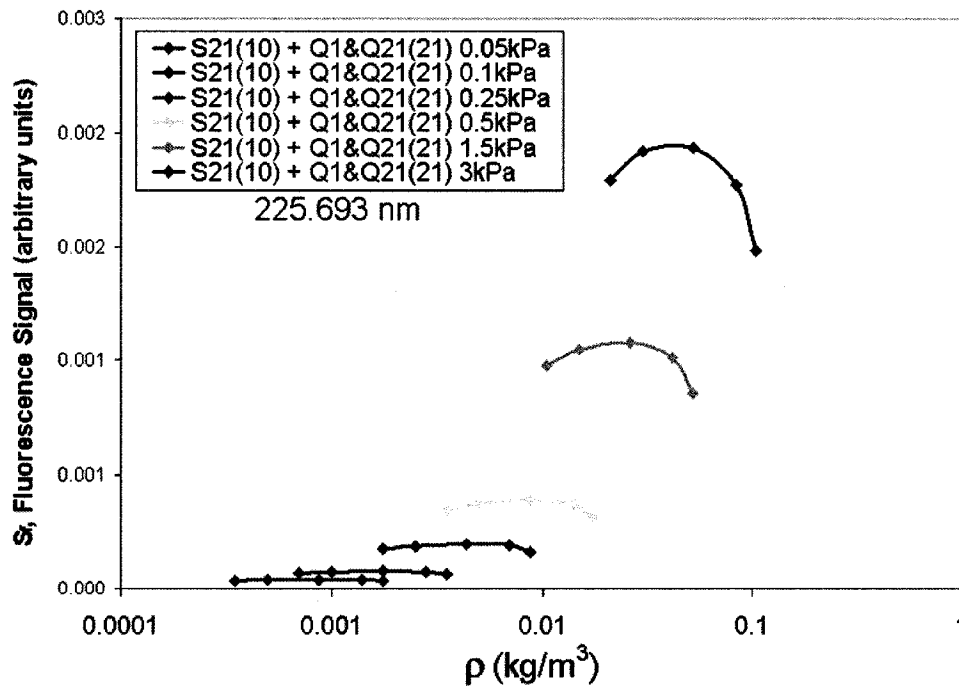
Figure 3.10: Fluorescence signal vs. density for line grouping #1, the leading candidate transitions for pressure-sensitive imaging.

88

3.4.2.3 Mole fraction-sensitive lines

In this experiment, the gas exiting the nozzle is seeded with a fixed mole fraction of nitric oxide, whereas the ambient gas (air) contains no nitric oxide. One quantity of potential interest is the mixing fraction of the jet fluid with the ambient fluid. As discussed earlier, this quantity helps to define two categories of flow: the jet core and the mixing regions. The 12 candidate line groupings listed in Table 3.3 were examined to determine their dependence on jet mixing fraction. Figure 3.11 shows the fluorescence signal for line grouping #10 plotted as a function of mixing fraction for 6 different pressures.
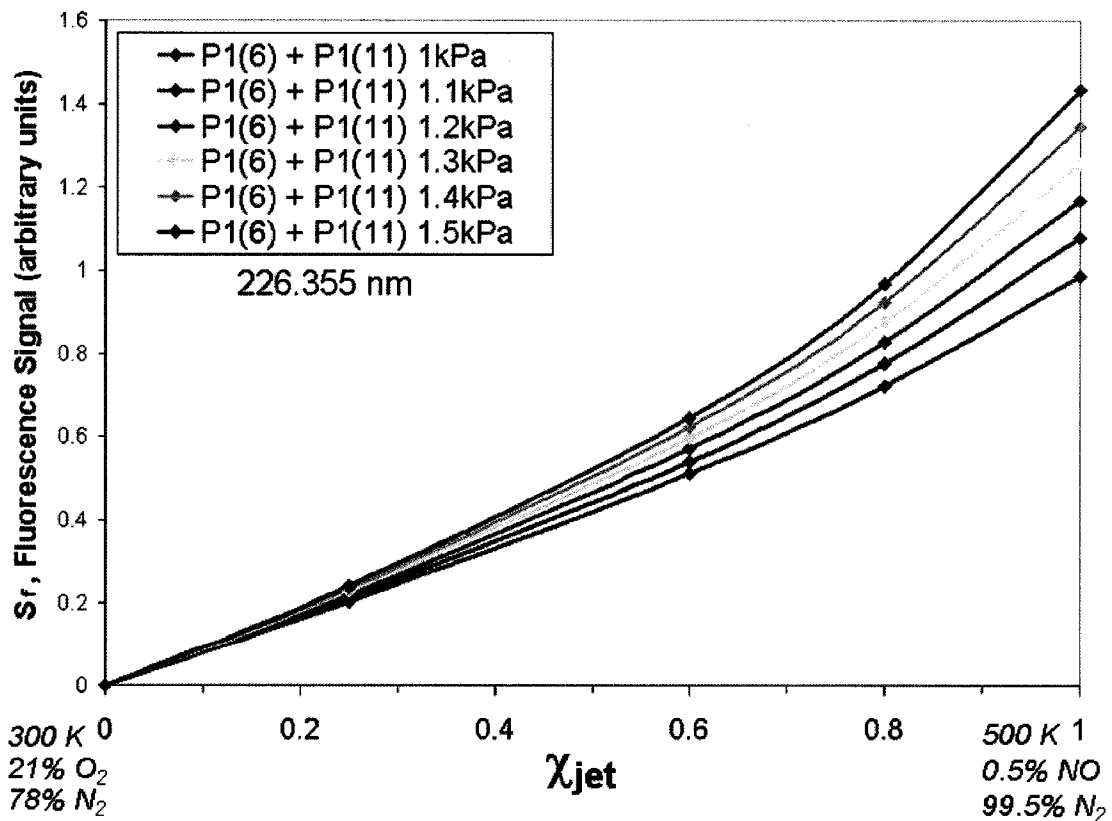
Figure 3.11: Fluorescence signal vs. jet mixing fraction for line grouping #10

89

This calculation assumed a mixture of 78% nitrogen / 21% oxygen / 1% other non-quenching species in the ambient gas. It also used a jet gas temperature of 500 K and an ambient temperature of 300 K. This line grouping was found to be monotonic and fairly linear with mole fraction *in the mixing region* for the conditions found in the cases with higher ambient pressures (greater than about 550 Pa, 4 Torr). However, the divergence in the curves increases at lower pressures. Additionally, while there is potentially good sensitivity to mole fraction in regions of small pressure differences, the technique does not look promising for providing reliable measurements in regions of large pressure gradients (e.g. near the nozzle exit). Figure 3.12 illustrates this point, with the data plotted for the full range of expected pressures.
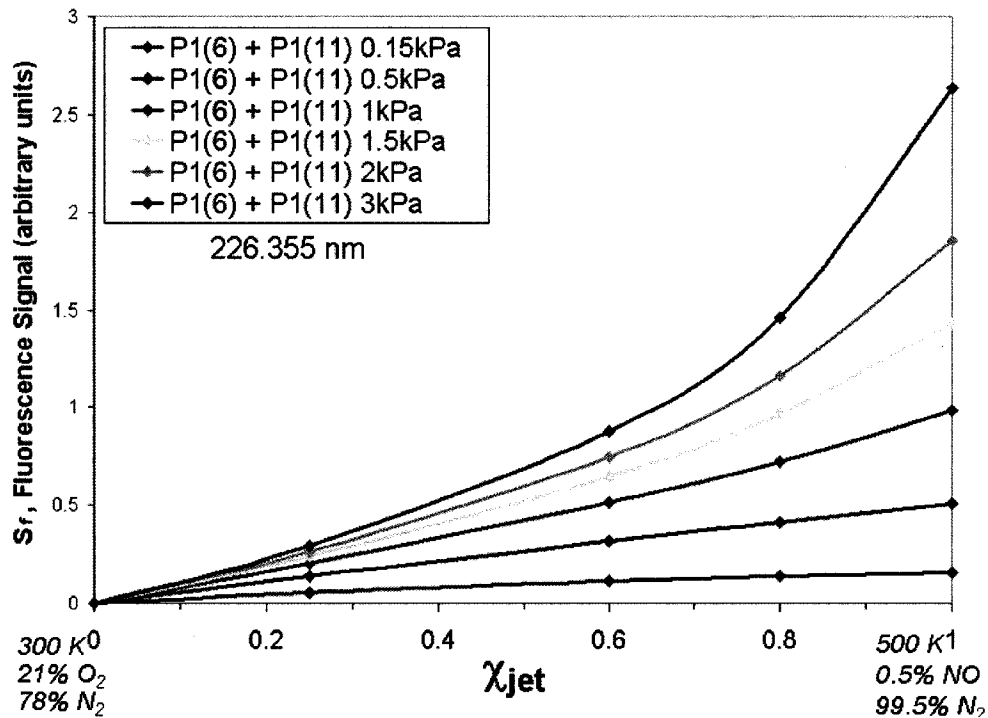
Figure 3.12: Fluorescence signal vs. jet mixing fraction for line grouping #10 over a broader range of pressures. This technique is seen to be valid only over narrow pressure ranges, which is fortunately typical of mixing regions (e.g. shear layers).

90
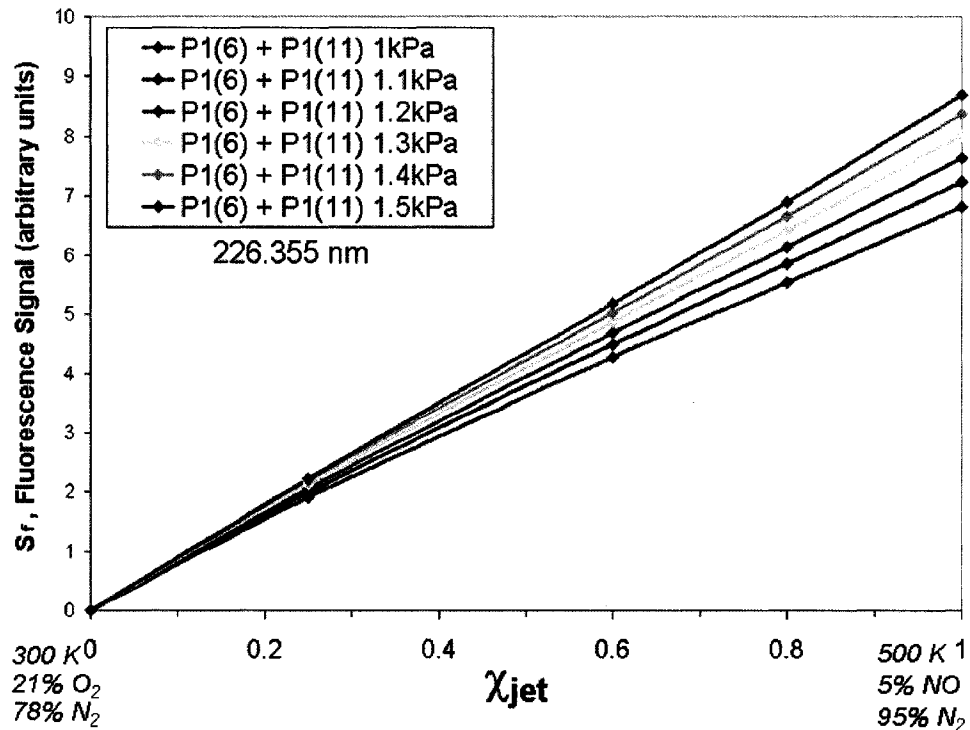
Figure 3.13: Fluorescence signal vs. jet mixing fraction for line grouping #10 with a 5% concentration of NO in the jet fluid.

Figures 3.11 and 3.12 both assume a 0.5% nitric oxide/99.5% nitrogen mixture in the jet fluid, which is the gas mixture elected for use in the majority of these experiments. Figure 3.13 shows the change in signal that results for a 5% nitric oxide/95% nitrogen jet gas composition. The resulting lines are more linear than those in Fig. 3.11. While higher concentrations of NO yield larger signal up to a point, we sought to use the lowest flow rate of NO that would produce images with sufficiently high signal-to-noise ratios. This was due partly to safety and environmental concerns, since NO is a toxic gas and partly to the limited supply of NO. From an experimental standpoint, the optimal mole fraction of NO is limited because above a certain concentration of NO, laser absorption

91

becomes significant, as does self-quenching by NO. Though it is possible to achieve linearity in this manner, it may be experimentally more expedient to use the lower concentration of NO and to correct the images for the slight nonlinearity in post-processing. Since the present experimental pressure-sensitive imaging was not quantitative, such corrections were not implemented, but could be in the future.
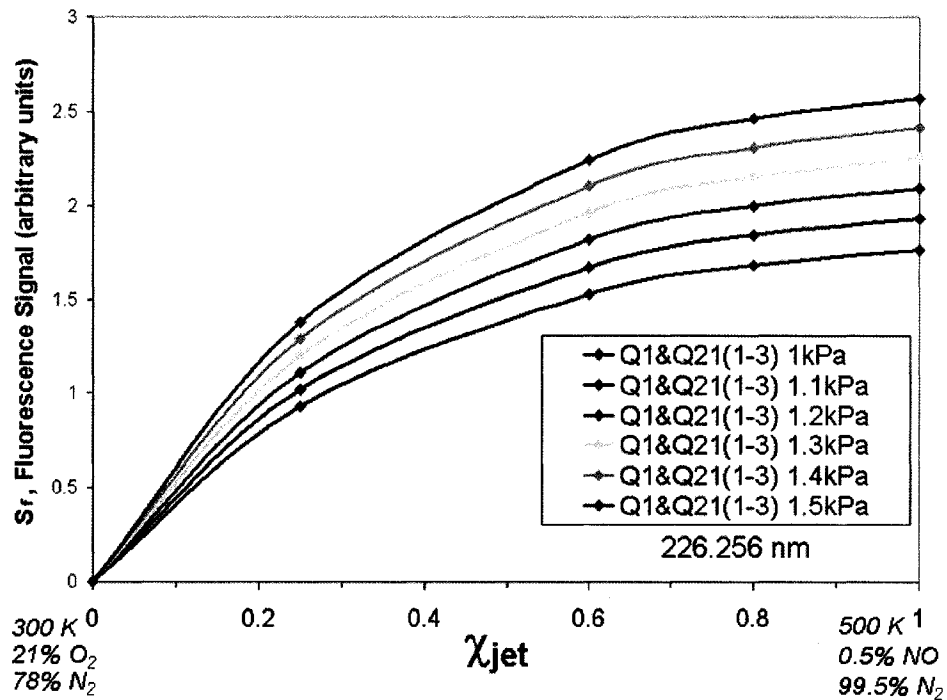
Figure 3.14: Fluorescence signal vs. jet mixing fraction for flow-visualization line grouping #4 with a 0.5% NO concentration in the jet fluid.

Finally, for comparison, Fig. 3.14 shows the fluorescence signal vs. mixing fraction relation for the flow-visualization lines (line grouping #4) used in the majority of the experiments reported herein. In Fig. 3.14, which assumes a 0.5% NO/99.5% N_2 jet composition, the signal is relatively insensitive to mixing fraction above about 50%, but drops off nearly linearly from 30-0%. Thus, the jets in the present experiments will

92

appear to be slightly larger in the PLIF images than if they were tagged by a true passive scalar.

3.5 Flow-tagging Velocimetry

Flow-tagging velocimetry is conceptually straightforward. A laser pulse excites a band of molecules in a gas. At the same time, a reference image of the fluorescence is captured. The image exposure time should be short enough to effectively "freeze" the flow; that is, the excited molecules should not move much (on the order of a few pixels or less) during the acquisition of this reference image. After the laser pulse, the excited molecules propagate downstream, emitting fluorescence as they move. An image of this fluorescence is then captured by a camera at a known delay time after the laser pulse. The delay time between the firing of the laser and the acquisition of this image should be sufficiently large so that the molecules have moved a measurable amount in the meantime. Because fluorescence has a finite lifetime, the gas must be moving sufficiently fast and the resolution of the imaging optics must be sufficiently high to result in a measurable shift. This image can then be compared to the reference image. By measuring the distance that the tagged molecules have moved and dividing by the time delay between the laser pulse and the acquisition of the second image, the velocity is calculated. The $1/e$ fluorescence lifetime in our experiments was ~200 ns, and the resolution of our imaging system was on the order of 7 pixels per mm. The image-processing procedure is capable of resolving about 0.1 pixel, at best, through a curve-fitting algorithm that finds the center of lines in the images. This limits the accuracy of the technique to 70 m/s at the slow end, though this can be improved by averaging. If a

93

20% error can be tolerated in a single measurement, this technique could be used for axial velocities as low as 360 m/s. For a more detailed overview of the technique, see Danehy et al. (2003).

Other investigations have applied this technique by exciting a single line of molecules, thus measuring a velocity profile at one downstream location in the flow (Danehy et al. 2003). We extended the technique by tagging approximately 25 lines in the flow. This was accomplished by inserting a comb into the path of the laser sheet, effectively creating evenly-spaced strips of much smaller (albeit lower intensity than past work) laser sheets. The acquisition of the reference image and shifted image were often separated by several minutes. Thus, this technique is best suited for steady flows, as unsteadiness may introduce biased systematic errors into the measurement.

Images were acquired in much the same way as flow visualization images, using the same spectroscopic transitions to ensure signal throughout the image. The main differences were that the gate width of the intensifier was reduced to 200 ns and the gate delay, relative to the laser pulse, was varied. Typical delay times were 0, 200, 500, and 750 ns. Delays of 1000 ns resulted in a fluorescence signal that was generally too faint to yield an acceptable signal-to-noise ratio in the images. Due to low signal-to-noise ratios at longer delays, 100 (and in some cases, 200) images were acquired for a given delay and combined into an averaged image. Data processing was done using a combination of MATLAB and Microsoft Excel programs. In MATLAB, each raw data image was first cut into multiple strips, one for each measurement line in the image. Each strip basically consisted of a bright vertical line, with the left-to-right intensity starting low, increasing toward the center of the strip, and then decreasing again. One row at a time, a quadratic

94

polynomial was fit to the 9 brightest pixels. By setting the second derivative of the fitted polynomial to zero and solving for the horizontal distance, a sub-pixel value for the center of the line was calculated. After this calculation was performed for each row, the process was repeated for the next strip. Finally, the data were saved to a text file. Such text files were then imported into Excel for both the reference image and the delayed image. The fitted line center locations of the reference image were subtracted from those of the delayed image. A velocity measurement at each row of each strip was made by incorporating the known delay between images and the spatial scale of the images.

Although data were taken with the aim of making *quantitative* velocity measurements, unidentified errors have inhibited an absolute determination of appropriate error bars. In summary, it appears at this time that the acquisition and readout processes of the intensified CCD may be contributing in a poorly understood manner to the measured shifts in intensity. Calibration and parameterization studies of the intensified CCD are presently underway. Relative velocities, however, can be extracted from the data for most cases.

One further note about flow-tagging velocimetry bears mentioning. Using helium in place of nitrogen has the potential to enable measurements with greater precision, measured as a fraction of the maximum velocity. This is because for the same exit Mach number, helium velocities are much higher than nitrogen velocities. Considering the sonic nozzle (quantities associated with Mach 1 flow will be labeled with an asterisk), the exit temperature is related to the plenum pressure by (Anderson, 2003):

$$\frac{T^*}{T_0} = \frac{2}{\gamma + 1}.$$

(3.21)

95

Nitrogen is a diatomic molecule, so $\gamma_{N2} = 7/5 = 1.4$; helium is monatomic, so $\gamma_{He} = 5/3 \approx 1.7$. So for identical plenum temperatures, T_0,

$$\frac{T_{N2}^*}{T_{He}^*} = \frac{2.7}{2.4} = \frac{9}{8} = 1.125.$$

(3.22)

The specific gas constants for nitrogen and helium are listed in Table 3.2. Because the velocity at Mach 1 is equal to the sound speed, $a = \sqrt{\gamma RT}$, this gives a ratio of exit velocities of

$$\frac{v_{He}^*}{v_{N2}^*} = \sqrt{\frac{\gamma_{He} R_{He} T_{He}^*}{\gamma_{N2} R_{N2} T_{N2}^*}} = 2.72.$$

(3.23)

That is, helium can potentially yield velocities that are about 2.7 times larger than N_2. Mixing in 0.5% NO with the helium would change the effective adiabatic index only slightly, to 1.665. Larger absolute velocities result in smaller percentage errors for a given pixel size and camera magnification. So in future investigations, helium may a good candidate for velocimetry studies.

96

CHAPTER 4

Steady Laminar Free Jet Flow

The jet flows that have been studied in the present experiments have been divided into three main categories: laminar steady free jets; laminar, transitional, and turbulent unsteady free jets; and impinging jets. This chapter covers free jet flows in the *laminar steady* category. "Free" is used to distinguish these flows from impinging flows. Steady flows are those that exhibit no time dependence; measurements or images of steady flows are essentially identical for any arbitrary instant in time. Laminar flows are characterized by their "smoothness," namely, their lack of turbulent vortex structures. This chapter introduces the fluid mechanical concepts relevant to all of these categories, including the basics of supersonic flow, shock and expansion waves, flow through nozzles, and the resulting free jet structures. A representative sample of these flows is presented, and three selected cases are compared with computational fluid dynamics simulations. Laminar flows can broadly be divided into two classes—steady and unsteady laminar flows. Chapter 5 will introduce the concept of unsteadiness, following the natural progression from unsteady laminar flow to transitional and finally fully turbulent flows. Chapter 6 will present both steady and unsteady results from impinging jet cases.

97

4.1 Overview of Fluid Dynamics

The following sections will give only a brief overview of the basic equations governing the behavior of the underexpanded jets studied in these experiments. For a more detailed treatment, the reader is encouraged to consult the excellent texts by J. D. Anderson listed in the References section.

4.1.1 Definitions

4.1.1.1 Calorically perfect gas

The equations that follow have assumed that the gases involved in these flows are *calorically perfect* gases. A calorically perfect gas is one for which the specific heat capacity is a constant. This assumption is generally valid for gas temperatures well below the vibrational excitation temperature, at which higher-order vibrational modes become active. The highest temperatures seen in these experiments are on the order of 500 K, with the majority of the flow at much lower temperatures, so this assumption is a valid one for these tests. See Smith (2004, pp. 149-150) for detailed calculations of the relative partitions functions of nitrogen as a function of temperature.

4.1.1.2 Specific gas constant and adiabatic index

The specific gas constant for a given gas, R, is defined to be the difference between the specific heat capacity at constant pressure and the specific heat capacity at constant volume, $R \equiv c_p - c_v$. It is related to the universal gas constant $\mathcal{R}$ by the molar mass of the gas in question: $R_i = \mathcal{R}/M_i$. The adiabatic index, γ, is defined to be the ratio of the

98

specific heat capacities for a particular gas: $\gamma \equiv c_p / c_v$. Some constants for the gases used in these experiments are listed in Table 3.2 in the previous chapter.

4.1.2 Conservation Laws

The basic laws governing fluid flow arise from three simple laws: the conservation of mass, the conservation of momentum, and the conservation of energy. Derivations of practical forms of the conservation equations generally begin by defining a control volume. The time rate of change net amount of any one of the conserved quantities inside the control volume is defined to be the difference between the net flow of that quantity into the volume through the control surface to the net flow out through the surface. Steady state solutions are obtained by setting the rate of change to zero. If the control volume is defined in such a way so that flow is perpendicular to an inlet and outlet surface, and parallel to all other surfaces, the equations simplify considerably and result in simple conservation relations.

4.1.2.1 Mass (Continuity)

If the flow is steady, then conservation of mass dictates that there be no net mass flow through all control surfaces. The amount of mass flowing through a given control surface is the density of the gas multiplied by the component of gas velocity perpendicular to the control surface, times the infinitesimal area element. Mathematically, this conservation relation can be expressed as

$$\oiint_S \rho \vec{v} \cdot d\vec{A} = 0.$$ (4.1)

99

If the control surfaces are defined in such a way so that the velocity is perpendicular to two surfaces (an inflow and an outflow surface) but parallel to all other surfaces, then this equation becomes $\rho_1 A_1 v_1 = \rho_2 A_2 v_2$. This relation has practical application to computing flow through nozzles, for example, where the diameters of the plenum, throat and nozzle exit are known quantities, and the flow velocity can be assumed to be parallel to the nozzle walls. In calculating the flow across shock waves, the control volume can be chosen so that the areas of the inflow and outflow surfaces are identical. In that case, the equation becomes simply $\rho_1 v_1 = \rho_2 v_2$.

4.1.2.2 Momentum

The conservation of momentum dictates that the net change in the momentum of an element of fluid is equal to the sum of the forces acting upon it. In the jet flows studied here, external forces (e.g. gravity, electromagnetic forces) can be neglected. The remaining forces are then the internal forces due to pressure or viscosity. The majority of the flow features (i.e., shock structures) of steady laminar jet flows can be explained even if the effects of viscosity are neglected. This is obviously not the case for unsteady flows. Consider a control volume with inflow and outflow surfaces as defined above. In the inviscid approximation, the difference in momentum between the two surfaces is equal to the differences in the pressure forces acting on the two surfaces. The normal pressure force on a control surface is given by

$$F_{pressure} = \oiint_S \vec{p} \cdot d\vec{A} = -pA,$$
(4.2)

100

where the negative sign arises due to the opposite senses of the pressure and control surface unit vectors. Momentum conservation then says $m_2 v_2 - m_1 v_1 = p_1 A_1 - p_2 A_2$. Mass conservation determined that the amount of mass flowing through a control surface was a product of the density, velocity, and control surface area, so this expression becomes $\rho_2 A_2 v_2^2 - \rho_1 A_1 v_1^2 = p_1 A_1 - p_2 A_2$, or equivalently,

$$\left(p_1 + \rho_1 v_1^2\right) A_1 = \left(p_2 + \rho_2 v_2^2\right) A_2. \tag{4.3}$$

Again, this equation is convenient for calculating conditions in nozzle flows. For shock waves, the practical form of this equation results from setting the areas of the inflow and outflow surfaces equal.

4.1.2.3 Energy

The energy of a given volume of fluid is simply a sum of its kinetic and internal energies. Any change in the total energy is equal to the heat added to or work done on the element of fluid. If we again neglect any external forces and viscosity, and if we assume that no net heat is added to the system, then the work done on the fluid is just the pressure times the decrease in the volume of the fluid element. This is, of course, simply a way of stating the first law of thermodynamics. From the definition of heat capacity, we see that the heat capacity at constant volume is simply the change in the internal energy of the gas per unit change in temperature. If the internal energy is defined to be zero at zero temperature, than the internal energy is simply the product of the heat capacity at constant volume and the temperature. As a result, the total energy—internal and kinetic—of an element of fluid is given by $C_v T + pV + \frac{1}{2} mv^2$, which is a conserved quantity. The

internal energy terms are together called the *enthalpy*, H, of the gas: $H = C_v T + pV = C_p T$. In engineering analyses, the *specific enthalpy* (that is, the enthalpy per unit mass), $h = c_v T + p/\rho = c_p T$, is used instead of H, and the energy conservation equation becomes

$$h_1 + \frac{v_1^2}{2} = h_2 + \frac{v_2^2}{2}.$$ (4.4)

4.1.3 Second Law of Thermodynamics and Entropy

The differential form of the first law of thermodynamics is given by $dQ = c_v dT + pdV$. Dividing through by the temperature and using the perfect gas law gives a differential form of the definition of entropy, S:

$$dS \equiv \frac{dQ}{T} = C_v \frac{dT}{T} + n\mathcal{R}T \frac{dV}{V}.$$ (4.5)

Integrating gives

$$\Delta S = C_v \ln\left(\frac{T_2}{T_1}\right) + n\mathcal{R}T \ln\left(\frac{V_2}{V_1}\right).$$ (4.6)

By the second law of thermodynamics, reversible processes are defined to be those in which the change in entropy is zero. So for reversible processes, the following expression holds:

$$\left(\frac{T_2}{T_1}\right)^{-C_v} = \left(\frac{V_2}{V_1}\right)^{n\mathcal{R}T}.$$ (4.7)

A more common engineering relation uses the *specific* gas constant and the *specific* heat capacity, along with the definition of the adiabatic index, γ, and the fact that density is mass per volume, to arrive at the equivalent expression:

102

$$\left(\frac{T_2}{T_1}\right)^{\gamma/(\gamma-1)} = \left(\frac{\rho_2}{\rho_1}\right)^{\gamma} = \frac{p_2}{p_1}. \qquad\qquad (4.8)$$

This relation is extremely useful in calculating conditions at various places in the flow. For instance, nozzle exit conditions can easily be calculated from measured plenum conditions using this relation.

4.1.4 Shock and Expansion Waves

From the perspective of the laboratory frame of reference, a shock wave occurs whenever a component of velocity of a supersonic flow is decelerated to the point that it becomes subsonic. A shock wave can be understood by envisioning the following scenario. Imagine a supersonic flow, moving left to right in the laboratory frame. Now imagine a subsonic region adjacent to and to the right of the supersonic region. The two regions will be separated by a shock wave for the following reason: pressure waves (that is, sound waves) emanating from any point in the subsonic region will propagate away from that point at the speed of sound, in the reference frame of the gas. In the lab frame, these waves will propagate at the speed of sound plus or minus the local velocity of the gas. Because the gas is moving at less than the speed of wave propagation, there will be some waves which propagate to the left of the disturbance. But when they encounter the supersonic gas, they will not be able to travel toward the left any longer, as the gas will be moving left-to-right faster than the speed of the waves. Therefore, all left moving pressure waves will eventually meet and coalesce. The result is called a shock wave.

Expansion waves occur when a sonic or supersonic flow is accelerated to even higher Mach numbers. The flow through expansion waves can generally be treated as adiabatic

103

and isentropic, if the effects of viscosity can be neglected. Mach number is defined to be the ratio of the local flow velocity, v, to the local sound speed, a: $M = v/a$. For a calorically perfect gas, in which the heat capacities are constants with respect to temperature, the speed of sound is found to be a function of the adiabatic index, the specific gas constant, and the local gas temperature, as given by the relation $a = \sqrt{\gamma R T}$ (also defined in section 3.5). By combining these equations, the velocity of a gas can be expressed as $v = M\sqrt{\gamma R T}$. We can derive relations for flow parameters as a function of local Mach number by using the conservation equations and choosing one location to be the plenum. In the plenum, the pressure is defined to be the stagnation pressure, p_0, the temperature is the stagnation temperature, T_0, the density is ρ_0, and the velocity is essentially zero. Substituting the above relation into the equations for conservation of energy, and setting the velocity in the plenum equal to zero yields the following relation:

$$\frac{T}{T_0} = \left(1 + \frac{\gamma - 1}{2} M^2\right)^{-1}.$$

(4.9)

If this expression is then substituted into the isentropic flow relations given in the previous section, similar expressions for pressure and density result:

$$\frac{\rho}{\rho_0} = \left(1 + \frac{\gamma - 1}{2} M^2\right)^{1/(1-\gamma)},$$

(4.10)

and

$$\frac{p}{p_0} = \left(1 + \frac{\gamma - 1}{2} M^2\right)^{\gamma/(1-\gamma)}.$$

(4.11)

104

From these relations, we see that temperature, density, and pressure all decrease with increasing Mach number. Similar expressions can be derived for the conditions on either side of a shock wave. The text by J.D. Anderson (2003) contains an in-depth derivation. To summarize the results, flow across a shock wave is characterized by a decrease in Mach number. Suppose the flow velocity is expressed in terms of components of velocity that are parallel and perpendicular to the shock wave. Then the Mach number associated with the perpendicular component will be supersonic upstream of the shock wave and subsonic downstream of it, while the Mach number associated with the parallel component will be unaffected. Thus, flow across a normal shock wave is always subsonic downstream of the shock. This decrease in perpendicular Mach number is accompanied by corresponding increases in temperature, density, and pressure. Because fluorescence intensity is affected by these parameters, these relations will determine the relative PLIF intensity in various regions of the flow.

4.2 Underexpanded Jets

4.2.1 Sonic nozzles

Gas in the plenum (the high pressure reservoir upstream of a nozzle) is considered to be essentially at rest, with stagnation temperature and pressure T_0 and p_0, respectively. If a positive pressure differential exists between the plenum and the test section on the other side of the nozzle opening, then gas will naturally flow from high to low pressure. As gas flows through the nozzle, the diameter of the nozzle is decreasing, as is the cross-sectional area of the nozzle, and the nozzle is thus said to be "converging." The flow in

105

the plenum and in the converging portion of the nozzle will be subsonic and will obey Bernoulli's principle: as the area of the nozzle decreases, the velocity of the flow will increase. In a steady state condition, the same volume of air will pass through a given cross-sectional area of the flow for the same unit of time. As the area decreases, the gas has to move faster in order for this to happen. As the gas moves faster, the pressure of the gas drops. For subsonic flow below about Mach 0.3, it is actually a fairly valid approximation to treat the flow as incompressible; that is, to treat the density as constant (Anderson 2003). We are used to this assumption with liquid flows, but it is generally applicable to gaseous flows as well if there are no external applications of pressure so as to force a change in volume (as would be the case inside the cylinder of a piston engine, for example).

If the nozzle is merely a converging nozzle—that is, if the exit of the nozzle occurs at the plane of minimum diameter/area, then the velocity of the gas at the exit is determined, by the pressure differential between the plenum and test section. This is true until the pressure differential is large enough that the flow at the exit reaches the speed of sound. As the velocity at the exit approaches the speed of sound, the effect of any change in the pressure ratio—whether it is the plenum pressure or the ambient (i.e. test section) pressure that is being changed—travels downstream much faster (in the lab frame) than it travels upstream. Its upstream velocity is the speed of sound minus the local velocity of the flow. Its downstream velocity is just the speed of sound *plus* the local flow velocity. Eventually, if the pressure ratio is large enough, the exit velocity will be equal to the speed of sound. At this point, pressure waves cannot travel upstream into the nozzle and plenum; that is, information about the lower downstream pressure cannot travel upstream.

106

The flow is then said to be *choked*. Further decreases in the downstream pressure will affect the flow downstream of the nozzle, but the steady state of the flow through the plenum and nozzle will remain unchanged.

For converging nozzles, the jet flow into the test section will depend upon the nozzle exit-to-ambient pressure ratio. This pressure ratio will henceforth be called the *jet pressure ratio*, or *JPR*, and will be defined more precisely in section 4.2.4. Other sources use the plenum-to-ambient pressure ratio, which is often called the *nozzle pressure ratio*, or *NPR*. First, the *JPR* must be at least 1 if the flow is, in fact, choked. Clearly, a situation can exist where the *NPR* is positive—so there is gas flowing—but the flow is not choked. All of the case investigated in these experiments, however, involved choked flow. The nozzle exit pressure, p_e, will always be less than the plenum pressure. For a sonic nozzle flow, it will be approximately a factor of 2 lower, as given by the following expression (sonic conditions are usually indicated by an asterisk):

$$\frac{p_0}{p^*} = \left(\frac{\gamma+1}{2} \right)^{\gamma/(\gamma-1)} \tag{4.12}$$

For air, $\gamma = \gamma_{diatomic} = 1.4$, so $p_0/p^* = 1.893$. The pressure at the nozzle exit can never be *less* than the ambient pressure; in such a scenario, the exit velocity would simply drop to less than the speed of sound, and the exit pressure would rise until it was somewhere between the plenum and ambient pressures. So, in a choked condition, the *JPR* is greater than or equal to 1.

107

4.2.2 Converging-Diverging (Supersonic) Nozzles

Supersonic exit velocities require an additional section of the nozzle—a *diverging* section. The initial plenum and converging portion of the nozzle are identical to those for the sonic nozzle. The difference is that now an additional section has been added to the nozzle, and in this section, the cross-sectional area of the nozzle is increasing. This is called the *diverging* portion of the nozzle, and the whole nozzle is termed a *converging-diverging* nozzle. So we begin the discussion at the throat of this nozzle—the plane of minimum cross-sectional area—which is identical to the nozzle exit for the sonic nozzle. Assume that the flow here is choked. If the *NPR* is just large enough to create a choked condition, then the flow will pass through an infinitesimally weak shock wave and then decrease in velocity as the cross-sectional area of the nozzle increases, in accordance with Bernoulli's principle. If the *NPR* is increased, however, the gas beyond the throat actually accelerates, the velocity and Mach number increasing as the nozzle cross-sectional area increases.

Because the gas inside the nozzle is "protected" from the ambient pressure (that is, the walls of the nozzle prevent the ambient pressure from compressing or exerting suction on the gas in the nozzle), the gas can potentially *overexpand*, such that the pressure in the nozzle is lower than the ambient pressure. Depending on the pressure ratio, this leads to the formation of a shock wave (which acts to compress—and thus raise the pressure of—the overexpanded gas), either inside the nozzle (a normal shock), or at the nozzle exit (oblique shocks emanating from the nozzle lip). As the gas moves down the diverging part of the nozzle, not only is the pressure (and density and temperature) dropping, the

108

Mach number is increasing. Assuming the pressure ratio is great enough to prevent the formation of a normal shock inside the nozzle, the exit Mach number is then solely a function of the nozzle exit area, relative to the sonic throat area. The larger the ratio of exit-to-throat area, the greater the exit Mach number. This relation is given by the following equation, from J.D. Anderson (2003):

$$\left(\frac{A}{A^*}\right)^2 = \frac{1}{M^2}\left[\frac{2}{\gamma+1}\left(1+\frac{\gamma-1}{2}M^2\right)\right]^{(\gamma+1)/(\gamma-1)}.$$ (4.13)

In these experiments, the sonic nozzle had an exit diameter of 0.095 inches, and the supersonic nozzle was 0.165 inches. This exit-to-throat area ratio of 3.0 resulted in an exit Mach number of 2.6.

4.2.3 Characteristic flow structures

4.2.3.1 Sonic jet flows

If the *JPR* is equal to 1, the jet is said to be properly expanded, and results in a pressure matched condition. We expect such a flow to remain essentially collimated, with a jet diameter equal to the nozzle exit diameter. There will be an infinitely weak shock wave (called a *Mach wave*) at the exit plane of the nozzle, and the jet flow will gradually decrease in velocity and spread in diameter due to viscous effects (e.g. viscous diffusion). If the *JPR* is greater than 1, the situation becomes more interesting. In such a case, the jet is said to be *underexpanded*. Since pressure drops as a gas expands, the term *underexpanded* implies that the pressure at the nozzle exit is greater than the ambient pressure. And so, once the jet is free of the confines of the nozzle walls, the gas will expand into the relatively vacuous surrounding gas. The diameter of the jet will increase

109

and the pressure will begin to drop. The flow exiting the nozzle will expand around the lip of the nozzle, developing a radial component of velocity. If one were to draw a streamline through this region, the gas following that streamline would see decreasing pressure as the gas traveled through an *expansion fan*. If one were to draw lines perpendicular to the pressure gradient, they would resemble a fan, being tightly packed (indicating strong pressure gradients) at the lip of the nozzle, and spreading out from there.

A boundary develops between the jet and the quiescent gas. This boundary will generally be a *slip line*, meaning that the pressure is constant on either side, while the flow exhibits a sharp gradient in velocity across this boundary. If the pressures were not matched on either side of this boundary, the jet would either expand or be compressed until the pressure did match. As the expansion waves emanating from the nozzle lip encounter this free pressure boundary (called it a "free" boundary because it is not a rigid boundary imposed by, say, a wall, but rather can move and adjust until a steady state is reached), they are reflected as compression waves. A more in-depth explanation of the mechanisms behind this type of reflection off a free boundary can be found in *Modern Compressible Flow*, by J.D. Anderson. In some cases, the gas develops sufficient momentum through this expansion process that the expansion/compression processes continually overcorrect, giving rise to an oscillating flow structure.

For fairly low *JPR* (between about 1 and 3), the expansion waves emanating from the nozzle lip reflect from the constant pressure boundary as shock waves, which then travel back through the jet at an oblique angle and reflect from the free pressure boundary on the other side as expansion waves—back and forth—giving rise to a "diamond shock"

110

pattern. The details of the shock pattern are not always visible in PLIF images, depending on the fluorescence characteristics of the chosen excitation line(s) and the magnification of the imaging optics. However, these flows can be identified by their nearly collimated jet boundary, with a width comparable to the nozzle exit diameter, and their lack of a barrel shock structure, described below. Figure 4.1 shows a PLIF image of a diamond shock pattern in a jet issuing from the sonic nozzle.
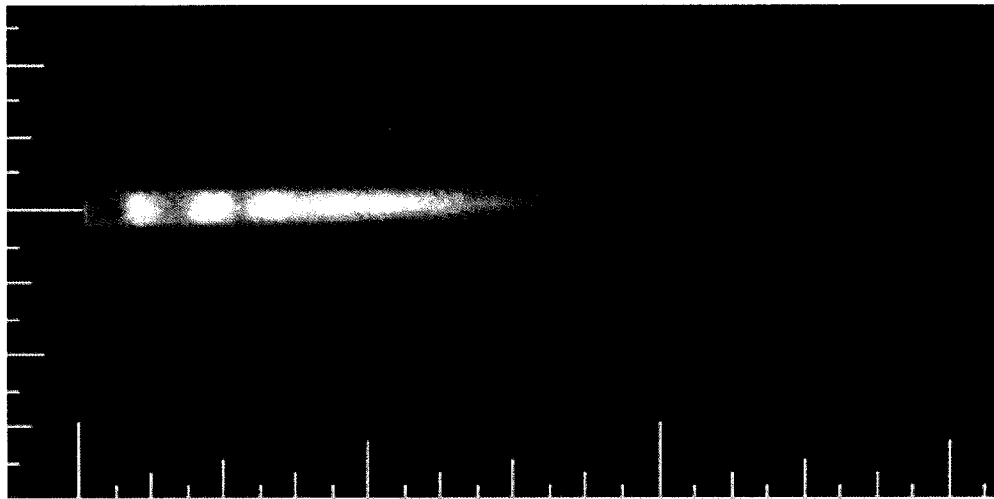
Figure 4.1: Diamond shock pattern in flow from sonic nozzle. Several diamond shock cells in the first several jet diameters downstream of the nozzle exit. This image is a 100-shot average of a flow with $JPR = 1.9$ and $Re_{exit} = 417$ (Run 5).

If the JPR is greater than about 3, the flow becomes even more complex. Figures 4.2 and 4.3 are schematics showing typical flow structures exhibited by these highly underexpanded jets. The expansion waves emanating from the nozzle lip reflect off the free pressure boundary as compression waves (weaker than shock waves initially), which rapidly coalesce into a shock wave—this specific type of shock being called a *barrel shock* structure, because in three dimensions, it resembles the shape of a barrel. Streamlines leading to the gas in the high velocity jet boundary may have passed through

111

this barrel shock, but the barrel shock is nearly tangential to the streamlines that end up in the shear layer, and so the shock wave that this gas encounters is a very oblique shock.
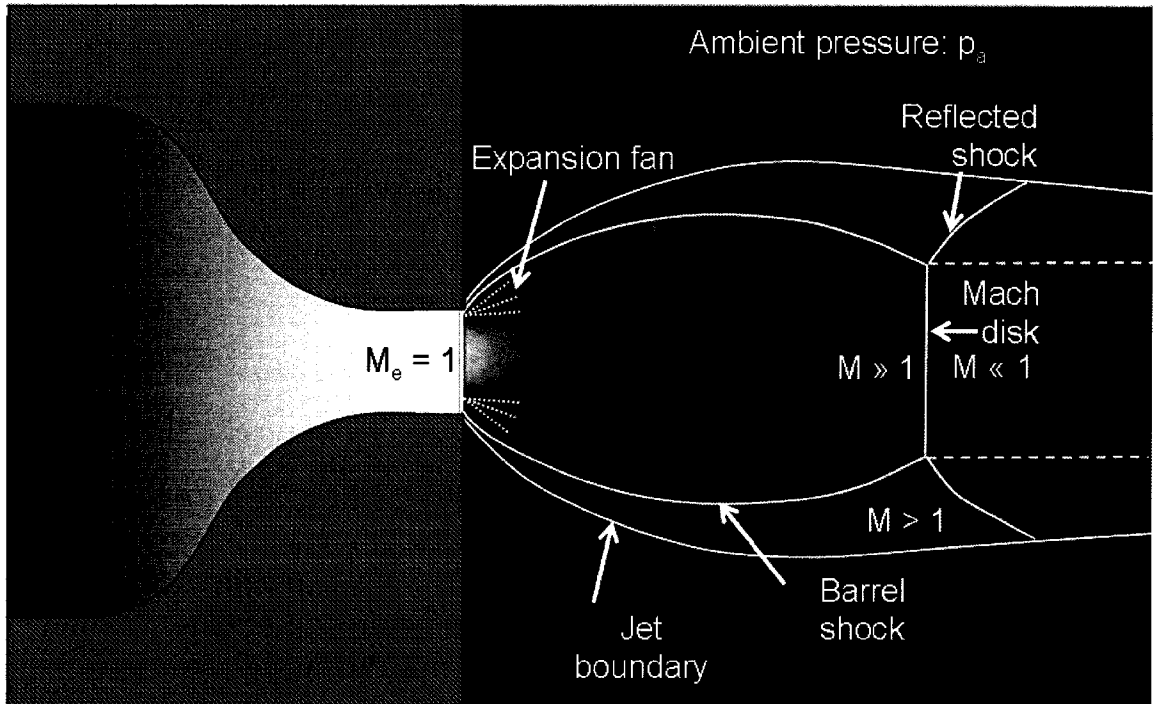
Figure 4.2: Sonic nozzle and highly-underexpanded jet flow structures. Large enough jet pressure ratios give rise to the jet structures shown above, namely, a barrel shock with a Mach disk. Additional flow structures are shown in Fig. 4.3.
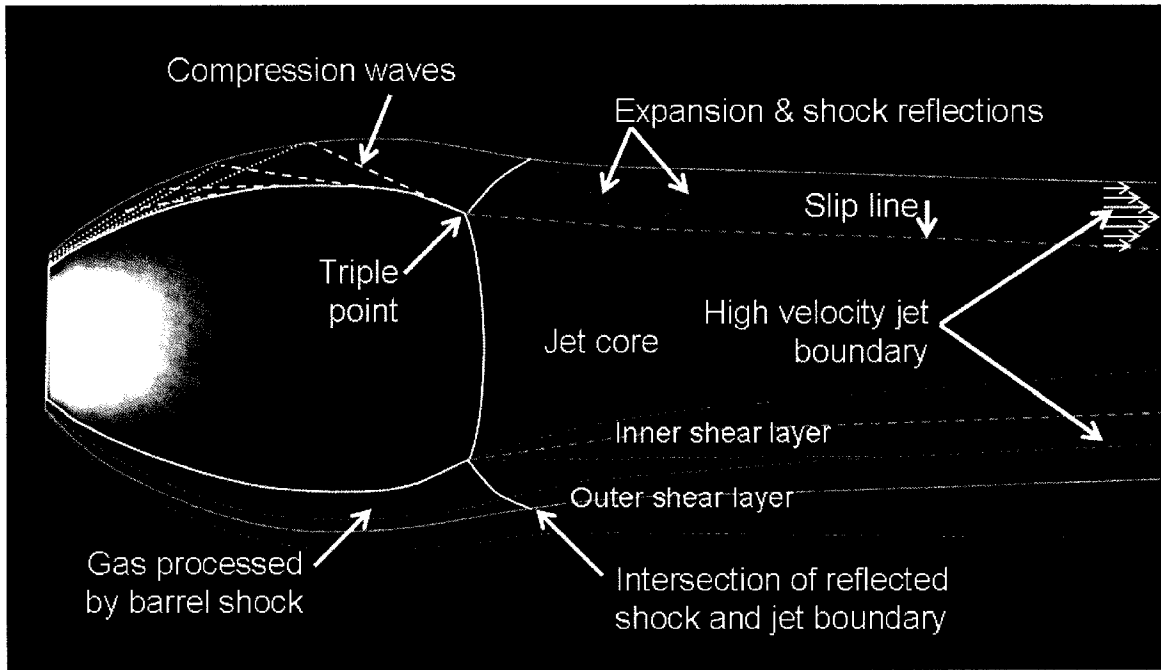
Figure 4.3: Highly-underexpanded sonic jet flow structures. (PLIF image is from Run 56 with $JPR = 29.1$ and $Re_{exit} = 4,294$.) Viscosity gives rise to the development of shear layers, both along the slip line adjacent to the jet core and along the jet boundary itself.

As previously mentioned, when computing flow conditions across oblique shock waves, it is instructive to decompose the velocity vectors of the gas into components that are perpendicular and parallel to the shock wave. Only the normal velocity components of the gas will be affected. That is, the equations relating the effects of a shock wave on the pressure, density, and temperature of the gas depend only on the component of the gas that is perpendicular to the shock. As discussed in section 4.1.4, the perpendicular component of velocity (and thus, the Mach number of this component) is always subsonic downstream of a shock wave. But the parallel component is unaffected, and thus, the gas downstream of an oblique shock wave may still be significantly supersonic. That is the case for gas in the outer shear layer of underexpanded jets (so long as the shear layer has

113

not yet gone turbulent). To illustrate the fact that the gas along the jet boundary is moving faster than the gas in the core of the jet, a raw velocity-sensitive PLIF image is presented in Fig. 4.4. For an explanation of flow-tagging velocimetry, see section 3.5. This image was acquired 1 μs after the firing of the laser. As a result of the gas moving during this time delay, lines of molecules that were once straight lines are instead curved. This is especially evident in the first few lines downstream of the Mach disk, where the gas in the high-velocity jet boundary has moved noticeably further downstream than the gas in the jet core.

Figure 4.4: Velocity sensitive image. This is a 100-shot average image of Run 69, taken at a delay of 1 μs, for a free jet sonic nozzle flow with $JPR = 12.8$ and $Re_{exit} = 2,685$. The curvature in the lines indicates the difference in velocity between the inner and outer parts of the jet, showing that the jet boundary is moving at a higher velocity than the jet core, particularly in the region just downstream of the Mach disk (which is in the vicinity of the fourth line). Also notice the decrease in curvature further downstream, where viscous effects have had an effect and have reduced the gradient in velocity along a given line.

The gas in the core of the jet undergoes expansion and the accompanying increase in Mach number, and decrease in density, pressure and temperature. The increase in Mach number is actually largely due to the drop in temperature, so while the velocity of the gas is increasing, it is not increasing as rapidly as the Mach number might seem to indicate.

114

Instead, the sound speed is dropping as the square root of temperature, and so the Mach number increases far more rapidly than does the velocity.

Through this supersonic expansion, the pressure in the core of the jet drops below the pressure in the shear layer (which is nearly the same as the ambient pressure, except for the effect of reflecting shock and expansion waves within the shear layer). This large pressure difference eventually gives rise to a normal shock wave ("normal" meaning perpendicular to the axis of the jet), or *Mach disk*. (In three dimensions, the shock is thin and round and somewhat lens-shaped). The supersonic gas in the core of the jet passes through this shock wave and becomes subsonic. The pressure rises abruptly, as does the temperature and density of the gas. The gas velocity is as low as it will get at this point. Viscous interaction with the (much faster-moving) shear layer acts to accelerate the flow back up to higher—potentially supersonic—speeds.

When two shock waves intersect, reflections can generate additional shock waves. This is the case where the barrel shock structure intersects the Mach disk. The intersection is termed a *triple point*. The shock wave that is generated at this triple point reflects off the constant pressure boundary and leads to a series of reflected shocks and expansion waves inside the shear layer. As will be seen in the following chapters, this triple point plays a key role in the development of instabilities in the flow.

4.2.3.2 Supersonic jets

The basic flow structures described in the preceding section on underexpanded jet flow out of sonic nozzles also appear in flows from nozzles with supersonic exit velocities. Supersonic jets do, however, have several distinguishing features. For low jet

115

pressure ratios, an analog of the diamond shock pattern is seen. A Mach disk is either not present or is too small to be resolved in these flows, as seen in Figure 4.5.
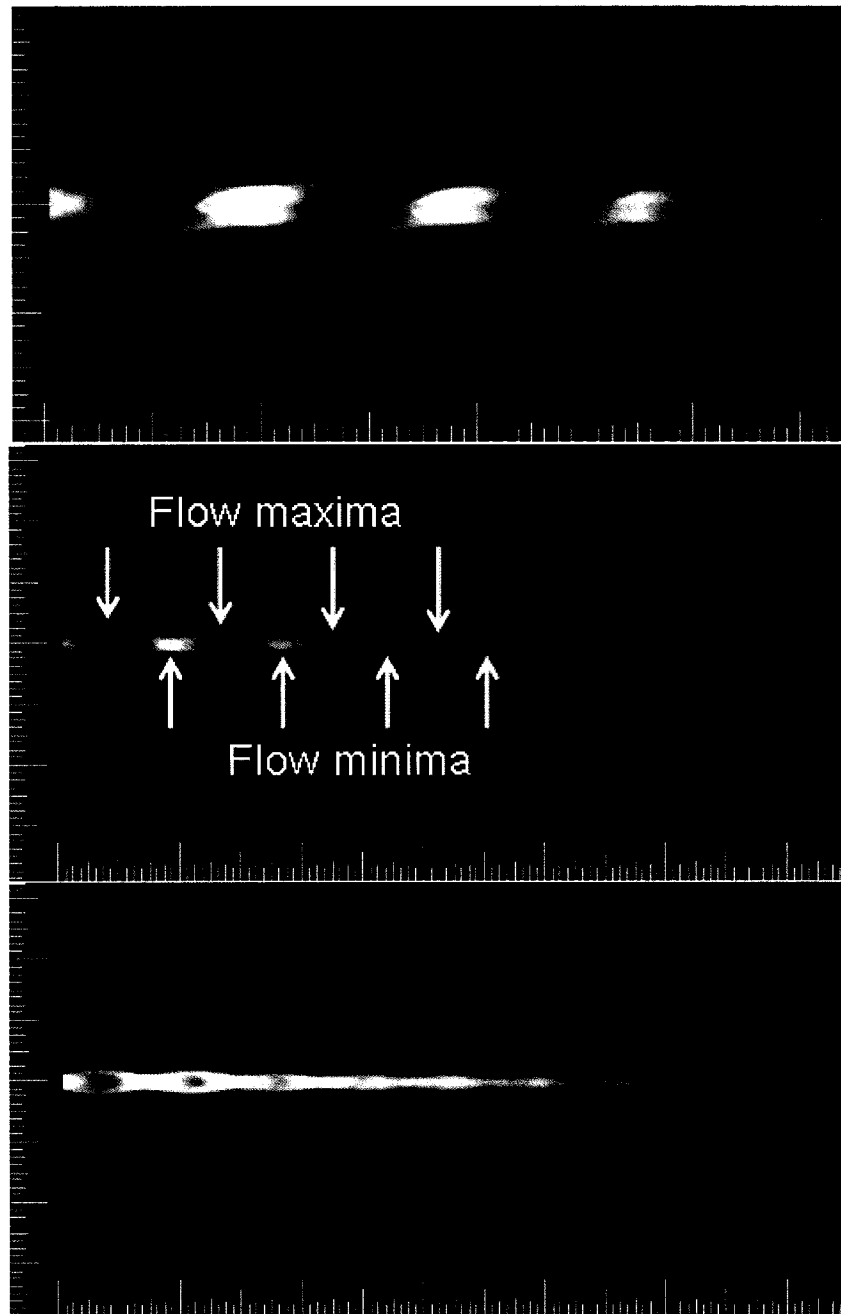
Figure 4.5: Underexpanded supersonic jets at low pressure ratios. The images are all 100-shot averages. (a) Run 354, $JPR = 2.0$, $Re_{exit} = 4,605$; (b) Run 222, $JPR = 3.0$, $Re_{exit} = 3,370$, with arrows marking examples of flow minima and maxima; (c) Run 225, $JPR = 2.1$, $Re_{exit} = 3,399$. The largest hash marks on the scales along the edges of the images are whole inches.

116

The flow does bear similarities to a diamond shock pattern, in that the flow goes through successive minima (contractions) and maxima (expansions), but the individual cells are no longer diamond-shaped. Rather, each cell is elongated and rounded into something more "egg-shaped." Viscous diffusion effects cause the magnitude of these oscillations to decrease with time, resulting in smaller and smaller cell structures, as in the diamond shock case.
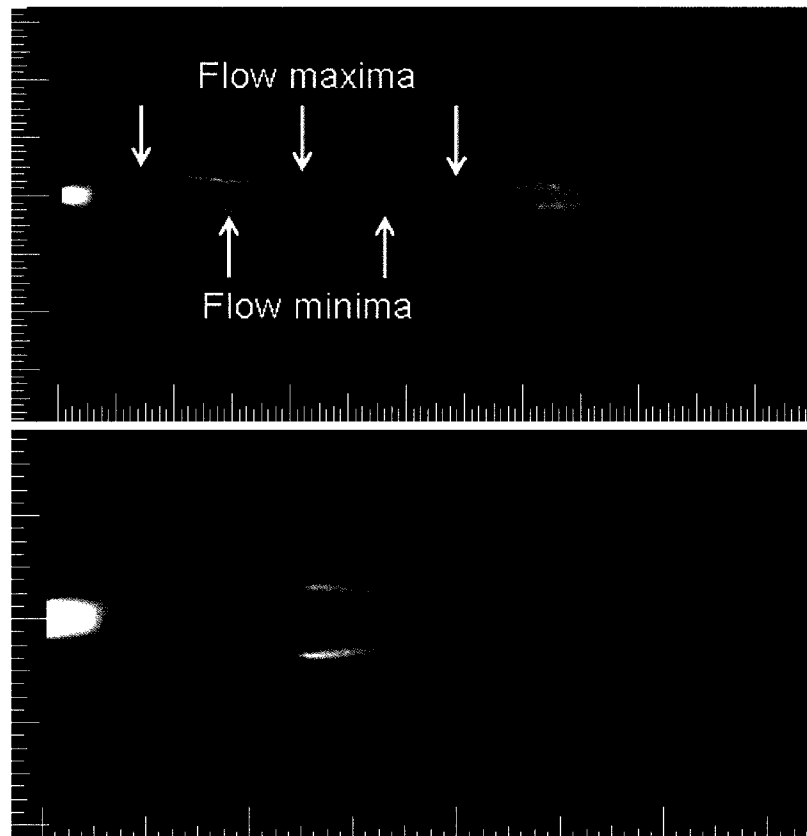
Figure 4.6: Supersonic free jets with Mach disks and oscillating high-velocity jet boundaries. Both images are 100-shot averages. The first image is from Run 230, with $JPR = 6.9$ and $Re_{exit} = 4,557$. Arrows mark examples of flow minima and maxima. The second image is from Run 348 with $JPR = 5.3$ and $Re_{exit} = 4,560$.

As the pressure ratio increases further still for supersonic jets, a Mach disk appears, along with the triple point, reflected shock, and the impingement point between this

117

reflected shock and the shear layer, as in the sonic jet case. The barrel shock of supersonic jets is noticeably elongated compared to that of sonic jets. This is due, in part, to the fact that the flow in the diverging part of the nozzle already has acquired a radial component of velocity. Thus, the flow exiting the nozzle does not expand around as sharp of a corner as in the sonic nozzle geometry. Before the pressure ratio is too great, the oscillating minima/maxima structures are still evident, although they no longer meet in the center of the jet. Figure 4.6 shows an example of such a case. As the pressure ratio is increased still further, these oscillations become increasingly damped, until finally, the shear layer is essentially parallel to the jet axis. An example of this type of flow is seen in Figure 4.7.
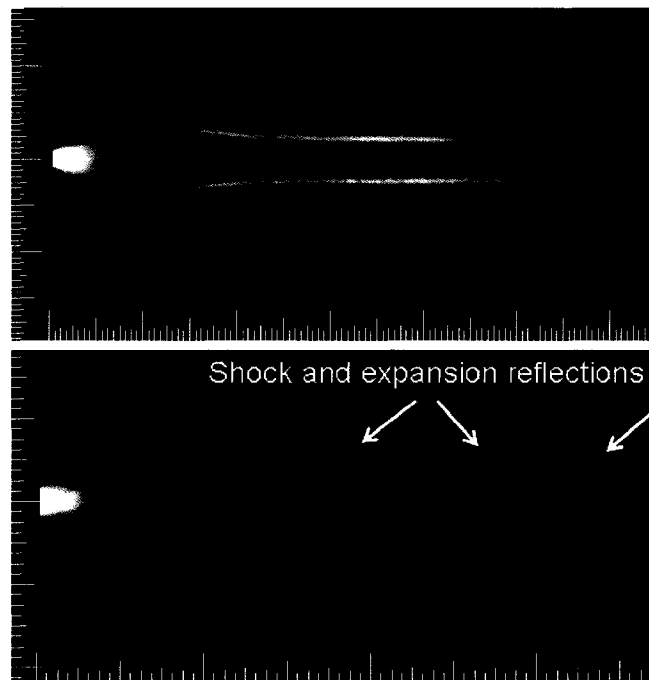
Figure 4.7: Supersonic free jets with Mach disks and parallel high-velocity jet boundaries. Both images are 100-shot averages. The first image is from Run 236, with $JPR = 16.2$ and $Re_{exit} = 13,104$; the second is from Run 347 with $JPR = 12.6$ and Re_{exit} = 10,173. The shock and expansion reflections in the high-velocity jet boundary, diagrammed in Fig. 4.2 are visible in this second image.

118

4.2.4 Experimental parameters

Two parameters were independently varied: Reynolds number (Re_{exit}) and jet pressure ratio (JPR). Re_{exit} was defined in terms of the diameter D_e (m), density ρ_e (kg/m^3), velocity V_e (m/s), and dynamic viscosity μ_e (Pa·s) at the nozzle exit (conditions at the nozzle exit are indicated by the subscript e), as given by Eq. (4.14).

$$Re_{exit} = \frac{\rho_e V_e D_e}{\mu_e} \qquad (4.14)$$

The nozzles used in these tests had exit diameters of $D_e = 2.4$ mm (0.095 in.) for the sonic nozzle and 4.2 mm (0.164 in.) for the supersonic nozzle. Re_{exit} was varied by changing the mass flow rates and gas temperature, and was calculated based on measured plenum conditions, as described below.

JPR was defined as the ratio of the static pressure at the nozzle exit, p_e, to the ambient pressure in the test chamber, p_a, according to Eq. (4.15), and was varied by changing the test chamber pressure.

$$JPR = \frac{p_e}{p_a} \qquad (4.15)$$

For a given Re_{exit}, the maximum attainable JPR was limited by the minimum attainable pressure in the vacuum chamber, which was typically about 133 Pa (1 Torr, 0.02 psi). Figures 4.8 and 4.9 show PLIF images of steady laminar sonic and supersonic free jets, respectively, for a several jet pressure ratios.

119
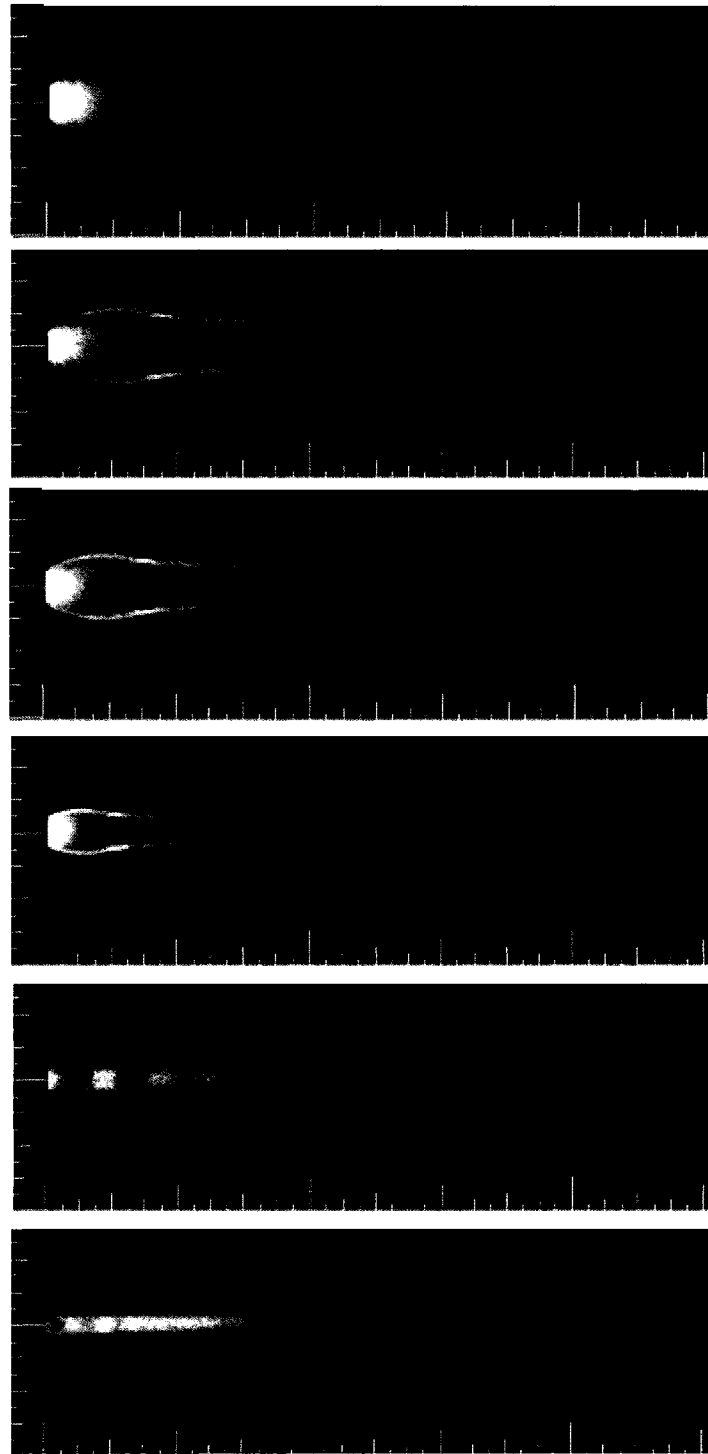
Figure 4.8. Single-shot PLIF images of underexpanded sonic jet flows at six different jet pressure ratios. From top to bottom, these *JPR*s are: 37.4, 21.9, 16.3, 8.3, 3.9, and 1.9 for Runs 55, 58, 60, 48, 4, and 5, respectively. The presence of a Mach disk characterizes high *JPR* flows, while low *JPR* flows are characterized by a diamond shock pattern. Mach disks were observed in flows with *JPR*s greater than about 3.

120
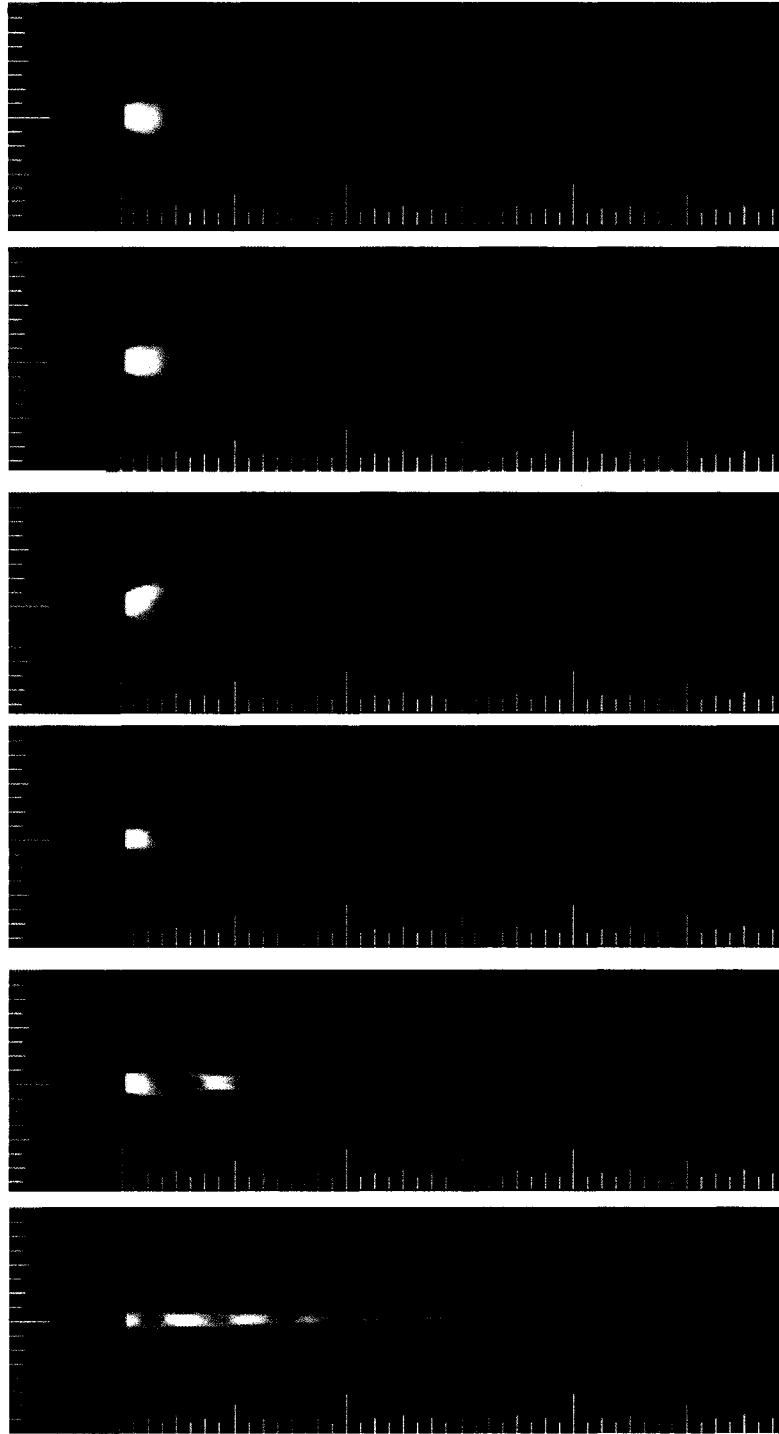
Figure 4.9.   Single-shot PLIF images of underexpanded sonic jet flows at six different jet pressure ratios and similar exit Reynolds numbers.   From top to bottom, these *JPR*s are: 19.2, 15.1, 7.7, 3.7, 2.1, and 1.1 for Runs 650, 652, 658, 646, 648, and 649, respectively.   The presence of a Mach disk characterizes high *JPR* flows, while low *JPR* flows are characterized by an oscillating shock pattern. Mach disks were observed in flows with *JPR*s greater than about 4.

121

A thermocouple and a pressure transducer measured the gas temperature T_0 and pressure p_0 in the plenum, upstream of the converging nozzle. Measuring these quantities made it possible to calculate conditions at the nozzle exit, and therefore the exit Reynolds number. Nozzle exit temperature T_e (K) and velocity V_e (m/s) were calculated from the measured quantities T_0, and pressure, p_0, assuming inviscid adiabatic flow at the nozzle exit, and an exit Mach number of 1, according to Eqs. (4.16) and (4.17) (Anderson 2003):

$$T_e = \frac{T_0}{1 + \left(\frac{\gamma - 1}{2}\right)} \tag{4.16}$$

$$V_e = \sqrt{\gamma R T_e} . \tag{4.17}$$

where γ is the ratio of specific heats of the gas ($\gamma = 1.4$ for nitrogen), and R is the specific gas constant with a value of 287 J/(kg·K). Furthermore, with the added assumption of isentropic flow, nozzle exit pressure p_e (Pa) and density ρ_e (kg/m³) can be calculated using Eqs. (4.18) and (4.19), also from J.D. Anderson (2003):

$$p_e = \frac{p_0}{\left(1 + \frac{\gamma - 1}{2}\right)^{\gamma/(\gamma-1)}} \tag{4.18}$$

$$\rho_e = \frac{p_0}{RT_0\left(1 + \frac{\gamma - 1}{2}\right)^{1/(\gamma-1)}} . \tag{4.19}$$

The dynamic viscosity μ_e (Pa·s) at the nozzle exit was calculated using the power law approximation given in Eq. (4.20):

122

$$\mu_e = \mu_{ref}\left(\frac{T_e}{T_{ref}}\right)^n .$$
(4.20)

This power law accounts for the effect of temperature on dynamic viscosity while neglecting the slight dependence on pressure. Table 3.2 lists empirical values of n and μ_{ref} from White (1991) where $T_{ref} = 273$ K (32 °F), for the gases used in these jet flows.

4.2.5 Matrix of test cases

JPR\Re$_{exit}$	350	850	1100	1500	2500	3500	4500	5500	6500	8500	10000	16000	20000	27000	35000
1	.	.	.	.	.	.	.	.	.	.	.	.	.	.	.
1.5	.	.	.	.	.	.	.	.	.	.	.	.	.	.	.
1.7	.	.	.	.	2	.	.	.	.	.	.	.	.	.	.
2	2	1	.	3	1	.	.	.	.	.	.	.	.	.	.
3	.	.	.	.	4	.	4	.	.	.	.	2	.	.	.
4	2	4	.	3	1	5	5	.	.	.	1	2	.	.	2
5	1	.	.	.	.	.	.	.	.	.	.	.	1	.	.
6	.	.	.	.	2	.	.	.	.	4	.	.	.	.	.
7	.	.	.	.	2	.	.	.	.	.	.	.	.	.	.
8	.	1	.	2	1	4	.	.	.	1	.	.	.	.	1
9	.	1	.	.	.	2	.	.	.	.	.	.	.	.	.
10	.	.	.	.	.	3	.	.	.	.	.	.	.	.	.
11	.	.	.	.	.	.	.	.	.	.	.	.	.	.	.
12	.	.	.	.	.	.	.	.	.	.	.	.	.	.	.
13	.	.	.	.	.	.	3	.	.	.	.	.	.	.	.
14	.	1	.	.	.	.	1	1	1	.	1	4	.	.	.
15	.	.	.	2	.	.	3	4	2	.	3	.	.	1	.
16	.	2	2	1	3	1	.	1	1	1	.	.	.	.	3
17	.	.	1	.	.	.	.	.	.	.	.	.	.	.	.
18	.	.	.	.	.	.	.	.	.	.	.	.	.	.	.
19	.	.	.	.	.	.	.	.	.	.	.	.	.	.	.
20-23	.	1	.	.	2	.	2	2	2	1	4	4	4	4	.
24-29	.	.	1	.	2	.	2	1	2	2	.	4	4	4	4
30+	.	.	.	1	1	.	2	2	1	3	2	.	.	.	.

Table 4.1: Test matrix for sonic nozzle flow-visualization cases. Entries indicate the number of runs acquired at each combination of jet pressure ratio and exit Reynolds number. This test matrix includes both free and impinging jet cases, but does not include velocity, pressure-sensitive, or density-sensitive runs.

Table 4.1 shows the number of sonic nozzle runs that were acquired at different combinations of JPR and Re$_{exit}$. Table 4.2 shows the same for the supersonic nozzle. The lack of data at low Reynolds number / high pressure ratio cases in Table 4.2 is a direct

123

result of the limitation presented by the minimum attainable test section pressure of 1-2

Torr (133-267 Pa, 0.02-0.04 psi).

JPR\Re$_{exit}$	600	1000	1400	2200	3500	4500	7500	8500	10500	14000	18500	22000
1	12	1	.	2	1	1	1	13	1	1	.	.
1.5	.	11	9	11	.	.	1	2	.	.	.	.
1.7	.	12	5	1	.	.	.	11	.	.	.	.
2	.	2	9	15	1	17	1	1	5	1	1	1
3	.	.	3	16	3	18	1	18	2	.	1	.
4	.	.	.	10	11	18	1	8	1	.	1	1
5	.	.	.	.	1	7	.	12	.	.	.	.
6	.	.	.	.	.	22	1	1	1	.	1	1
7	.	.	.	.	.	4	.	12	.	.	.	.
8	.	.	.	.	.	.	1	3	1	.	1	1
9	.	.	.	.	.	.	.	13	1	.	.	1
10	.	.	.	.	.	.	2	3	.	.	1	.
11	.	.	.	.	.	.	.	8	1	.	.	.
12	.	.	.	.	.	.	.	10	2	.	1	1
13	.	.	.	.	.	.	.	1	2	.	.	.
14	.	.	.	.	.	.	.	.	5	1	.	.
15	.	.	.	.	.	.	.	.	4	4	1	1
16	.	.	.	.	.	.	.	.	1	10	.	.
17	.	.	.	.	.	.	.	.	.	.	.	.
18	.	.	.	.	.	.	.	.	.	.	.	.
19	.	.	.	.	.	.	.	.	.	.	2	1

Table 4.2: Test matrix for supersonic nozzle flow visualization cases. This test matrix includes both free and impinging jet cases, but does not include velocity, pressure-sensitive, or density-sensitive runs.

4.3 Comparison with Computational Results

Computational fluid dynamics (CFD) represents a vital tool for evaluating flight damage scenarios since no set of ground-based experiments could anticipate every potential vehicle damage scenario nor entirely replicate the high-energy flight environment. When applying computational tools to engineering applications, understanding the accuracy and limitations of that tool is obviously of critical importance. It was therefore desired to compare computations to experimental results. To that end, the present experimental work was designed to generate flows at conditions comparable

124

to those expected to be encountered in flight, but with relatively simple geometries and well-defined boundary conditions. The flow visualization images resulting from this work allowed the size and location of major flow features to be compared with the results of CFD simulations, as well as with previous experimental and computational results.

4.3.1 Selection of Test Cases

Three test cases were selected for the purposes of comparison with CFD. Three different jet pressure ratios were selected, and for ease of comparison with CFD, all three selected cases were laminar. Velocimetry data were taken at each of these three test conditions, although they are not reported herein as the results are still being analyzed. Measured parameters recorded by the data acquisition system during these velocimetry runs was processed and served as the input conditions to the CFD code, as described below. Flow visualization images were acquired at conditions similar to these three cases. Due to hardware limitations, the gas temperature was only coarsely controllable (within about 50 K), and the test chamber static pressure was only repeatable within about 0.1 Torr (0.002 psi, 13 Pa). This variability led to slight variations between the conditions at which velocimetry data were acquired (and at which CFD computations were performed) and those at which flow visualization images were acquired. Measured and calculated test conditions for the three test cases—A, B, and C—are summarized in Table 4.3, with data for flow visualization conditions in parentheses.

125

Test Case	JPR	Re_{exit}	T_0	p_0		p_a		
			K	Pa	psi	Pa	psi	Torr
A	4.2 (3.8)	835 (832)	588 (544)	5090 (4710)	0.738 (0.683)	646 (657)	0.094 (0.095)	4.84 (4.93)
B	18.2 (16.8)	1101 (1076)	605 (559)	6941 (6290)	1.01 (0.91)	201 (198)	0.029 (0.029)	1.51 (1.49)
C	31.4 (27.6)	1230 (1116)	580 (590)	7379 (6950)	1.07 (1.01)	124 (133)	0.018 (0.019)	0.93 (1.00)

Table 4.3: Test conditions. Jet pressure ratio, exit Reynolds number, plenum temperature, plenum pressure, and test chamber pressure for the three CFD test cases are presented in this table. Values in parentheses are conditions for three flow visualization runs taken at conditions similar to those for which CFD was performed.

4.3.2 Image Processing and Analysis

Sets of 100 single-shot images were acquired for a range of unit Re_{exit} (177 to 35,700) and JPR (1.8 to 38). Background images were also acquired on each day of testing for a range of vacuum chamber pressures. During the acquisition of these background images, the laser was fired but no gas was flowing through the nozzle. Any nonzero intensity in these background images is attributed to either camera dark current or the laser scatter and room light not blocked by the filter in front of the camera lens. Background images were created from the average of 100 single-shot images in order to smooth out random shot-to-shot variations in background intensity.

Single-shot images were processed to correct for background scattered light and camera dark current as well as spatial variations in laser sheet intensity. Conveniently, jet

126

gas containing nitric oxide diffused relatively uniformly into the test chamber in regions away from the jet. The fluorescence from the diffuse nitric oxide in these regions provided a convenient laser-energy reference, allowing the spatial variation in the laser intensity to be corrected. This was accomplished by first selecting an area of the image above the core of the jet flow and then establishing the average pixel intensity along each column in that region. Note that raw images were 512 x 512 pixels; images presented in this paper have been cropped top and bottom to show the regions of greatest interest. The image processing procedure is discussed in greater detail in section 5.2.1.

4.3.3 Computational Fluid Dynamics

The CFD for the present study was done by Chris Glass of the Aerothermodynamics branch at NASA Langley Research Center. He performed the computations using the General Aerodynamic Simulation Program (GASP) Version 4 software from AeroSoft, Inc. (GASP 2002). Previous use of the software for a similar study (McDaniel et al. 2002) showed that the computational and experimental results compared well; therefore, the software was considered well-suited for the present study.

The grid used to simulate the jet consisted of two zones: a subsonic plenum and nozzle zone and a free expansion zone. The plenum and nozzle zone profile matched that of the hardware used for the experiment. To capture the free jet, a grid larger than the jet was utilized in the jet expansion portion of the grid. The grids for both zones are shown in Fig. 4.10. Details about the boundary conditions and computational methodology employed in computing these three cases can be found in the paper by Wilkes et al. (2006).

127
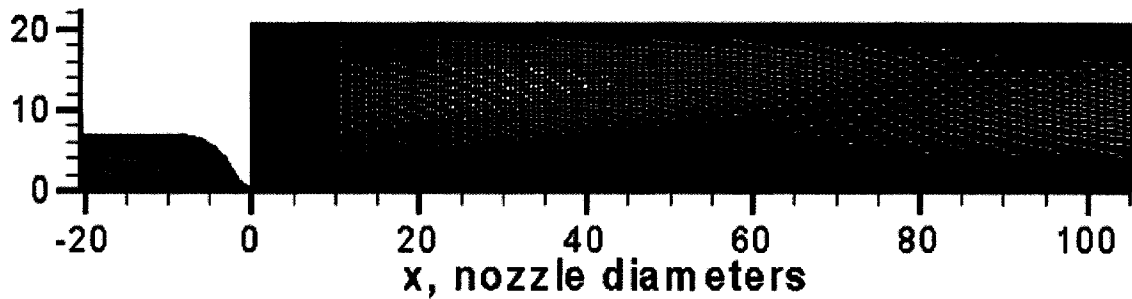
Figure 4.10: Grid geometry used in CFD computation. Here, the grid geometries for zones 1 (plenum and nozzle) and 2 (free expansion region) are shown, with distances given in terms of nozzle diameters (De = 0.095 inches). Image credit: Chris Glass.

In Case A, nonphysical, time-dependent, vortical flow features appeared beyond a downstream distance of approximately 12 nozzle diameters. These features are artifacts of the boundary conditions imposed on the outer grid boundary in the free expansion zone, and potentially could have been eliminated following the methodology outlined in Bivolaru et al. (2006). In that work, the authors encountered a similar problem with computations involving a jet issuing into quiescent air. To reduce these types of numerical artifacts, they imposed a slight pressure gradient across the external domain. They found that this produced an external flow with a velocity of approximately 7 m/s, but that good convergence was found in the downstream region within a reasonable number of integration cycles.

In the present work, we were interested in comparing PLIF flow visualization images with computational results. This comparison focused on the near field of the jet (that is, on the region within several jet diameters of the nozzle exit). For comparisons of flow structures, a converged solution was needed in regions near the Mach disk, as well as regions upstream of the Mach disk; this required distance was approximately 3 nozzle

128

diameter for Case A. Therefore, stability of the solution out to 12 nozzle diameters was considered more than sufficient for the purpose of jet structure comparisons. Figure 4.11 shows the GASP results for the mass fraction of nitric oxide, obtained by Chris Glass of NASA Langley Research Center, for all three cases.
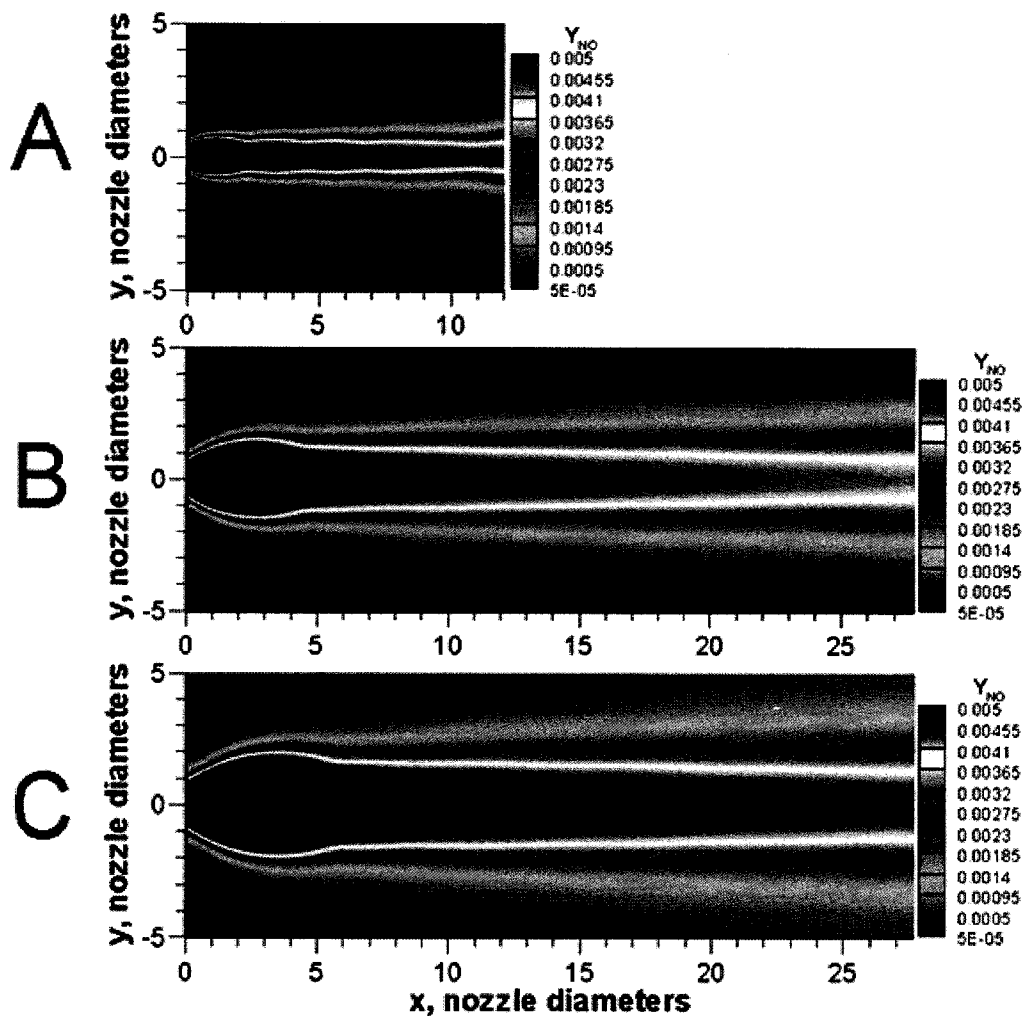
Figure 4.11: Nitric oxide mass fraction. Maps of the mass fraction of nitric oxide are shown for the three CFD test cases of the present study. Images have been cropped to show regions where minimal mixing has occurred in the core of the jet.

One additional consideration for Case A was that in the experimental flowfield, the mixing of the jet with the ambient air downstream resulted in quenching of NO

129

fluorescence by oxygen. In the flow visualization image similar to Case A, significant attenuation of the PLIF signal was observed beyond about 12 nozzle diameters because of this effect, as well as diffusion. For these reasons, we have chosen to limit our presentation of Case A results to 12 nozzle diameters downstream of the nozzle exit.

4.3.4 Jet Structure Comparison

Many of the flow structures described in the preceding sections, including Mach disks, barrel shocks, and shear layers, are clearly visible in the PLIF flow visualization images of this study. The location, shape, and size of such structures provide quantitative data that can be compared to CFD solutions.

4.3.4.1 Sonic jet structures

For the present study, we have chosen three readily identifiable flow structure dimensions to compare with computational results. These three dimensions, indicated in Fig. 4.12, are the Mach disk location, x_m, the Mach disk diameter, D_m, and the primary wavelength, w, of the flow.
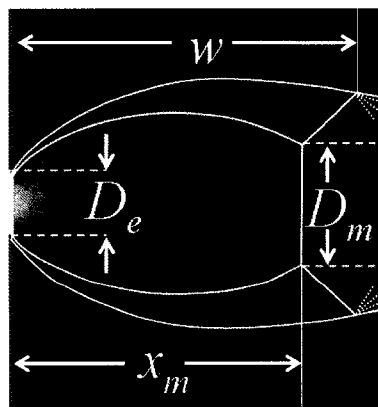
Figure 4.12: Flow structure dimensions. Major flow structures of interest include the following: D_e, the nozzle exit diameter; D_m, the Mach disk diameter; x_m, the distance to the Mach disk; and w, the primary wavelength of the jet.

130

To measure these dimensions from PLIF images, the magnification of the camera-lens system had to be accurately determined. Images of a scale (ruler) were obtained on nearly every day of testing. By measuring the pixel location of the hash marks on these scales and then fitting a line to these pixels locations, the spatial resolution of the imaging system was found. Flow feature locations were then recorded in terms of pixel location in the image, and these locations were then converted into a physical length. The locations of these flow features were determined by eye, generally in the camera software program, WinView32, where the location of a given feature was recorded in terms of the pixel location within an image. Figures 4.13, 4.14, and 4.15 show the results of these measurements, plotted in units of nozzle diameters (as noted above, $D_e = 0.095$ inches).
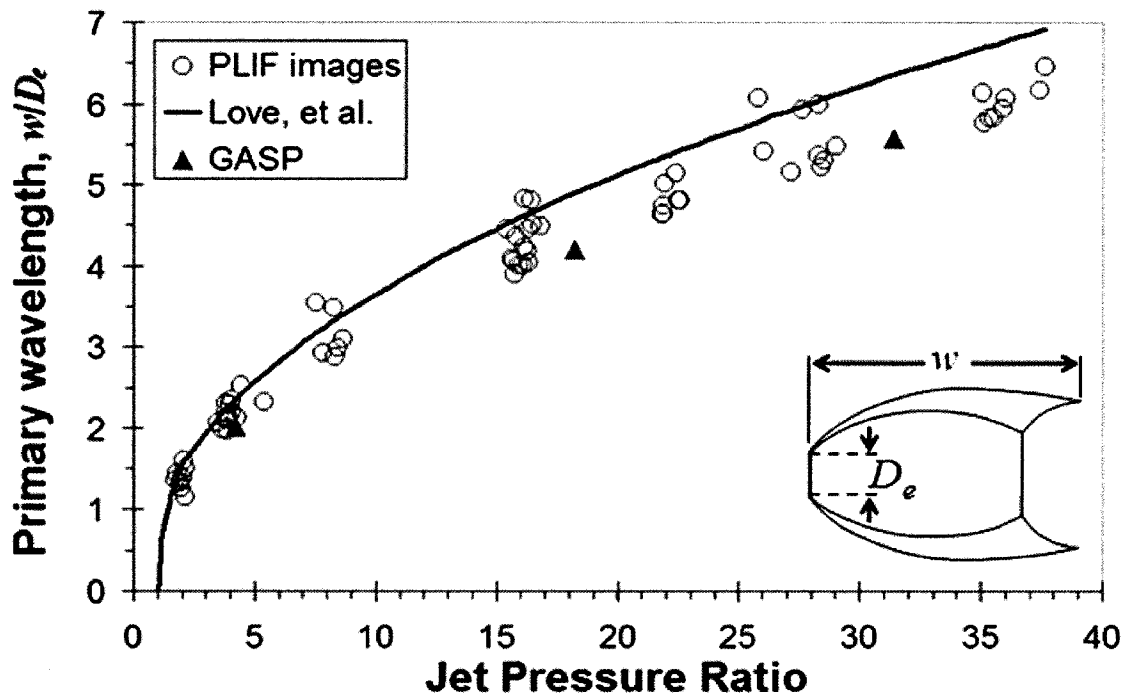
Figure 4.13: Jet primary wavelength. Primary jet wavelength is plotted for a range of jet pressure ratios. Data were taken at various exit Reynolds numbers.

131

In addition to experimental measurements of these quantities from approximately 100 test cases and measurements from computed results of the three CFD test cases, we have included comparisons with the seminal experimental and computational studies of Love et al. (1959). In Fig. 4.13, it can be seen that the semi-empirical relation for primary wavelength proposed by Love et al. tends to predict a longer primary wavelength than that indicated by either our data or our GASP computations. This result was anticipated, as Love et al. cite a "tendency at the higher jet pressure ratios to overpredict the wavelength" when the nozzle exit Mach number is low, as was the case in the present work where $M_e=1$ (although they note the opposite trend when the exit Mach number is high). Figure 4.14 shows relatively good agreement between our experimental results and those of Love, et al. for the measured Mach disk diameter. It appears that GASP tends to underpredict this parameter, especially at higher jet pressure ratios. Finally, Fig. 4.15 shows that our experimental data tends to indicate a greater distance to the Mach disk than either GASP or the experimental results of Love, et al., which show good agreement with each other.

132
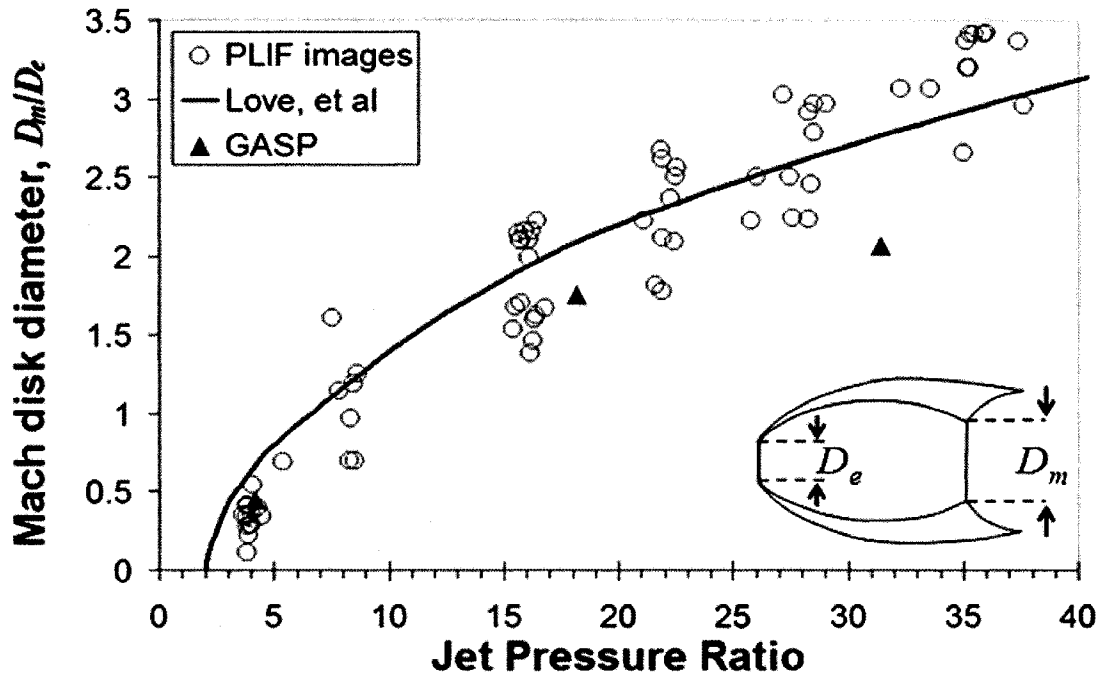
Figure 4.14: Mach disk diameter. Data were taken at various exit Reynolds numbers. GASP appears to underpredict this parameter at high JPR, by up to 35% for Case C.
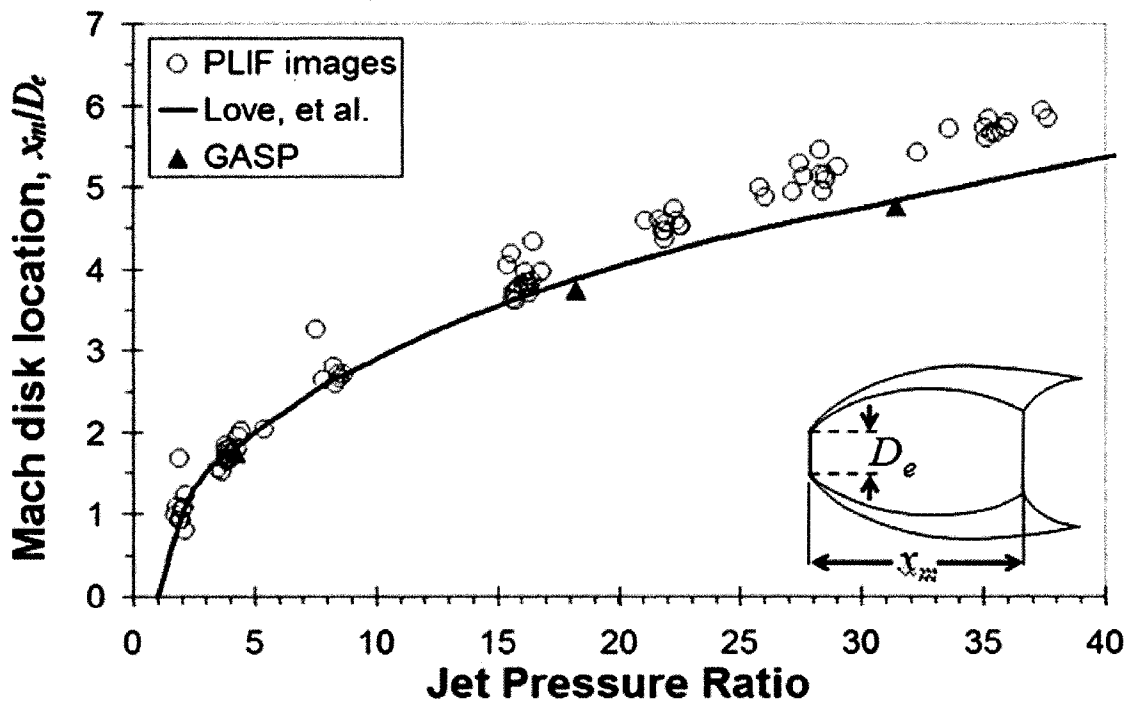
Figure 4.15: Mach disk location. Data were taken at various exit Reynolds numbers. While GASP solutions agree well with the results of Love, et al., they underpredict the present experimental PLIF results by approximately 15% for Case C.

133

4.3.4.2 Supersonic jet structures

Similar measurements of jet primary wavelength, Mach disk diameter, and Mach disk location were performed for supersonic free jets. The results of these measurements are presented in Figs. 4.16, 4.17, and 4.18. The empirical formula for jet primary wavelength of Love et al. (1959) is shown for a nozzle exit Mach number of 2.6 in Fig. 4.15. As they anticipated, the formula underpredicts the wavelength at high jet pressure ratios. The plots of data from Love et al. in Figs. 4.17 and 4.18 represent interpolations between their results for exit Mach numbers of 2.5 and 3.0. The empirical formula from Love et al. (1959), applied to a Mach 2.6 nozzle, underpredicts the Mach disk location for *JPR*s of greater than about 9, a trend which they anticipated for "higher Mach numbers." Their results underpredict the Mach disk diameter, by about 25%, as shown in Fig. 4.17. Agreement in Mach disk location (Fig. 4.18) is good for lower *JPR*s, but above a pressure ratio of about 9, the results of Love et al. underpredict the Mach disk location by about 15%.

134
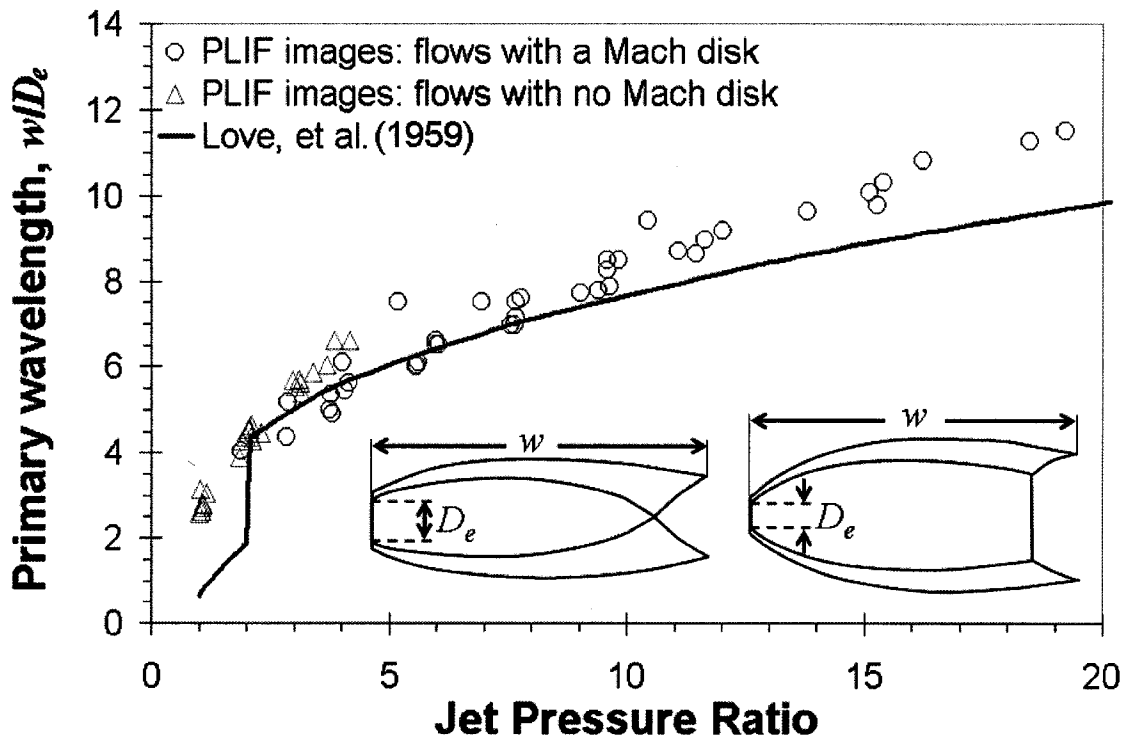
Figure 4.16: Primary wavelength for supersonic free jets. Blue circles are for runs with a Mach disk; orange triangles are for runs with no Mach disk. The empirical formula from Love et al. (1959) assumes the disappearance of a Mach disk at a *JPR* of 2. The present experiments observed this change for *JPR*s between 2 and 4.
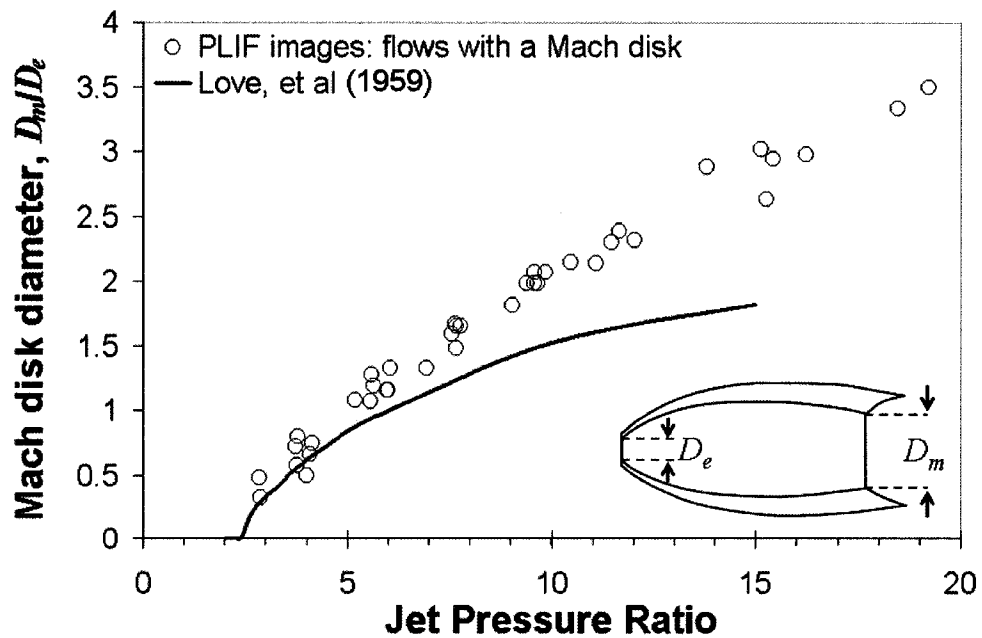
Figure 4.17: Mach disk diameter for supersonic free jets. The relation from Love et al. (1959) consistently underpredicts the size of the Mach disk for the present experiments, especially at high *JPR*s.
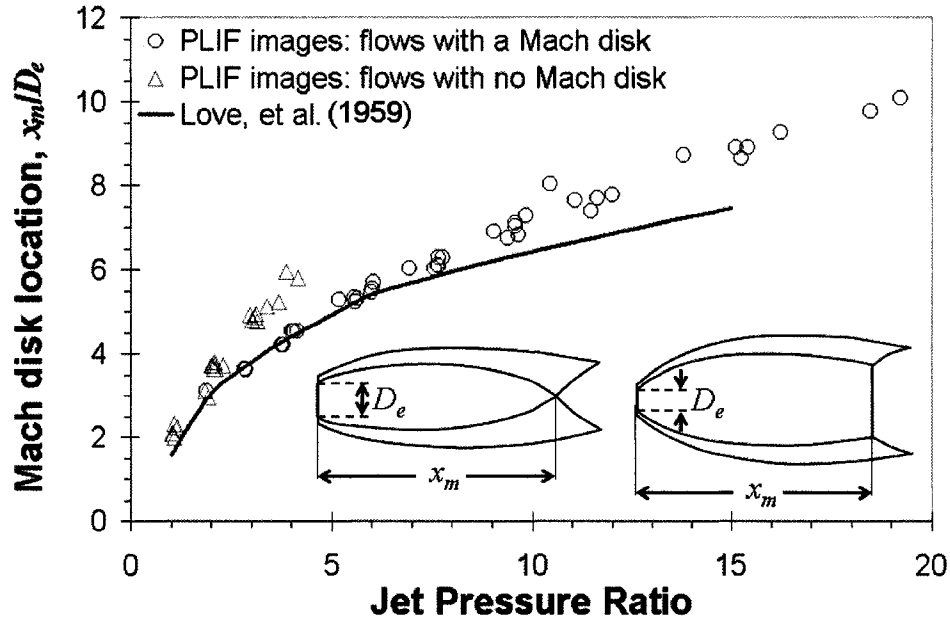
Figure 4.18: Mach disk location for supersonic free jets. For runs without a Mach disk, the location of the intersection of the oblique shocks surrounding the expansion region is recorded instead. Blue circles are for runs with a Mach disk; orange triangles are for runs with no Mach disk.

4.3.5 Qualitative Image Comparison

Section 3.4.1.2 in the previous chapter outlined the theory behind computational flow imaging, whereby computational maps of temperature, pressure, and mole fraction of nitric oxide could be processed to produce a "theoretical" PLIF image. That methodology was applied to the three CFD cases described above. PLIF flow visualization images taken at nearly identical conditions to the CFD computational cases were processed in MATLAB® (refer to Table 4.3 for a list of computational vs. experimental test conditions). Similar grayscale color maps were applied to both the Tecplot and MATLAB® images. The results for the three test cases are shown in Figs. 4.19, 4.20, and 4.21.

136
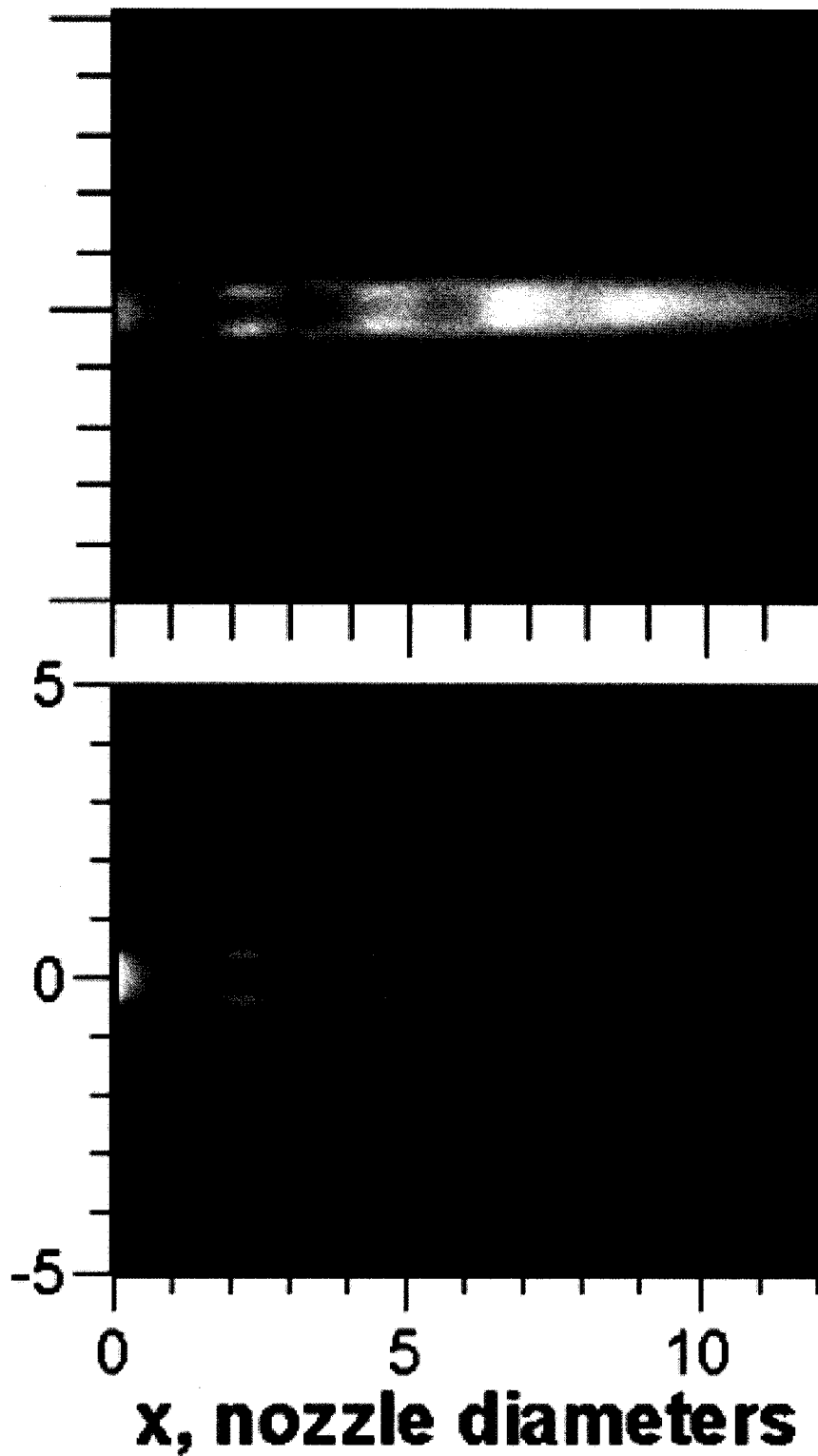
Figure 4.19: Case A. Qualitative comparison of PLIF flow visualization (top) and GASP CFI (bottom) for a JPR of approximately 4.

137

The images show relatively good qualitative agreement, although discrepancies do exist. The CFI images are brighter in regions immediately after the nozzle exit; as mentioned in section 3.4.1.2, this effect can partly be attributed to Doppler shifts of the absorption lineshape in regions where large radial components of the flow velocity are present on the top and bottom of the jet. The PLIF images show remnants of camera artifacts, such as a slight honeycomb pattern in very bright regions of Case B and Case C flows, which comes from the fiberoptic bundle in the intensifier of the CCD. They also appear to be brighter in some regions than the CFI images, suggesting that our method of correcting for nonuniformities in the laser sheet is imperfect.

It is worth noting that the CFI formulation presented herein assumes a gas mixture consisting of 0.5% NO and 99.5% N_2 throughout. Quenching by N_2 and self-quenching by NO has been included in the modeling, but by assuming this mixture of gases, the quenching by oxygen has been neglected. Refer again to Fig. 4.11, noting the regions of the flow where the NO mass fraction is less than the maximum value of 0.5%. In these regions, it is expected that the experimental PLIF images will exhibit an attenuation of the fluorescence signal due to quenching by oxygen relative to the calculated signal level (refer back to Fig. 3.14 for a graph of fluorescence signal versus jet mixing fraction that includes the effects of quenching by oxygen); this effect is evident downstream for the Case B and Case C images, whereas the Case A images have been cropped, as described previously, prior to this effect becoming wholly manifest downstream. This same effect tends to make the calculated jets appear wider than the measured jets since the O_2 quenching on the jet edges is not being computed.

138
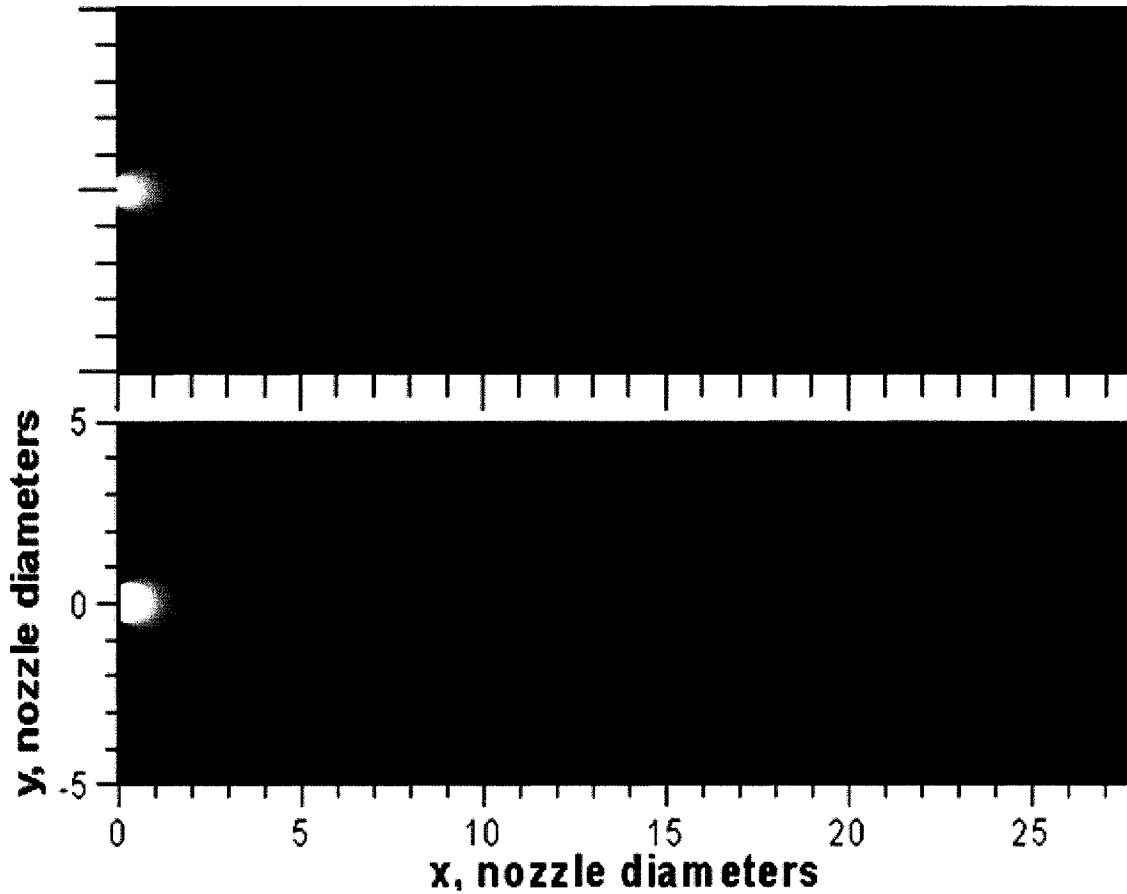
Figure 4.20: Case B. JPR is approximately 17 in this PLIF image (top) and 18 in this CFI image (bottom).

The CFI GASP images are also noticeably crisper; this is because of limitations in the focus attainable by the camera lens, coupled with the spatial blurring due to collecting fluorescence from a volume with the thickness of the laser sheet (~0.2 mm FWHM), and with the blurring resulting from applying a spatial filter to the data. Additionally, the fluorescence lifetime, which is on the order of 200 ns, coupled with the relatively long camera gate width of 1μs, can cause blurring in regions of high velocity in the images.

Other small discrepancies can be attributed to differences in the conditions at which the PLIF images were acquired and those that were used as input to the CFD code.

139

Overall, the images show similar flow structures. Mach disks, barrel shocks, reflected shocks, and shear layers are all similar in size, shape, and location in the CFI and PLIF images. The similarity, in particular, of the relative intensities of these flow structures demonstrates that the modeling we have done in our computational flow imaging is a suitable approximation for these flow conditions and for our purposes in this work.
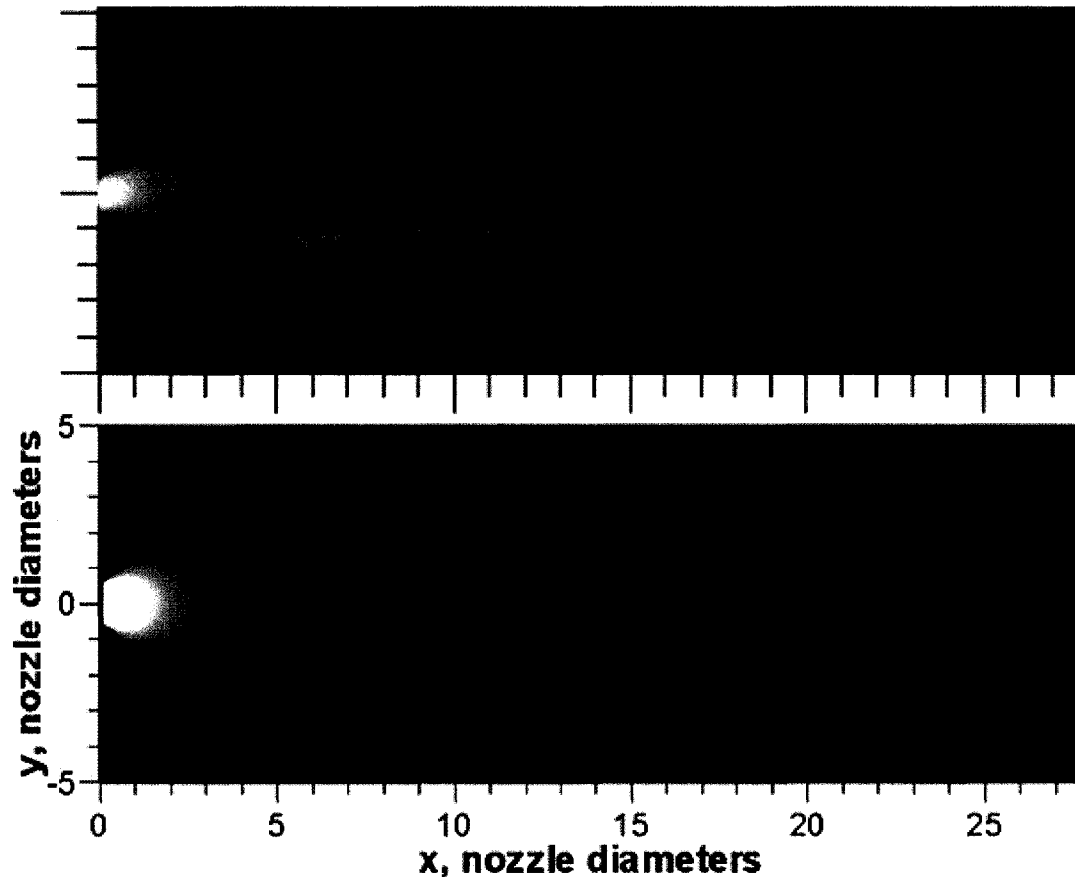
Figure 4.21: Case C. JPR is approximately 28 in this PLIF image (top) and 31 in this CFI image (bottom).

4.4 Summary

These studies have endeavored to improve the understanding of the nature of highly underexpanded axisymmetric sonic free jets, as well as to compare the predictions of the

140

CFD with experimental findings. Computation and experiment were found to be in agreement within the scatter of the experimental data for measurements of jet primary wavelength. Agreement was also found for measurements of Mach disk location and Mach disk diameter for the two cases with smaller jet pressure ratios; however, it was noted that the CFD results appear to overpredict the size of these flow features for the highest jet pressure ratio case by approximately 15% and 35%, respectively. CFD calculations at a larger range of conditions will help to confirm or modify these apparent tendencies.

141

CHAPTER 5

Unsteady, Transitional, and Turbulent Underexpanded Free Jets

Unsteady laminar free jet flows, transitional free jet flows, and turbulent free jet flows will be covered in this chapter. It will introduce the concept of unsteadiness, including the underlying flow properties of viscosity and vorticity. It will explain how viscosity plays a dual role, both as a stabilizing and destabilizing force. It will give an overview of the sources/origins of vorticity in a flow, namely, non-uniform flow velocity. Several primary sources of free jet instabilities will be identified. These include the nozzle lip, shock intersections, shear layers, and flow maxima (defined as flow locations where the jet diameter is locally a maximum compared to the diameter of the jet immediately upstream and downstream of that location. See Fig. 4.5 in the previous chapter). It will be shown that flows with a distinct high-velocity jet boundary have different modes to transition than do those with an oscillating flow structure. The concept of longitudinal (also called axial or streamwise) and azimuthal normal modes will be introduced as well, though in a limited capacity (here, *normal* refers to the fact that these modes are orthogonal to one another). Two primary longitudinal modes will be

142

considered—the sinuous (antisymmetric) and varicose (symmetric) modes. Finally, a brief introduction to azimuthal (cosine) modes will be given, along with some reconstructed flow cross-sections showing flows with active azimuthal modes.

We have developed an image processing technique, involving calculation of the standard deviation of the intensity in PLIF images in order to aid in the identification of turbulence, with the aim of empirically determining criteria governing the onset of turbulence. Jet scaling parameters were used to define a rescaled Reynolds number that incorporates the influence of a varying pressure ratio. The image processing procedure that we have employed will be described, as well as an explanation of the standard deviation images and how they can aid in the identification of flow unsteadiness, transition, and turbulence.

5.1 Definitions

5.1.1 Unsteady, Transitional, and Turbulent

The previous chapter covered steady laminar jet flows. The term "laminar" indicates flows that are smooth, that have structures that are not time-varying, that have no interfering vortices, and that are not "transitional" or "turbulent." *Unsteady* laminar flows still lack turbulent structures, but do exhibit time-dependent fluctuations. Such fluctuations may be periodic or chaotic, but the structures associated with these fluctuations are inherently dependent upon the geometry of the flow, and are generally of a spatial scale comparable to the scale of the flow structures of the underlying flow. Transition, by contrast, is characterized by flow structures that break down from larger

143

scales to smaller scales, with energy being redistributed to increasingly smaller spatial scales. Fully developed turbulence is the limiting case of this process.

In a fully developed turbulent flow, the local flow structures bear little memory of the larger flow from which they originated, are theoretically homogeneous and isotropic (that is, are statistically invariant under translation and rotation, respectively—a condition that never perfectly exists in physical flows), and are generally of a much smaller scale, down to the molecular dissipation scale (also called the *Kolmogorov* scale). For an in-depth discussion of the inherent ambiguities and difficulties involved in developing a precise definition for each of these categories, see the comprehensive texts by Pope (2000), Drazin and Reid (1981), and Lesieur (1987).

To understand the distinction between transitional and turbulent flows, it is instructive to consider the frequency realm measured and analyzed in hotwire anemometry turbulence studies. Briefly, hotwire anemometry works in the following way. A thin metallic wire at the end of a thin probe is heated to some temperature above the ambient. Flow past the wire cools the wire at a rate proportional to the velocity of the gas. Because the resistance of the metal is a function of temperature, the measured changes in resistance can be related to the flow velocity. Time-domain hotwire or pressure data can be converted to the frequency domain using a Fourier transform. Simply, turbulent flows exhibit broadband spectra, while transitional flows have structured spectra. The simplest unsteady flow would have a signature in the time domain that looked sinusoidal. In the frequency domain, this of course becomes a delta function, that is, a single frequency component. When a flow exhibits breakdown from large scales to small scales, this is the hallmark of transition. Fully developed turbulence

144

is marked by the presence of flow structures of all length scales (that is, all frequencies) from the scale of the flow down to the Kolmogorov (molecular dissipation) scale.

Even though many previous studies have made some measurement of turbulence using the hotwire technique outlined above, very few studies of supersonic free jets discuss turbulent flow *structures*. Notable exceptions include the free-jet studies of streamwise vortices in the outer shear layer of underexpanded jets by Krothapalli et al. (1991) and Zapryagaev et al. (2004). Krothapalli et al. successfully visualized cross-sectional slices through the flow using Mie scattering off of moisture in the ambient air that condensed when mixed with the cold fluid of the jet. In the study by Zapryagaev et al., the presence of these vortical flow structures was *inferred* from Fourier spectral analysis of pitot pressure surveys, being the most likely explanation for the measured azimuthal pressure variations. A major contribution of the present work is that the flow structures associated with the onset of unsteadiness and through the transitional, developing regimes have been visualized directly.

5.2 Identification of Unsteady Flow Behavior Using PLIF Images

5.2.1 Image processing

The image processing procedures that have been used for the PLIF images presented herein are described in the following sections. Raw images from the intensified CCD were stored as *.spe* files, a proprietary binary file format used by the Princeton Instruments WinView32 image acquisition software. These raw images were imported

into MATLAB, processed according to the procedures outlined below, and stored as images (*.png* or *.bmp* files) or movies (*.avi* files).

5.2.1.1 Background subtraction and laser sheet correction

The intensity at a given pixel in a PLIF image may be due to fluorescence, elastic scattering of laser light (Rayleigh scattering, glints, reflections, etc.), room lights, camera offset, or dark current. Experimental controls are used to reduce unwanted sources of intensity; the camera is cooled to reduce dark current, unused windows are covered to block room lights, filters in front of the camera lens block most of the light at the frequency of the laser, etc. In order to remove the remaining contributions of all but fluorescence, a *background image* is subtracted. A background image is an image acquired at conditions nearly identical to run conditions but without nitric oxide present in the test region. This includes using the same laser operating conditions, camera gain and gate settings, as well as acquiring images at the same ambient pressure. In practice, the conditions may not be identical. In order to minimize the effect of shot-to-shot variations in background intensity, 100 single-shot background images were acquired for a several gain settings and test section pressures on each day of running. An averaged image was created for each set of 100 images, and this averaged image was then smoothed by a 7 pixels x 7 pixels rotationally symmetric Gaussian filter with a sigma (standard deviation) of 2 pixels in order to further reduce random noise. The raw images are smoothed by a similar but smaller 3 pixels x 3 pixels filter (with a sigma of 1 pixel) prior to background subtraction. The smaller filter is used on the single shot images to minimize the blurring of flow structures while still reducing the effects of random noise.

146

After a background image is subtracted from each smoothed PLIF image, significant left-to-right variations in intensity remain. These variations are due to the left-to-right variations in both the laser sheet intensity and laser wavelength. The intensity of the laser sheet has an approximately Gaussian spatial profile, so near the edges where the laser intensity is lower, the resulting fluorescence signal is also lower. Additionally, the spectral profile of the laser sheet varies spatially: the right side of the sheet is slightly red shifted relative to the central frequency, while the left side is slightly blue-shifted. This effect is created by a spectrally-dispersive Pellin-Broca prism just prior to the output of the WEX, used to separate the final UV beam from the other residual beams. These spectral shifts result in a decrease in the spectral overlap integral, g, between the laser and molecular absorption profile, with a corresponding decrease in fluorescence intensity on the left and right edges of the laser sheet. (See the section in Chapter 7 on Recommendations for Future Work for a suggestion on how to minimize this effect in future applications.)

To correct for these effects, the images are divided by a *laser sheet profile*. For some runs, a laser sheet profile was created for each single shot: a region of the image far from the jet was selected, and the average intensity along each column in this region was calculated. Enough nitric oxide mixed into the ambient gas to provide a low fluorescence signal in this region. Each column in the PLIF image was then divided by the average intensity of the corresponding column in the region far from the jet. This had the effect of increasing the intensity on the left and right edges of the images, where the laser sheet was less intense and typically slightly detuned from the center of the absorption spectral line, as explained above. While this shot-by-shot laser sheet correction was effective for

147

many runs, it was computationally intensive. Some runs lacked sufficient intensity far from the jet, and impinging cases (covered in the next chapter) often had flow extending toward the top of the image, so no region "far from the jet" existed. For these reasons, the image processing procedure was modified and a single, averaged laser profile was generated for each run. Each single-shot image was then corrected using the same laser sheet profile. This method was experimentally much easier to implement than a two-camera reference system that others have used in past work (see, for example, Palma 1999).

As final steps in the image processing procedure, images were sometimes cropped, a mask was applied to cover the nozzle hardware in order to eliminate any persistent glints or scattered light, a scale was applied to the sides and bottom of the images based upon the measured spatial resolution, and a false-color mapping was applied. In some of the earlier tests, the spatial resolution was determined by imaging a ruler in the same plane as the laser sheet. This process was improved in later tests. A *dotcard* was used in place of a ruler. Dotcards consisted of a rigid metal plates covered with a sheet of paper. The paper was white with black squares printed in a regular grid pattern. Spatial resolution was calculated by capturing images of a dotcard positioned in the same plane as the laser sheet. The optical access in these experiments permitted perpendicular viewing of the measurement plane and no significant perspective distortion was found in the images. For experimental configurations where optical access is more limited and perpendicular viewing is not possible, dotcard imaging makes it possible to correct for perspective distortion (and in the case of lower-quality camera lenses, for lens distortion) (Danehy et al. 2007).

148

5.2.1.2 Standard deviation images

After background subtraction and laser sheet correction, an average image was created from all the images from a given run (each run consisting of either 100 or 200 single-shot images). A *standard deviation image* was then created in the following manner. Each single shot image was subtracted from the averaged image. The images contained intensities spanning a large dynamic range, and so the difference in intensity was divided by the average intensity, resulting in a percentage difference, rather than an absolute difference. This "percentage difference" in intensity at each pixel was squared, and the squares were summed over all images in the run. Finally, the sum of the squares was divided by the number of images and the square root was taken. The resulting image provides a map of the flow, highlighting regions of large percentage variations in intensity. For an explanation of the features that can be identified in standard deviation images, as well as examples of standard deviation images, see section 5.2.2. In general, steady laminar flows will have relatively consistent shot-to-shot intensity at a given location in the flow, resulting in percentage standard deviations of less than about 30%. Unsteady flows, by contrast, will have regions where the intensity varies in each image, resulting in typical percentage standard deviations of between about 35% and 100%. A drawback of this technique is that it tends to more prominently highlight variations in regions where there are steep intensity gradients in the average image (e.g. along jet boundaries).

149

5.2.1.3 Volume Imaging

In addition to data taken along the flow centerline, volumetric imaging was performed for many of the test cases. To obtain these data, a series of 200 single-shot images was acquired as the laser sheet was swept spanwise through the flow, providing slices of the flow field. These slices allow the reconstruction of cross-sections of the flow in planes perpendicular to the jet axis, a technique which will be referred to as *volume imaging*. Figures 5.1 and 5.2 display cross-sectional slices at six axial locations.
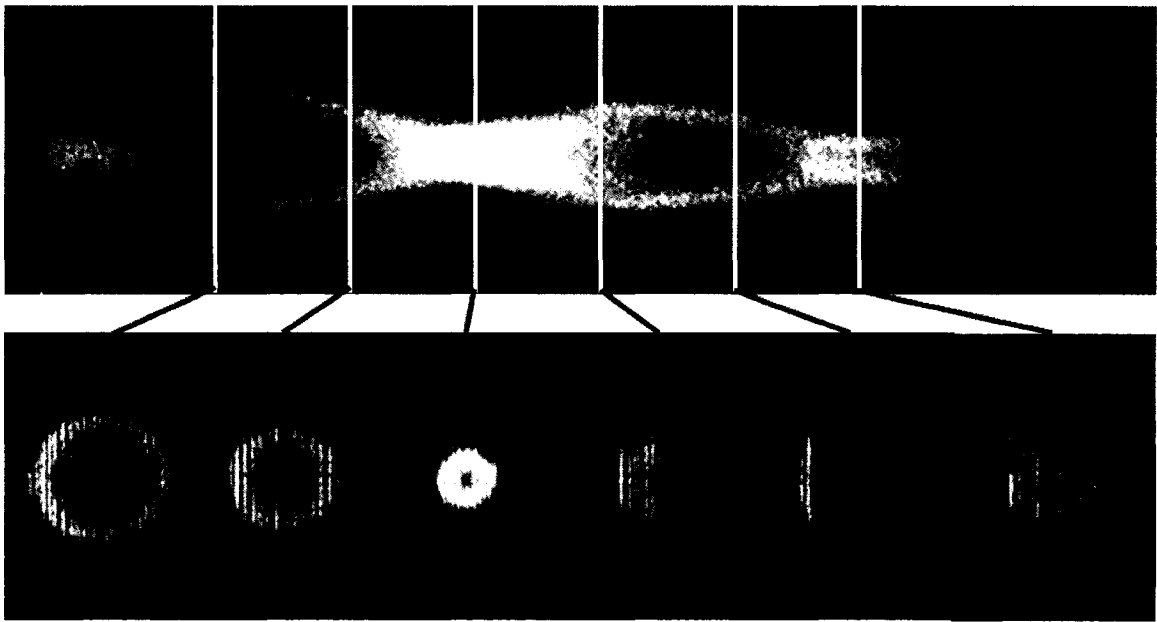
Figure 5.1: Six reconstructed slices and one single-shot centerline image. These images are from a supersonic nozzle run (Run 339) with $JPR = 3.9$ and $Re_{exit} = 4,303$. White vertical lines through the reference image indicate the axial locations of each of the slices. The fourth and fifth slices show evidence of the $cos(6\theta)$ azimuthal instability mode, a feature not evident in the centerline image. Being able to capture symmetry-breaking flow features represents one of the advantages of volume-imaging.

The single-shot images acquired on the flow centerline during the spatial scan of the laser sheet provide a reference for the relative locations of these slices. In both of these

150

figures, the axial symmetry of the jet is seen to be breaking down as azimuthal cosine modes (described in more detail in section 5.5) become manifest. While the centerline image in Fig. 5.2 shows some evidence of this breakdown, no such evidence can be seen on the centerline in Fig. 5.1. This demonstrates one of the advantages of this technique, since it can reveal non-axisymmetric flow structures that may not be evident in centerline imaging.
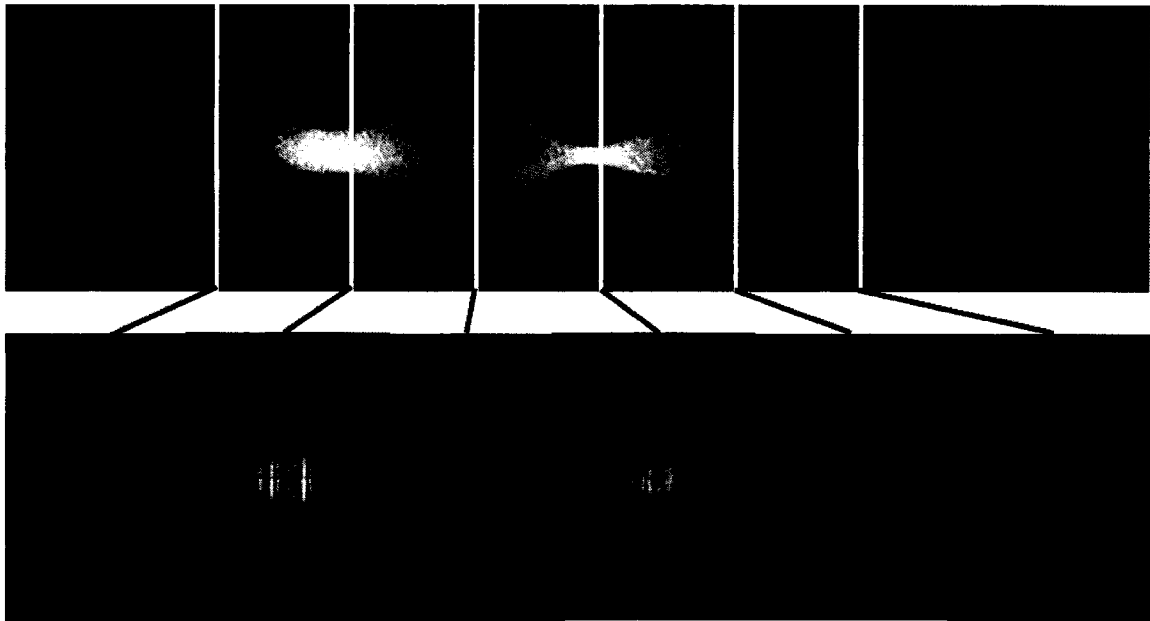
Figure 5.2: Six reconstructed slices and one single-shot centerline image. These images are from a supersonic nozzle run (Run 342) with $JPR = 2.1$ and $Re_{exit} = 9,501$. White vertical lines through the reference image indicate the axial locations of each of the slices. Note the growth of azimuthal instability modes stemming from the second flow maximum. The fact that the cross-sectional slices are constructed from ~200 single shots (which take 20 seconds to acquire) indicates that the breakdown mode shown here is relatively persistent and spatially stable.

Slices reconstructed from scans through unsteady flows could potentially be used to give an indication of the level of unsteadiness at a given axial location. For the relatively steady upstream slice location, the flow appears to be a smooth circle. As slices are

151

reconstructed further downstream, the circular outline of the flow becomes jagged, due to shot-to-shot variations in the position of the jet. Thus, a single slice image can provide a visual representation of the degree of flow unsteadiness. Volume imaging also represents a promising means of making PLIF measurements in flows where optical access constraint do not permit imaging in the most desirable measurement plane.

5.2.2 Identification of changes in flow state

Conceptually, a given flow can be divided into 4 regions—steady laminar, unsteady laminar, transitional, and turbulent, not all of which will necessarily be present. The standard deviation images described above have been used to distinguish each of these regions. Ideally, this would result in the creation of a map for each test condition, showing which regions are steady, unsteady, transitional, and turbulent. This would, however, be labor intensive to attempt for more than a few cases. Making such flowfield maps may be worthwhile and useful if a particular case is to be computed with CFD. Instead, we have divided the flow into these four regions as a function solely of the axial coordinate, x. This means, for example, that in the region we have called the *unsteady laminar* region, the core of the jet may still be unsteady laminar, while the edges of the jet are exhibiting transitional behavior. The criteria that have been used to define the boundaries between these regions are defined as follows.

x_{steady}—If the flow is entirely *steady laminar* within the field of view, the furthest downstream location is marked as x_{steady}. In standard deviation images, this means that

152

the intensity remains low and relatively constant across the image. An example of a steady laminar flow is given in Figure 5.3.
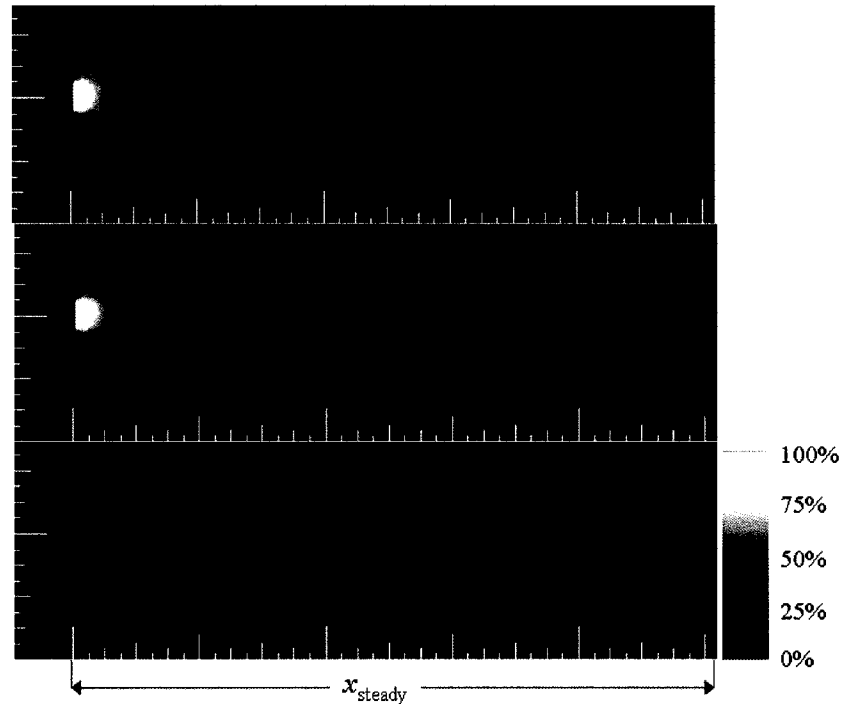
Figure 5.3: Image sequence for a steady laminar case (Run 49), with $JPR = 15.8$ and $Re_{exit} = 2644$. The top image is a single-shot image, the center image is the average of 100 single-shots, and the bottom image is a map of the percentage standard deviation in the image intensity at each pixel. The colorbar on the right indicates the color-scaling of the standard deviation image, with white corresponding to 100% variations in intensity, and black corresponding to no variation in intensity from shot-to-shot.

$x_{unsteady}$—This is defined to be the downstream location at which the flow first exhibits unsteady behavior. All locations upstream of this point are thought to be *steady laminar* flows; all locations downstream have some level of unsteadiness to them. In standard deviation images, this location is characterized by an increase in intensity above the background (noise) level. Figure 5.4 shows a flow exhibiting unsteady laminar behavior. In Wilkes et al. (2005), this distance was labeled x_{trans}. Although some transitional behavior may be observed in the region we are calling *laminar unsteady*,

153

especially along the boundaries of the jet, in the present work we have elected to wait to label a flow as *transitional* until the entire flow is transitional.
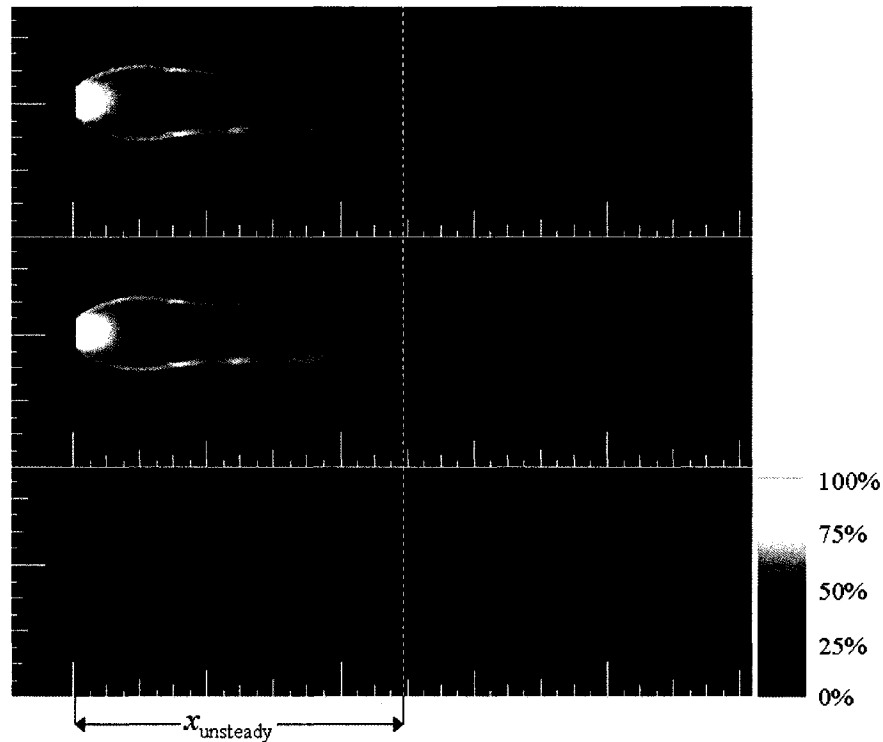
Figure 5.4: Image sequence for an unsteady laminar case (Run 35), with $JPR = 16.3$ and $Re_{exit} = 4435$. Notice the increase in intensity in the standard deviation image in the inner and outer shear layers. There may even be a small level of instability originating from jet boundary at the maximum jet diameter on the lower part of the image.

$x_{fullytrans}$—This is defined to be the location at which all of the jet, including the jet core, is exhibiting transitional behavior. In standard deviation images, it is the location where the intensity in the core of the flow has risen above the background level. Figure 5.5 shows such a case. This distance is similar to what was labeled the turbulent distance in Wilkes et al. (2005).

154
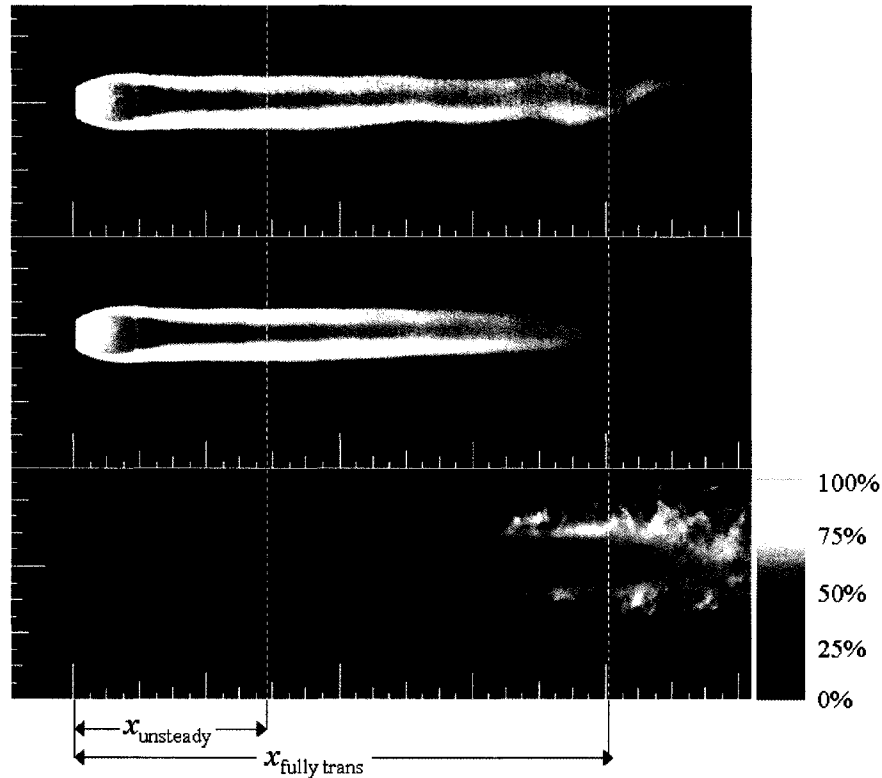
Figure 5.5: Image sequence for a fully transitional case (Run 31), with $JPR = 8.7$ and $Re_{exit} = 4481$. Notice the initially slow growth of instabilities as the jet becomes unsteady, followed by the relatively fast growth of instabilities at the onset of transition. The fully transitional point is marked where the instabilities penetrate to the core of the jet.

$x_{fullyturb}$— This is defined to be the location beyond which the flow can be said to be *fully developed*. In other words, all spatial modes are active, down to the smallest scales. This location is characterized by a *decrease* in the intensity in the standard deviation images relative to the peak transitional intensity. Figure 5.6 illustrates a run exhibiting fully developed turbulence. Prior to this point, "turbulent" structures may be seen, but the smaller scales may be missing. Once the flow is fully developed, however, it exhibits increased homogeneity (and thus, the lower standard deviation in intensity), with widespread small-scale structures.

155
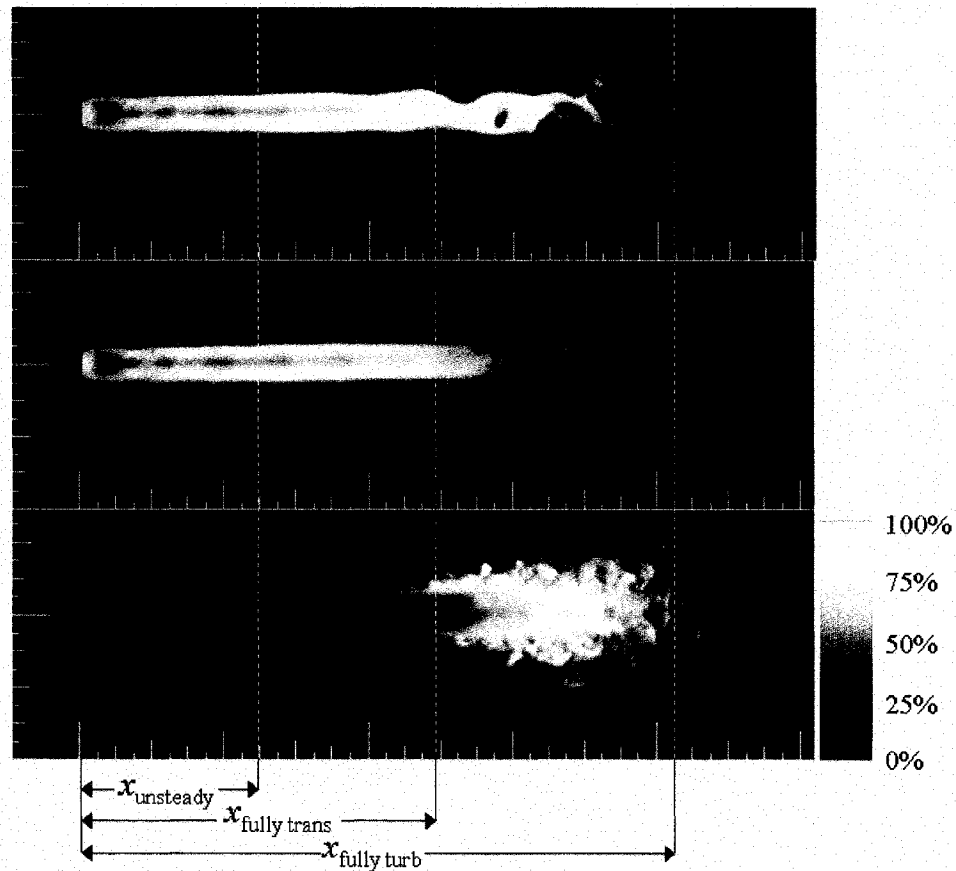
Figure 5.6: Image sequence for a fully turbulent case (Run 32), with $JPR = 3.9$ and $Re_{\text{exit}} = 4460$. Notice the decrease in intensity in both the PLIF images (due to turbulent mixing and diffusion) and the standard deviation image (due to the homogeneous nature of turbulence) in the fully-developed region. The fully turbulent location is marked where the intensity in the standard deviation in the center of the flow decreases below the level it has in the transitional region.

5.3 The Dual Nature of Viscosity

Vorticity is a measure of the amount of rotation in a flow. Flows lacking vorticity are said to be "irrotational." Vorticity plays a crucial role in the development of turbulence. Mathematically, vorticity is defined to be the curl of the velocity: $\vec{\Omega} = \nabla \times \vec{v}$.

The viscosity of the flow sets up a velocity gradient across the boundary between a jet and the ambient fluid, resulting in a region called a shear layer. In highly-underexpanded jet flows, there are two such shear layers. Refer back to Fig. 4.3 for an illustration of these

156

two shear layers. The *outer shear layer* lies between the jet boundary and the ambient gas. The *inner shear layer* lies between the high-velocity gas near the jet boundary and the slip line emanating from the triple point and separating the high velocity gas from the jet core. Interestingly, then, it is actually the *lack* of viscosity—or rather, the lack of sufficient viscosity—that results in the flow developing vorticity. That is, if the flow was fully viscous, momentum would be transferred to the surrounding fluid and velocity field would rapidly become uniform, with little or no vorticity, until the flow encountered a wall or other solid boundary.

Viscosity can be defined to be a measure of the resistance of a fluid to deform under shear stress, a measure of the internal resistance of a fluid to flow, and a measure of the internal friction of the fluid (Tipler 1976). In a fluid with low viscosity, the fluid is easily deformed and readily flows in different directions in response to applied or internal forces. Flows with high viscosity, by contrast, will resist applied forces to some extent. In this manner, viscosity acts as a type of damping force, and is thus a stabilizing force that counteracts small perturbations of a flow. It can decrease the internal vorticity of the flow by reducing velocity gradients, and thus can dampen out turbulent flow structures.

In addition to acting as a *stabilizing* force, viscosity can also act as a *destabilizing* force. Viscosity can introduce velocity gradients—and therefore, vorticity—into regions of a flow that would otherwise be irrotational. If velocity gradients are present in a flow (the slip line between the ambient gas and the high-velocity jet boundary is a perfect example in the jet flows under investigation), viscosity acts to increase the velocity of the slower fluid and decrease the velocity of the faster fluid. Thus, the velocity gradient that would have been a spatial step function in an inviscid fluid acquires a finite spatial extent

157

in a viscous fluid. That is, viscosity causes the velocity gradient that existed at the jet boundary to establish the outer shear layer, expanding the extent of the region containing velocity gradients, potentially all the way to the core of the jet. Given the existence of these competing processes, whether or not a given flow *actually* goes turbulent is a matter of which of all the possible mechanisms ultimately dominates.

5.4 Sources of Vorticity and Growth of Instabilities

The jet flows issuing from the nozzles used in these tests enter the test section as laminar jets. Perturbations to these flows are introduced by random fluctuations in the flow or by viscous effects, as described above. Such perturbations may be damped out or may be amplified. The following sections describe the origins of these perturbations.

5.4.1 Flow structures that introduce vorticity

Based on the measurements presented below, there appear to be three primary locations or flow structures that serve as sources of instability, or at least serve as sources of instability amplification. The first of these is the lip of the nozzle exit; the second is locations of shock wave intersections or reflections, such as the triple point that exists in flows with a barrel shock structure; the third are flow maxima that occur in flows with a spatially oscillating structure. Instabilities were not observed inside the supersonic portion of the barrel shock structure for any flow conditions. At most, the position of the Mach disk itself may fluctuate. Instead, for flow with a Mach disk, turbulent features always appear first in the inner and outer shear layers adjacent to the high-velocity jet boundary. In impinging jet flows, which will be covered in the next chapter, the

158

existence and location of the impingement of the high-velocity jet boundary on the impingement target also serves as a source of instability and/or instability amplification. It will also be shown that all these trends for instability sources are generally greatly amplified in impinging jet cases.

5.4.2 The destabilizing influence of deceleration

According to Drazin and Reid (1981), decelerations are more destabilizing than *accelerations*, in general. Accelerations and the associated pressure gradients tend to stretch the flow, whereas decelerations tend to make it crumple/fold back upon itself. The "stretching" of acceleration tends to oppose vortex/eddy formation, whereas the "crumpling" effect of deceleration tends to increase the vorticity of the flow and serves as a source of eddy formation. Most regions of these jets are decelerating. Exceptions include expansion regions, such as the region inside a barrel shock, as well as the jet core downstream of a Mach disk, where the inner (slip line) shear layer accelerates the core flow that had been slowed down by the normal shock wave. In the repeating diamond shock pattern, there are repeated expansions (accelerations) and contractions (decelerations). As will be shown below, for supersonic jets with an oscillating flow structure, transition often begins on the compression side of such an oscillation, where the diameter of the flow is a maximum locally.

5.4.3 Inner and outer shear layers

Refer back to Fig. 4.2 and Fig. 4.3 for diagrams identifying the flow structures described in the following discussion. If a jet structure has a discernible Mach disk, the

triple point and the intersection of the oblique shock that emanates from the triple point with the jet boundary both seem to serve as a source of instabilities. Figure 5.7 shows an example of a run where this was the case.

Sometimes, slight instabilities are evident in the jet boundary prior to these shock intersection points, but they seem to grow relatively slowly around the barrel shock. Notice the small increases in intensity around the barrel shock (compared to the background intensity level) in the standard deviation image. Then notice the increase in intensity in the inner and outer shear layers (starting at the triple point and reflected shock/jet boundary intersection, respectively). There are many steep velocity gradients in the triple point region. The triple point is the meeting point of four different velocity regions—inside the barrel shock (where the Mach number is greater than one), in the jet boundary upstream of the oblique shock (where the Mach number is also greater than one), in the high-velocity jet boundary downstream of the oblique shock, and in the jet core, after the Mach disk. The intersection of the shock emanating from the triple point with the free jet boundary is, in effect, surrounded by three regions of different velocities—the jet boundary before the oblique shock, the high-velocity jet boundary after the oblique shock, and the free stream/ambient gas.
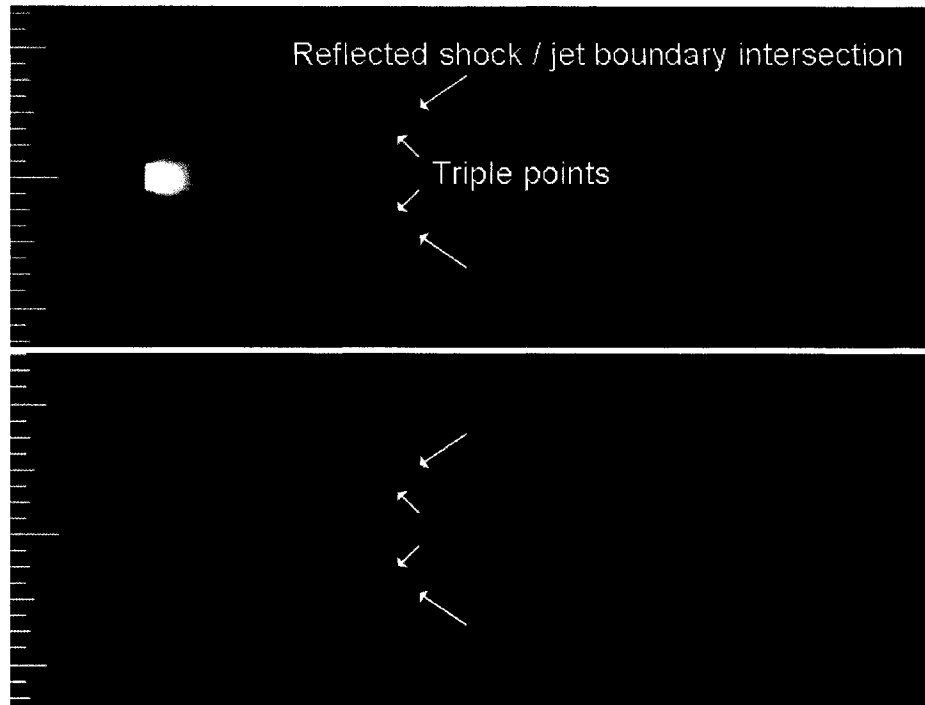
Figure 5.7: Triple point and reflected shock/jet boundary intersection as sources of instability. The upper image is a single-shot PLIF image of a supersonic nozzle flow (Run 650) with $JPR = 19.2$, and $Re_{exit} = 17,240$. The lower image is a standard deviation image. Note how instabilities in the inner and outer shear layers that border the high-velocity jet boundary stem back to the triple points and the reflected shock/jet boundary intersections.

The velocity profile of the jet boundary is greatly affected by the Mach disk shock. Prior to the Mach disk/triple point, the gas that has been processed by the oblique barrel shock is bordered to the outside (along the free jet boundary) by slower (stagnant) ambient fluid. To the inside, it is bordered by the faster moving gas inside the barrel shock. But at the Mach disk, this faster-moving gas inside the barrel shock is abruptly decelerated to subsonic speeds. The gas that flows through the reflected shock emanating from the triple point is now bordered both to the inside and to the outside by slower-moving fluids. As a result, this gas becomes the fastest-moving part of the flow downstream of the triple point. This *high velocity jet boundary* is bordered to the inside

161

and outside by shear layers. As previously described, the outer shear layer is established at the free boundary between the jet and the ambient fluid, while the inner shear layer is established at the slip line separating the high-velocity jet boundary from the slower jet core. So for the gas surrounding the barrel shock, the flow experiences the stabilizing influence of acceleration from inside, but the destabilizing influence of deceleration from the outside. After the triple point, both the inner and outer regions of the flow have a destabilizing effect on the gas processed by the barrel shock, since they both cause the high velocity gas to decelerate.

5.4.4 Flow maxima

If no Mach disk is present, then instabilities seem to originate in the jet boundary at a flow maximum, just as the flow begins to converge again. An example of two such runs is given in Fig. 5.8. Flow maxima (defined in the previous chapter and labeled in Fig. 4.5) are regions of curvature where fluid has been pulled away from the core flow, versus minima, which also have large curvature, but where the momentum of the flow has compressed it back toward the core of the flow. At a flow maximum, the flow is accelerating when it is expanding, but is decelerating as it converges. As indicated above, acceleration tends to be a stabilizing mechanism, whereas deceleration tends to be a destabilizing mechanism.

162
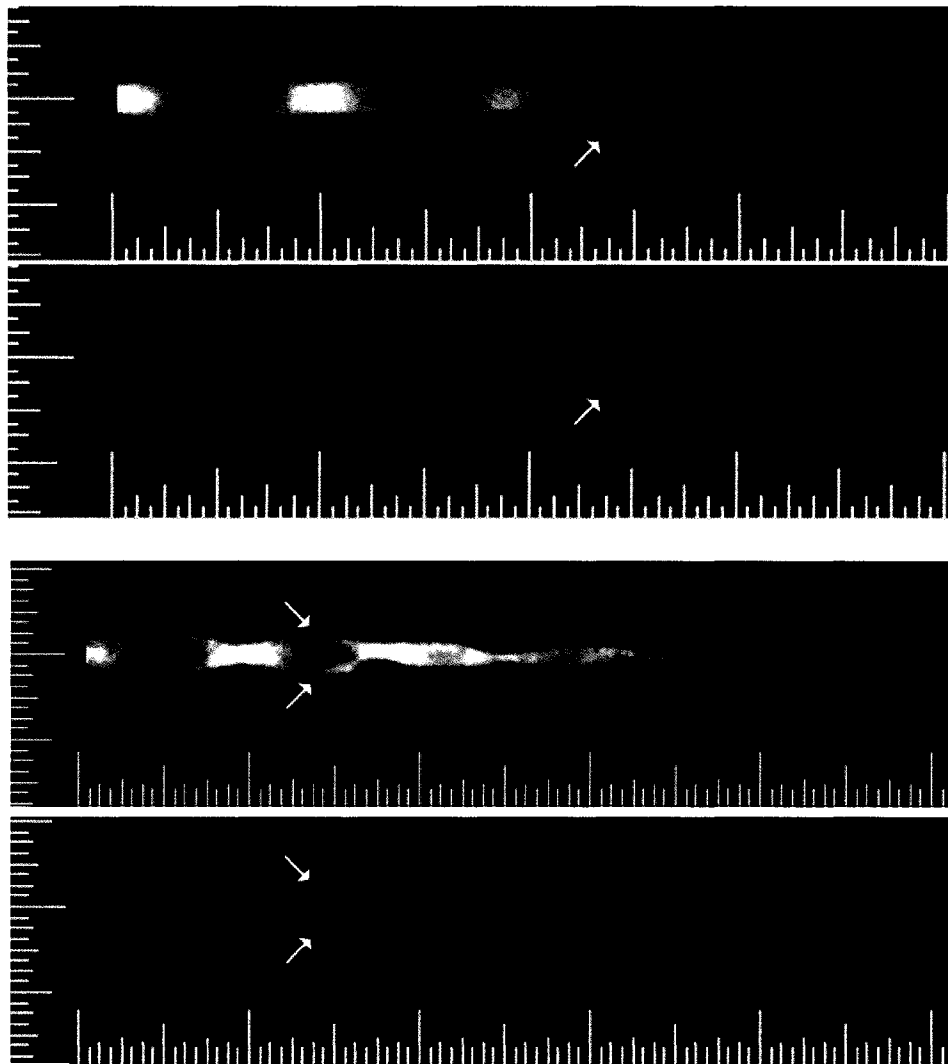
Figure 5.8: Flow maximum as a source of instability. The upper image is a single-shot PLIF image from a supersonic nozzle run (Run 143) with $JPR = 3.4$, $Re_{exit} = 4,269$. Note the beginnings of instability emanating from the third flow maximum on the bottom of the image. The lower image is from a run (Run 246) with a similar JPR (3.1) but at a higher exit Reynolds number (8,001). The standard deviation image highlights instabilities stemming from the top and bottom of the second flow maximum.

At a flow minimum, the core of the flow expands outwards toward the boundary of the jet where instabilities are likely to exist. This expansion may provide a stabilizing influence on the flow. At a flow maximum, however, unstable fluid elements simply travel along streamlines that are closer to straight than the high-curvature streamlines of

163

the more-stable core of the flow. At this point, the momentum forces are becoming commensurate with the viscous forces, and beginning to exceed them. In this way, the local Reynolds number is increasing to above a critical value. (Fluid mechanical literature often talk about the "critical Reynolds number," Re_c, above which a flow transitions. For example, in fluid flow through a pipe, Re_c is on the order of 2,000 (Lesieur 1987)).

5.4.5 Effect of Reynolds number

The Reynolds number is often used as a gauge of the susceptibility of fluid flow to become turbulent. At low Reynolds numbers, viscous forces dominate and the flow is expected to remain laminar. At high Reynolds numbers, momentum forces are greater and flows tend to become turbulent. As expected, the flows in the present investigation showed a strong dependence of transition location on Reynolds number. Figure 5.9 shows an example of several cases with the same JPR for a range of Reynolds numbers.

The figure shows single-shot images from six runs with similar jet pressure ratios but different exit Reynolds numbers. Clearly, the onset of transition to turbulence occurs earlier for higher Reynolds numbers, and not at all for the lowest Reynolds numbers.
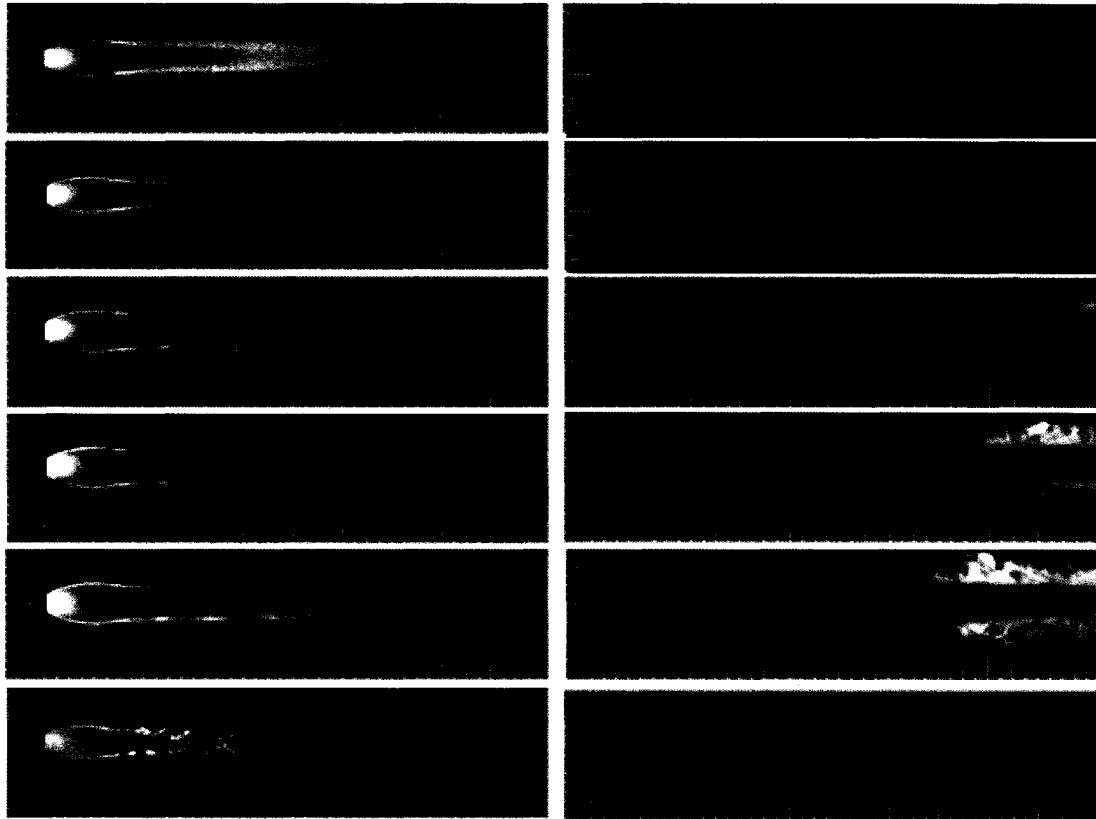
Figure 5.9: The effect of Reynolds number on transition to turbulence for a jet pressure ratio of about 16. Single-shot PLIF images (left) are displayed along with the corresponding standard deviation maps (right) for six values of Re_{exit} (top to bottom): 1529, 2731, 4425, 5524, 6606, and 35,695. (For reference, these are Runs 9, 60, 35, 38, 34, and 71).

5.4.6 Effect of the jet pressure ratio

An unexpected finding of the present work was that the transition location is somewhat dependent upon the jet pressure ratio and not just the Reynolds number. The reason for this dependency seems to stem from the different flow structures that exist in flows of different JPR. The previous chapter on steady laminar flows describes the general classes of flows that exist for the nozzles and range of pressures that were studied, including diamond shock patterns and barrel shock structures. As the pressure ratio varies, the flow structures may evolve smoothly or may undergo abrupt "jumps"

165

from one class of flow to another. This is sometimes termed *staging*. Staging behavior is the exhibition of non-continuous phenomena in a flow, or rather, discrete jumps from one continuous region to another, with a distinct discontinuity between them. In the next chapter, staging will be shown to play an important role in the evolution of some impinging flow structures, as well as in the resulting surface pressure signature.

Transition to turbulence results from the growth of instability modes (Drazin and Reid 1981). The turbulent mode that experiences the greatest amplification will depend strongly upon the underlying flow structure. As the Reynolds number is increased for a steady flow with a spatially periodic structure, the unstable modes of the flow will be different than those of, for example, a large barrel shock with a high-velocity jet boundary that is parallel to the axis of the jet. These "modes" are discussed in greater detail in the following section.

5.5 Characteristic Normal Modes of Instability

One way to model turbulent jet flow is to first model the underlying stable flow, and then introduce perturbations to this base flow. For jets issuing from an axisymmetric nozzle, the perturbations can be either axial (longitudinal) or azimuthal. All possible perturbations to a flow can theoretically be modeled as linear combinations of a complete set of normal modes.

The *axial* (or *longitudinal*) normal modes are of two types—symmetric and antisymmetric (van Cruyningen 1990). Symmetric modes consist of axially symmetric expansions and contractions of the jet around its axis. These modes are known as

166

varicose modes (also called the *sausage* instability) (Drazin and Reid 1981). Figure 5.10 illustrates a flow in which a varicose mode has become active.
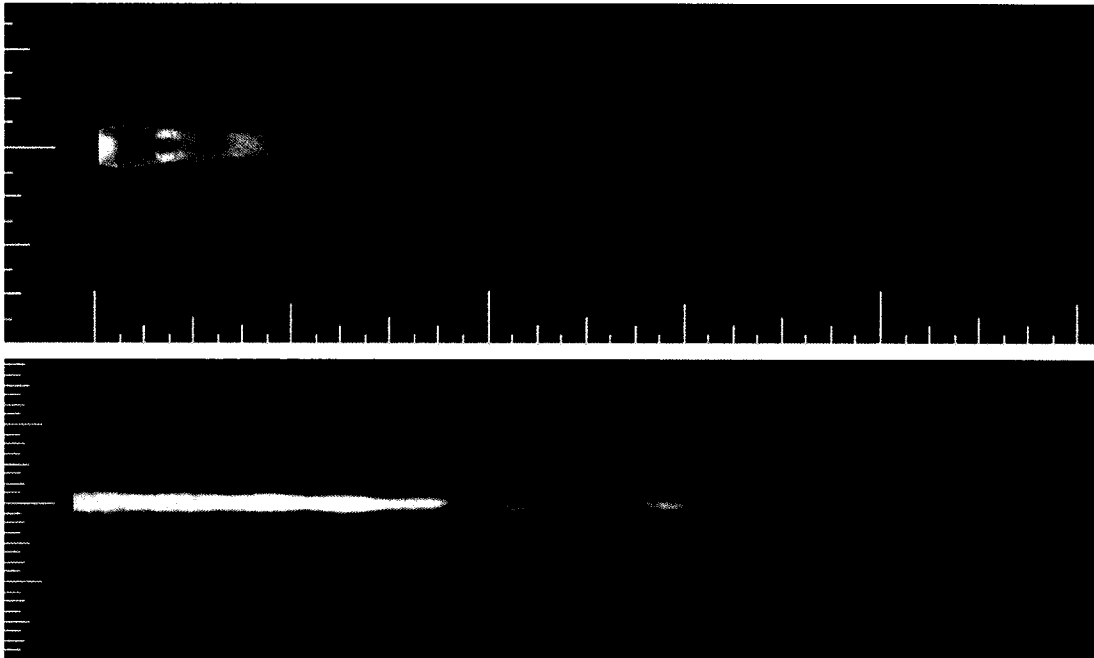
Figure 5.10: The varicose mode of unsteadiness. Both images are single-shot images. The upper image is a sonic nozzle flow (Run 46) $JPR = 3.9$, and $Re_{exit} = 2,593$; the lower image is a supersonic nozzle flow (Run 249) with $JPR = 1.1$, and $Re_{exit} = 6,698$.

Antisymmetric modes consist of sinusoidal oscillations or "flapping" around the jet axis. These modes are known as *sinuous* modes (Drazin and Reid 1981), and they break the axisymmetry of the flow. Figure 5.11 shows an example of a jet exhibiting the sinuous mode.

The other types of normal modes are *azimuthal* modes. They have some symmetry around the jet axis, though they are not purely axisymmetric. Mathematically, this symmetry is of the form $cos(m\theta)$, where m is an integer and θ is the angle in cylindrical coordinates. The only axially symmetric azimuthal mode is the trivial, non-perturbative

167

$m=0$ mode (Balakumar 2007). Figure 5.12 shows the geometry of azimuthal modes for several values of m.
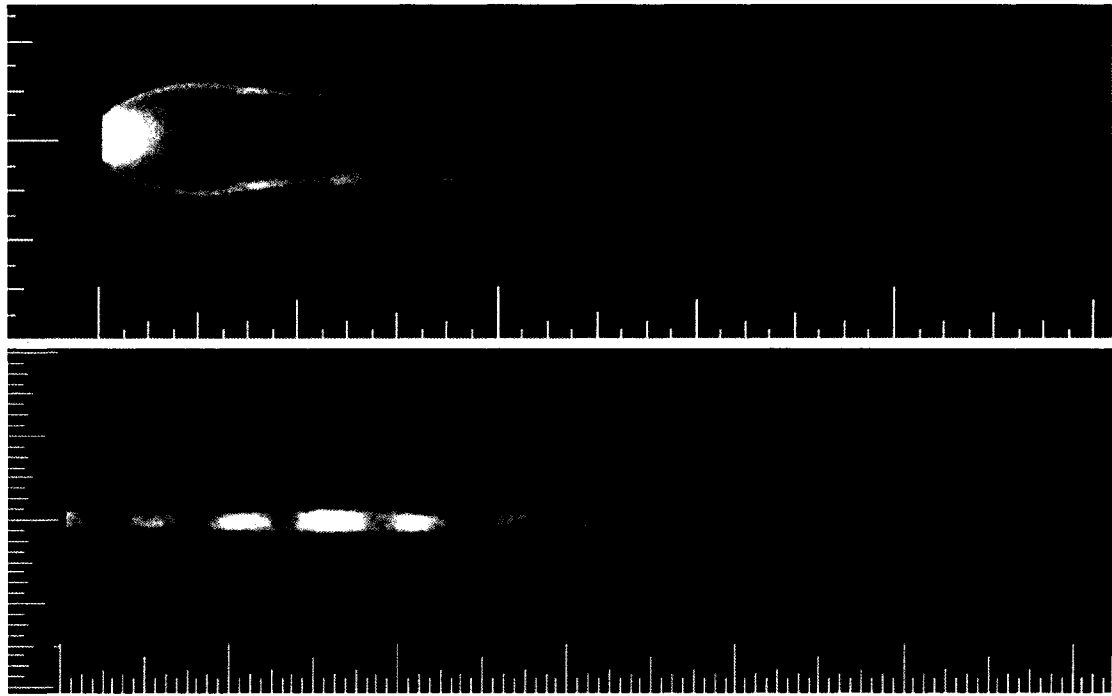
Figure 5.11: The sinuous mode of unsteadiness. Both images are single-shot images. The upper image is a sonic nozzle flow (Run35) $JPR = 16.3$, and $Re_{exit} = 4,361$; the lower image is a supersonic nozzle flow (Run 198) with $JPR = 1.2$, and $Re_{exit} = 9,064$.
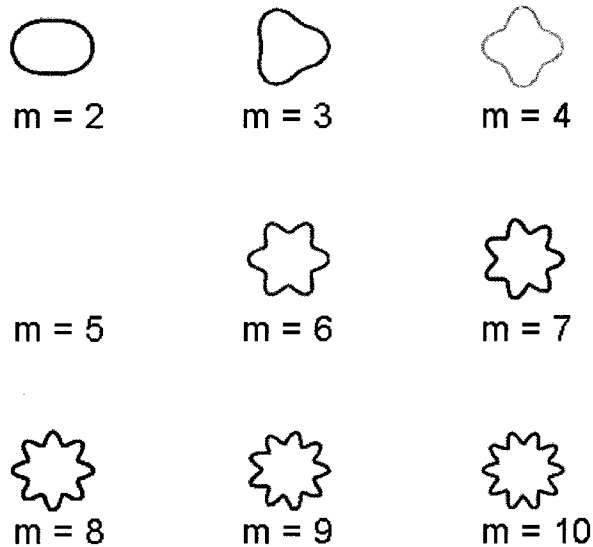
Figure 5.12: Azimuthal $cos(m\theta)$ modes for the first nine non-axisymmetric values of m.

When modeling these flows, the jet can be considered as being perturbed by all of these instability modes. As the modes compete with each other, the most dominant mode eventually takes over. A given jet flow will either amplify or dampen the growth of each normal mode of instability. Thus, a particular jet flow may be stable against one type of disturbance, but unstable against others. Additionally, some flows may be positively stable against small perturbations but unstable if the perturbations exceed some critical amplitude. The basic flow may be positively stable, neutrally stable, or negatively stable (unstable) against these perturbations. That is, these disturbances may be damped out, may persist, or may be amplified, respectively. Because most experimental investigations of turbulence have used hotwire anemometry measurements, most of the mathematics that has been developed actually deals with *temporal* evolution of these disturbances. The present investigation using PLIF is more concerned with the spatial propagation of these disturbances. There also are the peculiar restrictions on propagation of instabilities (or of any change, for that matter) in the supersonic regions of the flow, since "information" (anything that travels by pressure wave) can only propagate in the downstream direction.

In *Hydrodynamic Stability*, Drazin and Reid (1981) indicate that at first, one instability mode is active, and then other modes become active in turn. This happens at an ever-increasing rate (spatially, this would meant that the *distance* from the onset of the first mode to the onset of the second mode would be longer than, say, the distance between the onset of the second mode and the onset of the third mode). Finally, at the onset of fully-developed turbulence, all modes are active. This results in flow structures of all scales from the scale of the flow down to molecular scales.

5.5.1 Experimental results

The simulation of turbulence is an active area of research. The CFD (computational fluid dynamics) models that exist are generally based upon boundary layer flow along surfaces rather than free shear flow, and are often based on data taken in the incompressible (with a Mach number less than about 0.3) (Anderson 2003) regime, whereas the present experiments are in the compressible flow regime. In addition to these limitations of current turbulence models, the more difficult task of accurately predicting the transition from laminar to turbulent flow remains an unsolved problem for many ranges of conditions. The measurements of the unsteady, transitional, and/or turbulent locations resulting from these tests can therefore potentially be used to determine where turbulence models should be implemented in CFD simulations as well as providing data for comparison with CFD results.

For each test condition, the standard deviation image and the single-shot images were examined. The flow was then labeled steady laminar, unsteady, fully transitional, or fully turbulent based on the state of the flow at the most downstream location within the field of view of the camera. These locations were determined by eye, and so involved a measure of subjectivity. For steady laminar flows, x_{steady} was recorded as the location on the most downstream side of the image and for unsteady laminar flows, $x_{unsteady}$ was recorded; for transitional flows, both $x_{unsteady}$ and x_{trans} were recorded. For turbulent flows, $x_{unsteady}$, x_{trans} and x_{turb} were recorded.

170

5.5.1.1 Sonic Nozzle Results

The test matrix is plotted in Fig. 5.13, showing the range of Reynolds numbers and jet pressure ratios covered during the sonic nozzle, free jet phase of testing. Most data in this phase of testing were acquired with a 64 mm field of view. For selected test conditions, a wider field of view (165 mm) was employed in order to determine the jet behavior further downstream. A flow condition that appeared unsteady within the smaller field of view might have become fully transitional or turbulent within the wider field of view. Test points are shown for both the 64 mm and 165 mm fields of view; therefore some test points are labeled with two labels (e.g. the test point for $JPR = 35.2$ and Re_{exit} of about 4,500 is labeled as both transitional and turbulent).

In Fig. 5.13, points above a certain Reynolds number (perhaps 10,000, although data in this upper range are limited) appear to become fully turbulent, while points below a certain Reynolds number (about 800) appear to remain laminar, which was the expected trend. However, this leaves a Reynolds number range—spanning about an order of magnitude—over which flows exhibit mixed behavior. Clearly, additional parameters besides JPR and Re_{exit} need to be considered, not only to predict *if* a flow will become turbulent, but also at what downstream distance the transition to turbulence will occur.

171
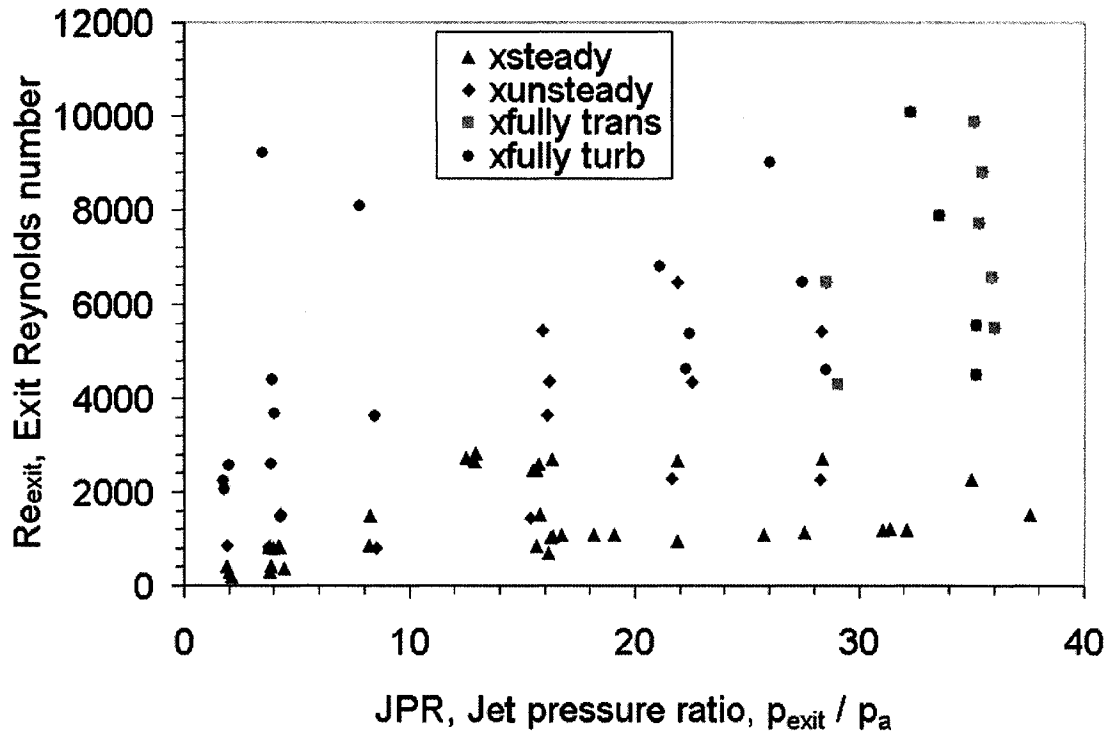
Figure 5.13: Exit Reynolds number versus jet pressure ratio. This plot shows the range of conditions over which these tests were conducted. Each case is labeled according to the state of the flow at the downstream edge of the field of view.

These same data are plotted in Fig. 5.14 in terms of exit Reynolds number versus downstream distance, rather than jet pressure ratio. The general and expected trend appears—flows with lower unit Reynolds numbers are more likely to remain laminar. However, a clear relationship indicating the distance at which one might expect a given flow to undergo transition to turbulence is not readily apparent. For many values of Re_{exit}, transition occurred at different distances for different test conditions. For instance, some flows with a unit Reynolds numbers near 2,500 became fully transitional in less than 20 mm, while others remained steady and laminar beyond 160 mm. These data seem to challenge the conventional wisdom that transition is solely a function of Reynolds

172

number based on nozzle diameter. Note that steady laminar data fall at one of two distances; these correspond to the extent of the camera's field of view, either 64 mm or 165 mm.
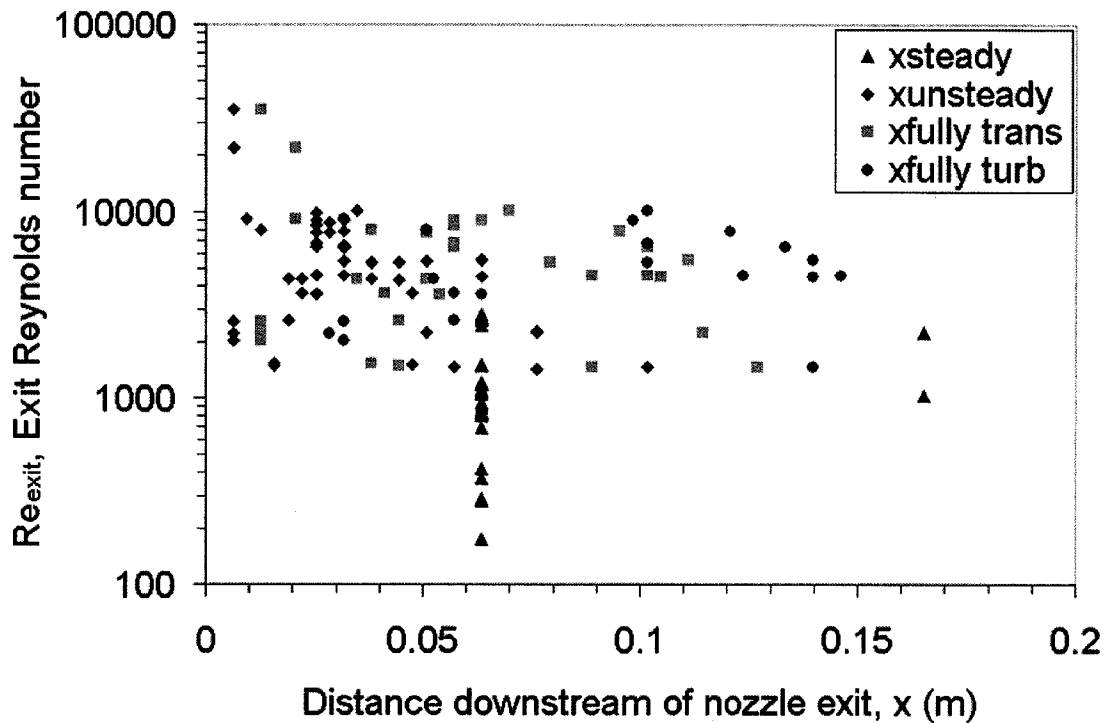
Figure 5.14: Exit Reynolds number vs. downstream distance at which flow becomes unsteady, transitional, and turbulent.

The lack of an obvious correlation in Fig. 5.14 led us to postulate that the jet behavior was a function not only of Reynolds number, but of jet pressure ratio as well. Scaling laws described by Yüceil and Ötügen (2002) provide a means of redefining the Reynolds number to include the effects of *JPR*. Conditions at the nozzle exit serve as initial conditions for defining an "equivalent jet." They assume that the initial jet is allowed to expand adiabatically until the pressure in the jet reaches the ambient pressure. At this point—which they call location 2—all of the flow conditions are recalculated.

173

The expressions for rescaled density ρ_2, velocity V_2, temperature T_2, and jet diameter D_2 are (Yüceil and Ötügen 2002):

$$\frac{\rho_2}{\rho_e} = \frac{2\gamma^2 M_e^2 JPR}{2\gamma M_e^2 JPR(\gamma + JPR - 1) - (\gamma - 1)(JPR - 1)^2} \tag{5.1}$$

$$\frac{V_2}{V_e} = 1 + \frac{JPR - 1}{\gamma M_e^2 \cdot JPR} \tag{5.2}$$

$$\frac{T_2}{T_e} = \frac{(\gamma + JPR - 1)}{\gamma JPR} - \frac{(\gamma - 1)}{2}\left(\frac{JPR - 1}{\gamma M_e JPR}\right)^2 \tag{5.3}$$

$$\frac{D_2}{D_e} = \sqrt{\frac{2\gamma M_e^2 JPR(\gamma + JPR - 1) - (\gamma - 1)(JPR - 1)^2}{2\gamma^2 M_e^2 JPR + 2\gamma(JPR - 1)}} \tag{5.4}$$

From Eq. 4.20 in the last chapter, the viscosity relation can be calculated from the temperature relation in Eq. 5.3. It becomes:

$$\frac{\mu_e}{\mu_2} = \left(\frac{T_e}{T_2}\right)^n \tag{5.5}$$

with the value of n taken from Table (3.2). Equation 4.14 can be combined with the preceding equations to arrive at an expression for the rescaled Reynolds number in terms of JPR and nozzle exit conditions. This expression is given in Eq. 5.6:

$$\mathrm{Re}_2 = \frac{\rho_2 V_2 D_2}{\mu_2} = \mathrm{Re}_{exit} \frac{\rho_2}{\rho_e} \frac{V_2}{V_e} \frac{D_2}{D_e} \frac{\mu_e}{\mu_2}$$

$$= \mathrm{Re}_{exit} \frac{\left(\gamma M_e^2 JPR + JPR - 1\right)^{1/2} \left(2^{1/2} \gamma^2 M_e^2 JPR^2\right)^n}{\left[2\gamma M_e^2 JPR(\gamma + JPR - 1) - (\gamma - 1)(JPR - 1)^2\right]^{n+1/2}} \cdot \tag{5.6}$$

174
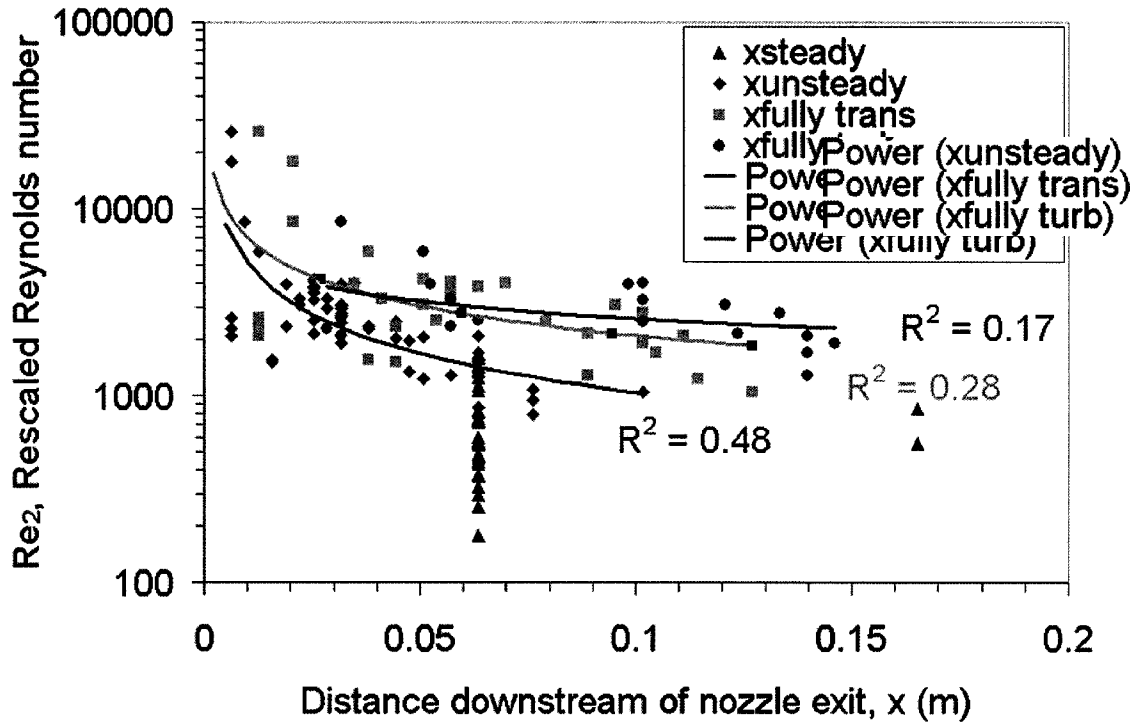
Figure 5.15: Rescaled Reynolds number vs. downstream distance for all sonic jet cases. Correlations are shown between rescaled Reynolds number and the distance downstream at which the jet flow became unsteady (red diamonds), transitional (orange squares) and fully turbulent (brown circles). Power law fits to the data are shown. This plot includes data for jet pressure ratios ranging from 1.7 to 38.

Figure 5.15 shows the data plotted in terms of this rescaled Reynolds number, Re_2. The relationship between this rescaled Reynolds number and transition length is more definitive. Independent power law fits to the unsteady, transitional, and turbulent data are shown as well. It is also important to note that all laminar points now lie below the fitted curve for turbulent and transitional test points, and most lie below the unsteady curve. This indicates that, for a given Re_2, there exists a distance beyond which the flow will likely be fully turbulent, and another distance below which the flow will likely remain laminar and steady. The fits to the data improve if the data are graphed in terms of a

175

rescaled length, x/D_2 (which is the number of "equivalent jet" diameters), rather than actual distance. This is shown in Fig. 5.16.
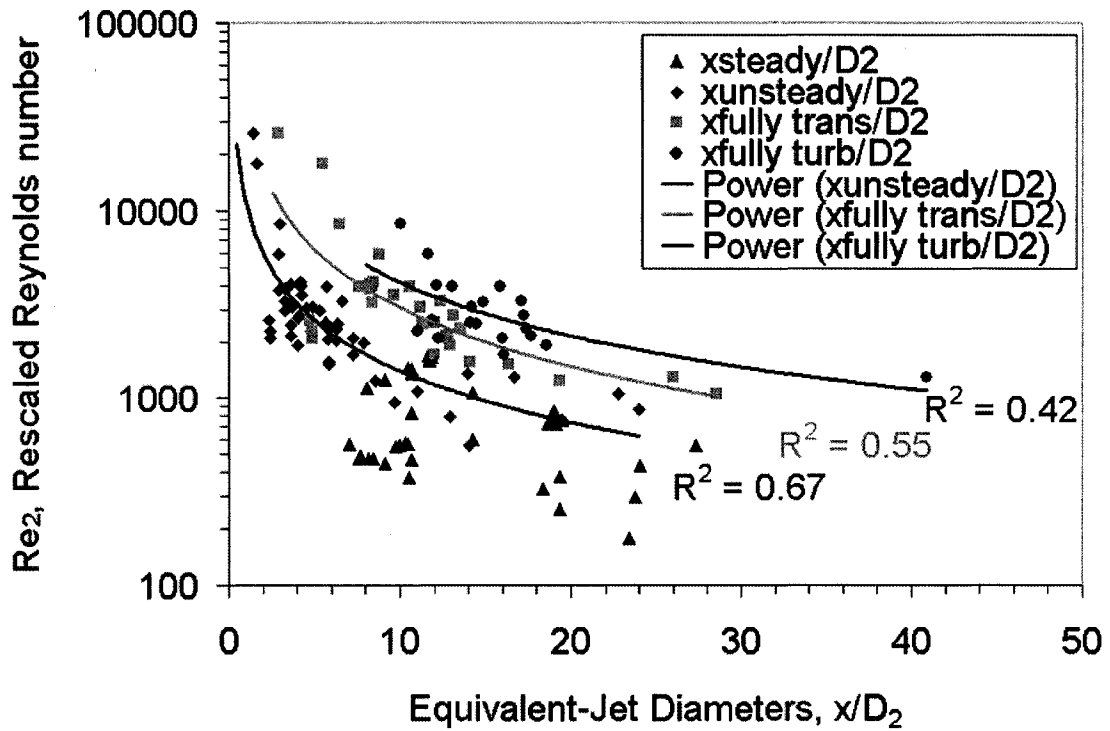
Figure 5.16: Rescaled Reynolds number vs. equivalent-jet diameters for all sonic free jet cases. The fits to the data improve when plotted in terms of a rescaled distance, rather than actual distance.

Note that caution must be exercised in attempting to extrapolate these results to flows at conditions that fall outside those of the current data set. At a low enough Reynolds number, all flows will likely simply dissipate without ever becoming transitional. That is, the actual curves probably asymptote at some Reynolds number, rather than continuing to decrease for greater distances. Additionally, at high Reynolds numbers, the definitions of unsteady, transitional, and turbulent distances break down. This is because unsteadiness or even fully-developed turbulence may exist in the barrel-

shock-processed gas along the jet boundary, while the accelerating flow inside the barrel shock is still steady and laminar. Peters and Phares (1970) report on such jets with a turbulent mixing layer along the jet boundary of the barrel shock. Krothapalli et al. (1991) and Zapryagaev et al. (2004) report streamwise vortices in the curved outer shear layer, which they attribute to a *Taylor-Görtler* instability, usually associated with flow along curved walls (described in *Turbulent Flows*, Pope 2000).
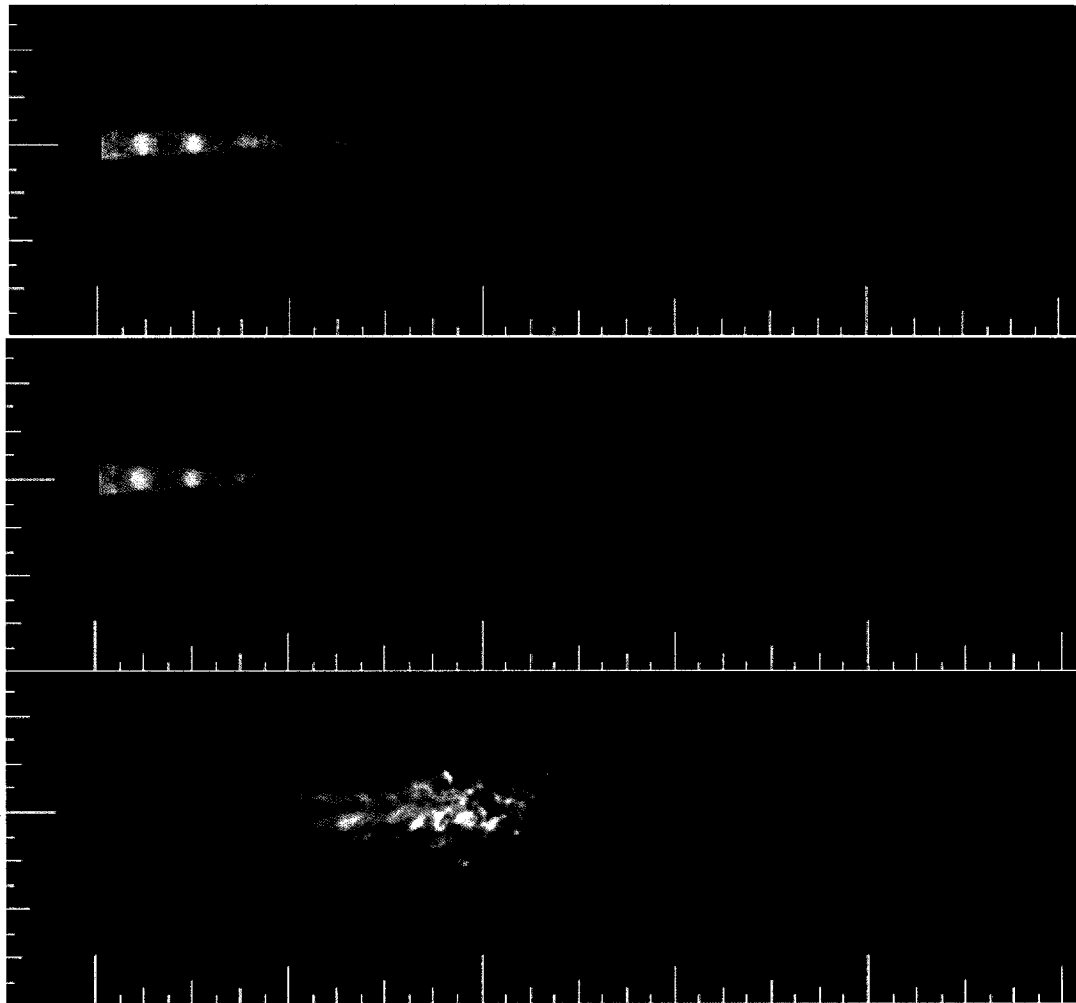
Figure 5.17: Image sequence (single-shot, 100-shot average, and standard deviation image) illustrating the varicose mode to turbulence. This mode is characteristic of diamond shock pattern flows. This case (Run 45) has $JPR = 2.0$ and $Re_{exit} = 2,609$.

177

As described in the previous chapter, flows with jet pressure ratios of less than about 3 exhibit different physical characteristics than flows with higher *JPR*s. Flows with low jet pressure ratios also exhibit different instability patterns when and if they became turbulent. Figure 5.17 illustrates this for a flow with a *JPR* of 2. As the flow becomes unstable, the diamond shock pattern appears to become distorted, and globules of jet fluid begin to be pinched off as the varicose mode becomes the dominant mode of unsteadiness. Flows with larger *JPR*s, by contrast, have a discernible high-velocity jet boundary which is approximately parallel to the jet axis. In these larger *JPR* flows, instabilities grow in the inner and outer shear layers, eventually reaching the core of the flow for transitional and turbulent cases. While both sinuous and varicose instability modes have been observed for high and low *JPR* cases, it is the absence of a separate high-velocity jet boundary that seems to set the low *JPR* cases apart from the rest in terms of the distance to transition.

Donaldson and Snedeker (1971) use a *JPR* of approximately 2 to delineate the boundary between moderately underexpanded and highly underexpanded jets. They also note that the differences in physical flow structures—such as the appearance of a slip line and high-velocity jet boundary in highly underexpanded jets—affect jet diffusion, spreading, mixing, and dissipation rates.

These differences in transition-mechanism physics between flows of different pressure ratios led us to separate data points corresponding to *JPR*s less than 3 from those with *JPR*s of greater than 3 in the sonic free jet correlations. The data were plotted separately and fitted with separate curves. The final correlations that were found between the rescaled Reynolds number and the non-dimensionalized transition length are

178

displayed in Figs. 5.18 and 5.19 for *JPR*s of greater than and less than 3, respecitvely. In Fig. 5.18, the lower line shows the correlation between the rescaled Reynolds number and distance to unsteadiness, the middle line shows the distance to transition, and the upper line shows the distance to turbulence.
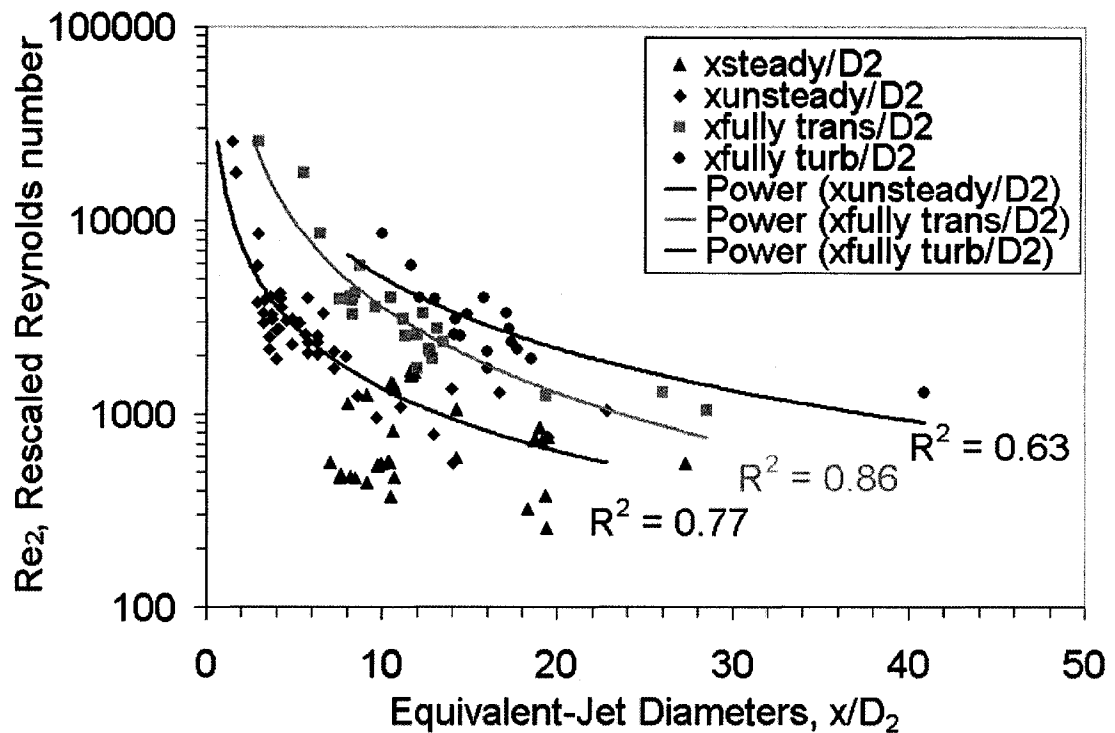
Figure 5.18: Final correlation for highly-underexpanded (*JPR* > 3) sonic free jets.

Scatter in the data has been reduced by limiting the correlation to highly underexpanded jets with *JPR*s greater than 3. Results previously reported in Wilkes et al. (2003) demonstrated a better "goodness of fit," with an R^2 value of 0.99. The complete set of data shown here includes additional test cases obtained subsequently; small changes in experimental variables (e.g. plenum temperature) may explain the slight increase in scatter of the complete data set relative to the previously reported results.

179

Figure 5.19 shows these correlations between rescaled Reynolds number and the distance

to unsteadiness and transition for low jet pressure ratios. The apparent "goodness of fit,"

indicated by the high R^2 values, is potentially misleading, due to the small number of data

points. Confidence in these trends could be increased by acquiring additional data for

flows with low jet pressure ratios.
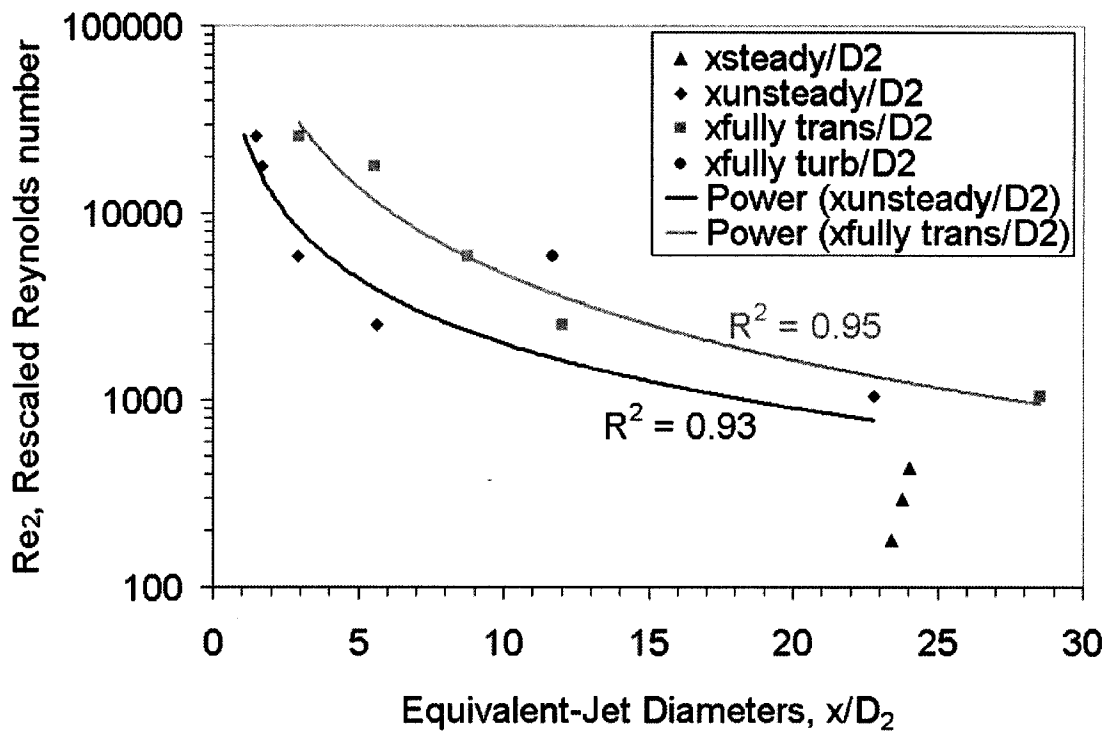
Figure 5.19: Correlation for sonic free jets with *JPR*s of less than 3.

From these correlations, one can predict whether a given sonic underexpanded jet

will remain steady over a certain distance, or whether turbulent effects will become

manifest. These predictions provide valuable information to researchers running CFD

simulations of such flows, indicating whether turbulence models need to be included in

the simulation of a given flow. This data set has been used by a group of researchers at

Boeing, lead by Don Picetti, to help prioritize which test cases to simulate. The correlations also help to define the range over which underexpanded jet flows will be neither steady laminar nor fully turbulent, regions where experimental measurements may prove to be most critical.

5.5.1.2 Supersonic Nozzle Results

The correlation data for the supersonic nozzle cases show different trends than the sonic nozzle data. Refer back to Figs. 5.7 and 5.8, which show typical images for two transitional supersonic cases. The first pair of images (Fig. 5.7) is for a *JPR* of 19.2. This flow has a Mach disk and parallel high-velocity jet boundary. For this flow, instabilities grow in the inner and outer shear layers, starting from the triple point and from the intersection of the jet boundary and the oblique reflected shock. The second set of images (Fig. 5.8) is for a lower *JPR* of about 3. Note the repeating, oscillating flow structures, and the resulting differences in the standard deviation images. In these standard deviation images, instabilities can be seen to be originating from the flow maxima. Figure 5.20 shows a plot of rescaled Reynolds number, Re_2, versus nondimensionalized downstream distance. For these data, a clear Reynolds number boundary emerges. Below Re_2 of about 2000, all cases remained laminar and steady within the imaged region. This is a powerful result, as it lends confidence to the assumption that cases with lower Reynolds numbers could be computed using laminar CFD codes, irrespective of the *JPR*.

Although the unsteady data exhibit a great deal of scatter, a grouping of cases (orange squares) occurs at approximately two equivalent jet diameters. Upon closer investigation, these cases all consist of flows with a large barrel shock and Mach disk,

181

and the location marked $x_{unsteady}$ occurs at the triple point and Mach disk of the flow. Unsteadiness is clearly originating from or being amplified by these points, as stated previously.
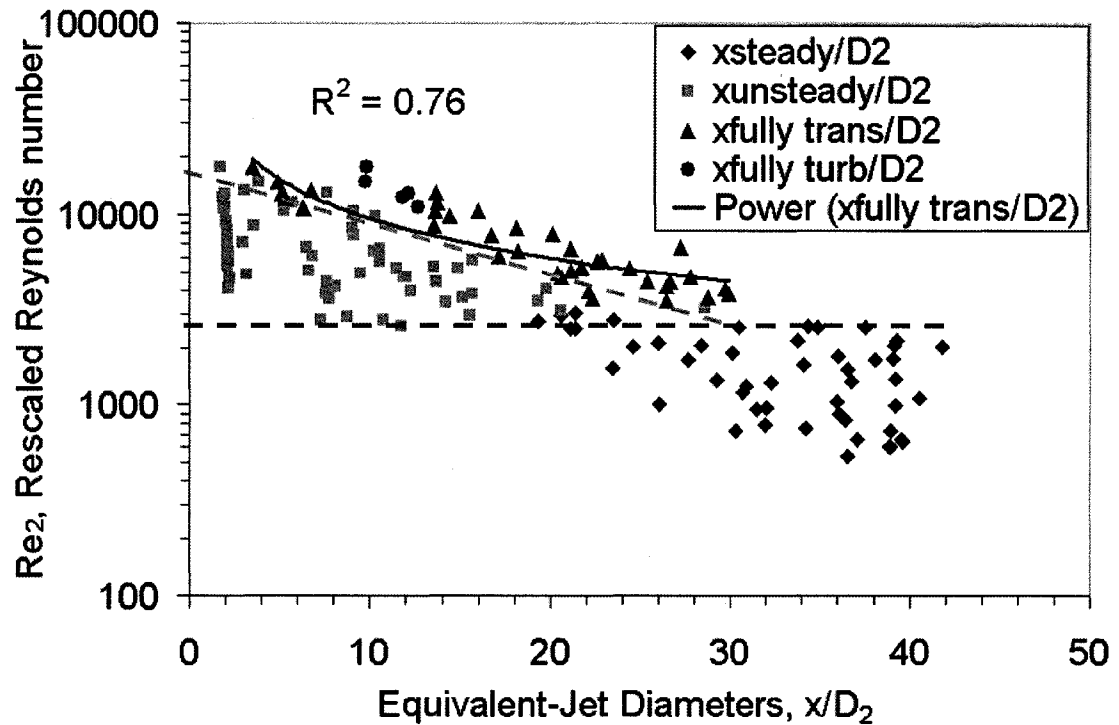
Figure 5.20: Transition correlation for supersonic free jet cases. A dashed blue line marks the boundary between steady and unsteady flow at a rescaled Reynolds number of 2000. An orange dashed line marks the approximate boundary between unsteady and fully transitional cases. A solid red line shows a power-law fit to the data, with a resulting R^2 value of 0.76.

The other apparent trend in the supersonic data is the approximate boundary between the unsteady and transitional data. This boundary and the Reynolds number boundary dividing steady and unsteady flows have both been marked with dashed lines in Figure 5.20. Additionally, a power law fit to the fully transitional points is displayed, with an R^2 value of 0.76. Only five cases in these tests were identified as becoming fully turbulent within the imaged region. Thus, no clear boundary can be established between

182

transitional and turbulent cases. However, when the data are separated by *JPR*, additional trends are evident. Figure 5.21 illustrates these same data, but with jet pressure ratios greater than 3.5 indicated by open symbols. Note the clustering of data for the low *JPR*, non-Mach disk cases versus those at higher *JPR* with a Mach disk. This reemphasizes the dependence on flow structure of the transition behavior of underexpanded jet flows.
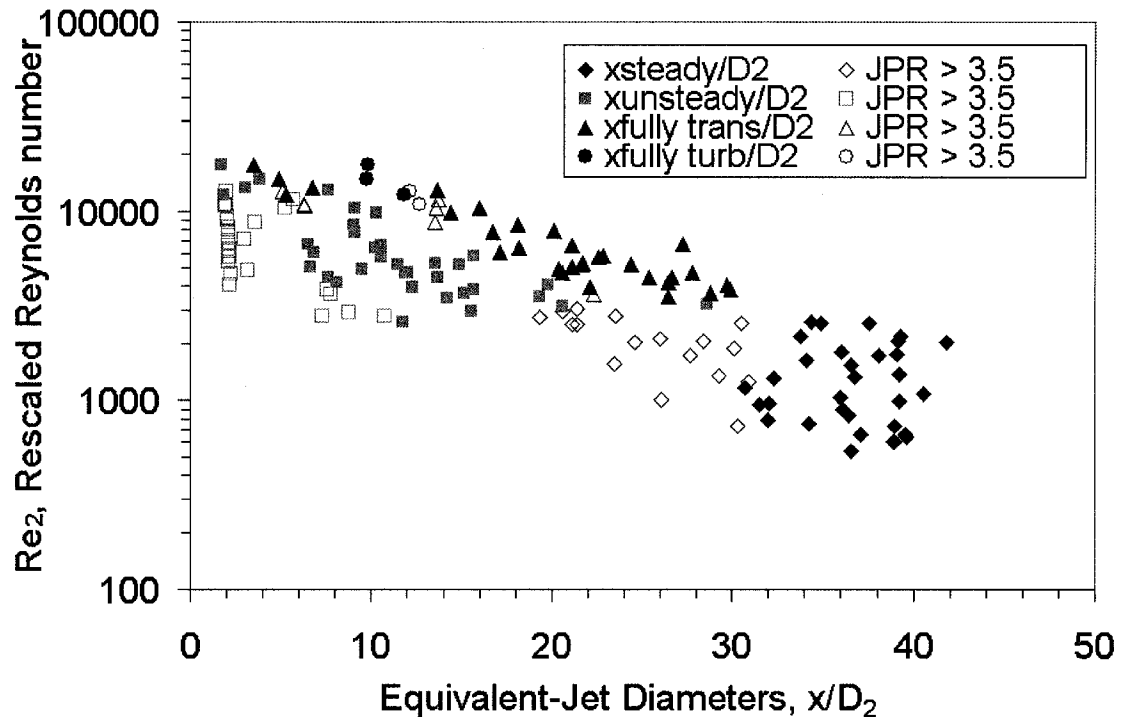
Figure 5.21: Supersonic free jet cases, with data separated by jet pressure ratios above 3.5 (open symbols) and below 3.5 (solid symbols).

5.6 Summary

In this work, we have demonstrated a powerful image processing technique to aid in the identification of turbulence using PLIF flow visualization images. This technique highlights turbulent regions of a flow by visualizing the standard deviation of fluorescence intensity throughout the flow. The image processing technique employed in

183

this work could also readily be extended to studying transition and/or turbulence effects in other flows, particularly for tests in which spatially and temporally resolved flow visualization data is desired. In the current study, we have used the information gathered from such images to identify a correlation between a rescaled Reynolds number and downstream distance to transition for highly underexpanded axisymmetric sonic and supersonic free jet flows.

184

CHAPTER 6

Impinging Jet Flows

The tests described herein were designed to create a simplified simulation of the flow through a hole in the surface of a hypersonic aerospace vehicle and the subsequent impingement of the flow on internal structures. In addition to PLIF flow visualization, pressure measurements were recorded on the surface of an impingement target. The PLIF images themselves provide quantitative spatial information about structure of the impinging jets. They also help in the interpretation of impingement surface pressure profiles by highlighting the flow structures corresponding to distinctive features of these pressure profiles. Additionally, PLIF images can be used to characterize the effect that impingement has on the process of transition to turbulence as compared to corresponding free jet cases.

This chapter will cover both steady and unsteady impinging jet flows. For steady flows, new flow structures associated with impingement will be introduced, including plate shocks, recirculation bubbles and wall jets. Surface pressure data will be presented, showing the relationship between impinging flow structures and impingement pressure. For unsteady impinging flows, the effect of impingement on the instability mechanisms

185

introduced in Chapter 5 will be discussed. Additional sources of flow unsteadiness will also be discussed; in particular, the impingement of the high-velocity jet boundary will be shown to be a source of flow vorticity and therefore a source or amplification mechanism for unsteadiness. The current experimental design is shown to provide an excellent means of identifying flow structures and flow instabilities in the free jet and impingement regions.

6.1 Overview of Previous Studies

A major difference between this work and the bulk of the literature is that for impinging flows, previous studies were concerned with near-field impingement, on the order of a few jet diameters, where the impingement plane was often intersecting the Mach disk. Refer back to Table 1.1 in the first chapter for a summary of the test conditions for several past investigations. In studies of rocket plume/ground interaction, ground erosion was a primary concern, and the near field was thus of greatest significance (Stitt 1961). The impinging jet configurations in the present work, with the closest impingement distance being about 10.5 nozzle diameters and the furthest being 39.5 nozzle diameters, are all relatively far-field compared to previous studies (with the exception of Stitt, 1961). Note that even though the studies of Donaldson and Snedeker, 1971, had some data at about 40 nozzle diameters, the majority of their data were within about 15 nozzle diameters. Of the studies listed in Table 1.1, only those of Stitt (1961) and Love et al. (1958) investigated flows into sub-atmospheric pressure environments. For those studies, the intended application was rocket and thruster use in the vacuum of space, and so the pressures they used were one to two orders of magnitude lower than

186

those of the present study. The Reynolds numbers of these previous studies were relatively high—up to three orders of magnitude higher than the very highest Reynolds numbers investigated in the present work.

Many, including Donaldson and Snedeker (1971), made hotwire anemometry measurements of the mean and fluctuating components of velocity as a means of quantifying the level of turbulence in these flows. Since the impingement targets were so close to the nozzle exit, the turbulence was largely confined to the outer boundary of the jets (as turbulent structures are not observed inside the barrel shock). Additionally, the atmospheric pressure conditions and correspondingly high Reynolds numbers resulted in fine-scale turbulence rather than flows that bordered on transitional. By contrast, the experiments presented herein were designed to straddle the region between steady and turbulent flow conditions and to gain insight into the effect of impingement on the transition process itself. The time response of the pressure instrumentation used in the present experiment (~1 s) was too slow to observe high-frequency turbulent oscillations. Instead, turbulent flow structures were visualized directly.

6.2 Test Parameters

Table 6.1 shows the range of conditions and hardware configurations for which data were taken during the impinging jet cases of the present study. The Reynolds numbers listed were based on nozzle exit conditions, which were calculated based on measured plenum conditions. This results in a somewhat higher range of Re_{exit} and *JPR* for the sonic nozzle than for the supersonic nozzle for the same range of achievable plenum-pressure-to-ambient-pressure ratios (p_0/p_a). The table lists the number of cases that were

187

studied for each combination of hardware configuration and type of PLIF imaging that was investigated in these tests. For each flow visualization case, either 100 or 200 single-shot images were acquired. In addition, volume imaging was performed for the majority of cases by sweeping the laser sheet spanwise through the flow.

Impingement configuration	Supersonic Nozzle				Sonic Nozzle		
	FV / VI	*V*	*P*	ρ	*FV / VI*	*V*	*P*
1" @ 90°					25		5
1.75" @ 90°	25	22	22	1	25		
2.5" @ 90°	22	19	21		24		
2.5" @ 60°	18						
3.75" @ 90°	23				23		
3.7" @ 45°	23						
5" @ 90°	22						
∞ (free jet)	88	11		12	53	8	8
Re$_{exit}$	600-14,000				2,400-35,000		
JPR	1-16				3-27		

Table 6.1: Matrix of configurations for which data were acquired in the impinging jet cases. *FV/VI* indicates *flow-visualization* and *volume-imaging* runs, *V* indicates *velocity* runs, *P* indicates *pressure-sensitive* runs, and ρ indicates *density-sensitive* runs.

188

6.3 Steady Flows

6.3.1 Stable Flow Structures

Impinging jet flows can be divided roughly into three regions: the jet flow upstream of the impingement region, the impingement region, and the wall jet flow (where the flow has become parallel to the surface of the impingement target). The flow structures that are observed in the upstream region are similar to those in free jet cases, as described in Chapter 4. The pressures in the impingement zone can approach the plenum pressure, and because mixing with the ambient gas is enhanced by any vortices that may be present as well as by the physical dispersion of the jet gas, quenching rates are increasing and the mole fraction of nitric oxide is decreasing. These both result in a reduction of fluorescence signal near the plate, and so the details of the flow in the wall jet region are not necessarily well-resolved. Structures in the impingement region will be discussed in this section.

When the flow impinging on the flat plate is supersonic, a normal shock parallel to the impingement surface, called a *plate shock*, may be formed. Under certain flow conditions, a high pressure bubble of gas may build up between this shock and the impingement surface, causing the shock to move further away from the surface. Choosing to excite a pressure-sensitive line grouping (see the section on pressure-sensitive imaging in Chapter 3) makes identification of such a *stagnation bubble* (also called a *recirculation bubble*) and/or normal plate shock much easier, as the pressure rise inside the recirculation region results in a large increase in intensity compared to the free jet region. Figure 6.1 illustrates this, with two images of similar flows, taken with the

189

laser at two different frequencies. Note the well defined boundaries of the recirculation bubble in the pressure-sensitive image as compared with the flow-visualization image. By contrast, note the lack of signal in the low pressure region inside the barrel shock in the pressure-sensitive as compared to the flow-visualization image, where there is signal throughout the flow and the jet boundary is more clearly defined.
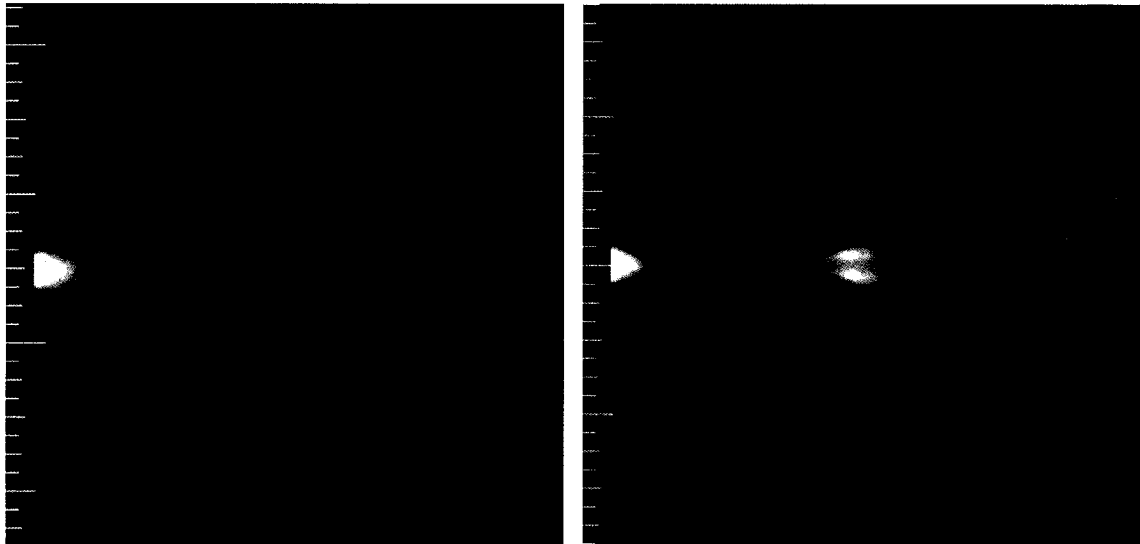
Figure 6.1: Pressure-sensitive imaging can help to identify certain flow features, such as plate shocks and recirculation bubbles. Both images are averages of 100 single-shots of supersonic flows, taken at an impingement distance of 1.75 in. (10.7 nozzle diameters). The image on the left was acquired with the laser tuned to the flow visualization lines (line grouping #4 in Table 3.3; Run 363, JPR = 3.1, Re_{exit}= 2,082). The image on the right was taken with the laser tuned to pressure-sensitive lines (line grouping #1 in Table 3.3; Run 451, JPR = 3.0, Re_{exit} = 1,196). The scales are in inches, with the smallest hash marks measuring 1/16th in.

Several studies in the literature have discussed the formation of recirculation bubbles for some combinations of jet pressure ratio and impingement distance. Alvi et al. (2002) give a good description of recirculation bubble formation. Mackie and Taghavi (2002) found, not surprisingly, that recirculation bubble formation was purely a three-dimensional phenomena; that is, two dimensional jets (quasi-two dimensional in

190

experimental studies, or truly two-dimensional in computational studies) never resulted in recirculation bubble formation. This is less surprising in the experimental cases (which can never be truly two-dimensional), since the recirculation bubble is shaped like a bell, and requires the annular pressure "seal" around the ring where it intersects with the impingement plate in order to be a stable feature. The gas inside the recirculation bubble acts as a high-pressure reservoir, contained by the plate shock upstream, and the high-velocity jet boundary impingement along the outer edges.

6.3.2 Pressure profiles

As mentioned in the introduction to this chapter, pressure measurements were recorded along the impingement plate surface. In order to understand the results of these measurements, first consider an impinging jet flow with a uniform momentum profile throughout the core of the jet. One would expect the pressure profile of such a jet to resemble a top hat function, with roughly uniform pressure across the intersection of the jet with the impingement target, dropping to near ambient pressure away from the core of the jet.

Modifying the situation to include viscous effects, one would expect to see a decrease in momentum—and therefore a decrease in pressure on the impingement surface—along the edges of the jet. This modified pressure profile would be peaked in the center, smoothly dropping off to the ambient pressure toward the edges of the jet flow. In fact, for some cases, this describes the measured pressure profiles well. An example is shown in Fig. 6.2.

191
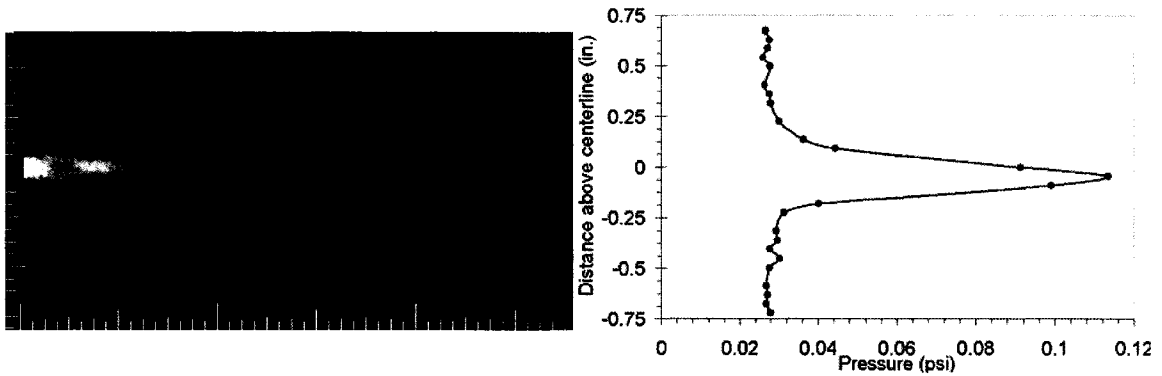
Figure 6.2: Single-shot PLIF image and corresponding ressure profile with a single, central peak. This profile is for supersonic nozzle Run 528 with $JPR = 1.0$, $Re_{exit} = 382$, $\theta_{imp} = 90°$ and $D_{imp}/D_e = 15.2$. The scale on the image is in inches, with the smallest hash marks equal to 1/16th in.

But for other cases, the measured profiles are markedly different. Such profiles typically exhibit a double-peaked structure, with the maximum pressure occurring away from the flow centerline. The peaks in pressure are found to coincide with the location of the impingement of the high-velocity jet boundary or with the intersection of the shock structure surrounding a recirculation bubble. Fluid mechanically, this can be understood because the high-velocity jet boundary carries with it a great deal of the momentum and thus creates a larger pressure rise as it impinges on the flat plate, compared to the slower jet core. (Refer back to Fig. 4.4 for a qualitative velocity image, showing the large velocity of the jet boundary as compared to the gas in the jet core.) The pressure between these peaks is often nearly constant, while the pressure outside these peaks drops off toward—and sometimes dips briefly below—the ambient pressure. Figure 6.3 shows an example of this type of profile. Flow visualization images help to elucidate the origin of these features by highlighting the flow structures associated with presence of the impingement surface. These images also help to explain the observed sensitivities (and

192

insensitivities) of the pressure profiles to Reynolds number and jet pressure ratio, as explained further in the following sections.
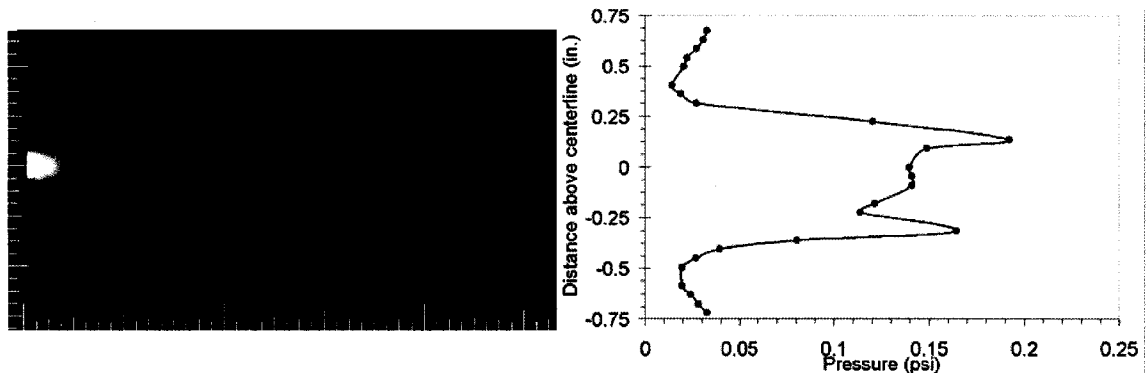
Figure 6.3: Single-shot PLIF image and corresponding pressure profile with a double peak. This profile is for supersonic nozzle Run 536 with $JPR = 5.4$, $Re_{exit} = 2,302$, $\theta_{imp} = 90°$ and $D_{imp}/D_e = 15.2$. The scale on the image is in inches, with the smallest hash marks equal to 1/16th in.

6.3.3 Review of free jet structure

The data show that free jet cases having the same JPR exhibit the similar flow structures over a range of Reynolds numbers, so long as the cases under consideration are all laminar. In Chapter 4, sonic nozzle flows were divided into two major groups: those with a repeating diamond shock structure (seen for flows with JPRs less than about 3), and those with a barrel shock structure, a Mach disk, and a streamwise high-velocity jet boundary (seen for flows with JPRs greater than about 3)(Wilkes et al. 2005). For cases with the supersonic nozzle, the division happens at a JPR of about 3.5. For smaller JPRs, a repeating pattern, analogous to the diamond shock pattern, is evident, with a chain-like pattern of alternating spatial minima and maxima. As JPR increases, the repeating pattern becomes less pronounced, until a JPR of about 5. Larger JPRs lead to a modified

193

barrel shock structure—elongated into a more egg-like shape than its comparable sonic jet counterpart—with a Mach disk and a streamwise high-velocity jet boundary.

6.3.4 Single-peaked vs. double-peaked pressure profiles

In the case of steady laminar impingement, the high-velocity jet boundary impinges on the flat plate, and is partly reflected. That is, the flow does not immediately become tangent with the wall, but rather first appears to bounce off the surface before becoming a pure wall jet, as shown in Fig. 6.3. This results in an annular suction region beneath the place where the flow is skipping above the surface, where the pressure is actually *lower* than ambient. Figure 6.4 shows a close up of the flow in Fig. 6.3,.

194
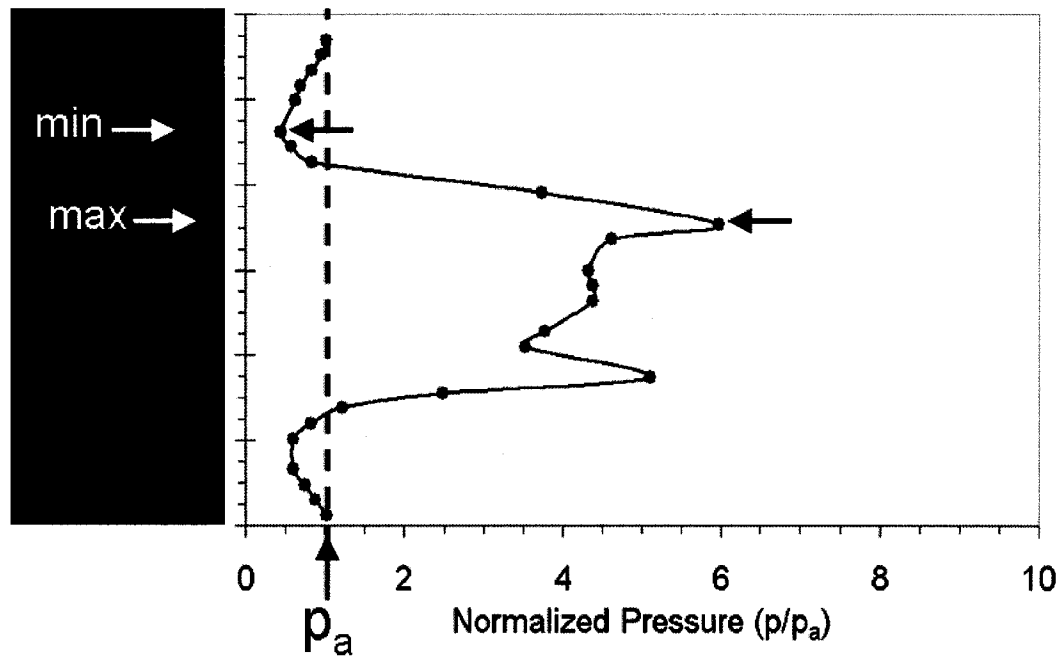
Figure 6.4: Close-up of the impingement region for the flow in Fig. 6.3 (supersonic, Run 536, $JPR = 5.4$, $Re_{exit} = 2{,}302$, $\theta_{imp} = 90°$ and $D_{imp}/D_e = 15$) showing the relation of flow features to the maximum and minimum measured pressures. A dashed vertical line indicates the ambient pressure (all pressures have been normalized by this pressure). The reflection of the flow off the surface results in an annular suction region where the pressure is lower than the ambient pressure. The actual peak pressures may occur between pressure taps, and thus may be greater than the measured peak pressure. The smallest hash marks on the vertical scale of the graph are 1/16th in.

This is a case with such a suction ring, indicating the corresponding features in the pressure profile. Arrows identify the regions of maximum and minimum pressure, clearly illustrating the connection between flow features and surface pressures.

Figure 6.5 shows single-shot PLIF images and corresponding pressure profiles for several cases with distinct flow features over a range of jet pressure ratios. Notice that the cases without a recirculation bubble have single-peaked pressure profiles, while those with a recirculation bubble have double-peaked structures. It is possible that the second peak in Run 541 was missed in the second figure due to the spacing of pressure taps along the surface. Slight asymmetry in the pressure profiles may be due to pressure tap spacing, but may also be due to the target being at an angle not perfectly perpendicular to the flow.

195

The angle was measured to be 90°±1°. Also notice that the peaks are slightly flattened over a small region for the third and fourth images, indicative of a stagnant region behind the plate shock.
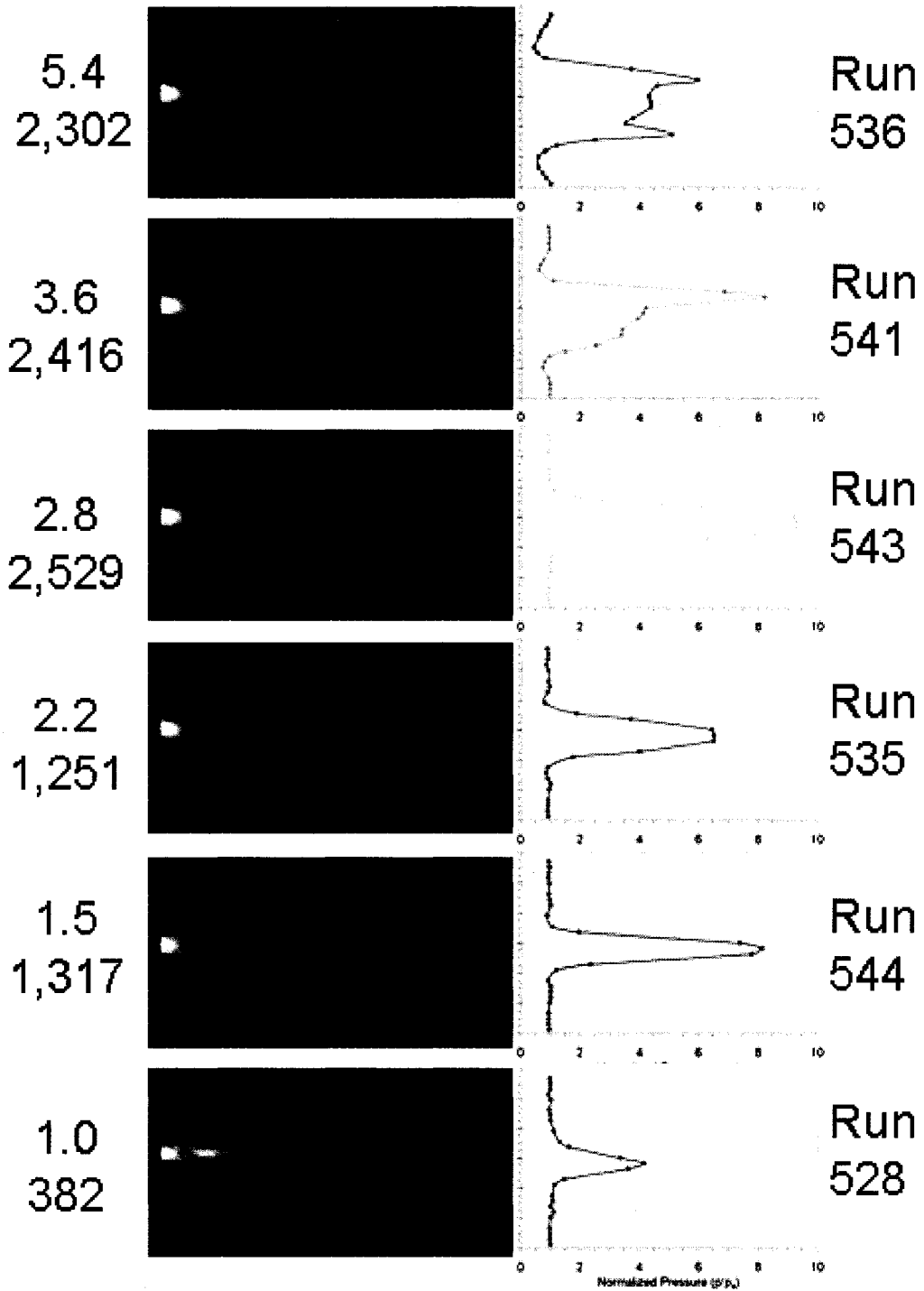
Figure 6.5: PLIF images and corresponding Impingement pressure profiles, for θ_{imp} =

196

90 and D_{imp}= 15 nozzle diameters (2.5 in.). All PLIF images are single-shot images of supersonic nozzle flows. Corresponding values of *JPR* and Re_{exit} are listed to the left of each image, with the run number to the right. Pressures have been normalized by the ambient pressure, pa. Scales on images and vertical scales on graphs are in inches, with smallest hash marks equal to 1/16th in.

6.3.5 Angled Impingement

In the literature, some studies (most notably, the experimental studies of Lamont and Hunt 1980, as well as the computational studies of Wu et al. 2001 which simulated flows at conditions identical to those of Lamont and Hunt) found that the maximum impingement pressure on angled impingement targets could be much greater (up to a factor of three greater) than the maximum pressure in the corresponding normal impingement cases. In our experiments, we have observed a similar result. For the supersonic impingement case at 15 nozzle diameters (2.5 in.), we have observed approximately a factor of two increase in the maximum pressure for the 60 degree impingement angle versus the 90 degree impingement angle. However, for the supersonic impingement distance of 23 nozzle diameters (3.75 in.), we did not observe this effect for the 45 degree impingement angle, when compared to the 90 degree case.

6.3.6 Effect of Reynolds Number on Pressure Profiles for Steady Laminar Flows

Like their free jet counterparts, impinging jet flow structures are similar for runs that have similar *JPR*s (for a given nozzle type), including in regions near the impingement disk, as long as the runs are all laminar. It is then not surprising that the shapes of the pressure distributions for runs with the same *JPR* have similar features. However, for runs with matching *JPR* but different values of Re_{exit}, the magnitude of the

197

measured pressure profiles increases with increasing Re_{exit}. This is expected to be the case because, for constant gas plenum temperatures, plenum pressure (p_0) is proportional to Re_{exit}. Self-similar pressure profiles can be obtained for runs with the same *JPR* by normalizing all the measured impingement disk pressures by the ambient chamber pressure, p_a. Figures 6.6 and 6.7 graphically depict the effect of normalization by p_a. The first figure shows pressure profiles from two runs with essentially the same *JPR* (2.8), but different values of Re_{exit} (4448 and 2476). The second figure shows these same data after they have been normalized by the plenum pressure for each run. The two normalized profiles show a high degree of similarity.
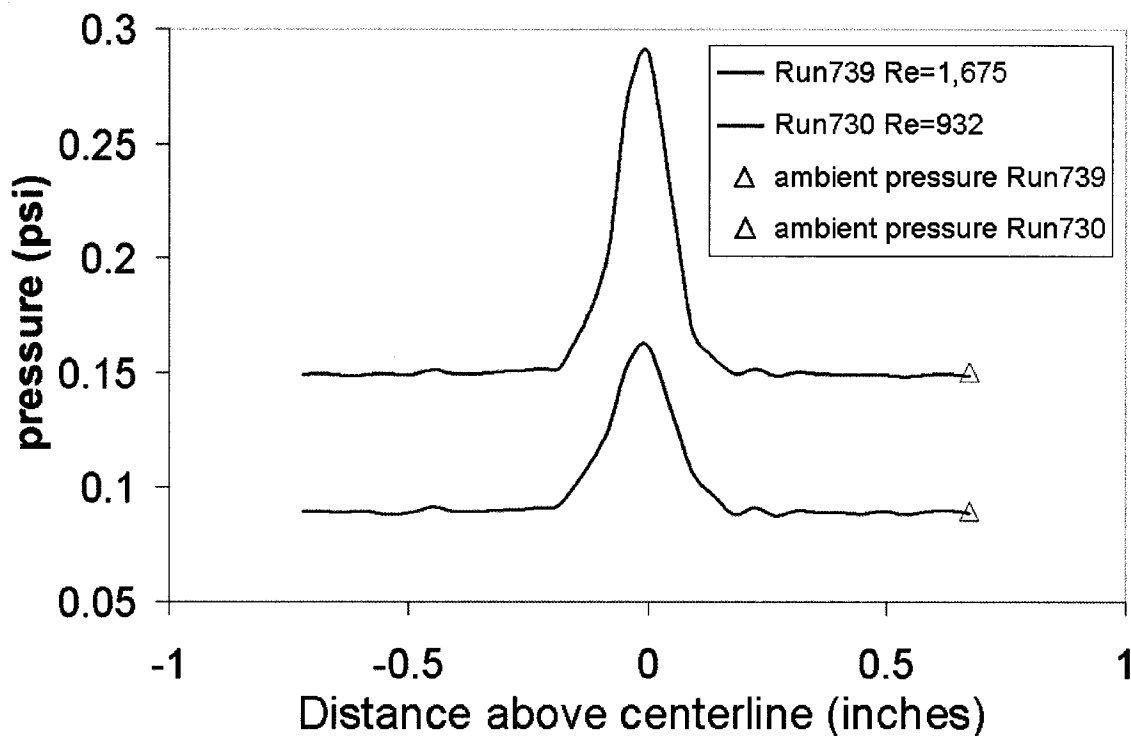
Figure 6.6: Two laminar impingement surface pressure profiles from runs with the same jet pressure ratio but different exit Reynolds numbers.
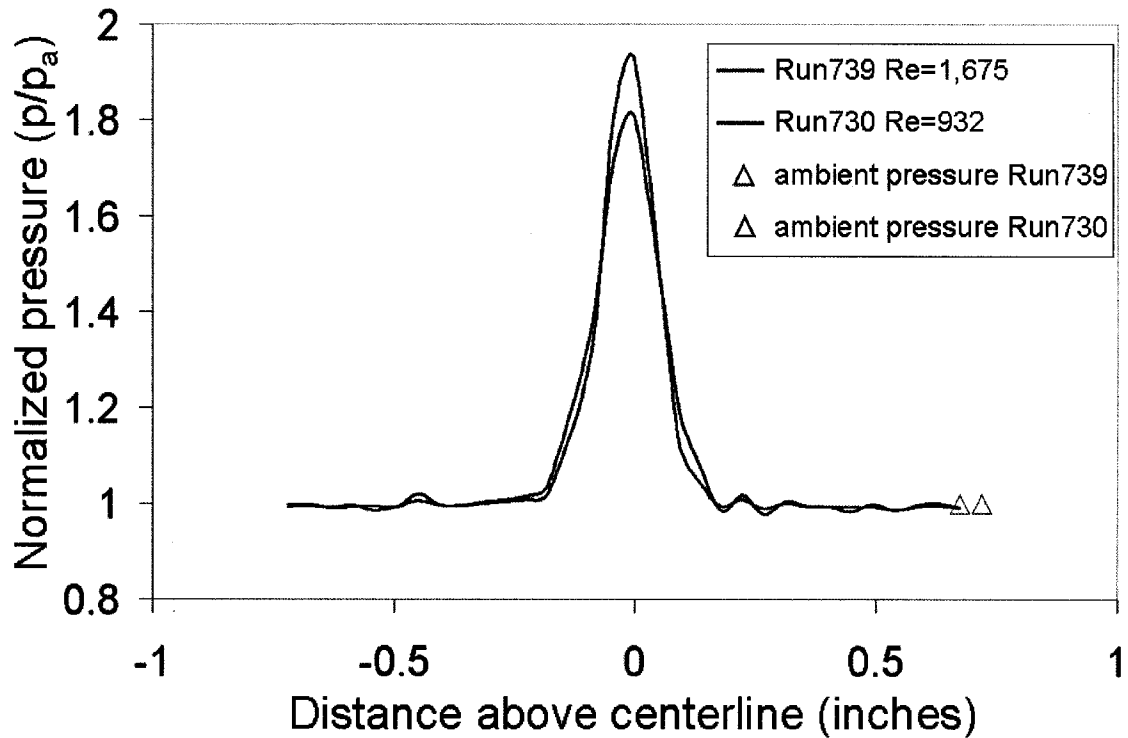
Figure 6.7: Two impingement surface pressure profiles from runs with the same jet pressure ratio but different exit Reynolds numbers, normalized by the ambient (chamber) pressure of each run. This normalization results in nearly self-similar profiles.

6.3.7 Jet Pressure Ratio Effect on Pressure Profiles

The shape of the pressure profile was found to depend strongly on the jet pressure ratio for laminar runs where the impingement target was located in a region of large local spatial variations. That is, small (a few percent) variations in *JPR* were seen to cause significant variations in the pressure profile for flows where the spatial cross-section is strongly varying with distance in the streamwise direction. This can be explained by considering that small changes in *JPR* are roughly equivalent to small changes in impingement distance. So, small changes in *JPR* result in the intersection of the impingement plane with successive flow structures.

199

A related effect, known as *staging*, is evident in these impinging cases. The impingement flow structures, and the associated pressure distributions, change smoothly and predictably for certain *JPR* ranges, but then suddenly hop to a distinct flow pattern and the associated pressure profile when the *JPR* is just right. When one of the shock cells is at just the right distance away from the impingement target, a bubble from near the impingement plate shrinks as the *JPR* increases and the shock structure moves toward the plate, making the plate shock move closer to the plate. But then, abruptly, the next shock cell pops open, reforming the recirculation bubble.

For supersonic cases, this staging behavior was seen for flows with *JPR*s less than about 5. This effect is illustrated in Fig. 6.8, where PLIF images show the flow structures associated with impinging supersonic axisymmetric jets for decreasing *JPR*s, from about 4 to 1. In the first three images, the jet impinges on the disk just upstream of what would have been the second diameter maximum of the flow. As *JPR* decreases in the fourth image, the jet then impinges near the second flow minimum. In this image, the recirculation bubble has disappeared or has at least shrunk to the point that there is a single region of maximum pressure. By the fifth image, the profile is narrowly peaked, with no recirculation bubble. In the sixth image, the recirculation bubble has reappeared, disappearing again in the final image. Figure 6.9 shows normalized pressure profiles from these seven runs, showing a variety of different profiles, explained above.

200
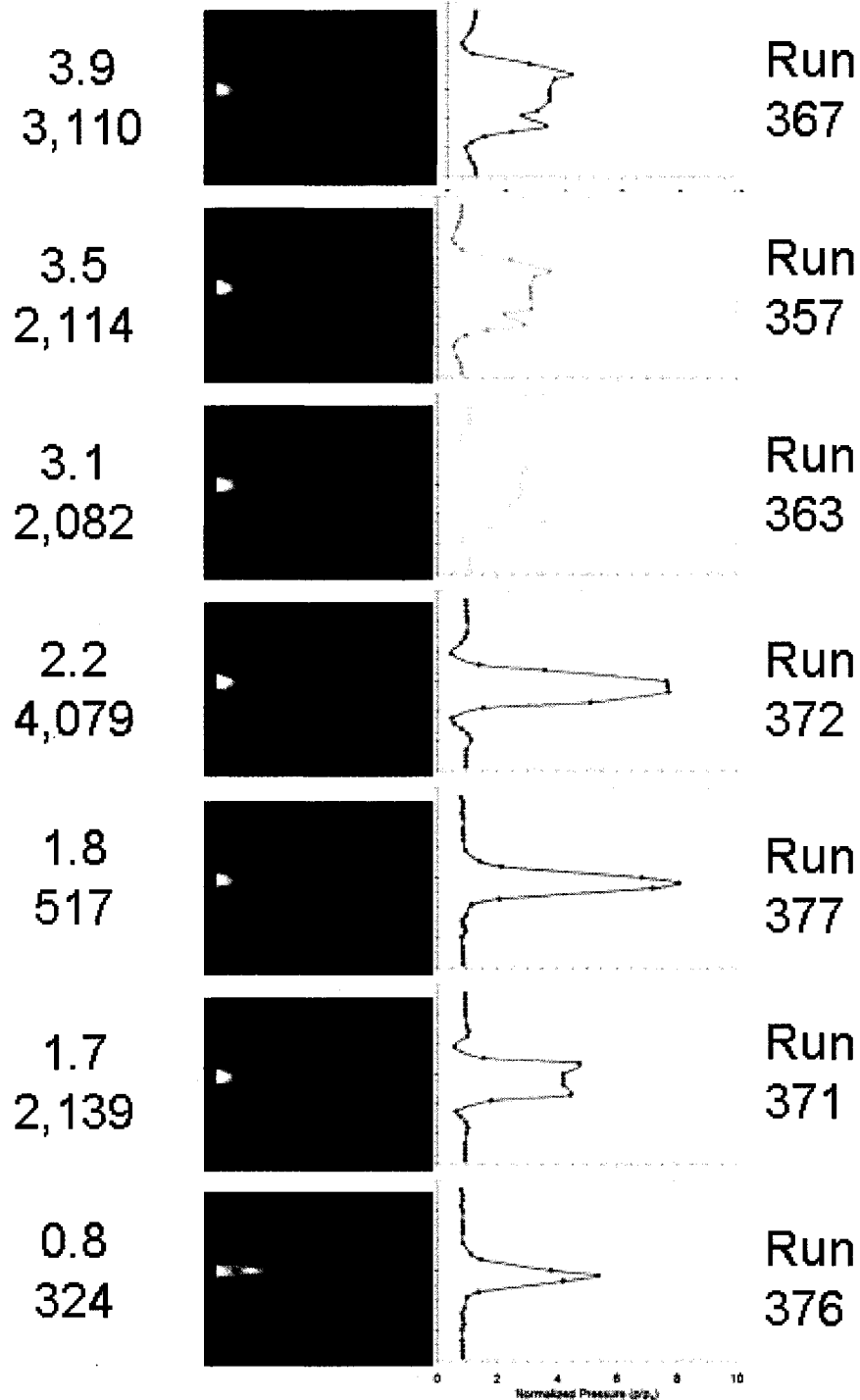
Figure 6.8: PLIF images and impingement pressure profiles showing the sensitivity to small changes in *JPR*, for $\theta_{imp}= 90°$ and $D_{imp}/D_e = 10.7$ nozzle diameters (1.75 in.). All PLIF images are single-shot images of supersonic nozzle flows. Corresponding values of *JPR* and Re_{exit} are listed to the left of each image, with the run number to the right. Pressures have been normalized by the ambient pressure, pa. Scales on images and vertical scales on graphs are in inches, with smallest hash marks equal to 1/16th in.

201
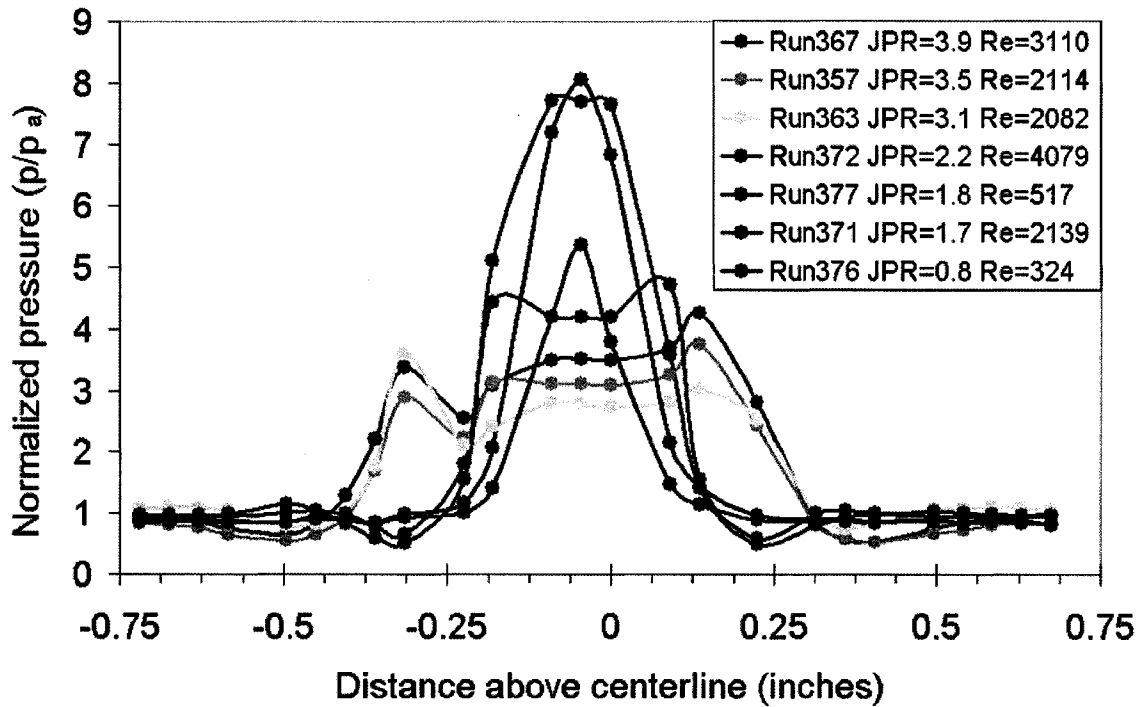
Figure 6.9: Impingement pressure profiles showing the sensitivity to small changes in *JPR*, for $\theta_{imp}=$ 90° and $D_{imp}=$ 10.7 nozzle diameters (1.75 in.). Run numbers and corresponding values of *JPR* and Re_{exit} are listed in the legend. Pressures have been normalized by the ambient pressure, p_a.

Similar sensitivity and the resulting staging behavior was not definitively seen for the sonic cases that were studied in these tests. This is likely due to the impingement distances that were chosen and to the lack of resolution in *JPR*, meaning there were insufficient cases with closely spaced *JPR*s available to compare. The minimum impingement distance was approximately 11 nozzle diameters (1.0 in. for sonic nozzle cases and 1.75 in. for supersonic nozzle cases). Moderately underexpanded supersonic nozzle flows (with *JPR*s less than about 3.5) exhibited repeating flow patterns with wavelengths on the order of 3 to 8 nozzle diameters (0.5 in. to 1.25 in.). In contrast, moderately underexpanded sonic nozzle flows (with *JPR*s of less than about 2) had smaller spatial frequencies—on the order of 2 nozzle diameters (0.2 in.). PLIF images

202

show that diamond shock structures for the sonic case tended to dissipate within about 2 or 3 oscillations, with diffusion and damping processes being the likely causes. Laminar impingement structures for the sonic cases were thus rather indistinct, with little sensitivity to small changes in *JPR*. Large changes in *JPR*, however, did significantly affect wall pressures, causing, for example, the flow to switch from the diamond shock structures to the barrel shock structures. It is possible that staging behavior may have been observed for sonic cases at low *JPR*s if smaller impingement distances had been investigated.

In 2005, a related series of tests led by R.J. Nowak were conducted at NASA Langley Research Center. In these tests (hereafter called the "Box Model" tests), a box evacuated by a vacuum dump tank was placed in the 31-Inch Mach 10 Air Wind Tunnel. The wind tunnel flow fed the high pressure side of either a sonic or supersonic nozzle (identical to the ones used in the PLIF tests), which was embedded in the upstream side of the box. PLIF images were not obtained during these tests. An instrumented impingement disk was located inside the box, measuring impingement surface pressures and heat transfer. Due to the finite volume of the vacuum dump tank, the *JPR* was continuously varying (decreasing) during a run. This factor, combined with the slow time response of the pressure instrumentation, resulted in pressure profiles whose characteristics were a source of confusion. The PLIF test findings of the work reported herein—in particular, the effect of small changes in *JPR* on impingement surface pressures (i.e. staging)—helped to explain some of the otherwise puzzling results of the Box Model tests.

6.4 Unsteady Flows

This section will examine the effect of impingement on jet stability. As anticipated, these experiments have found that the presence of an impingement target modifies the transition process, often resulting in an earlier onset of transition. They also found that the transition process itself was sometimes modified, with different unsteady modes dominating when compared to free jet cases, or with new sources of instability being created. The description of unsteadiness will concentrate on the upstream jet flow and the impingement region, with little discussion of the wall jet region, for the reasons outlined below.

6.4.1 Comments on wall jet instabilities

There are very few cases where we can clearly, unambiguously identify a location where the wall jet flow exhibits fully developed turbulence. There are several probable reasons for this. First, the flow in the wall jet region is flowing radially, which has a pressure relieving effect due to the associated expansion of the flow. As the flow expands, vortical flow structures are stretched and thus damped. This is in contrast to the "crumpling" effect of flow contraction. While decelerations can be destabilizing, here the rate of jet diffusion and expansion may combine with the decrease in velocity to effect a decrease in the local Reynolds number of the flow. Second, neither the impingement target nor the field of view of the camera used in these experiments was designed to be large enough to investigate the downstream behavior of the wall jet. This is because that for vehicle damage scenarios, the primary region of interest is the region of peak impingement pressures and heat transfer. Third, the rate of jet fluid dispersion, diffusion,

204

and mixing is sometimes high enough so as to reduce the resulting fluorescence to levels too low to adequately visualize the flow in theses regions using the same camera settings. A few changes could be made if the far-field wall jet were of interest. However, the literature on transition in boundary layer flows is fairly extensive and the results of previous studies could likely be applied in this region. For the purposes of the present study, the wall jet far-field is of limited interest, as the heat transfer to the impingement surface is far lower in this region than in the impingement near-field.

6.4.2 Sources of Impinging Jet Instabilities

Impinging flows bear many similarities to their free jet counterparts in terms of unsteady behavior. For example, the sinuous and varicose instability modes are seen in impinging cases, and the triple point and flow diameter maxima are once again seen to serve as sources of instability. However, the presence of the impingement plate may amplify certain instability modes relative to the free jet cases. Figures 6.10-6.14 illustrate examples of the sinuous mode, varicose mode, nozzle lip instability, triple point instability, and flow maxima instability, respectively. Refer back to sections 5.4 and 5.5 for more details on each of these instability modes. The amplification seen in impinging cases may be due to feedback of pressure variations resulting from the impingement process though the subsonic regions of the flow or to the presence of new flow structures, described in more detail later in this section.
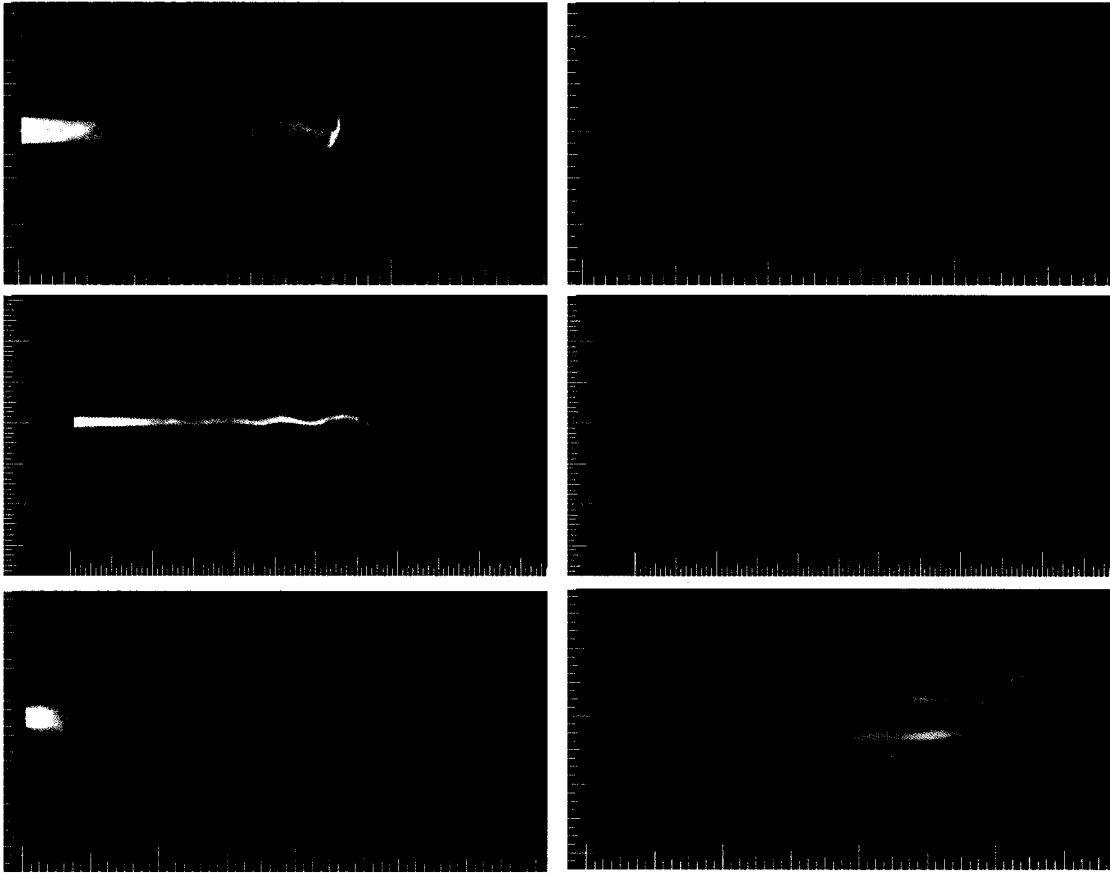
Figure 6.10:   Sinuous mode for three supersonic impinging cases: single-shot and standard deviation images. From top to bottom they are Run 379 ($JPR = 1$, $Re_{exit} = 7{,}553$, $\theta_{imp} = 90°$ and $D_{imp}/D_e = 11$), Run 644 ($JPR = 1$, $Re_{exit} = 7{,}251$, $\theta_{imp} = 45°$ and $D_{imp}/D_e = 23$), and Run 581 (supersonic, $JPR = 14.5$, $Re_{exit} = 12{,}361$, $\theta_{imp} = 90°$ and $D_{imp}/D_e = 23$). The smallest hash marks on the scales along the images are 1/16th in.

The presence of the impingement target can be seen to amplify the sinuous mode of instability in Fig. 6.10. The sinuous mode is identifiable by the sinusoidal displacement of the jet from the jet axis in single-shot PLIF images. The top two image pairs show the sinuous mode for flows with a low jet pressure ratio, for both normal and angled impingement cases. The third image pair shows this mode for a flow with a higher jet pressure ratio.

206
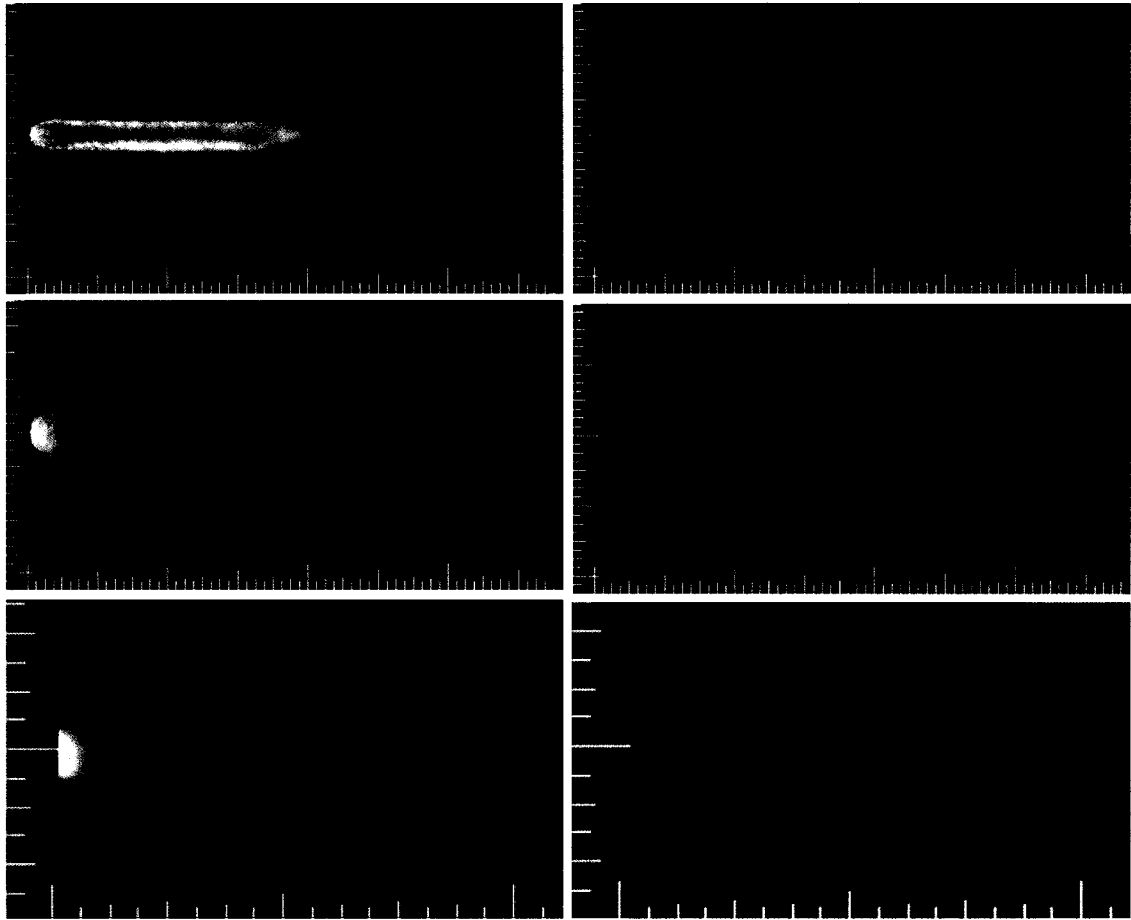
Figure 6.11: Varicose mode for three sonic impinging cases: single-shot and standard deviation images. From top to bottom they are Run 713 ($JPR = 6.1$, $Re_{exit} = 3{,}337$, $\theta_{imp} = 90°$ and $D_{imp}/D_e = 26.3$), Run 707 ($JPR = 27.4$, $Re_{exit} = 10{,}319$, $\theta_{imp} = 90°$ and $D_{imp}/D_e = 26.3$), and Run 765 ($JPR = 15.7$, $Re_{exit} = 12{,}334$, $\theta_{imp} = 90°$ and $D_{imp}/D_e = 10.5$). The smallest hash marks on the scales along the images are 1/16th in.

The varicose mode was also observed for some impinging jet cases. Three such cases can be seen in Fig. 6.11. The varicose mode is evidenced by displacement of the jet from the jet axis that is nearly symmetric across this axis. In the upper image pair, a ring of jet fluid can be seen as it pinches off from a flow with a moderate jet pressure ratio of 6.1. The middle image pair shows the varicose mode for the same impingement distance, but at a higher pressure ratio. The bottom image pair shows a case with a smaller

207

impingement distance, with apparent mushroom-like vortical structure. This mode was not seen in angled impingement cases, possibly because the symmetry of any pressure feedback mechanisms from the impingement target is broken in angled impingement geometries.
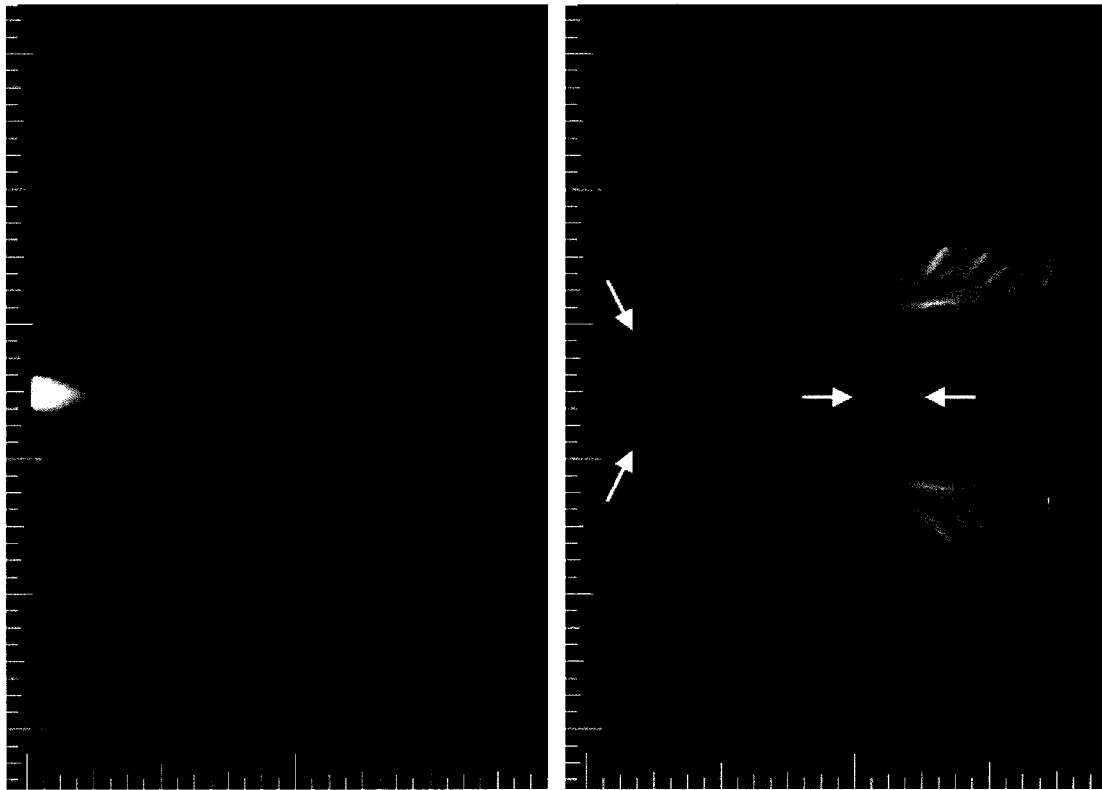
Figure 6.12: Instabilities in jet boundary around barrel shock, presumably stemming from the nozzle lip. Note also the fluctuations in Mach disk location indicated by the blurred region in the standard deviation image. (Run 365, supersonic, $JPR = 15.2$, $Re_{exit} = 12,352$, $D_{imp}/D_e = 11$). Smallest hash marks on scales are 1/16th in.

Instabilities can be seen to be originating from near the nozzle lip in Fig. 6.12. The standard deviation image indicates that the boundaries of the barrel shock structure are not stable, nor is the position of the Mach disk. It is also evident that the location of the

208

impingement of the high-velocity jet boundary is highly variable, and that the impingement process contributes to the breakup and diffusion of the jet.
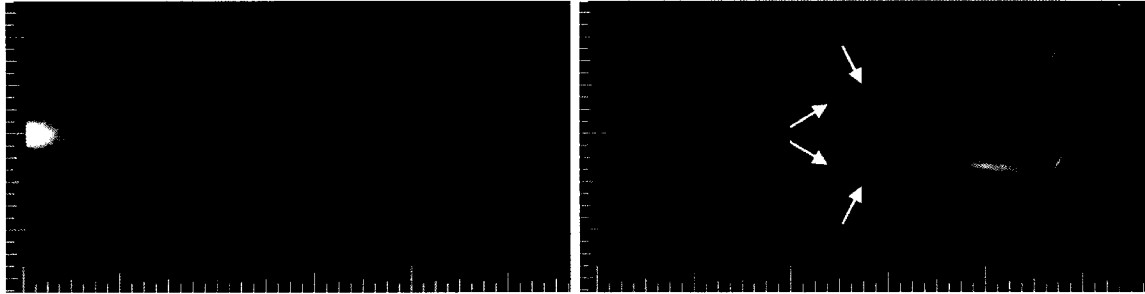
Figure 6.13: Triple point and intersection of reflected shock from triple point with jet boundary both act as sources of instability. This single-shot PLIF image and standard deviation image are for Run 552 (supersonic, JPR = 11.1, Re_{exit} = 7,300, θ_{imp} = 60° and D_{imp}/D_e = 15). The scales are in inches with the smallest hash marks measuring 1/16th in.

Shock intersections can be clearly seen to be locations of instability amplification in Fig. 6.13. Both the triple point and the intersection of the shock reflected from the triple point with the jet boundary are discernable in the standard deviation image. Although some instabilities are evident upstream of these points, the level of instability increases at these points. Also notice the difference in the effect of the impingement target on the impingement of the high-velocity jet boundary on the upper and lower parts of the jet. The lower impingement region appears to contribute to jet diffusion, whereas the upper region appears to turn the flow, with fluctuations persisting to the edge of the field of view.

Flow maxima may also serve as sources of flow instability for some supersonic impinging jet cases. In Fig. 6.14, the flow can be seen to be exhibiting instability starting near the second flow maximum in both the single-shot PLIF image and the standard

209

deviation image. The flow also has a small recirculation bubble. Instabilities persist in the wall jet region, as evidenced in the standard deviation image.
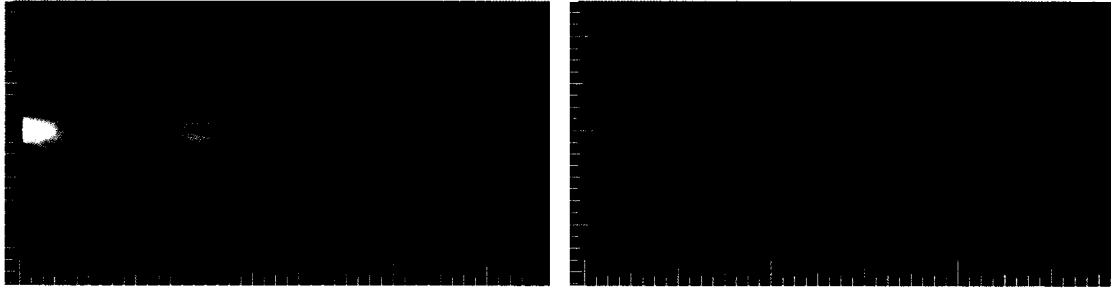
Figure 6.14: An example of an impinging flow where a flow maximum upstream of the impingement regions serves as a source of instabilities (Run 547, supersonic, $JPR = 3.4$, $Re_{exit} = 7,699$, $D_{imp}/D_e = 15$).

Two primary new flow structures are seen to be sources of instability in the impingement region. The first is the location of the intersection of the plate shock with the inner and outer shear layers that border the high-velocity jet boundary. Figure 6.15 shows an example of such a flow. The standard deviation image highlights this intersection, illustrating the growth of instabilities that stem from this point. In this image pair, no significant fluctuations are evident upstream of this intersection. The impingement of the jet boundary on the impingement plate also appears to promote the development of instabilities in the jet.

210
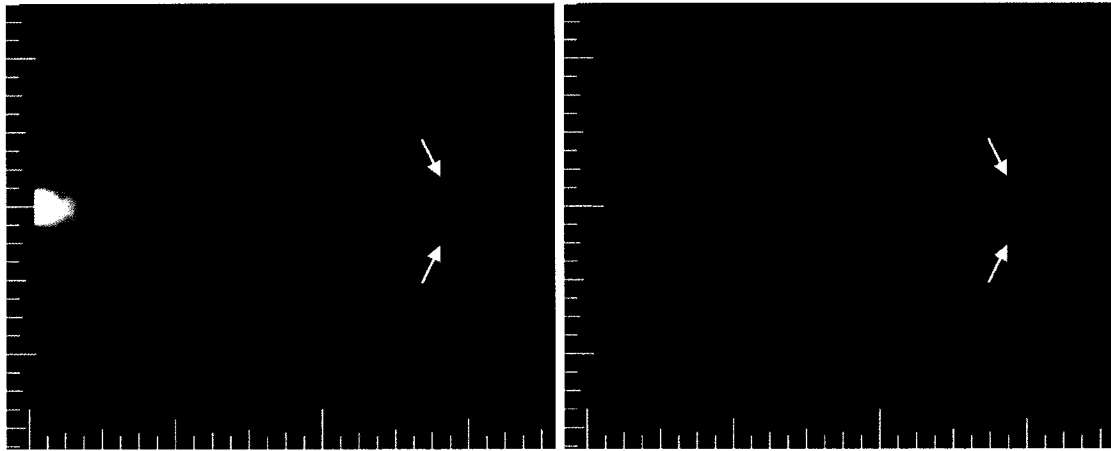
Figure 6.15: Intersection of plate shock and high-velocity jet boundary acts as a source of instability. This single-shot PLIF image and standard deviation image are for Run 370 (supersonic, $JPR = 3.0$, $Re_{exit} = 4,097$, $\theta_{imp} = 90°$ and $D_{imp}/D_e = 11$). The scales are in inches with the smallest hash marks measuring 1/16th in.

As illustrated above, if the flow is not already unsteady by the time it encounters the impingement target, the points at which the outer edges of the jet impinge on the target are likely to be a source of instabilities. If the flow is already unsteady, this impingement point is likely to increase the rate of development of these instabilities. Three examples are shown in Fig. 6.16. Sometimes this high velocity flow reflects off the surface, causing oscillations in the wall jet. The flow maxima associated with these oscillations may also serve as instability sources. Figure 6.17 shows one such example. Note the oscillations in the wall jet which can be seen in the standard deviation image.

211
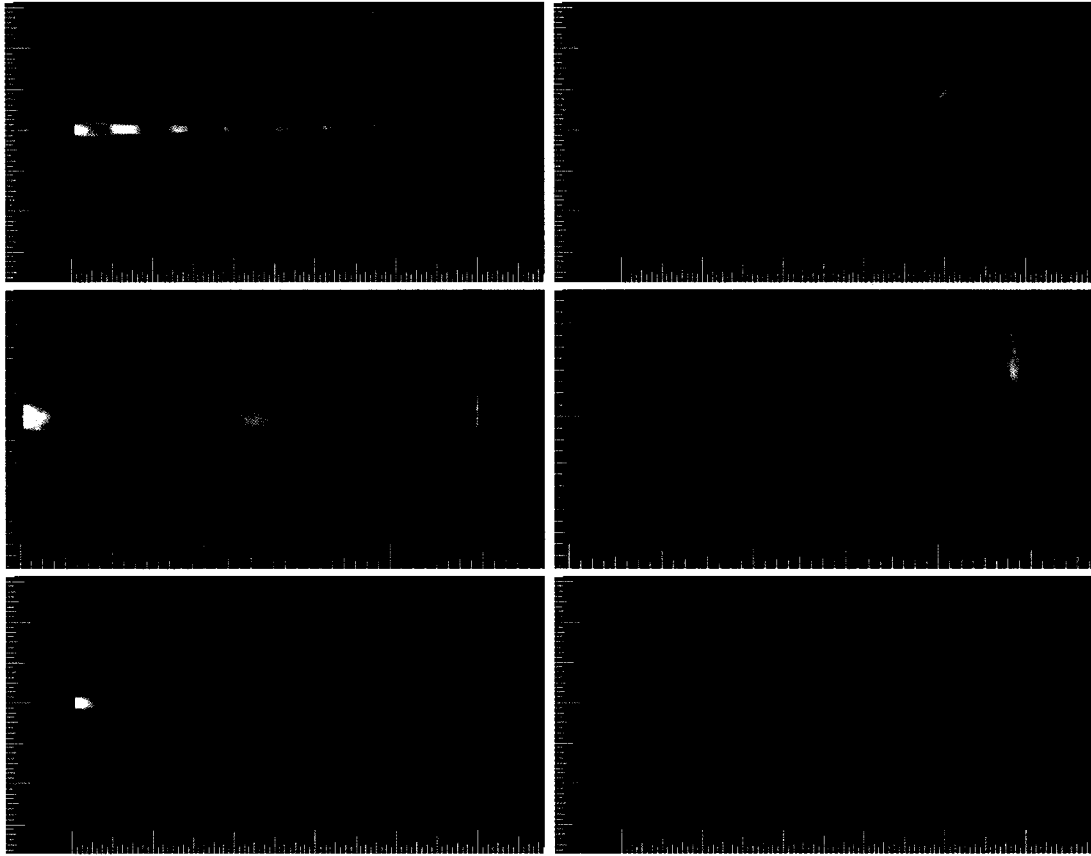
Figure 6.16: The impingement of the jet boundary is a source for instability amplification. These single-shot and standard deviation images are from three supersonic runs. From top to bottom they are Run 643 ($JPR = 1.8$, $Re_{exit} = 7{,}223$, $\theta_{imp} = 45°$ and $D_{imp}/D_e = 22.5$), Run 549 ($JPR = 1.7$, $Re_{exit} = 7{,}659$, $\theta_{imp} = 90°$ and $D_{imp}/D_e = 15.2$), and Run 631 ($JPR = 15.6$, $Re_{exit} = 11{,}656$, $\theta_{imp} = 45°$ and $D_{imp}/D_e = 22.5$). The smallest hash marks on the scales along the images are 1/16th in.
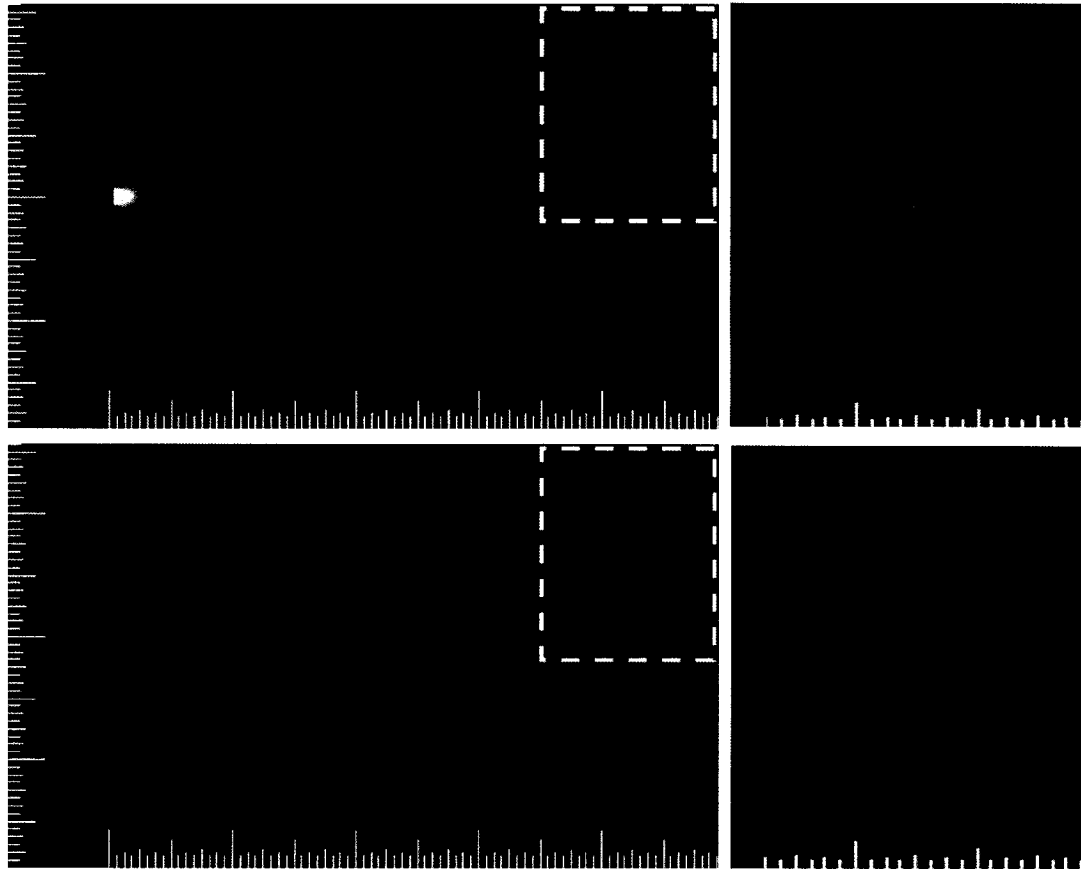
Figure 6.17: Flow maxima in wall jet compressions and expansions serves a sources of instability. Close-ups are shown of the regions indicated by white dashed boxes. This single-shot image and standard deviation image are from supersonic Run 641 (JPR = 3.6, Re_{exit} = 7,268, θ_{imp} = 45° and D_{imp}/D_e = 22.5). Scales are in inches, with smallest hash marks measuring 1/16th in.

6.4.3 Effect of impingement distance and angle

As explained above, the presence of the impingement target was found to sometimes promote the development of instabilities. In some cases, this meant that unsteadiness was observed to begin further upstream. In other cases, the impingement region was found to amplify existing instabilities or to generate new instabilities. For the 45° and 60° impingement configurations, the majority of the flow was found to be deflected through the oblique angle ("up" the plate in the arrangements as shown, where the top of the plate

213

is further away from the nozzle exit plane than the bottom of the plate), with little flow being deflected backward through the steeper acute angle ("down" the plate). In general, the normal (90°) configurations were found to be more perturbative than the oblique configurations. Figures 6.18 and 6.19 illustrate this. Seven normal impingement cases are presented in Fig. 6.18. Corresponding 60° cases at similar jet pressure ratios are presented in Fig. 6.19. The intensity in the standard deviation images can be seen to be greater for the normal impingement cases, indicating a stronger influence on jet flow transition. Note especially the differences in the instability modes that are evident in the oblique cases as compared to the normal impingement cases. At the higher jet pressure ratios, the jet boundary appears to flap around its mean position. By comparing the standard deviation images, it seems that the spatial extent of this flapping is greater in the normal cases than in the oblique cases, indicating a more perturbative effect in the normal cases. At intermediate jet pressure ratios (1.7 and 3.4), the growth of instabilities stemming from flow maxima can be seen for both normal and oblique cases. Finally, at the lowest jet pressure ratio (0.8), both normal and oblique cases exhibit sinuous mode behavior.
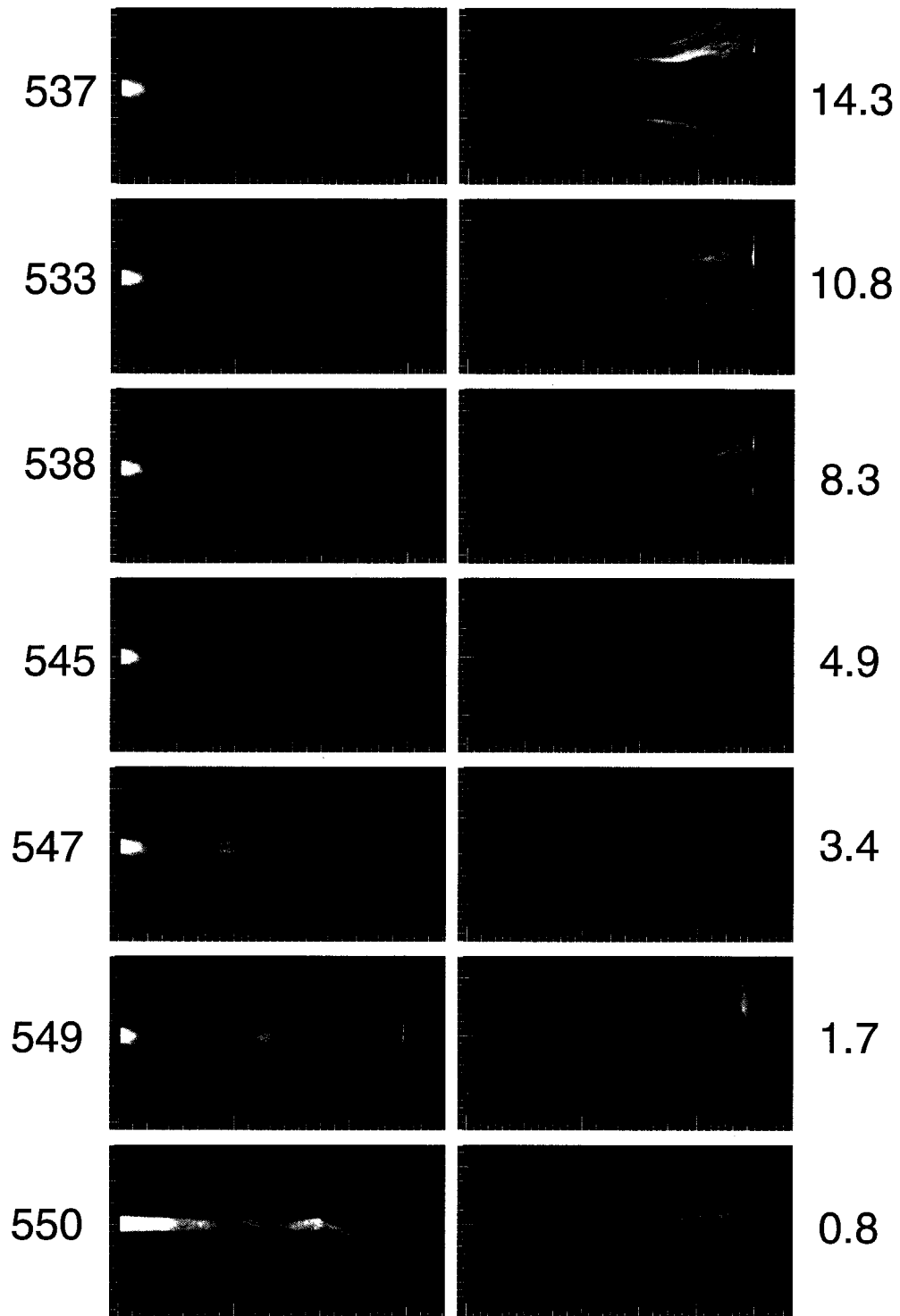
Figure 6.18: Effect of normal (90°) impingement for supersonic flows over a range of pressure ratios. The run number associated with each single-shot and standard deviation image is listed on the left of the images. The jet pressure ratios are indicated on the right. The exit Reynolds numbers are all approximately 7,500, with the exception of the first set of images at the highest *JPR*. For this run, Re_{exit} is 12,505. Scales are in inches, with smallest hash marks measuring 1/16th in.

215
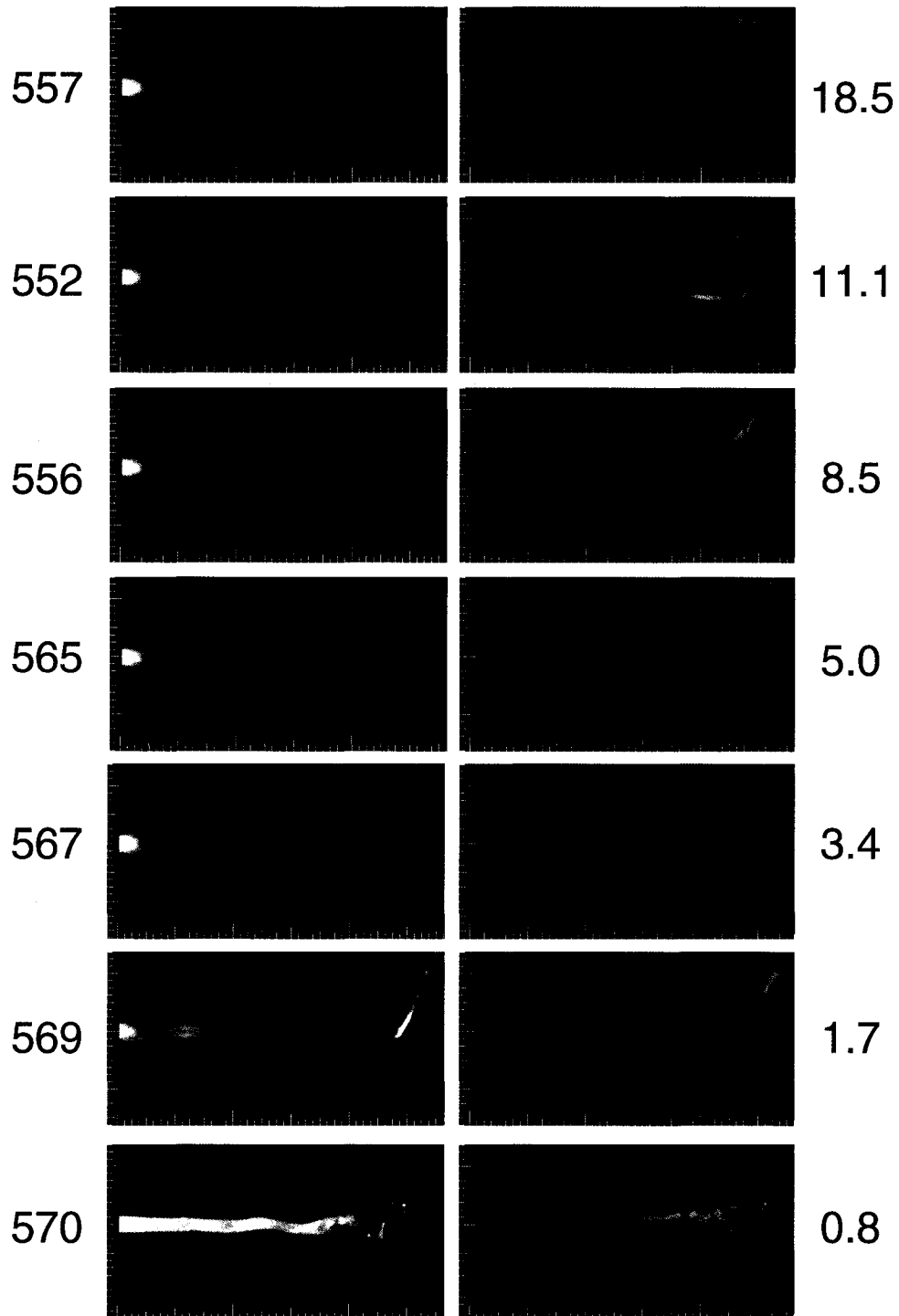
Figure 6.19: Effect of oblique (60°) impingement for supersonic flows over a range of pressure ratios. The run number associated with each single-shot and standard deviation image is listed on the left of the images. The jet pressure ratios are indicated on the right. The exit Reynolds numbers are all approximately 7,500, with the exception of the first set of images at the highest JPR. For this run, Re_{exit} is 14,975. Scales are in inches, with smallest hash marks measuring 1/16th in.

216

Figures 6.20 and 6.21 show the effect of different impingement configurations on two different nominal combinations of jet pressure ratio and exit Reynolds number. In Fig. 6.20, the free jet case is seen to become turbulent within the measurement region. The impingement target has little effect at the furthest impingement distance of 30.5 nozzle diameters (5 in.), but its effect is evident for smaller impingement distances. In Fig. 6.21, a case is shown where the free jet (i.e. no impingement target) remains steady within the measurement region. Here, the effect of the impingement target is even more evident. In general, it appears that the closer the impingement target, the further upstream that transition occurs. At the nearest impingement distance of 10.7 nozzle diameters (1.75 in.), instabilities are evident in the jet boundary surrounding the barrel shock soon after the nozzle exit. Note that flow maxima instabilities are evident for the lower jet pressure ratios, as presented in Fig. 6.20. The varicose mode also appears at the larger impingement distances for this jet pressure ratio. By contrast, the sinuous mode is seen for the majority of the runs at the higher jet pressure ratio, as presented in Fig. 6.21. Jet flapping is seen increasingly at the smaller impingement distances. Flow maxima instabilities are not seen for this higher jet pressure ratio, since the base flow does not have a spatially recurring structure.

217
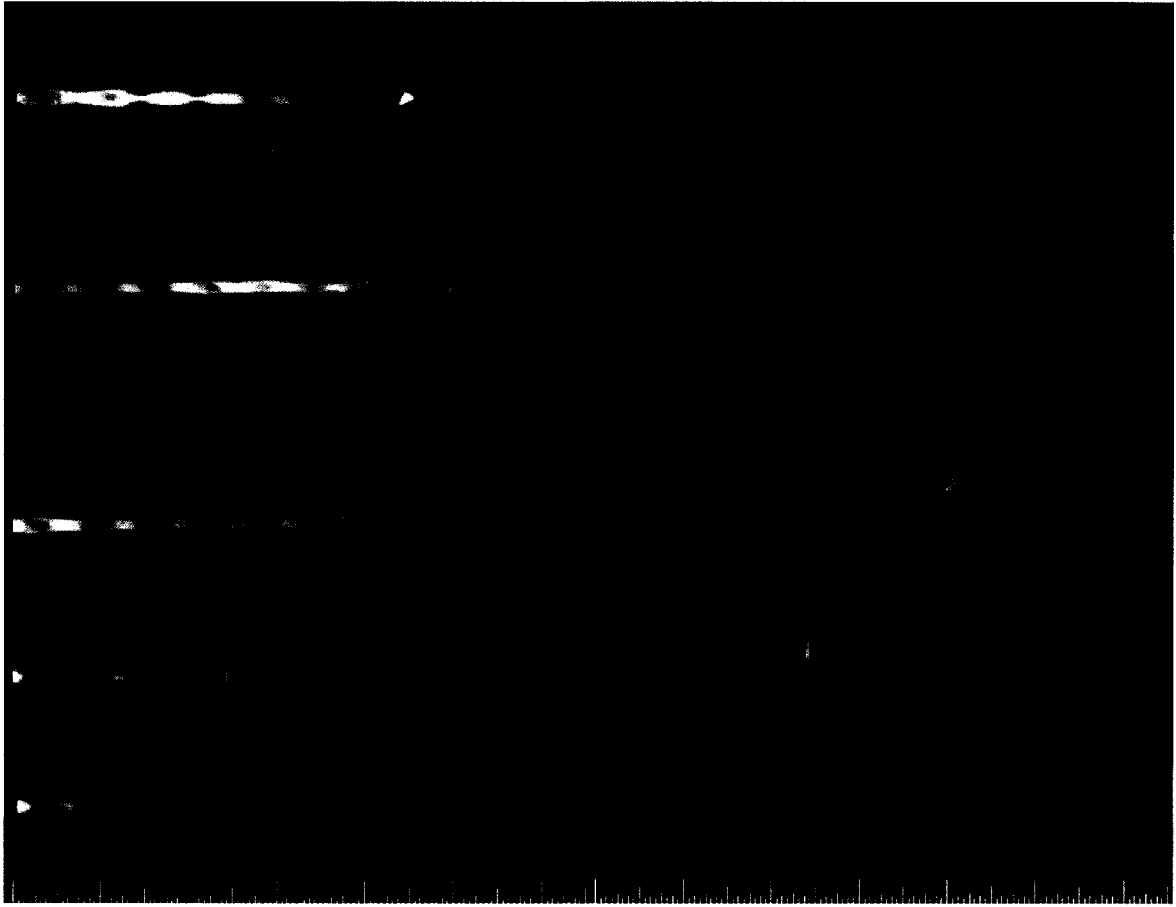
Figure 6.20: Effect of impingement for a moderately underexpanded supersonic jet with a jet pressure ratio of about 1.7 and exit Reynolds number of about 7,500. The run numbers associated with each single-shot and standard deviation image are, from top to bottom: 248, 619, 643, 549, and 380. The jet pressure ratios for these five cases are, from top to bottom: 2.0, 1.7, 1.8, 1.7, 1.6. The exit Reynolds numbers are, from top to bottom: 7,986; 7,332; 7,223; 7,659; 7,661. Scales are in inches, with smallest hash marks measuring 1/16th in.

218
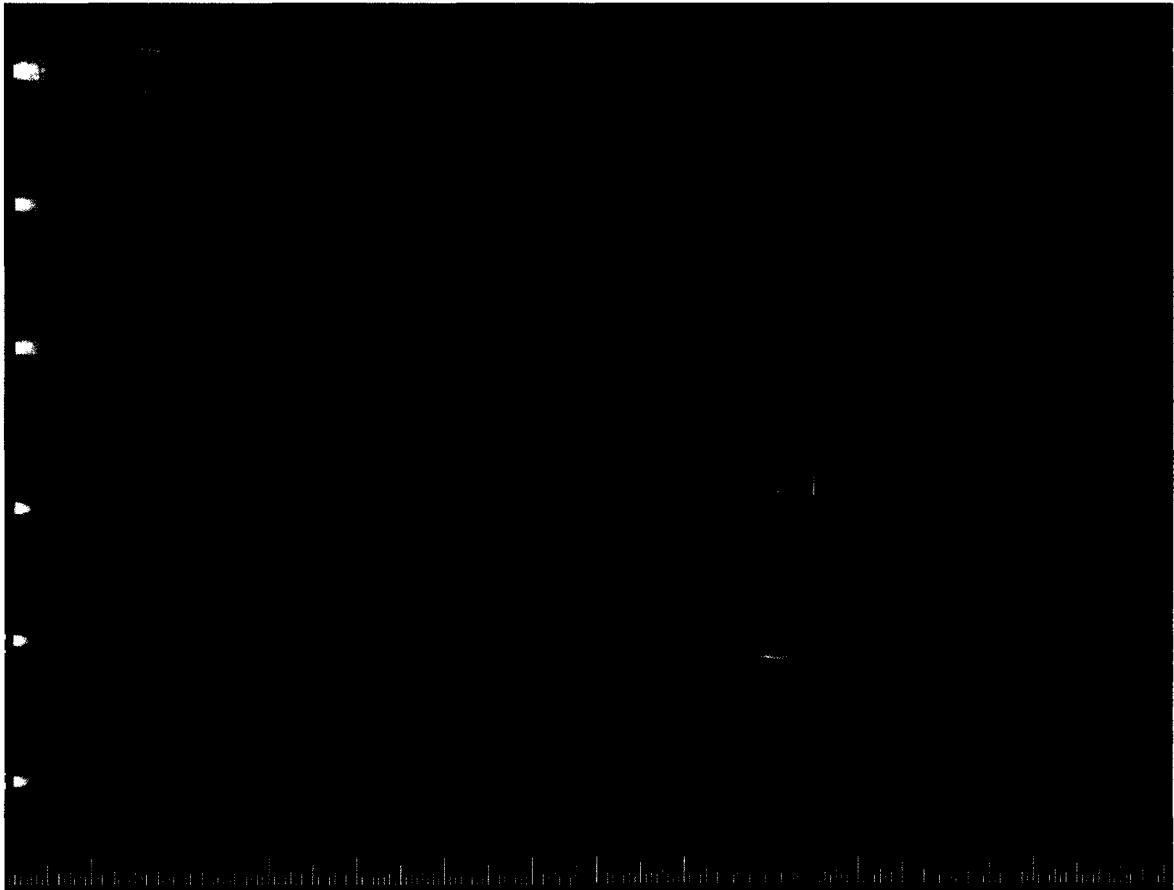
Figure 6.21: Effect of impingement for a highly underexpanded supersonic jet with a jet pressure ratio of about 11 and exit Reynolds number of about 7,500. The run numbers associated with each single-shot and standard deviation image are, from top to bottom: 229, 602, 577, 533, 552, and 366. The jet pressure ratios for these six cases are, from top to bottom: 10.5, 11.1, 11.2, 10.8, 11.1, 9.2. The exit Reynolds numbers are, from top to bottom: 8,091; 7,226; 7,437; 7,545; 7,300; 7,547. Scales are in inches, with smallest hash marks measuring 1/16th in.

6.4.4 Effect on distance to unsteadiness, transition, and turbulence

In section 5.5.1, results indicating measured distances to various stages of transition were presented for sonic and supersonic free jets. Similar measurements were made for impinging jet cases. In addition to x_{steady}, $x_{unsteady}$, $x_{fully\ trans}$, and $x_{fully\ turb}$, distances along the impingement target were recorded as well. Because the flow becomes a wall jet after impingement, these distances were called $x_{wall\ unsteady}$, $x_{wall\ fully\ trans}$, and $x_{wall\ fully\ turb}$

219

("steady" distances were not recorded for the wall jet; if the flow remained steady and laminar within the field of view in an impinging case, the impingement distance was recorded for x_{steady}). These distances along the impingement target were measured from the intersection of the jet centerline with the target. Before plotting the measured points, the distance along the plate was added to the impingement distance, to indicate the total distance the jet had traveled to get to the location where, for instance, it became fully transitional. Results for sonic normal impingement are shown in Fig. 6.21.
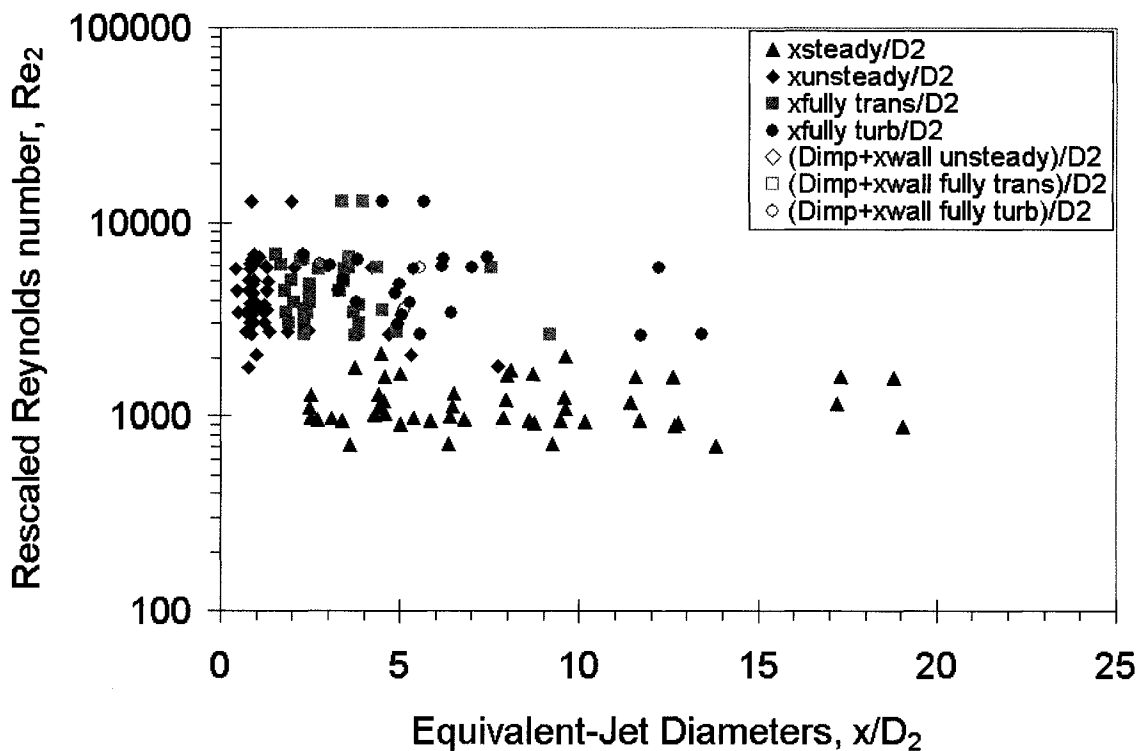
Figure 6.21: Distances to unsteady jet behavior for impinging sonic jet cases at a normal (90°) impingement angle, in equivalent-jet diameters. Open symbols indicate locations along the face of the impingement plate.

Impinging sonic jet runs with rescaled Reynolds numbers below about 1,700 were observed to remain laminar. When compared to free jet cases (see Fig. 5.16), unsteady, transitional, and turbulent distances were seen to occur sooner, i.e., closer to the nozzle

exit. For the pressure ratios and impingement distances studied in these experiments, the majority of the impinging sonic jet cases that did become unsteady, transitional, or turbulent were observed to do so prior to the impingement target (as evidenced by the paucity of open symbols in Fig. 6.21). The clustering of unsteady points near an equivalent-jet diameter of about 1 is largely associated with the triple point instability mode.

Results for similar measurements in supersonic normal impingement cases are shown in Fig. 6.21. With the exception of two runs, flows with a rescaled Reynolds number of less than about 1,700 were observed to remain steady and laminar, as in the sonic results shown above. These two runs both had recirculation bubbles that exhibited unsteadiness and appeared to be close to a staging behavior transition.
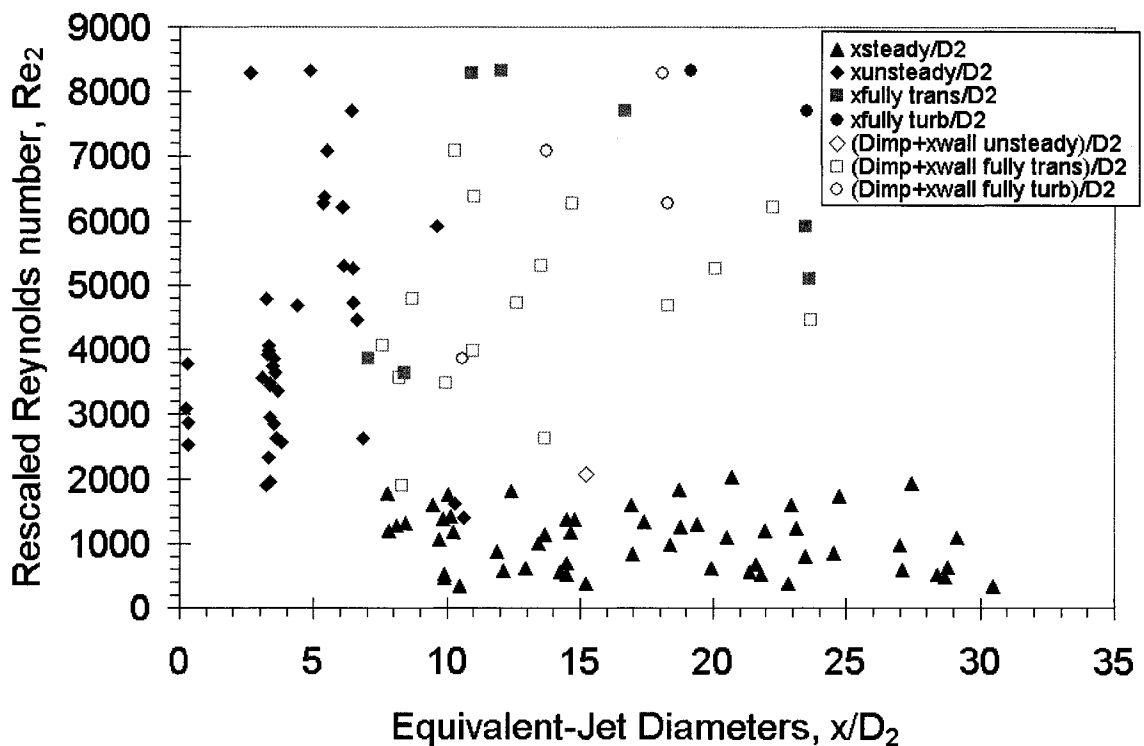
Figure 6.22: Distances to unsteady jet behavior for impinging supersonic jet cases at a normal (90°) impingement angle, in equivalent-jet diameters. Open symbols indicate locations along the face of the impingement plate.

221

Two clusterings are evident in the unsteady symbols. The first is for equivalent-jet diameters of less than 1; the second is between 3 and 4 diameters. These correspond to nozzle lip and triple point instabilities, respectively. Upon further consideration, it may be that the relevant length scale needs to be redefined for flows beyond the impingement reason. Flow structures play a key role in the development of flow instabilities upstream of the impingement target, and so a length scale based on the jet diameter is appropriate in the free jet region. After impingement, however, the flow becomes a wall jet. Since this is essentially flow over a flat plate for a diverging flow, the physical distance along the plate may be a more suitable length scale. Figure 6.23 is a graph of the same data set presented in Fig. 6.22, plotted in terms of downstream distance, in nozzle diameters.
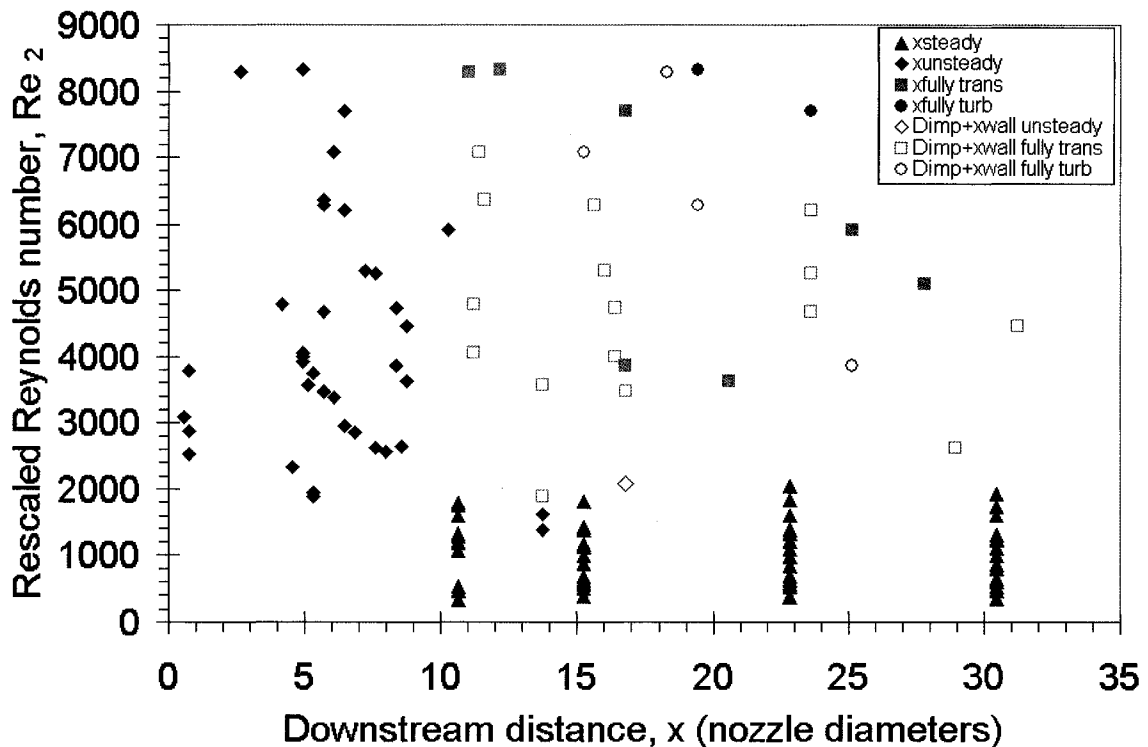
Figure 6.23: Distances to unsteady jet behavior for impinging supersonic jet cases at a normal (90°) impingement angle, in nozzle diameters (one nozzle diameter is 0.164 in., or 4.17 mm). Open symbols indicate locations along the face of the impingement plate.

The steady distances are now clustered according to the four impingement distances for supersonic normal impingement cases. Trends are also now evident for those runs in which the flow became fully transitional after impingement. These distances tend to fall just downstream of the impingement location, indicating that the impingement location itself (or, more precisely, the location of the impingement of the jet boundary, which is slightly downstream of the impingement of the jet centerline) was the location of the onset of transition.

6.5 Summary

PLIF images have been used to visualize free and impinging underexpanded jet flows. They have provided detailed information about flow structures and have allowed determination of the laminar, unsteady, or turbulent state of the flow. The insights into flow structure characteristics provided by PLIF images have helped to elucidate the results of pressure measurements taken at the surface of a flat impingement target and have shed light on the features of the pressure distributions across the face of the disk. Under certain conditions, the shape of these pressure distributions was seen to be a very sensitive function of jet pressure ratio, leading to the phenomenon called staging; under other conditions, the dependence was rather insensitive to *JPR*. In all cases, the absolute magnitude of the measured pressures was seen to be a linear function of plenum pressure, and therefore, of Reynolds number. The details of the flow structures associated with the impingement region have been shown to play a role in the process of transition to turbulence. Finally, the presence of the impingement target has been shown to amplify existing instabilities as well as introduce new instability modes.

223

CHAPTER 7

Conclusion

7.1 Summary of Major Results

Planar laser-induced fluorescence of nitric oxide has been successfully applied to the study of free and impinging supersonic jets, their flow structures, and the process of transition to turbulence. In the case of steady flows, PLIF images were used to measure the size and location of flow structures, including Mach disks and jet primary wavelengths. These measurements were compared to empirical relations from previous studies (Love et al. 1959) for both sonic (exit Mach number of 1) and supersonic (exit Mach number of 2.6) nozzle flows. Additionally, computational flow imaging was performed on three laminar steady cases, generating theoretical PLIF images from the results of computational fluid dynamics simulations performed by other researchers at NASA Langley. These CFI images were compared to measured PLIF images at similar flow conditions and relatively good agreement was found, with the major discrepancies attributable to approximations and simplifications in the CFI calculations.

224

For unsteady flows, an image-processing technique was used to highlight flow instabilities by mapping the shot-to-shot percentage standard deviation in fluorescence intensity. These maps were used to quantitatively identify unsteady, transitional, and turbulent jet behavior. For sonic nozzle flows, correlations were found between a Reynolds number (referred to as the *rescaled Reynolds number*) based on an equivalent-jet diameter and the number of these equivalent-jet diameters downstream at which a flow became unsteady, transitional, or turbulent. Separate correlations were found for jet pressure ratios of greater than and less than 2, a division corresponding to sonic flows with and without a Mach disk, respectively.

For supersonic nozzle flows, it was found that flows for which this rescaled Reynolds number was less than about 2,000 remained laminar and steady. All flows above this rescaled Reynolds number were found to become unsteady, in some cases transitioning to turbulent. A correlation was found between the rescaled Reynolds number and the distance to the onset of transition. Unsteady behavior was found to fall into groups based on whether the flows did have Mach disks (*JPR*s > 3.5) or had oscillating flow structures with no Mach disk (*JPR*s < 3.5). These findings are being used by researchers at Boeing to help guide their computational approach to modeling underexpanded jet flows at conditions relevant to flight conditions of interest and/or specific damage scenarios. These studies inform whether repairs to the Shuttle Orbiter will be made.

Several normal modes of instability were observed. These included the sinuous and varicose axial modes, as well as cosine azimuthal modes. Standard deviation maps have also helped to identify the flow features associated with the development of instabilities

225

in these jet flows. Regions characterized by gradients in velocity—which therefore also contain vorticity—were found to be instrumental in the creation and amplification of flow instabilities. These included shock intersections (e.g. the triple point, the reflected shock/jet boundary intersection, and the plate shock/jet boundary intersection in impinging cases), shear layers (the outer shear layer along the jet boundary and the inner shear layer along the slip line emanating from the triple point), and locations of local jet diameter maxima in flows with oscillating flow structures. For impinging cases, the presence of the impingement target was found to promote the development of instabilities in the flow.

PLIF images have also been used to show the connection between flow structures and specific features (e.g. peaks, valleys, and plateaus) in surface pressure measurements. In addition, the results of these PLIF tests have helped to elucidate the otherwise confounding results of the Nowak Box Model tests (described in Chapter 6). These results have done this primarily by identifying the jet staging behavior responsible for extreme sensitivity of pressure profiles to small changes in jet pressure ratio.

Volume imaging has been successfully demonstrated as an additional means of extracting flow visualization information from regions of the flow other than the flow centerline. In particular, the technique has been shown to effectively highlight departures from axisymmetric behavior. Volume imaging will also be useful in future experiments where limited optical access prevents imaging in the desired measurement plane.

226

7.2 Recommendations for Future Work

Many improvements to the measurement system are suggested, and several have been incorporated since the completion of these tests. We have replaced the hand-pressed camera trigger with an automated camera "trigger" signal read into the data system, enabling better correlation between individual PLIF images and the data acquired by the data acquisition system. We have improved our technique for characterizing the magnification and spatial resolution of our imaging system by using a two dimensional dotcard in place of a scale. From the image of this dotcard (a rectangular sheet with evenly spaced square dots in both directions), we can account for perspective effects and distortion due to the camera lens. (This means of determining spatial resolution was used for Runs 200-778, whereas the scale method was used for the first 199 runs. Image dewarping was not deemed to be necessary, as the dotcard images showed negligible perspective or lens distortion.)

Future experiments investigating underexpanded jets structure and transition characteristics would benefit from being conducted in a facility capable of achieving lower chamber pressures than those that were attainable in these tests (about 1 Torr, 0.02 psi, 0.0013 atm). It would also be preferable to have a test section in which the chamber pressure could be controlled more precisely, resulting in greater repeatability and more precise attainment of target test conditions. Temperature control of the model would have made possible the attainment of desired Reynolds number conditions with greater accuracy.

227

For computational flow imaging, the effects of both quenching by oxygen and Doppler broadening should be taken into account to draw more accurate comparisons between theory and experiment. Additionally, the combined contributions of Gaussian inhomogeneous Doppler broadening and Lorentzian homogeneous pressure broadening should properly be modeled as a Voigt function, rather than being approximated as Gaussian.

The image processing technique used in these tests could be improved by incorporating a separate laser profiling system, in which a second camera images the spatial profile of the beam for every laser pulse. This will be especially important in applications where a convenient freestream region away from the main region of interest is not present for the purpose laser-sheet corrections. In the present experiments, some of the left-to-right variations in fluorescence intensity were found to be due to left-to-right *spectral* variations in the laser sheet profile, rather than true *spatial* variations in laser sheet intensity, and the resulting decrease in the spectral overlap integral between the laser and the absorption profiles. This variation could be rotated by 90° so that it occurs across the thickness of the laser sheet, rather than across its width, by the insertion of an additional turning prism at the outlet of the WEX (wavelength extender). Fluorescence from the near and far surfaces of the laser sheet would be somewhat reduced due to being spectrally shifted away from the central absorption frequency. This would have the added benefit of slightly improving the out-of-plane spatial resolution of the technique by effectively reducing the thickness of the laser sheet.

Additional challenges remain in extending the quantitative measurement capabilities of the PLIF technique for hypersonic flow facilities. As-yet unexplained errors in the

228

velocimetry technique need to be explored and mitigated. In order to do this, details about the operation of the intensified CCD as well as its interaction with the laser and timing hardware need to be investigated further. This will also become important in making pressure- and density-sensitive imaging quantitative. Background images will need to be acquired under more precise conditions (for instance, a 100-shot accumulation by the intensified CCD is not quite equivalent to the sum of 100 single-shots acquired with otherwise identical camera settings). Finally, improvements in the laser system, such as new doubling and mixing crystals in the wavelength extender and perhaps improvements to the tracking photodiodes and feedback electronics, should be explored in order to increase the output laser energy.

229

APPENDIX A

Additional Notes on Nitric Oxide Spectroscopy

The following two figures provide additional details about the $A^2\Sigma^+ \leftarrow X^2\Pi_\Omega(0,0)$ transitions in nitric oxide and the resulting excitation spectrum. A schematic energy level diagram is presented in Fig. A.1. For the arbitrary choice of $N'' = 3$ for the rotational quantum number, this diagram shows the allowed transitions, labeled using the $\Delta N_{\alpha\beta}$ notation. An NO excitation spectrum, calculated using LIFBASE spectral simulation software (Luque and Crosley 1999), is presented in Fig. A.2 with the various bands plotted in different colors.

230
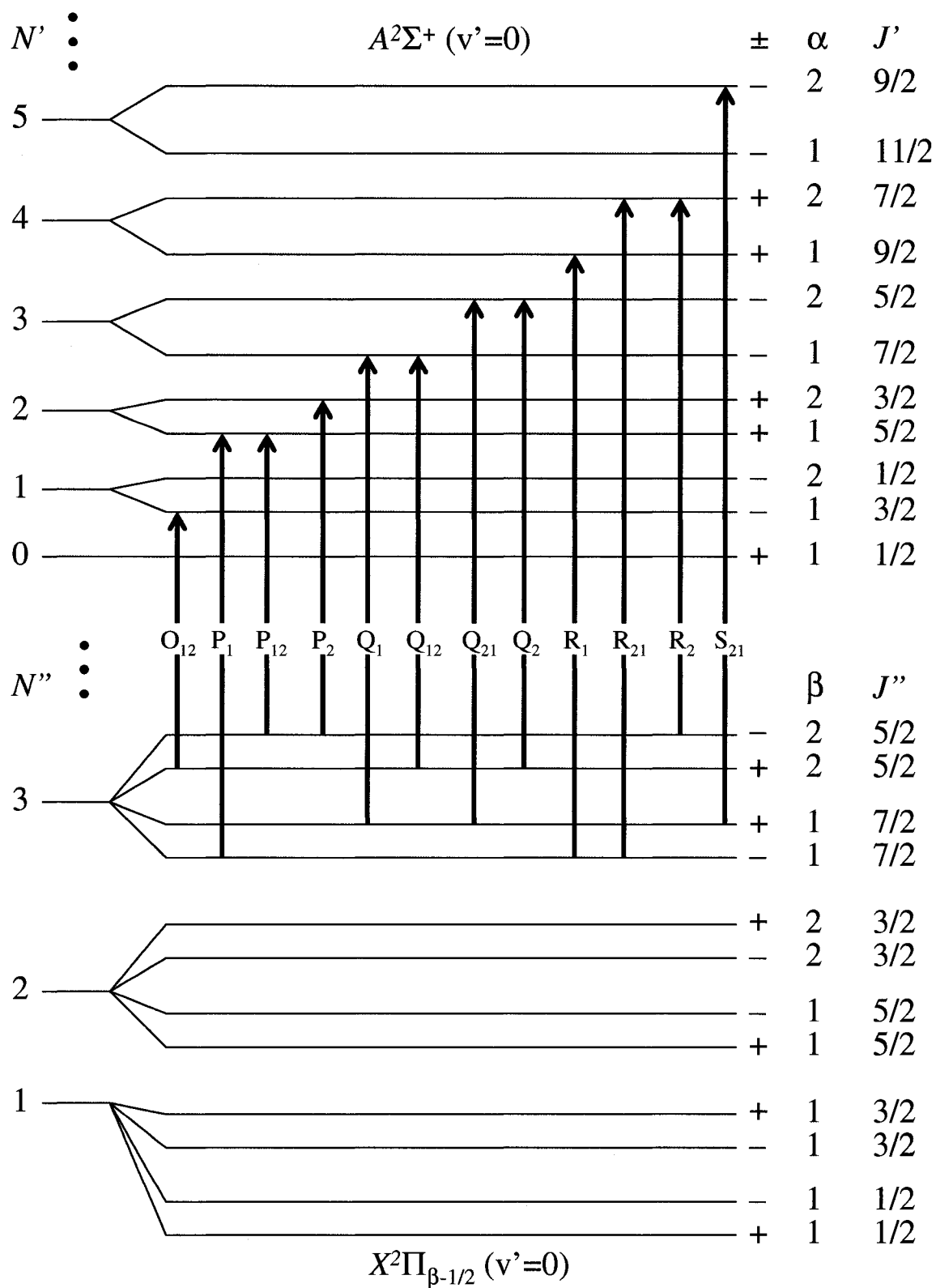
Figure A.1: Energy level diagram for the $A^2\Sigma^+ \leftarrow X^2\Pi_\Omega(0,0)$ transitions in nitric oxide (after Palma 1999 and DiRosa 1996). Energy level separations are not to scale.

231

Calculated Nitric Oxide UV Excitation Spectrum
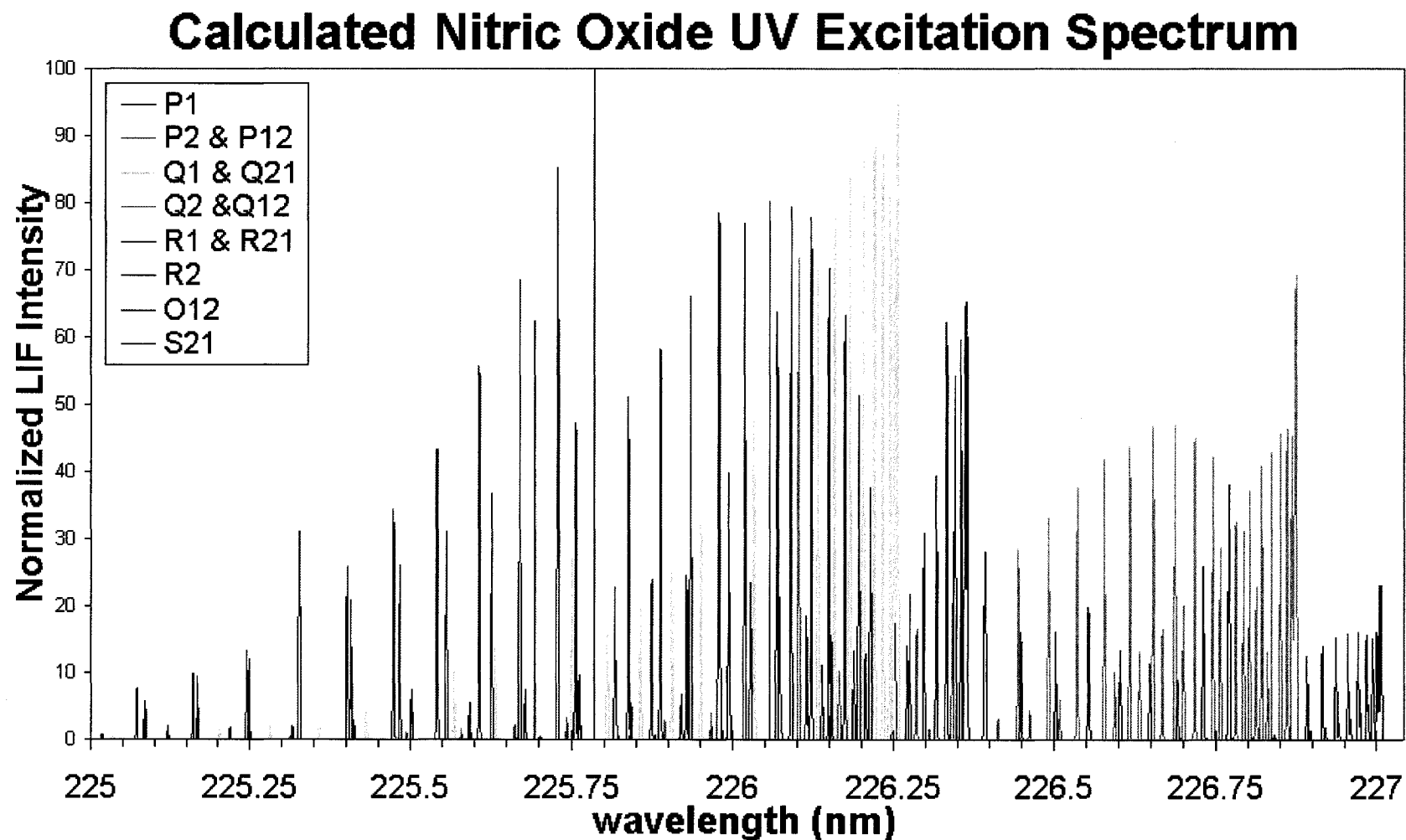
Figure A.2: Calculated excitation spectrum for nitric oxide. Individual bands are indicated by different colors. Spectrum was calculated using LIFBASE spectral simulation software (Luque and Crosley 1999). Wavelengths are vacuum wavelengths. Calculations were performed at a temperature of 300 K.

APPENDIX B

List of Run Parameters

The following table contains a limited list of some of the parameters associated with each run of the experiments described in this work. The columns of this table contain the following data:

1) jet pressure ratio (*JPR*); see section 4.2.4.

2) Reynolds number based on nozzle exit conditions (Re_{exit}); see section 4.2.4.

3) type of nozzle

   - sonic, with an exit Mach number of 1 and an exit diameter of 2.41 mm (0.095 in.); see section 4.2.1.

   - supersonic, with an exit Mach number of 2.6 and an exit diameter of 4.17 mm (0.164 in.); see section 4.2.2.

4) type of data

   - D = density-sensitive imaging; see section 3.4.2.2.

   - C = system checkout run (limited or no data)

   - FV = flow visualization; see section 3.4.1.

   - P = pressure-sensitive imaging; see section 3.4.2.1.

- pitot = run with pitot pressure probe (results not presented herein)

- SS = spatial scan; see section 5.2.1.3.

- TD = technique development run (results not presented herein)

- V = velocity-sensitive imaging; see section 3.5.

5) plenum temperature (T_0); see Eq. 4.9.

6) plenum pressure (p_0); see Eq. 4.11.

7) ambient (chamber) pressure (p_a)

8) Reynolds number based on rescaled jet diameter (Re_2); see Eq. 5.6.

9) rescaled jet diameter (D_2); see Eq. 5.4.

B.1 Run Numbers and Flow Data

Run #	JPR	Re_{exit}	type of nozzle	Type of Data	T_0 (K)	p_0 (kPa)	p_a (Pa)	Re_2	D_2 (mm)
1	3.8	281	sonic	FV	485	1.39	191	255	3.3
2	2.1	174	sonic	FV	491	0.87	217	177	2.7
3	4.5	371	sonic	FV	499	1.90	225	324	3.5
4	3.9	419	sonic	FV	504	2.17	297	380	3.3
5	1.9	417	sonic	FV	508	2.18	600	428	2.6
6	2.0	289	sonic	FV	508	1.51	400	295	2.7
7	16.2	694	sonic	FV	532	3.83	125	374	6.0
8	15.7	849	sonic	FV	530	4.66	157	464	5.9
9	15.8	1,504	sonic	FV	548	8.59	287	820	6.0
10	8.2	843	sonic	FV	536	4.69	301	599	4.4
11	16.8	1,076	sonic	FV	559	6.29	198	572	6.1
12	3.8	832	sonic	FV	544	4.71	658	758	3.3
13	8.3	1,486	sonic	FV	560	8.70	556	1,054	4.4
14	14.3	840	sonic	FV	536	4.68	172	477	5.7
15	15.2	1,482	sonic	FV	554	8.56	298	822	5.8
16	3.8	834	sonic	FV	544	4.72	650	757	3.3
17	4.1	1,465	sonic	FV	559	8.56	1101	1,306	3.4
18	2.1	1,465	sonic	FV	558	8.54	2129	1,488	2.7

234

Run #	JPR	Re_{exit}	type of nozzle	Type of Data	T_0 (K)	p_0 (kPa)	p_a (Pa)	Re_2	D_2 (mm)
19	35.4	1,493	sonic	P	540	8.39	125	566	8.7
20	15.5	1,530	sonic	P	543	8.65	295	842	5.9
21	3.8	851	sonic	P	531	4.69	647	774	3.3
22	4.2	1,509	sonic	P	549	8.63	1094	1,340	3.4
23	2.1	1,510	sonic	P	549	8.64	2140	1,533	2.7
24	2.1	1,507	sonic	P	549	8.62	2142	1,531	2.7
25	15.5	1,506	sonic	P	550	8.63	294	827	5.9
26	37.6	1,521	sonic	FV	550	8.72	122	560	9.0
27	4.3	1,514	sonic	FV	553	8.73	1078	1,335	3.4
28	2.1	1,494	sonic	FV	553	8.61	2143	1,517	2.7
29	16.1	3,645	sonic	FV	532	20.08	658	1,970	6.0
30	22.5	4,342	sonic	FV	526	23.62	554	2,023	7.0
31	8.7	4,407	sonic	FV	528	24.10	1470	3,070	4.5
32	3.9	4,386	sonic	FV	527	23.90	3201	3,953	3.3
33	4.0	3,674	sonic	FV	529	20.13	2640	3,293	3.3
34	15.7	6,496	sonic	FV	519	34.77	1171	3,553	5.9
35	16.3	4,361	sonic	FV	526	23.71	771	2,349	6.0
36	21.9	6,457	sonic	FV	516	34.37	829	3,048	6.9
37	21.8	8,564	sonic	FV	508	44.72	1082	4,047	6.9
38	15.9	5,432	sonic	FV	521	29.26	971	2,951	6.0
39	35.9	6,570	sonic	FV	512	34.62	509	2,470	8.8
40	35.5	8,785	sonic	FV	503	45.39	675	3,320	8.7
41	22.5	5,420	sonic	FV	512	28.59	672	2,528	7.0
42	35.3	7,725	sonic	FV	502	39.84	595	2,926	8.7
43	8.5	3,624	sonic	FV	518	19.38	1210	2,547	4.5
44	1.7	2,219	sonic	FV	528	12.15	3721	2,293	2.6
45	2.0	2,566	sonic	FV	531	14.13	3727	2,623	2.7
46	3.9	2,593	sonic	FV	534	14.37	1966	2,350	3.3
47	16.1	7,763	sonic	FV	501	39.94	1310	4,197	6.0
48	8.3	2,597	sonic	FV	530	14.26	904	1,836	4.5
49	15.8	2,600	sonic	FV	534	14.40	482	1,419	5.9
50	5.4	21,719	sonic	FV	449	98.11	9631	17,882	3.7
51	27.2	9,006	sonic	FV	487	44.79	870	3,853	7.7
52	36.0	5,491	sonic	FV	506	28.56	419	2,061	8.8
53	28.3	5,407	sonic	FV	517	28.81	537	2,270	7.8
54	35.1	9,867	sonic	FV	499	50.50	759	3,748	8.7
55	37.4	4,321	sonic	FV	529	23.70	335	1,594	9.0
56	29.1	4,294	sonic	FV	534	23.78	432	1,782	7.9
57	28.5	6,464	sonic	FV	523	34.94	647	2,705	7.9

235

Run #	JPR	Re_{exit}	type of nozzle	Type of Data	T_0 (K)	p_0 (kPa)	p_a (Pa)	Re_2	D_2 (mm)
58	21.9	2,661	sonic	FV	503	13.75	331	1,256	6.9
59	28.4	2,699	sonic	FV	508	14.09	262	1,132	7.8
60	16.3	2,685	sonic	FV	513	14.21	459	1,443	6.0
61	15.6	2,473	sonic	V	532	13.65	462	1,356	5.9
62	15.6	2,464	sonic	V	534	13.65	461	1,349	5.9
63	15.6	2,468	sonic	V	535	13.69	463	1,352	5.9
64	15.6	2,467	sonic	V	535	13.68	463	1,351	5.9
65	15.6	2,463	sonic	V	535	13.66	464	1,352	5.9
66	15.5	2,461	sonic	V	535	13.65	466	1,353	5.9
67	13.0	2,820	sonic	V	404	11.28	460	1,672	5.4
68	12.5	2,725	sonic	V	412	11.14	471	1,640	5.3
69	12.8	2,685	sonic	V	419	11.19	461	1,600	5.4
70	12.9	2,645	sonic	V	427	11.28	463	1,572	5.4
71	7.5	35,101	sonic	FV	395	136.54	9578	25,761	4.3
72	3.5	9,200	sonic	FV	452	41.95	6362	8,555	3.2
73	7.8	8,067	sonic	FV	468	38.32	2597	5,846	4.3
74	1.8	2,041	sonic	FV	508	10.67	3172	2,105	2.6
75	2.1	1,533	sonic	FV	531	8.43	2134	1,560	2.7
76	3.8	829	sonic	FV	542	4.68	648	754	3.3
77	21.9	939	sonic	FV	563	5.53	133	443	6.9
78	27.6	1,116	sonic	FV	590	6.95	133	474	7.7
79	1.9	844	sonic	FV	534	4.68	1282	866	2.6
80	3.8	827	sonic	FV	544	4.68	656	754	3.3
81	8.3	1,471	sonic	FV	561	8.63	550	1,042	4.5
82	4.3	1,459	sonic	FV	566	8.66	1062	1,284	3.4
83	15.4	1,427	sonic	FV	576	8.63	296	786	5.9
84	8.5	794	sonic	FV	561	4.66	289	557	4.5
85	16.3	1,025	sonic	FV	585	6.32	205	552	6.0
86	21.7	2,275	sonic	FV	579	13.86	338	1,079	6.9
87	15.6	2,237	sonic	FV	587	13.83	470	1,227	5.9
88	28.3	2,254	sonic	FV	587	13.95	261	947	7.8
89	35.0	2,247	sonic	FV	588	13.94	210	855	8.7
90	32.3	10,080	sonic	FV	459	46.76	765	3,983	8.3
91	26.0	8,999	sonic	FV	467	42.57	864	3,927	7.5
92	21.1	6,803	sonic	FV	472	32.62	816	3,264	6.8
93	33.6	7,869	sonic	FV	473	37.87	596	3,053	8.5
94	22.3	4,606	sonic	FV	488	22.98	545	2,157	7.0
95	28.5	4,591	sonic	FV	496	23.34	432	1,921	7.9
96	35.2	5,542	sonic	FV	496	28.18	423	2,103	8.7

236

Run #	JPR	Re_{exit}	type of nozzle	Type of Data	T_0 (K)	p_0 (kPa)	p_a (Pa)	Re_2	D_2 (mm)
97	35.2	4,480	sonic	FV	504	23.20	348	1,700	8.7
98	27.5	6,474	sonic	FV	507	33.72	649	2,757	7.7
99	22.4	5,365	sonic	FV	513	28.34	668	2,506	7.0
100	25.8	1,071	sonic	P	571	6.42	132	470	7.5
101	16.4	1,052	sonic	P	577	6.38	206	565	6.1
102	4.0	805	sonic	P	566	4.77	638	725	3.3
103	16.5	4,067	sonic	P	561	23.86	765	2,177	6.1
104	4.1	4,210	sonic	P	559	24.62	3189	3,761	3.3
105	31.1	1,186	sonic	V	598	7.50	127	477	8.2
106	32.1	1,183	sonic	V	601	7.53	124	469	8.3
107	31.4	1,210	sonic	V	580	7.38	124	484	8.2
108	19.1	1,082	sonic	V	605	6.93	191	543	6.5
109	19.1	1,083	sonic	V	604	6.94	192	544	6.5
110	18.2	1,083	sonic	V	605	6.95	201	555	6.4
111	4.2	820	sonic	V	588	5.09	634	724	3.4
112	4.2	819	sonic	V	589	5.09	642	727	3.4
113	4.2	821	sonic	V	588	5.09	646	730	3.4
114	15.5	4,853	sonic	V	458	22.44	766	2,669	5.9
115	15.4	4,860	sonic	V	457	22.45	772	2,682	5.9
116	15.1	4,869	sonic	V	456	22.44	784	2,705	5.8
117	15.5	8,422	sonic	V	450	38.21	1305	4,633	5.9
118	15.4	8,436	sonic	V	449	38.18	1308	4,648	5.9
119	15.3	8,461	sonic	V	448	38.14	1318	4,679	5.9
120	3.8	4,757	sonic	V	472	22.80	3208	4,342	3.2
121	3.7	4,765	sonic	V	471	22.80	3213	4,352	3.2
122	3.7	4,778	sonic	V	470	22.78	3222	4,368	3.2
123	3.6	9,497	sonic	V	456	43.75	6364	8,742	3.2
124	3.6	9,511	sonic	V	455	43.70	6364	8,758	3.2
125	3.6	9,540	sonic	V	454	43.66	6372	8,789	3.2
126	3.6	9,485	sonic	V	457	43.74	6374	8,735	3.2
127	3.6	9,504	sonic	V	455	43.69	6378	8,756	3.2
128	3.6	9,535	sonic	V	453	43.63	6392	8,793	3.2
129	15.8	4,716	sonic	P	480	23.07	772	2,572	6.0
130	15.7	8,239	sonic	P	465	38.81	1310	4,510	5.9
131	3.8	4,747	sonic	P	478	23.09	3193	4,314	3.3
132	3.8	4,729	sonic	P	479	23.09	3207	4,303	3.3
133	3.7	9,342	sonic	P	465	44.02	6360	8,584	3.2
134	0.7	432	supersonic	FV	546	2.63	200	536	4.5
135	1.1	683	supersonic	FV	564	4.31	200	662	4.2

237

Run #	JPR	Re_{exit}	type of nozzle	Type of Data	T_0 (K)	p_0 (kPa)	p_a (Pa)	Re_2	D_2 (mm)
136	1.1	651	supersonic	FV	578	4.23	200	635	4.2
137	2.9	1,482	supersonic	FV	584	9.74	166	959	5.2
138	5.2	1,993	supersonic	FV	586	13.14	127	1,005	6.3
139	3.8	2,321	supersonic	FV	585	15.27	200	1,340	5.6
140	2.4	2,316	supersonic	FV	585	15.25	320	1,636	4.8
141	10.3	4,286	supersonic	FV	572	27.49	133	1,565	8.5
142	5.3	4,261	supersonic	FV	569	27.17	256	2,123	6.4
143	3.4	4,269	supersonic	FV	568	27.15	402	2,602	5.4
144	2.5	4,293	supersonic	FV	570	27.42	552	2,980	4.9
145	31.8	19,257	supersonic	FV	525	111.65	176	4,071	14.3
146	21.8	19,169	supersonic	FV	527	111.75	257	4,876	12.0
147	10.2	19,276	supersonic	FV	525	111.75	550	7,089	8.4
148	6.7	19,380	supersonic	FV	520	111.25	835	8,691	7.0
149	4.6	19,582	supersonic	FV	513	110.62	1199	10,391	6.1
150	3.6	19,349	supersonic	FV	521	111.36	1540	11,441	5.5
151	1.7	6,394	supersonic	FV	552	39.31	1183	5,225	4.4
152	2.5	6,415	supersonic	FV	552	39.46	805	4,480	4.9
153	3.9	6,388	supersonic	FV	557	39.73	508	3,651	5.7
154	6.4	6,348	supersonic	FV	556	39.40	309	2,907	6.9
155	4.2	3,667	supersonic	FV	573	23.56	284	2,041	5.8
156	2.3	3,614	supersonic	FV	574	23.29	502	2,580	4.8
157	1.5	3,643	supersonic	FV	575	23.49	808	3,137	4.3
158	1.7	4,323	supersonic	FV	570	27.61	797	3,475	4.5
159	1.3	4,324	supersonic	FV	570	27.65	1056	3,879	4.2
160	1.2	2,334	supersonic	FV	587	15.41	650	2,176	4.2
161	2.0	2,341	supersonic	FV	587	15.47	397	1,796	4.6
162	3.1	1,488	supersonic	FV	583	9.76	159	944	5.2
163	1.2	1,487	supersonic	FV	583	9.76	403	1,375	4.2
164	0.7	1,482	supersonic	FV	586	9.77	669	1,720	4.3
165	0.7	1,073	supersonic	FV	589	7.13	537	1,322	4.5
166	1.2	1,068	supersonic	FV	592	7.13	296	990	4.2
167	2.4	1,060	supersonic	FV	599	7.17	152	752	4.8
168	1.7	811	supersonic	FV	587	5.37	157	655	4.5
169	1.3	669	supersonic	FV	594	4.49	172	601	4.2
170	1.3	669	supersonic	FV	595	4.50	175	604	4.2
171	1.3	813	supersonic	FV	587	5.37	209	734	4.2
172	0.7	667	supersonic	FV	596	4.49	345	834	4.5
173	0.6	812	supersonic	FV	588	5.38	424	1,034	4.6
174	3.3	1,903	supersonic	FV	607	13.09	198	1,169	5.4

238

Run #	JPR	Re_{exit}	type of nozzle	Type of Data	T_0 (K)	p_0 (kPa)	p_a (Pa)	Re_2	D_2 (mm)
175	1.2	1,903	supersonic	FV	608	13.12	528	1,742	4.2
176	0.8	1,903	supersonic	FV	608	13.11	789	2,065	4.2
177	0.9	3,462	supersonic	FV	593	23.16	1339	3,685	4.2
178	1.2	3,505	supersonic	FV	593	23.44	944	3,209	4.2
179	2.2	3,508	supersonic	FV	594	23.50	536	2,565	4.7
180	6.7	3,506	supersonic	FV	596	23.61	176	1,568	7.0
181	11.6	5,110	supersonic	FV	587	33.77	145	1,762	8.9
182	12.8	6,100	supersonic	FV	580	39.77	156	2,012	9.3
183	13.2	7,075	supersonic	FV	572	45.41	173	2,298	9.5
184	8.6	7,047	supersonic	FV	575	45.52	266	2,809	7.8
185	4.3	5,120	supersonic	FV	584	33.62	393	2,812	5.9
186	4.3	7,060	supersonic	FV	573	45.34	530	3,874	5.9
187	2.5	5,107	supersonic	FV	580	33.32	662	3,527	4.9
188	2.9	6,115	supersonic	FV	572	39.26	669	3,959	5.2
189	2.8	7,107	supersonic	FV	567	45.17	808	4,695	5.1
190	1.8	5,126	supersonic	FV	578	33.26	926	4,060	4.5
191	1.8	5,136	supersonic	FV	576	33.18	932	4,083	4.5
192	2.1	7,077	supersonic	FV	567	44.89	1061	5,250	4.7
193	2.1	7,128	supersonic	FV	563	44.88	1071	5,307	4.7
194	1.7	7,115	supersonic	FV	565	44.99	1321	5,758	4.4
195	1.3	5,173	supersonic	FV	572	33.19	1326	4,723	4.2
196	1.2	6,167	supersonic	FV	567	39.14	1597	5,678	4.2
197	1.2	7,126	supersonic	FV	566	45.10	1858	6,586	4.2
198	1.2	9,064	supersonic	FV	558	56.49	2393	8,468	4.2
199	0.6	9,065	supersonic	FV	555	56.17	5086	13,239	5.1
200	25.2	13,498	supersonic	pitot	381	62.04	124	3,265	12.8
201	22.6	13,354	supersonic	pitot	404	65.71	147	3,411	12.1
202	17.9	13,374	supersonic	pitot	402	65.48	184	3,823	10.9
203	13.4	13,433	supersonic	pitot	401	65.47	247	4,420	9.5
204	11.0	13,398	supersonic	pitot	403	65.69	301	4,839	8.7
205	9.8	13,409	supersonic	pitot	404	66.04	340	5,122	8.3
206	7.5	13,345	supersonic	pitot	406	65.97	445	5,779	7.4
207	5.6	13,267	supersonic	pitot	410	66.46	597	6,554	6.5
208	3.9	13,157	supersonic	pitot	417	67.25	869	7,644	5.7
209	2.9	13,073	supersonic	pitot	422	67.60	1182	8,637	5.1
210	2.4	22,397	supersonic	pitot	295	66.27	1379	15,767	4.8
211	6.1	22,215	supersonic	pitot	295	65.76	536	10,352	6.8
212	13.8	9,933	supersonic	FV	451	51.26	186	3,178	9.7
213	15.3	9,982	supersonic	FV	447	50.97	168	3,043	10.1

239

Run #	JPR	Re_{exit}	type of nozzle	Type of Data	T_0 (K)	p_0 (kPa)	p_a (Pa)	Re_2	D_2 (mm)
214	11.1	10,027	supersonic	FV	444	50.82	230	3,565	8.7
215	9.0	10,069	supersonic	FV	442	50.82	282	3,944	8.0
216	7.7	10,094	supersonic	FV	441	50.73	332	4,272	7.4
217	5.6	10,133	supersonic	FV	439	50.61	457	4,975	6.5
218	3.8	10,159	supersonic	FV	436	50.40	669	5,928	5.6
219	2.9	10,189	supersonic	FV	434	50.34	878	6,684	5.1
220	1.9	10,240	supersonic	FV	432	50.24	1307	7,912	4.6
221	1.0	10,281	supersonic	FV	428	49.98	2608	10,446	4.2
222	3.0	3,370	supersonic	FV	477	18.56	311	2,174	5.2
223	4.0	4,520	supersonic	FV	471	24.55	307	2,569	5.7
224	3.0	4,528	supersonic	FV	470	24.51	405	2,903	5.2
225	2.1	3,399	supersonic	FV	476	18.66	447	2,541	4.7
226	2.1	4,500	supersonic	FV	470	24.38	588	3,375	4.7
227	1.1	3,438	supersonic	FV	474	18.78	876	3,336	4.2
228	1.0	4,521	supersonic	FV	468	24.38	1175	4,447	4.2
229	10.5	8,091	supersonic	FV	472	44.04	211	2,957	8.5
230	6.9	4,557	supersonic	FV	483	25.43	184	2,019	7.1
231	9.8	6,660	supersonic	FV	474	36.44	186	2,506	8.3
232	5.2	3,403	supersonic	FV	489	19.25	186	1,722	6.3
233	9.6	6,596	supersonic	FV	479	36.48	191	2,513	8.2
234	12.0	7,998	supersonic	FV	469	43.19	180	2,736	9.1
235	6.1	4,480	supersonic	FV	483	25.06	208	2,116	6.7
236	16.2	13,104	supersonic	FV	457	68.62	212	3,877	10.4
237	9.6	8,043	supersonic	FV	466	43.07	225	3,063	8.2
238	4.2	3,388	supersonic	FV	486	19.02	229	1,892	5.8
239	7.7	6,639	supersonic	FV	474	36.29	237	2,808	7.4
240	7.8	8,004	supersonic	FV	469	43.21	279	3,363	7.5
241	6.0	6,677	supersonic	FV	472	36.36	304	3,164	6.7
242	6.0	8,019	supersonic	FV	470	43.38	364	3,806	6.7
243	4.2	6,732	supersonic	FV	481	37.49	454	3,770	5.8
244	4.1	8,020	supersonic	FV	477	44.18	543	4,523	5.8
245	3.1	6,686	supersonic	FV	482	37.28	595	4,225	5.3
246	3.1	8,001	supersonic	FV	475	43.91	707	5,074	5.3
247	2.1	6,646	supersonic	FV	479	36.77	880	4,968	4.7
248	2.0	7,986	supersonic	FV	473	43.58	1073	6,037	4.6
249	1.1	6,698	supersonic	FV	492	38.27	1750	6,449	4.2
250	2.0	12,953	supersonic	FV	471	70.39	1757	9,846	4.6
251	1.1	7,982	supersonic	FV	485	44.80	2103	7,766	4.2
252	1.0	12,964	supersonic	FV	474	70.85	3487	12,858	4.2

240

Run #	JPR	Re_{exit}	type of nozzle	Type of Data	T_0 (K)	p_0 (kPa)	p_a (Pa)	Re_2	D_2 (mm)
253	3.9	2,163	supersonic	FV	547	13.95	181	1,248	5.7
254	3.4	2,157	supersonic	FV	547	13.93	205	1,316	5.4
255	2.3	2,143	supersonic	FV	548	13.87	301	1,541	4.8
256	1.2	2,142	supersonic	FV	549	13.88	599	2,017	4.2
257	6.4	4,176	supersonic	V	534	26.24	204	1,916	6.9
258	6.9	4,169	supersonic	V	533	26.12	190	1,853	7.1
259	6.9	4,176	supersonic	V	532	26.12	191	1,860	7.1
260	11.7	7,488	supersonic	V	512	44.79	193	2,596	9.0
261	11.8	7,534	supersonic	V	508	44.64	190	2,600	9.0
262	11.7	7,558	supersonic	V	506	44.57	192	2,623	8.9
263	15.8	12,509	supersonic	V	485	70.29	224	3,752	10.3
264	16.3	12,584	supersonic	V	482	70.16	217	3,722	10.4
265	16.5	12,638	supersonic	V	479	69.94	212	3,706	10.5
266	3.8	3,227	supersonic	V	517	19.51	256	1,872	5.6
267	4.0	3,204	supersonic	V	521	19.56	247	1,828	5.7
268	3.8	3,201	supersonic	V	523	19.60	258	1,862	5.6
269	15.2	9,033	supersonic	V	515	54.40	180	2,764	10.1
270	14.8	9,232	supersonic	V	502	53.97	183	2,860	10.0
271	15.7	9,307	supersonic	V	498	53.89	172	2,796	10.3
272	13.7	9,405	supersonic	V	492	53.73	197	3,025	9.6
273	13.5	9,452	supersonic	V	490	53.75	199	3,053	9.6
274	13.2	9,491	supersonic	V	488	53.68	204	3,099	9.5
275	5.8	4,292	supersonic	V	509	25.49	219	2,062	6.6
276	5.7	4,290	supersonic	V	510	25.55	225	2,084	6.6
277	5.7	4,268	supersonic	V	513	25.58	227	2,077	6.6
278	4.2	4,267	supersonic	V	514	25.64	310	2,387	5.8
279	4.1	4,270	supersonic	V	514	25.68	317	2,411	5.8
280	3.9	4,261	supersonic	V	515	25.65	328	2,446	5.7
281	9.2	7,642	supersonic	V	498	44.27	243	2,976	8.0
282	8.6	7,668	supersonic	V	496	44.22	259	3,081	7.8
283	8.9	7,687	supersonic	V	494	44.12	250	3,040	7.9
284	3.1	4,295	supersonic	V	510	25.56	410	2,718	5.3
285	3.0	4,293	supersonic	V	511	25.61	424	2,754	5.2
286	3.1	4,277	supersonic	V	512	25.57	421	2,738	5.2
287	2.2	4,266	supersonic	V	513	25.59	595	3,151	4.7
288	2.1	4,265	supersonic	V	514	25.60	599	3,159	4.7
289	2.2	4,266	supersonic	V	514	25.64	595	3,150	4.7
290-				TD					
330				TD					

Run #	JPR	Re_{exit}	type of nozzle	Type of Data	T_0 (K)	p_0 (kPa)	p_a (Pa)	Re_2	D_2 (mm)
331	4.1	3,158	supersonic	SS	523	19.36	238	1,781	5.8
332	16.8	12,467	supersonic	SS	482	69.64	208	3,625	10.6
333	11.7	7,673	supersonic	SS	493	43.97	188	2,657	9.0
334	6.3	4,266	supersonic	SS	510	25.41	204	1,984	6.8
335	5.5	4,234	supersonic	SS	515	25.47	231	2,081	6.5
336	9.2	7,620	supersonic	SS	499	44.19	241	2,958	8.1
337	12.2	9,509	supersonic	SS	487	53.66	221	3,233	9.1
338	14.9	9,554	supersonic	SS	483	53.48	180	2,949	10.0
339	3.9	4,303	supersonic	SS	508	25.47	326	2,472	5.7
340	3.1	4,295	supersonic	SS	510	25.54	419	2,745	5.2
341	2.2	4,286	supersonic	SS	512	25.64	595	3,163	4.7
342	2.1	9,501	supersonic	SS	487	53.66	1309	7,155	4.6
343	2.0	9,533	supersonic	SS	484	53.46	1315	7,203	4.6
344	13.9	10,161	supersonic	D	433	50.01	181	3,240	9.7
345	10.4	8,221	supersonic	D	436	40.78	196	3,010	8.5
346	5.8	4,595	supersonic	D	447	23.42	203	2,212	6.6
347	12.6	10,173	supersonic	D	432	49.95	200	3,407	9.3
348	5.3	4,560	supersonic	D	447	23.26	219	2,280	6.4
349	14.6	13,395	supersonic	D	430	65.34	225	4,179	9.9
350	8.7	8,217	supersonic	D	439	41.02	238	3,283	7.8
351	3.6	3,472	supersonic	D	454	18.03	252	2,069	5.5
352	3.7	4,628	supersonic	D	454	24.04	325	2,722	5.6
353	3.0	4,613	supersonic	D	458	24.19	412	2,995	5.2
354	2.0	4,605	supersonic	D	461	24.38	601	3,483	4.6
355	2.0	10,014	supersonic	D	453	51.98	1320	7,665	4.6
356				DC					
357	3.5	2,114	supersonic	FV+SS	569	14.28	205	1,276	5.5
358	3.8	2,063	supersonic	FV+SS	571	14.00	183	1,196	5.7
359	14.3	9,113	supersonic	FV+SS	514	54.79	192	2,863	9.8
360	12.0	7,375	supersonic	FV+SS	530	45.92	192	2,520	9.1
361	6.3	4,070	supersonic	FV+SS	542	26.02	207	1,886	6.9
362	12.0	9,035	supersonic	FV+SS	516	54.62	228	3,090	9.1
363	3.1	2,082	supersonic	FV+SS	554	13.63	220	1,321	5.3
364	5.7	4,005	supersonic	FV+SS	539	25.41	225	1,947	6.6
365	15.2	12,352	supersonic	FV+SS	486	69.51	230	3,775	10.1
366	9.2	7,547	supersonic	FV+SS	496	43.51	236	2,925	8.1
367	3.9	3,110	supersonic	FV+SS	524	19.07	243	1,781	5.7
368	2.1	2,153	supersonic	FV+SS	540	13.68	322	1,599	4.7
369	4.0	4,094	supersonic	FV+SS	524	25.19	318	2,336	5.7

242

Run #	JPR	Re_{exit}	type of nozzle	Type of Data	T_0 (K)	p_0 (kPa)	p_a (Pa)	Re_2	D_2 (mm)
370	3.0	4,097	supersonic	FV+SS	527	25.36	421	2,631	5.2
371	1.7	2,139	supersonic	FV+SS	547	13.78	414	1,749	4.4
372	2.2	4,079	supersonic	FV+SS	530	25.40	591	3,015	4.7
373	2.0	9,324	supersonic	FV+SS	490	53.07	1322	7,081	4.6
374	1.5	6,655	supersonic	FV+SS	499	39.59	1363	5,741	4.3
375	1.5	7,122	supersonic	FV+SS	496	41.86	1376	6,035	4.3
376	0.8	324	supersonic	FV+SS	544	3.63	237	339	4.2
377	1.8	517	supersonic	FV+SS	540	5.66	169	460	4.5
378	1.8	584	supersonic	FV+SS	534	6.31	189	520	4.5
379	0.8	7,553	supersonic	FV+SS	489	42.85	2532	8,106	4.2
380	1.6	7,661	supersonic	FV+SS	493	43.84	1369	6,362	4.4
381	2.5	7,702	supersonic	FV+SS	486	43.32	869	5,357	4.9
382	3.3	7,741	supersonic	FV+SS	477	42.60	646	4,785	5.4
383	4.9	7,786	supersonic	FV+SS	473	42.49	438	4,060	6.2
384	6.5	7,813	supersonic	FV+SS	471	42.44	328	3,572	6.9
385	1.5	1,386	supersonic	FV+SS	523	7.99	268	1,181	4.3
386	1.9	1,377	supersonic	FV	526	8.01	207	1,059	4.6
387	0.9	608	supersonic	V	559	3.63	196	628	4.2
388	1.0	569	supersonic	V	559	3.63	182	569	4.2
389	1.1	570	supersonic	V	560	3.64	169	552	4.2
390	1.4	893	supersonic	V	550	5.57	196	776	4.3
391	1.0	894	supersonic	V	551	5.56	267	878	4.2
392	1.5	893	supersonic	V	552	5.56	182	754	4.4
393	1.4	880	supersonic	V	552	5.57	195	763	4.3
394	1.4	891	supersonic	V	553	5.58	204	785	4.3
395	1.3	892	supersonic	V	553	5.57	214	802	4.2
396	1.8	1,218	supersonic	V	575	7.98	224	969	4.5
397	1.8	1,201	supersonic	V	575	7.92	225	960	4.5
398	1.7	1,197	supersonic	V	576	7.93	234	971	4.4
399	2.2	1,221	supersonic	V	582	8.13	181	885	4.8
400	2.2	1,212	supersonic	V	582	8.13	184	885	4.7
401	1.7	1,013	supersonic	V	552	6.34	185	818	4.5
402	1.7	1,007	supersonic	V	554	6.35	190	822	4.4
403	3.6	1,989	supersonic	V	577	13.27	186	1,185	5.5
404	3.4	2,015	supersonic	V	576	13.27	197	1,230	5.4
405	6.2	3,828	supersonic	V	553	24.26	196	1,779	6.8
406	5.8	3,875	supersonic	V	552	24.23	208	1,853	6.6
407	2.9	2,036	supersonic	V	570	13.23	229	1,329	5.1
408	2.7	2,031	supersonic	V	571	13.19	246	1,366	5.0

243

Run #	JPR	Re_{exit}	type of nozzle	Type of Data	T_0 (K)	p_0 (kPa)	p_a (Pa)	Re_2	D_2 (mm)
409	5.5	3,862	supersonic	V	551	24.19	220	1,896	6.5
410	5.5	3,904	supersonic	V	548	24.17	222	1,924	6.5
411	3.9	2,918	supersonic	V	556	18.38	236	1,671	5.7
412	3.6	2,926	supersonic	V	556	18.40	255	1,731	5.5
413	1.6	1,236	supersonic	V	578	8.14	261	1,035	4.4
414	1.6	1,238	supersonic	V	575	8.15	256	1,030	4.4
415	11.6	7,249	supersonic	V	540	46.15	200	2,526	8.9
416	11.3	7,308	supersonic	V	526	45.14	201	2,579	8.8
417	15.6	12,049	supersonic	V	506	71.19	229	3,636	10.2
418	14.9	12,122	supersonic	V	502	70.87	239	3,737	10.0
419	9.1	7,379	supersonic	V	513	44.26	244	2,879	8.0
420	9.3	7,383	supersonic	V	512	44.18	238	2,852	8.1
421	2.1	1,444	supersonic	V	555	13.02	311	1,109	4.7
422	2.1	1,344	supersonic	V	556	13.06	322	1,059	4.7
423	3.9	2,328	supersonic	V	537	23.89	321	1,541	5.7
424	3.9	2,296	supersonic	V	537	23.93	320	1,540	5.7
425	6.9	7,542	supersonic	V	515	45.39	332	3,362	7.1
426	6.9	7,527	supersonic	V	511	44.91	325	3,337	7.1
427	2.9	2,561	supersonic	V	532	23.79	422	1,797	5.1
428	2.9	2,450	supersonic	V	532	23.76	424	1,753	5.1
429	1.6	1,292	supersonic	V	550	13.06	430	1,130	4.4
430	1.6	1,244	supersonic	V	552	13.06	422	1,092	4.4
431	5.2	7,564	supersonic	V	513	45.41	435	3,814	6.4
432	5.1	7,554	supersonic	V	509	44.93	440	3,846	6.3
433	2.0	2,524	supersonic	V	529	23.65	597	2,016	4.6
434	2.1	2,444	supersonic	V	529	23.73	600	1,974	4.6
435	3.5	7,541	supersonic	V	507	44.60	644	4,564	5.5
436	3.4	7,525	supersonic	V	505	44.30	653	4,593	5.4
437	2.6	7,489	supersonic	V	500	43.64	852	5,151	4.9
438	2.5	7,502	supersonic	V	499	43.58	863	5,191	4.9
439	1.7	7,519	supersonic	V	496	43.37	1275	6,098	4.4
440	1.7	7,538	supersonic	V	495	43.34	1285	6,134	4.4
441	0.9	7,582	supersonic	V	491	43.18	2532	8,106	4.2
442	0.8	7,581	supersonic	V	490	43.11	2549	8,137	4.2
443	1.1	391	supersonic	P	533	3.51	169	382	4.2
444	1.6	572	supersonic	P	525	5.46	174	495	4.4
445	1.9	627	supersonic	P	521	6.06	170	525	4.5
446	2.2	725	supersonic	P	542	7.57	183	589	4.7
447	1.6	703	supersonic	P	546	7.62	251	630	4.4

244

Run #	JPR	Re_{exit}	type of nozzle	Type of Data	T_0 (K)	p_0 (kPa)	p_a (Pa)	Re_2	D_2 (mm)
448	3.5	1,123	supersonic	P	548	12.26	182	802	5.5
449	11.4	7,123	supersonic	P	512	44.68	198	2,520	8.8
450	5.8	2,247	supersonic	P	530	22.49	203	1,265	6.6
451	3.0	1,196	supersonic	P	544	12.27	216	865	5.2
452	5.3	2,201	supersonic	P	530	22.70	226	1,328	6.4
453	16.0	12,274	supersonic	P	491	70.33	221	3,660	10.3
454	9.3	7,141	supersonic	P	502	43.77	236	2,776	8.1
455	2.0	1,261	supersonic	P	542	12.27	316	1,017	4.6
456	3.7	2,291	supersonic	P	526	22.67	317	1,526	5.6
457	6.5	7,121	supersonic	P	503	43.72	337	3,267	7.0
458	2.8	2,284	supersonic	P	523	22.70	417	1,691	5.1
459	1.5	1,138	supersonic	P	542	12.29	429	1,037	4.3
460	5.0	7,171	supersonic	P	501	43.85	443	3,722	6.2
461	2.0	2,126	supersonic	P	556	23.33	606	1,783	4.6
462	3.6	6,953	supersonic	P	529	45.25	641	4,187	5.5
463	2.6	6,879	supersonic	P	516	43.54	854	4,756	4.9
464	1.7	6,948	supersonic	P	508	43.23	1279	5,659	4.4
465	0.9	7,009	supersonic	P	503	43.03	2517	7,474	4.2
466	1.1	312	supersonic	P	570	3.59	170	305	4.2
467	1.7	502	supersonic	P	559	5.62	172	443	4.4
468	1.9	602	supersonic	P	549	6.58	182	517	4.6
469	2.3	694	supersonic	P	578	8.04	184	565	4.8
470	1.6	698	supersonic	P	578	8.09	267	626	4.4
471	3.7	1,075	supersonic	P	580	12.61	179	762	5.6
472	12.3	6,817	supersonic	P	541	45.55	186	2,322	9.2
473	6.0	2,137	supersonic	P	559	23.30	204	1,213	6.7
474	3.0	1,123	supersonic	P	572	12.62	219	825	5.2
475	5.7	2,118	supersonic	P	557	23.35	213	1,247	6.6
476	16.1	11,931	supersonic	P	513	71.90	224	3,549	10.4
477	9.6	6,924	supersonic	P	526	44.81	236	2,658	8.2
478	2.1	1,233	supersonic	P	567	12.61	312	979	4.7
479	3.8	2,209	supersonic	P	549	23.26	323	1,481	5.6
480	6.8	6,927	supersonic	P	525	44.78	333	3,126	7.1
481	2.9	2,232	supersonic	P	546	23.21	418	1,636	5.1
482	1.5	1,175	supersonic	P	564	12.60	424	1,042	4.4
483	5.1	6,995	supersonic	P	522	44.89	440	3,581	6.3
484	2.0	2,205	supersonic	P	543	23.21	604	1,836	4.6
485	3.5	7,015	supersonic	P	518	44.56	649	4,276	5.4
486	2.6	7,000	supersonic	P	514	44.07	859	4,826	5.0

Run #	JPR	Re_{exit}	type of nozzle	Type of Data	T_0 (K)	p_0 (kPa)	p_a (Pa)	Re_2	D_2 (mm)
487	1.7	7,001	supersonic	P	507	43.44	1274	5,682	4.4
488	0.9	7,034	supersonic	P	510	43.96	2533	7,450	4.2
489	1.2	333	supersonic	V	557	3.75	165	321	4.2
490	1.1	333	supersonic	V	558	3.75	181	327	4.2
491	1.6	526	supersonic	V	547	5.74	184	470	4.4
492	1.8	526	supersonic	V	548	5.75	169	460	4.5
493	2.1	593	supersonic	V	541	6.38	159	496	4.7
494	1.6	592	supersonic	V	541	6.38	214	535	4.4
495	2.5	717	supersonic	V	574	8.24	169	566	4.9
496	2.7	715	supersonic	V	574	8.24	161	557	5.0
497	1.7	714	supersonic	V	576	8.26	256	631	4.4
498	1.6	715	supersonic	V	576	8.26	263	636	4.4
499	3.7	1,413	supersonic	V	573	12.82	175	867	5.6
500	3.5	1,348	supersonic	V	571	12.84	189.	864	5.5
501	11.4	7,230	supersonic	V	536	45.60	200	2,532	8.9
502	12.3	7,247	supersonic	V	528	45.00	184	2,453	9.2
503	6.3	2,412	supersonic	V	545	23.68	195	1,258	6.8
504	2.3	1,117	supersonic	V	574	12.95	296	916	4.8
505	2.3	1,111	supersonic	V	574	12.92	301	919	4.8
506	4.2	2,168	supersonic	V	557	23.94	301	1,446	5.8
507	4.2	2,169	supersonic	V	554	23.95	296	1,447	5.9
508	7.6	7,305	supersonic	V	532	45.68	304	3,114	7.4
509	7.2	7,314	supersonic	V	527	45.31	314	3,181	7.3
510	3.0	2,418	supersonic	V	546	23.78	404	1,685	5.2
511	3.0	2,321	supersonic	V	545	23.78	410	1,661	5.2
512	1.6	1,191	supersonic	V	564	12.91	417	1,047	4.4
513	1.6	1,180	supersonic	V	565	12.90	428	1,048	4.4
514	5.2	7,413	supersonic	V	524	45.63	439	3,745	6.4
515	5.1	7,415	supersonic	V	521	45.33	443	3,774	6.3
516				DC					
517	2.1	2,374	supersonic	V	540	23.71	581	1,901	4.7
518	3.6	7,463	supersonic	V	514	44.88	632	4,466	5.5
519	3.5	7,441	supersonic	V	513	44.57	640	4,491	5.5
520	2.6	7,393	supersonic	V	509	43.98	836	5,029	5.0
521	2.6	7,389	supersonic	V	508	43.84	838	5,039	5.0
522	1.8	7,361	supersonic	V	514	44.28	1240	5,856	4.5
523	1.8	7,449	supersonic	V	508	44.19	1242	5,935	4.5
524	0.9	7,455	supersonic	V	505	43.86	2514	7,889	4.2
525	0.9	7,465	supersonic	V	503	43.75	2504	7,895	4.2

246

Run #	JPR	Re_{exit}	type of nozzle	Type of Data	T_0 (K)	p_0 (kPa)	p_a (Pa)	Re_2	D_2 (mm)
526	3.1	820	supersonic	FV+SS	511	7.59	128	575	5.2
527	2.5	797	supersonic	FV+SS	513	7.63	161	612	4.9
528	1.0	382	supersonic	FV	506	3.49	187	387	4.2
529	1.6	580	supersonic	FV+SS	497	5.38	178	512	4.4
530	1.7	644	supersonic	FV	493	5.98	182	557	4.4
531	1.6	771	supersonic	FV+SS	522	7.75	259	688	4.4
532	3.3	1,231	supersonic	FV+SS	523	12.19	195	866	5.3
533	10.8	7,545	supersonic	FV+SS	495	43.43	202	2,717	8.6
534	5.0	2,374	supersonic	FV+SS	513	22.78	237	1,408	6.2
535	2.2	1,251	supersonic	FV+SS	527	12.33	292	997	4.7
536	5.4	2,302	supersonic	FV+SS	514	22.84	222	1,370	6.4
537	14.3	12,505	supersonic	FV	479	69.22	243	3,937	9.8
538	8.3	7,600	supersonic	FV+SS	486	42.80	258	3,091	7.7
539	3.3	2,137	supersonic	FV+SS	510	17.19	266	1,385	5.4
540	2.0	1,437	supersonic	FV+SS	521	12.30	310	1,129	4.6
541	3.6	2,416	supersonic	FV+SS	508	22.82	326	1,615	5.5
542	6.7	7,703	supersonic	FV+SS	489	43.67	328	3,476	7.0
543	2.8	2,529	supersonic	FV+SS	506	22.82	417	1,812	5.1
544	1.5	1,317	supersonic	FV+SS	523	12.37	427	1,166	4.3
545	4.9	7,705	supersonic	FV	490	43.83	445	3,988	6.2
546	2.0	2,557	supersonic	FV+SS	507	22.85	604	2,074	4.6
547	3.4	7,699	supersonic	FV+SS	489	43.62	651	4,725	5.4
548	2.5	7,660	supersonic	FV+SS	485	42.98	853	5,303	4.9
549	1.7	7,659	supersonic	FV+SS	481	42.57	1286	6,277	4.4
550	0.8	7,674	supersonic	FV+SS	478	42.35	2529	8,277	4.2
551	3.6	1,343	supersonic	FV+SS	550	12.56	181	861	5.5
552	11.1	7,300	supersonic	FV	516	44.07	200	2,597	8.7
553	5.7	2,530	supersonic	FV+SS	530	23.22	209	1,345	6.6
554	2.9	1,378	supersonic	FV+SS	544	12.58	223	953	5.1
555	5.1	2,416	supersonic	FV+SS	530	23.29	237	1,388	6.3
556	8.5	7,430	supersonic	FV	508	44.06	260	2,993	7.8
557	18.5	14,975	supersonic	FV	481	83.39	227	4,163	11.0
558	8.8	7,492	supersonic	FV	497	43.26	247	2,974	7.9
559	3.4	2,104	supersonic	FV+SS	523	17.50	262	1,346	5.4
560	2.0	1,435	supersonic	FV+SS	535	12.49	325	1,138	4.6
561	3.7	2,454	supersonic	FV+SS	519	23.13	323	1,601	5.6
562	6.4	7,571	supersonic	FV	498	43.87	342	3,473	6.9
563	2.9	2,564	supersonic	FV+SS	516	23.09	417	1,814	5.1
564	1.5	1,375	supersonic	FV+SS	533	12.50	426	1,203	4.3

Run #	JPR	Re_{exit}	type of nozzle	Type of Data	T_0 (K)	p_0 (kPa)	p_a (Pa)	Re_2	D_2 (mm)
565	5.0	7,572	supersonic	FV+SS	498	43.81	443	3,913	6.2
566	2.0	2,599	supersonic	FV+SS	514	23.01	596	2,081	4.6
567	3.4	7,588	supersonic	FV+SS	495	43.62	640	4,623	5.4
568	2.5	7,543	supersonic	FV+SS	490	42.83	861	5,250	4.9
569	1.7	7,572	supersonic	FV+SS	486	42.60	1278	6,189	4.4
570	0.8	7,597	supersonic	FV+SS	481	42.29	2523	8,188	4.2
571	1.0	381	supersonic	FV	529	3.60	180	376	4.2
572	1.6	583	supersonic	FV	514	5.57	185	514	4.4
573	1.7	641	supersonic	FV	512	6.18	188	553	4.4
574	2.3	773	supersonic	FV	542	8.03	184	615	4.8
575	1.6	772	supersonic	FV	543	8.04	257	678	4.4
576	3.8	1,328	supersonic	FV+SS	534	12.34	170	842	5.6
577	11.2	7,437	supersonic	FV+SS	501	43.37	194	2,626	8.8
578	5.7	2,594	supersonic	FV+SS	515	22.88	208	1,380	6.6
579	3.0	1,426	supersonic	FV+SS	530	12.42	214	972	5.2
580	5.4	2,421	supersonic	FV+SS	515	23.00	222	1,378	6.4
581	14.5	12,361	supersonic	FV	481	68.80	238	3,864	9.9
582	9.1	7,560	supersonic	FV	489	42.91	237	2,953	8.0
583	3.5	2,082	supersonic	FV+SS	515	17.31	254	1,326	5.5
584	2.0	1,389	supersonic	FV	527	12.38	310	1,095	4.6
585	3.8	2,459	supersonic	FV+SS	512	22.89	314	1,597	5.6
586	6.6	7,596	supersonic	FV+SS	492	43.36	330	3,447	7.0
587	2.8	2,570	supersonic	FV+SS	508	22.86	419	1,830	5.1
588	1.5	1,369	supersonic	FV	526	12.38	426	1,203	4.3
589	5.0	7,608	supersonic	FV+SS	491	43.32	437	3,926	6.2
590	2.0	2,511	supersonic	FV+SS	511	22.86	600	2,038	4.6
591	3.3	7,602	supersonic	FV+SS	490	43.19	650	4,683	5.4
592	2.5	7,558	supersonic	FV+SS	486	42.50	854	5,260	4.9
593	1.7	7,575	supersonic	FV+SS	481	42.16	1275	6,211	4.4
594	0.8	7,637	supersonic	FV	484	42.83	2612	8,319	4.2
595				DC					
596	1.0	344	supersonic	FV	553	3.67	185	341	4.2
597	1.7	539	supersonic	FV	541	5.68	177	472	4.4
598	1.7	604	supersonic	FV	535	6.29	188	524	4.5
599	2.1	726	supersonic	FV	567	8.14	201	599	4.7
600	1.6	725	supersonic	FV	569	8.16	260	641	4.4
601	3.4	1,152	supersonic	FV+SS	570	12.63	194	801	5.4
602	11.1	7,226	supersonic	FV+SS	535	45.54	206	2,568	8.7
603	6.1	2,324	supersonic	FV+SS	548	23.53	200	1,247	6.8

248

Run #	JPR	Re_{exit}	type of nozzle	Type of Data	T_0 (K)	p_0 (kPa)	p_a (Pa)	Re_2	D_2 (mm)
604	3.0	1,189	supersonic	FV+SS	565	12.78	223	859	5.2
605	5.6	2,209	supersonic	FV+SS	548	23.66	220	1,296	6.5
606	15.5	12,026	supersonic	FV	511	71.78	232	3,635	10.2
607	9.2	7,356	supersonic	FV+SS	521	44.89	244	2,853	8.1
608	3.5	1,910	supersonic	FV+SS	549	17.83	259	1,226	5.5
609	2.2	1,250	supersonic	FV+SS	562	12.73	305	984	4.7
610	7.0	7,324	supersonic	FV+SS	523	43.87	315	3,228	7.2
611	3.6	2,471	supersonic	FV+SS	541	23.58	337	1,599	5.5
612	6.5	7,373	supersonic	FV+SS	520	44.98	348	3,371	6.9
613	2.9	2,440	supersonic	FV+SS	540	23.54	420	1,727	5.1
614	1.5	1,262	supersonic	FV	559	12.70	424	1,104	4.4
615	5.2	7,407	supersonic	FV+SS	520	45.18	436	3,748	6.3
616	2.0	2,381	supersonic	FV+SS	540	23.52	601	1,925	4.6
617	3.5	7,420	supersonic	FV+SS	518	45.01	637	4,452	5.5
618	2.5	7,336	supersonic	FV+SS	522	44.92	902	5,103	4.9
619	1.7	7,332	supersonic	FV+SS	524	45.08	1307	5,913	4.5
620	0.9	7,351	supersonic	FV+SS	523	45.11	2526	7,699	4.2
621	1.1	354	supersonic	FV+SS	587	3.80	186	348	4.2
622	1.6	526	supersonic	FV+SS	576	5.87	188	462	4.4
623	1.9	588	supersonic	FV+SS	570	6.53	177	494	4.6
624	2.3	709	supersonic	FV+SS	600	8.41	188	566	4.8
625	1.7	707	supersonic	FV+SS	600	8.43	261	620	4.4
626	3.6	1,137	supersonic	FV+SS	597	13.06	186	764	5.5
627	12.4	6,908	supersonic	FV+SS	558	45.73	185	2,328	9.2
628	6.4	2,282	supersonic	FV+SS	573	24.18	197	1,197	6.9
629	3.2	1,236	supersonic	FV+SS	592	13.11	210	837	5.3
630	5.7	2,211	supersonic	FV+SS	574	24.22	219	1,242	6.6
631	15.6	11,656	supersonic	FV+SS	533	73.10	235	3,515	10.2
632	9.5	7,147	supersonic	FV+SS	541	45.63	242	2,739	8.2
633	3.8	1,882	supersonic	FV+SS	572	18.21	244	1,166	5.6
634	2.2	1,251	supersonic	FV+SS	586	13.03	311	977	4.7
635	3.9	2,223	supersonic	FV+SS	567	24.09	318	1,454	5.7
636	7.0	7,189	supersonic	FV+SS	542	46.00	329	3,170	7.2
637	3.0	2,337	supersonic	FV+SS	562	24.05	414	1,646	5.2
638	1.6	1,242	supersonic	FV+SS	583	13.03	421	1,074	4.4
639	5.3	7,213	supersonic	FV+SS	539	45.88	434	3,618	6.4
640	2.1	2,298	supersonic	FV+SS	559	24.07	601	1,855	4.7
641	3.6	7,268	supersonic	FV+SS	535	45.75	642	4,344	5.5
642	2.6	7,214	supersonic	FV+SS	529	44.82	854	4,911	5.0

249

Run #	JPR	Re_{exit}	type of nozzle	Type of Data	T_0 (K)	p_0 (kPa)	p_a (Pa)	Re_2	D_2 (mm)
643	1.8	7,223	supersonic	FV+SS	526	44.56	1271	5,788	4.5
644	0.9	7,251	supersonic	FV+SS	523	44.46	2540	7,662	4.2
645				DC					
646	3.7	1,103	supersonic	FV+SS	589	12.37	173	732	5.6
647	3.2	1,122	supersonic	FV+SS	590	12.39	202	780	5.3
648	2.1	1,120	supersonic	FV+SS	591	12.40	301	893	4.7
649	1.1	1,115	supersonic	FV+SS	591	12.46	592	1,087	4.2
650	19.2	17,240	supersonic	FV	520	98.85	258	4,665	11.3
651	18.5	20,802	supersonic	FV	495	112.55	305	5,740	11.1
652	15.1	17,591	supersonic	FV	503	97.03	322	5,350	10.1
653	15.4	21,081	supersonic	FV+SS	485	111.61	363	6,349	10.2
654	11.6	17,928	supersonic	FV+SS	486	95.07	409	6,183	8.9
655	11.5	21,354	supersonic	FV+SS	474	109.89	480	7,419	8.9
656	9.7	18,146	supersonic	FV+SS	476	93.99	488	6,843	8.2
657	9.4	21,592	supersonic	FV+SS	466	108.91	581	8,247	8.1
658	7.7	18,345	supersonic	FV+SS	468	93.03	609	7,722	7.4
659	7.6	21,797	supersonic	FV+SS	459	107.97	715	9,224	7.4
660	5.6	18,424	supersonic	FV+SS	461	91.90	817	8,934	6.5
661	5.6	22,016	supersonic	FV+SS	451	107.01	960	10,720	6.5
662	3.8	18,659	supersonic	FV+SS	454	91.30	1204	10,806	5.6
663	3.8	21,885	supersonic	FV+SS	453	106.91	1428	12,747	5.6
664	2.8	18,656	supersonic	FV+SS	453	91.16	1608	12,255	5.1
665				DC					
666	1.9	18,914	supersonic	FV+SS	445	90.46	2400	14,700	4.5
667	1.9	22,518	supersonic	FV+SS	435	104.81	2833	17,632	4.5
668				DC					
669	15.0	1,690	sonic	FV+SS	574	5.93	209	943	10.0
670	13.0	1,570	sonic	FV+SS	577	5.54	226	933	9.4
671	14.6	1,924	sonic	FV+SS	605	7.17	260	1,088	9.9
672	6.4	890	sonic	FV+SS	597	3.27	270	693	6.9
673	9.5	1,400	sonic	FV+SS	586	5.03	281	944	8.2
674	14.7	2,218	sonic	FV+SS	608	8.32	299	1,250	9.9
675	7.7	1,253	sonic	FV+SS	590	4.54	310	912	7.5
676	25.4	5,998	sonic	FV+SS	582	21.41	445	2,652	12.8
677	14.6	3,589	sonic	FV+SS	595	13.14	476	2,029	9.9
678	21.1	3,559	sonic	FV+SS	599	13.14	329	1,712	11.8
679	25.3	7,497	sonic	FV+SS	574	26.32	549	3,321	12.8
680	20.2	6,039	sonic	FV+SS	578	21.36	557	2,959	11.5
681	2.7	883	sonic	FV+SS	597	3.24	645	870	5.0

250

Run #	JPR	Re_exit	type of nozzle	Type of Data	T_0 (K)	p_0 (kPa)	p_a (Pa)	Re_2	D_2 (mm)
682	3.6	1,251	sonic	FV+SS	588	4.52	661	1,155	5.5
683	27.5	10,007	sonic	FV+SS	570	34.63	666	4,260	13.3
684	22.0	8,242	sonic	FV+SS	569	28.50	684	3,881	12.0
685	14.4	6,045	sonic	FV+SS	576	21.28	778	3,430	9.9
686	22.2	10,177	sonic	FV+SS	559	34.42	819	4,775	12.0
687	3.6	1,715	sonic	FV+SS	563	5.87	871	1,587	5.5
688	27.0	13,419	sonic	FV+SS	551	44.70	874	5,759	13.2
689	6.1	3,275	sonic	FV+SS	590	11.85	1019	2,585	6.8
690	2.8	1,599	sonic	FV+SS	569	5.54	1058	1,563	5.1
691	15.6	11,848	sonic	FV+SS	548	39.18	1324	6,490	10.2
692	3.5	6,152	sonic	FV+SS	563	21.10	3188	5,722	5.5
693	14.6	1,749	sonic	FV+SS	545	5.77	209	987	9.9
694	12.8	1,618	sonic	FV+SS	552	5.41	224	966	9.3
695	14.2	1,968	sonic	FV+SS	581	7.00	260	1,125	9.8
696	6.3	916	sonic	FV+SS	572	3.20	269	718	6.8
697	9.2	1,433	sonic	FV+SS	564	4.93	281	975	8.1
698	14.1	2,283	sonic	FV+SS	584	8.16	306	1,309	9.8
699	7.5	1,284	sonic	FV+SS	568	4.45	313	945	7.4
700	20.0	3,640	sonic	FV+SS	579	12.90	341	1,793	11.5
701	25.1	6,117	sonic	FV+SS	565	21.07	444	2,721	12.8
702	14.5	3,665	sonic	FV+SS	577	12.93	471	2,076	9.9
703	24.9	7,649	sonic	FV+SS	557	25.92	550	3,414	12.7
704	20.0	6,149	sonic	FV+SS	562	21.04	555	3,027	11.5
705	2.7	903	sonic	FV+SS	579	3.20	628	887	5.0
706	3.6	1,279	sonic	FV+SS	572	4.47	647	1,177	5.5
707	27.4	10,319	sonic	FV+SS	552	34.41	662	4,396	13.3
708	20.0	7,648	sonic	FV+SS	557	25.89	682	3,763	11.5
709	14.4	6,152	sonic	FV+SS	562	21.03	774	3,501	9.8
710	21.9	10,383	sonic	FV+SS	545	34.13	824	4,903	12.0
711	3.5	1,722	sonic	FV+SS	558	5.83	869	1,596	5.5
712	26.4	13,619	sonic	FV+SS	537	43.99	879	5,903	13.1
713	6.1	3,337	sonic	FV+SS	573	11.67	1019	2,647	6.7
714	2.7	1,629	sonic	FV+SS	554	5.47	1061	1,596	5.0
715	15.7	12,062	sonic	FV+SS	538	39.03	1315	6,599	10.2
716	3.5	6,228	sonic	FV+SS	553	20.92	3173	5,798	5.5
717	15.8	1,848	sonic	FV+SS	541	6.05	203	1,010	10.3
718	13.6	1,760	sonic	FV+SS	525	5.56	216	1,024	9.6
719				DC					
720	14.9	1,980	sonic	FV+SS	582	7.06	251	1,110	10.0

Run #	JPR	Re_{exit}	type of nozzle	Type of Data	T_0 (K)	p_0 (kPa)	p_a (Pa)	Re_2	D_2 (mm)
721	6.5	930	sonic	FV+SS	573	3.25	264	720	6.9
722	9.5	1,448	sonic	FV+SS	563	4.96	275	974	8.2
723	15.1	2,294	sonic	FV+SS	583	8.19	288	1,279	10.0
724	7.9	1,302	sonic	FV+SS	566	4.49	299	939	7.6
725	21.0	3,673	sonic	FV+SS	574	12.89	324	1,769	11.7
726	25.4	6,199	sonic	FV+SS	558	21.04	438	2,742	12.8
727	14.4	3,712	sonic	FV+SS	569	12.90	472	2,108	9.9
728	25.7	7,730	sonic	FV+SS	550	25.80	531	3,401	12.9
729	20.6	6,239	sonic	FV+SS	553	20.97	539	3,037	11.6
730	2.8	932	sonic	FV+SS	569	3.24	618	911	5.1
731	3.6	1,312	sonic	FV+SS	559	4.45	645	1,207	5.5
732	27.0	10,370	sonic	FV+SS	540	33.71	659	4,450	13.2
733	20.1	7,784	sonic	FV+SS	544	25.61	675	3,829	11.5
734	14.4	6,288	sonic	FV+SS	547	20.85	763	3,570	9.9
735	21.8	10,520	sonic	FV+SS	531	33.51	812	4,976	11.9
736	3.6	1,742	sonic	FV+SS	557	5.89	856	1,605	5.5
737	26.8	13,974	sonic	FV+SS	524	43.88	863	6,013	13.2
738	6.1	3,414	sonic	FV+SS	559	11.59	1006	2,704	6.8
739	2.8	1,675	sonic	FV+SS	539	5.46	1036	1,635	5.1
740	14.7	11,279	sonic	FV+SS	533	36.14	1301	6,346	9.9
741	3.4	6,225	sonic	FV+SS	550	20.78	3200	5,817	5.4
742	3.7	13,909	sonic	FV+SS	530	44.20	6306	12,742	5.6
743	15.0	1,744	sonic	FV+SS	554	5.84	206	973	10.0
744	13.0	1,626	sonic	FV+SS	556	5.48	222	963	9.4
745	15.4	1,986	sonic	FV+SS	581	7.05	243	1,097	10.1
746	6.6	925	sonic	FV+SS	573	3.23	258	712	7.0
747	9.6	1,443	sonic	FV+SS	563	4.94	272	967	8.2
748	14.9	2,303	sonic	FV+SS	582	8.18	291	1,289	10.0
749	7.7	1,292	sonic	FV+SS	566	4.45	304	940	7.5
750	21.1	3,673	sonic	FV+SS	575	12.88	322	1,764	11.8
751	25.9	6,183	sonic	FV+SS	559	20.99	428	2,709	13.0
752	15.0	3,703	sonic	FV+SS	570	12.87	454	2,069	10.0
753	25.6	7,742	sonic	FV+SS	549	25.74	531	3,409	12.9
754	20.5	6,235	sonic	FV+SS	553	20.91	539	3,038	11.6
755	2.7	918	sonic	FV+SS	570	3.19	618	900	5.0
756	3.7	1,297	sonic	FV+SS	562	4.43	640	1,193	5.6
757	27.0	10,284	sonic	FV+SS	543	33.64	657	4,412	13.2
758	20.1	7,750	sonic	FV+SS	546	25.61	672	3,805	11.5
759	13.9	6,320	sonic	FV+SS	542	20.74	786	3,642	9.7

252

Run #	JPR	Re_{exit}	type of nozzle	Type of Data	T_0 (K)	p_0 (kPa)	p_a (Pa)	Re_2	D_2 (mm)
760	22.0	10,575	sonic	FV+SS	527	33.42	801	4,977	12.0
761	3.6	1,734	sonic	FV+SS	554	5.82	855	1,601	5.5
762	26.6	14,034	sonic	FV+SS	518	43.49	864	6,066	13.1
763	6.1	3,403	sonic	FV+SS	556	11.49	1001	2,698	6.7
764	2.7	1,661	sonic	FV+SS	537	5.39	1043	1,627	5.0
765	15.7	12,334	sonic	FV+SS	524	38.73	1306	6,748	10.2
766	3.4	6,281	sonic	FV+SS	543	20.62	3178	5,869	5.4
767	3.7	13,986	sonic	FV+SS	523	43.84	6188	12,778	5.6
768				TD					
769				TD					
770	20.7	3,783	sonic	TD	551	12.65	323	1,834	11.7
771	21.2	3,789	sonic	TD	552	12.68	316	1,818	11.8
772	21.0	3,786	sonic	TD	553	12.70	320	1,824	11.7
773	20.5	3,778	sonic	TD	554	12.71	327	1,840	11.6
774	21.5	3,775	sonic	TD	556	12.77	313	1,800	11.9
775	20.9	3,764	sonic	TD	558	12.76	323	1,820	11.7
776	20.3	3,762	sonic	TD	558	12.77	333	1,841	11.5
777	20.7	3,762	sonic	D	559	12.78	326	1,823	11.7
778	20.7	3,756	sonic	P	559	12.78	326	1,822	11.7

B.2 Parameters for Impinging Runs

Type of nozzle	θ_{imp} (°)	D_{imp} (mm)	Runs
sonic	90	25.4	19-25
			743-767
		44.2	717-778
		63.5	693-716
		68.3	14-18
		95.3	669-692
supersonic	45	93.9	621-644
	60	63.5	551-570
	90	44.5	357-465
		63.5	466-550
		95.3	571-594
		127.0	596-620

APPENDIX C

Glossary and Nomenclature

C.1 Terms and Acronyms

adiabatic	without the addition of heat to or removal of heat from a system. This is a necessary but not sufficient condition for a process to be *isentropic* (it must also be *reversible*).
adiabatic index	The ratio of the specific heat at constant pressure to the specific heat at constant volume. Usually, the quantity is denoted by γ where $\gamma = c_P/c_V$
axisymmetric	rotationally symmetric around an axis. For jet flows, this is generally the jet axis. An axisymmetric jet flow will look the same in any plane that contains the jet axis.
CAIB	Columbia Accident Investigation Board; the organization responsible for determining the cause of the Columbia disaster and making recommendations to NASA based upon their findings.
CCD	Charge Coupled Device
CEV	Crew Exploration Vehicle

CFI	Computational Flow Imaging
DNS	Direct Numerical Simulation. A type simulation that solves the Navier-Stokes equations numerically without a separate turbulence model. This requires that the computational mesh be fine enough to resolve all scales of turbulence, all the way down to the dissipative scales. In general, this is an extremely computationally intensive type of simulation.
ICCD	Intensified CCD
inviscid	Lacking viscosity. Inviscid fluids exhibit no resistance to deformation by an applied shear stress. Essentially, such a fluid had no internal friction, in contrast with viscous fluids. See *viscosity*.
isentropic	Without a change in entropy. In order for a process to be isentropic, it must be both *adiabatic* and *reversible*.
JPR	Jet Pressure Ratio. Defined to be the ratio of the pressure at the nozzle exit, p_e, to the ambient pressure, p_a. See also NPR.
LES	Large Eddy Simulation. A type of turbulence modeling that models the large turbulent eddies based on the geometry of the flow, and then uses a subgrid model with the assumption that smaller scales of turbulent eddies are self-similar and have a universal character. It generally requires less computational time than DNS, but more than RANS. The advantage over DNS is that the computational grid only has to be fine enough to resolve the largest turbulent eddies. RANS only provides

255

averaged flow parameters, whereas LES predicts instantaneous flow structures. LES does tend to have problems near walls.

LIF   Laser-Induced Fluorescence. Non-intrusive measurement technique in which a spectrally narrowband laser is used to excite a resonance in the chosen molecular species [typical species include: nitric oxide (NO), the hydroxyl radical (OH), iodine (I_2), and acetone (CH_3COCH_3)]. The resulting fluorescence constitutes the LIF signal. The fluorescence intensity may be recorded by focusing the fluorescence onto a PMT or imaging it onto a CCD (or ICCD) camera. Because the laser is tuned to a specific (usually single) resonance in the chosen molecular species, the resulting fluorescence process is a function of the energetic state of the molecules of the gas both before and after excitation. It is also a function of the bulk properties of the gas, including temperature, pressure, density, and species mole fraction. The LIF measurement volume can either be a single point (in the case of a focused laser beam), along a line, or in a plane (see PLIF). If imaged by a CCD, the spatial resolution of the measurement is a function of the magnification and field of view of the camera, as well as the size of the laser beam itself. If fluorescence is collected and focused onto a PMT, the spatial resolution of the resulting measurement is also a function of the collection angle of the focusing lens.

location 2   This is defined to be the axial location at which the pressure in a jet that expanded adiabatically would reach the ambient pressure. Flow

256

conditions calculated at this hypothetical location are labeled with a subscript of 2. The Reynolds number calculated using these conditions is called the *rescaled Reynolds number*. See section 5.5.1.1 and Eqs. 5.1-5.6.

MMOD	Micrometeorid/Orbital Debris
NASA	National Aeronautics and Space Administration
NO	Nitric oxide
NPR	Nozzle Pressure Ratio. The ratio of the plenum pressure, p_0, to the ambient pressure, p_a. NPR is often used instead of JPR in describing jet flows. Converting between NPR and JPR is straightforward, because the plenum to exit pressure ratio is a fixed constant for a given nozzle (assuming that the ratio is high enough to achieve sonic flow at the nozzle throat). For sonic nozzles ($M_e = 1$), $p_0/p_e = 1.89$; to get JPR, divide NPR by about 2. For our supersonic nozzle ($M_e = 2.6$), $p_0/p_e = 19.95$; to get JPR, divide NPR by about 20.
PDL	Pulsed Dye Laser
plenum	a region (usually upstream of a nozzle) where the flow is essentially at rest. The conditions (temperature, pressure, density, etc.) in the plenum are often equated with the stagnation conditions of the flow and are denoted with subscripts of "0."
PLIF	Planar Laser-Induced Fluorescence. See *LIF*. PLIF differs from LIF in that the laser beam is stretched into a laser sheet (typically by using a

257

combination of cylindrical and spherical lenses), resulting in a two-dimensional (planar) measurement volume.

PMT   Photomultiplier Tube.

RANS   Reynolds-Averaged Navier-Stokes. RANS is used to refer to a method of computing turbulent flows that results in time-averaged solutions to the Navier-Stokes equations in which turbulence effects are modeled with simplified empirical or semi-empirical equations. Because it requires less computational time than other techniques (like LES and DNS), it is used when averaged values are sufficient, or in sub-regions requiring more computational resources than are available in these more precise techniques. This is the most-commonly-used method for computing hypersonic flows.

rescaled Re   the Reynolds number calculated using conditions at *location 2*. Defined in Eq. 5.6.

reversible   A process is reversible if no dissipative mechanisms are active. Examples of irreversible, dissipative mechanisms include friction, viscosity (the internal friction of a fluid), thermal conductivity, and mass diffusion. This is a necessary but not sufficient condition for a process to be *isentropic*(it must also be *adiabatic*).

sonic   having a Mach number equal to 1; at the speed of sound. $\sqrt{\gamma RT} = 1$

stagnation   This adjective indicates a quantity (e.g. temperature, pressure, density) of a fluid element as it would be measured if the fluid were brought to rest.(in the lab frame) isentropically (adiabatically and reversibly). The

258

kinetic energy of the fluid would thus be converted into other forms (increased temperature, increased pressure, etc.). "Stagnation" quantities are usually denoted by "0" subscripts and are also called "total" properties (e.g. stagnation temperature or total temperature T_0, and stagnation pressure or total pressure p_0).

static This adjective indicates a quantity (e.g. temperature, pressure, density) of a fluid element as it would be measured *in the rest frame of the fluid*. "Static" quantities are usually indicated by the usual variable with no subscripts or superscripts (e.g. T is static temperature; p is static pressure).

throat the narrowest part of a nozzle. The Mach number at the throat of a nozzle is less than or equal to 1

viscosity The resistance of a fluid to deformation by shear forces. A measure of a fluid's resistance to flowing, of the internal friction of a fluid. The opposite of a viscous fluid is an inviscid fluid, which has no internal friction and does not exhibit resistance to flowing.

wavenumber the inverse wavelength, in units of cm^{-1}. Also called Kaisers. The units (cm^{-1}) remind you that the wavenumber is, in fact, the number of wavelengths that would fit into one centimeter. Wavenumber is often used in place of wavelength or frequency, and is an entirely equivalent means of describing the color of light, i.e. the energy of a photon. Its advantage is that it is linearly proportional to the energy of the light in question, such that a photon with three times the energy of a second

259

photon will have a wavenumber that is three times as large as that of the second photon. If you know the wavenumber associated with a particular transition, you have an idea of how much energy is involved relative to other transitions, whereas wavelength and frequency are nonlinear in this respect.

WEX   Wavelength Extender. This is a laser system component consisting of one or more birefringent crystals. It is pumped by an external pulsed laser source and the crystals act to double the frequency of the incoming laser light, or alternatively, to combine two colors of laser light into a third color, the wavenumber of which is a sum of the wavenumbers of the constituent two colors. It may include electronics designed to change the angle of the crystals in order to maximize the intensity of the output laser light. The most efficient angle of the crystals is a function of both the frequency of the incoming light and the temperature of the crystals themselves.

C.2 Latin Symbols

1   = indicates upper level of a molecular transition

2   = indicates lower level of a molecular transition, or conditions at *location 2*

B_{12} = Einstein absorption coefficient

D_2 = equivalent-jet diameter at *location 2* (m)

D_e = nozzle exit diameter (m)

D_m = Mach disk diameter (m)

260

e   = conditions at the nozzle exit

E = laser pulse energy (J)

f_B = Boltzmann fraction

g_i = spectral overlap integral

J = rotational quantum number (half-integer values)

n = temperature ratio coefficient

N = quantum number for total angular momentum, excluding spin (integer values)

p = local pressure (Pa)

p_2 = static pressure at *location 2* (Pa)

p_a = ambient pressure in test chamber (Pa)

p_e = static pressure at nozzle exit (Pa)

p_0 = plenum pressure (Pa)

Q_1 = spectroscopic notation for transitions where $\Delta J=0$ and where $J=N+1/2$ in the

         upper and lower states

R = specific gas constant, 287 J/(kg·K) for air

S_f = fluorescence signal

T = local temperature (K)

T_2 = temperature at *location 2* (K)

T_{ref} = reference (standard) temperature (K)

T_0 = plenum temperature (K)

V_2 = velocity at *location 2* (m/s)

V_e = velocity at nozzle exit (m/s)

w = primary wavelength of jet (m)

x_m = distance to Mach disk (m)

Y_{NO} = mass fraction of nitric oxide

C.3 Greek Symbols

γ = ratio of specific heats

μ_e = dynamic viscosity at nozzle exit (Pa·s)

μ_{ref} = reference (standard) dynamic viscosity (Pa·s)

ρ = gas density (kg/m^3)

ρ_2 = gas density at *location 2* (kg/m^3)

ρ_e = gas density at nozzle exit (kg/m^3)

Φ = fluorescence yield

χ_{N2} = mole fraction of nitrogen

χ_{NO} = mole fraction of nitric oxide

χ_{O2} = mole fraction of oxygen

REFERENCES

Alden, M., H. Edner, G. Holmstedt, S. Svanberg, and T. Hogberg (1982). "Single-Pulse Laser-Induced OH Fluorescence in an Atmospheric Flame, Spatially Resolved with a Diode-Array Detector," *Applied Optics* **21** (7): 1236-1240.

Alvi, F.S. and K.G. Iyer (10-12 May 1999). "Mean and Unsteady Flowfield Properties of Supersonic Impinging Jets with Lift Plates," *5th AIAA/CEAS Aeroacoustics Conference*, Bellevue (Greater Seattle), WA. AIAA 99-1829.

Alvi, F.S., J.A. Ladd, and W.W. Bower (April 2002). "Experimental and Computational Investigation of Supersonic Impinging Jets," *AIAA Journal* **40** (4): 599-609.

Anderson, J. D., Jr. (2003). *Modern Compressible Flow: With Historical Perspective*, 3rd ed., McGraw-Hill, Boston.

Balakumar, Ponnampalam (Jan 2007), Flow Physics and Control Branch, NASA Langley Research Center, Hampton, VA. Private communication.

Beresh, S.J., N.T. Clemens, and D.S. Dolling (Dec 2002). "Relationship between upstream turbulent boundary-layer velocity fluctuations and separation shock unsteadiness," *AIAA Journal* **40** (12): 2412-2422.

Birkby, P., and G. J. Page (2001). "Numerical Predictions of Turbulent Underexpanded Sonic Jets using a Pressure-Based Methodology," *Proc. Instn. Mech. Engrs., Part G, Journal of Aerospace Engineering* **215**: 165-173.

Bivolaru, D., P. M. Danehy, J. W. Lee, R. L. Gaffney, Jr., and A. Cutler (9-12 Jan 2006). "Single-pulse Multi-point Multi-component Interferometric Rayleigh Scattering Velocimeter," *44th AIAA Aerospace Sciences Meeting and Exhibit*, Reno, NV. AIAA 2006-0836.

Boyce, R.R., D.R.N. Pulford, A.F.P. Houwing, and C. Mundt (1996). "Rotational and vibrational temperature measurements using CARS in a hypervelocity shock layer flow and comparisons with CFD calculations," *Shock Waves Journal* **6**: 41-45.

Carter, C. D., and N. M. Laurendeau (June 1994). "Wide- and narrow-band saturated fluorescence measurements of hydroxyl concentration in premixed flames from 1 bar to 10 bar," *Applied Physics B (Lasers and Optics)* **58** (6): 519-28.

Chang, A. Y., E. C. Rea, Jr., and R. K. Hanson (1992). "Temperature Dependence of Collision Broadening and Shift in the NO A→X(0,0) Band in the Presence of Argon and Nitrogen," *Journal of Quantitative Spectroscopy and Radiative Transfer* **47**: 375-390.

Cheng, S., M. Zimmermann, and R.B. Miles (1983). "Separation of Time-Averaged Turbulence Components by Laser-Induced Fluorescence," *Physics of Fluids* **26** (4): 874-877.

Cheng, S., M. Zimmermann, and R.B. Miles (1983). "Supersonic-Nitrogen Flow-Field Measurements with the Resonant Doppler-Velocimeter," *Applied Physics Letters* **43** (2): 143-145.

Cockrell, Charles E., Jr., R. S. Barnes, H. L. Belvin, J. Allmen, and A. Otero (10-13 July 2005). "NASA Research Center Contributions to Space Shuttle Return to Flight (SSRTF)," *41st AIAA/ASME/SAE/ASEE Joint Propulsion Conference & Exhibit*, Tuscon, AZ. AIAA 2005-3626.

CRC Handbook of Chemistry and Physics: A Ready-Reference Book of Chemical and Physical Data, 51st edition, Robert C. Weast, ed. (1970). The Chemical Rubber Company, Cleveland, OH: p. B-115.

Crist, S., P. M. Sherman, and D. R. Glass (1966). "Study of the Highly Underexpanded Sonic Jet," *AIAA Journal* 4 (1): 68-71.

Cutler, A. D., P. M. Danehy, R. R. Springer, S. O'Byrne, D. P. Capriotti, and R. DeLoach (14-17 Jan 2002). "CARS thermometry in a supersonic combustor for CFD code validation," *40th AIAA Aerospace Sciences Meeting and Exhibit*, Reno, NV. AIAA 2002-743.

Danehy, P. M., P. C. Palma, A. F. P. Houwing, and T. J. McIntyre (17-20 June 1996). "Comparison of Theoretical Laser-Induced Fluorescence Images with Measurements Performed in a Hypersonic Shock Tunnel," *19th AIAA Advanced Measurement and Ground Testing Technology Conference*, New Orleans, LA. AIAA-1996-2236.

Danehy, P. M., P. C. Palma, R. R. Boyce, and A. F. P. Houwing (1999). "Numerical Simulation of Laser-Induced Fluorescence Imaging In Shock-Layer Flows," *AIAA Journal* 37 (6): 715-722.

Danehy, P.M., S. O'Byrne, A.F.P. Houwing, J.S. Fox, D.R. Smith (Feb 2003). "Flow-Tagging Velocimetry for Hypersonic Flows Using Fluorescence of Nitric Oxide," *AIAA Journal* 41 (2): 263-271.

Danehy, P.M., J.A. Wilkes, G.J. Brauckmann, D.W. Alderfer, S.B. Jones, and D.P. Patry (9-12 Jan 2006). "Visualization of a Capsule Entry Vehicle Reaction-Control System (RCS) Thruster," *44th AIAA Aerospace Sciences Meeting and Exhibit*, Reno, NV. AIAA 2006-1532.

Danehy, P.M., A.P. Garcia, S. Borg, A.A. Dyakonov, S.A. Berry, J.A. (Wilkes) Inman, and D.W. Alderfer (8-11 Jan 2007). "Fluorescence visualization of hypersonic flow past triangular and rectangular boundary-layer trips." *45th AIAA Aerospace Sciences Meeting and Exhibit*, Reno, NV. AIAA 2007-0536.

DeOtte, Robert E., Jr., Gerald L. Morrison, and Robert D. Sewell (6-9 Jan 1992). "LDV measurements of the velocity field in an underexpanded supersonic jet (Ma = 1.5)," *30th AIAA Aerospace Sciences Meeting and Exhibit*, Reno, NV. AIAA 1992-504.

DiRosa, M. D. (May 1996). "High-Resolution Line Shape Spectroscopy of Transitions in the Gamma Bands of Nitric Oxide," HGTL Report T-327, Ph.D. Dissertation, Dept. of Mechanical Engineering, Stanford Univ., Stanford, CA.

Donaldson, C. D., and R. S. Snedeker (1971). "A study of free jet impingement. Part 1. Mean properties of free and impinging jets," *J. Fluid Mech.* 45, Part 2: 281-319.

Donaldson, C. D., R. S. Snedeker, and D. P. Margolis (1971). "A study of free jet impingement. Part 2. Free jet turbulent structure and impingement heat transfer," *J. Fluid Mech.* 45, Part 3: 477-512.

Donohue, J. M., and J. C. McDaniel, Jr. (Aug 1996). Computer-controlled multiparameter flowfield measurements using planar laser-induced iodine fluorescence, *AIAA Journal* 34 (8): 1604-1611.

Drazin, P.G., and W.H. Reid (1981). *Hydrodynamic Stability*, edited by G.K. Batchelor and J.W. Miles, Cambridge University Press, Cambridge, U.K.

Dyer, M.J., and D.R. Crosley (1982). "Two-Dimensional Imaging of OH Laser-Induced Fluorescence in a Flame," *Optics Letters* 7 (8): 382-384.

264

Eckbreth, A.C. (1996). *Laser Diagnostics for Combustion Temperature and Species*, 2nd ed., Combustion Science & Technology Book Series, Vol. 3, Taylor & Francis, New York, NY.

Exton, R.J., R.J. Balla, B. Shirinzadeh, M.E. Hillard, and G.J. Brauckmann (1999). "Flow visualization using fluorescence from locally seeded I$_2$ excited by an ArF excimer laser," *Experiments in Fluids* **26**: 335-339.

Fletcher, D.G. and J.C. McDaniel (1987). "Temperature-Measurement in a Compressible Flow Field using Laser-Induced Iodine Fluorescence," *Optics Letters* **12** (1): 16-18.

Fourguette, D.C., M.G. Mungal, and R.W. Dibble (July 1991). "Time evolution of the shear layer of a supersonic axisymmetric jet," *AIAA Journal* **29** (7): 1123-1130.

Fox, J.S., A.F.P. Houwing, and P.M. Danehy (March-April 2001). "Mole-Fraction-Sensitive Imaging of Hypermixing Shear Layers," *Journal of Propulsion and Power* **17** (2): 284-292.

GASP Version 4.0 User's Manual, Aerosoft, Inc. (2002). Blacksburg, VA. ISBN 09652780-5-0.

Gehman, Harold W., Jr., et al. (August 2003). *Columbia Accident Investigation Board Report*, Vol. 1, Government Printing Office, Washington, D.C.

Grisch, F., P. Bouchardy, M. Pealat, B. Chanetz, T. Pot, and M.C. Coet (1993). "Rotational temperature and density measurements in a hypersonic flow by dual-line CARS," *App. Phys. B* **B56**: 14-20.

Grieser, D.R., and R.H. Barnes (1980). "Nitric-Oxide Measurements in a Flame by Laser Fluorescence," *Applied Optics* **19** (5): 741-743.

Gross, K.P., and R.L. McKenzie (1983). "Single-Pulse Gas Thermometry at Low-Temperatures Using 2-Photon Laser-Induced Fluorescence in NO-N2 Mixtures," *Optics Letters* **8** (7): 368-370.

Hanson, R.K. (1993). "Laser Diagnostics for Combustion and Propulsion," in *Laser Applications in Combustion and Combustion Diagnostics*, L.C. Liou, ed., Soc. Photo-Opt. Instrum. Eng. (SPIE) Proc. **1862**: 98-112.

Henderson, Brenda (Feb 2002). "The connection between sound production and jet structure of the supersonic impinging jet," *Journal of the Acoustical Society of America* **111** (2): 735-747.

Henderson, B., J. Bridges, and M. Wernet (2005). "An experimental study of the oscillatory flow structure of tone-producing supersonic impinging jets," *Journal of Fluid Mechanics*, Cambridge University Press, **542**: 115-137.

Herzberg, G. (1950). *Molecular Spectra and Molecular Structure: I. Spectra of Diatomic Molecules*, 2nd ed., with J.W.T. Spinks. Van Nostrand Reinhold Company, New York.

Horvath, Thomas J. (5-8 Jan 2004). "Experimental Aerothermodynamics in Support of the Columbia Accident Investigation," *42nd AIAA Aerospace Sciences Meeting and Exhibit*, Reno, NV. AIAA 2004-1387.

Horvath, T.J., S.A. Berry, N.R. Merski, K.T. Berger, G.M. Buck, D.S. Liechty, and S.P. Schneider (5-8 June 2006). "Shuttle Damage/Repair from the Perspective of Hypersonic Boundary Layer Transition—Experimental Results," *9th AIAA/ASME Joint Thermophysics and Heat Transfer Conference*, San Francisco, CA. AIAA 2006-2919.

Houwing, F., P. Danehy, P. Palma, S. O'Byrne, J. Fox, S. Mallinson, and M. Gaston (9-10 December 1999). "The Application of Laser-Based Diagnostic Techniques to Supersonic

and Hypersonic Flows," *2ⁿᵈ Australian Conference on Laser Diagnostics in Fluid Mechanics and Combustion*, Monash University, Melbourne, Australia.

Kalghatgi, G.T. and B.L. Hunt (Aug 1976). "Experiments on the Impingement of a Supersonic Jet on a Flat Plate," *The Aeronautical Quarterly* **27**: 169-185.

Kim, Sung In, and Seung O. Park (2005). "Oscillatory behavior of supersonic impinging jet flows," *Shock Waves* **14** (4): 259-272.

Kim, Sung In, and Seung O. Park (6-9 Jan 2003). "Unsteady Flow Simulation of Supersonic Impinging Jet," *41st AIAA Aerospace Sciences Meeting and Exhibit*, Reno, NV. AIAA 2003-621.

Kohse-Höinghaus, Katharina, and Jay B. Jeffries, eds. (2002). *Applied Combustion Diagnostics (Combustion: An International Series)*. Taylor & Francis, New York.

Krothapalli, A., G. Buzyna, and L. Lourenco (Aug 1991). "Streamwise vortices in an underexpanded axisymmetric jet," *Phys. Fluids A* **3** (8): 1848-1851.

Kychakoff, G., R.D. Howe, and R.K. Hanson (1982). "Quantitative Visualization of Combustion Species in a Plane," *Applied Optics* **21** (18): 3225-3227.

Kychakoff, G., K. Knapp, R.D. Howe, and R.K. Hanson (Jan 1984). "Flow Visualization in Combustion Gases Using Nitric Oxide Fluorescence," *AIAA Journal* **22** (1): 153-154.

Lachney, E. R., and N. T. Clemens (1998). "PLIF imaging of mean temperature and pressure in a supersonic bluff wake," *Experiments in Fluids* **24**: 354-363.

Lamont, P.J., and B.L. Hunt (1980). "The Impingement of Underexpanded Axisymmetric Jets on Perpendicular and Inclined Flat Plates," *Journal of Fluid Mechanics* **100**: 471-511.

Lee, M.P., McMillin, B.K., and Hanson, R.K. "Temperature Measurements in Gases Using Planar Laser-Induced Fluorescence Imaging of NO," *Applied Optics* **32**, pp.5379-5396 (1993).

Lesieur, M. (1987). *Turbulence in Fluids: Stochastic and Numerical Modeling*. Martinus Nijhoff Publishers, Dordrecht, The Netherlands.

List, E. J. (1982). "Turbulent jets and plumes," *Ann. Rev. Fluid Mech.* **14**: 189-212.

Love, E. S., C. E. Grigsby, and L. P. Lee (Jan 1958). "Shape of Initial Portion of Boundary of Supersonic Axisymmetric Free Jets at Large Pressure Ratios," NACA TN 4195.

Love, E. S., C. E. Grigsby, L. P. Lee, and M. J. Woodling (1959). "Experimental and theoretical studies of axisymmetric free jets," NASA Technical Report R-6.

Luque, J., and D. R. Crosley (1999). *LIFBASE: Database and Spectral Simulation Program (Version 1.5)*, SRI International Report MP 99-009. Available for free download at http://www.sri.com/psd/lifbase/

Mackie, S. and R. Taghavi (14-17 Jan. 2002). "Supersonic Impinging Jets: A Computational Investigation," *40ᵗʰ AIAA Aerospace Sciences Meeting and Exhibit*, Reno, NV. AIAA 2002-0671.

Malik, Tariq (5 Oct 2006). "NASA: Atlantis Shuttle Radiator Struck by Object in September Flight." SPACE.com, Imaginova. http://www.space.com/missionlaunches/061005_sts115_atlantis_damage.htm.

Massey, G.A., and C.J. Lemon (1984). "Feasibility of Measuring Temperature and Density-Fluctuations in Air Using Laser-Induced O2 Fluorescence," *IEEE Journal of Quantum Electronics* **20** (5): 454-457.

Matsuda, T., Y. Umeda, R. Ishii, A. Yasuda, and K. Sawada (8-10 June 1987). "Numerical and Experimental Studies on Choked Underexpanded Jets," *19ᵗʰ AIAA Fluid*

266

Dynamics, Plasma Dynamics and Lasers Conference, Honolulu, Hawaii. AIAA 87-1378.

McDaniel, J.C., Jr., B. Hiller, and R.K. Hanson (1983). "Simultaneous Multiple-Point Velocity-Measurements Using Laser-Induced Iodine Fluorescence," *Optics Letters* **8** (1): 51-53.

McDaniel, J.C., Jr., C. E. Glass, D. Staack, and C. G. Miller, III (14-17 Jan 2002). "Experimental and Computational Comparison of an Underexpanded Jet Flowfield," *40th AIAA Aerospace Sciences Meeting and Exhibit*, Reno, NV. AIAA 2002-0305.

McKenzie, R.L., D.J. Monson, and R.J. Exberger (4-6 June 1979). "Time-Dependent Local Density Measurements in Unsteady Flows," *14th AIAA Thermophysics Conference*, Orlando, FL. AIAA 1979-1088.

McKenzie, R.L. (7-10 Jan 1991). "Progress in Laser-Spectroscopic Techniques for Aerodynamic Measurements—An Overview," *29th AIAA Aerospace Sciences Meeting*, Reno, NV. AIAA 1991-59.

McMillin, B.K, M.P. Lee, and R.K. Hanson (1992). "Planar laser-induced fluorescence imaging of shock-tube flows with vibrational nonequilibrium," *AIAA Journal* **30** (2): 436-443.

McMillin, B.K., J.M. Seitzman, and R.K. Hanson (28-30 June 1993). "Comparison of NO and OH PLIF Temperature Measurements in a SCRAMJET Model Flowfield," *AIAA/SAE/ASME/ ASEE 29th Joint Propulsion Conference and Exhibit*, Monterey, CA. AIAA 93-2035.

Miles, R.B., E. Udd, and M. Zimmermann (1978). "Quantitative Flow Visualization in Sodium Vapor Seeded Hypersonic Helium," *Applied Physics Letters* **32** (5): 317-319.

Miles, R.B., C. Cohen, J. Connors, P.J. Howard, S. Huang, E. Markovitz, and G. Russell (Nov 1987). "Velocity Measurements by Vibrational Tagging and Fluorescent Probing of Oxygen," *Optics Letters* **12** (11): 861-863.

O'Byrne, S., P. M. Danehy, and A. F. P. Houwing (24-26 June 2002). "Nonintrusive temperature and velocity measurements in a hypersonic nozzle flow, " *22nd AIAA Aerodynamic Measurement Technology and Ground Testing Conference*, St. Louis, MO. AIAA 2002-2917.

Palma, P.C. (submitted May 1998, revised February 1999). *Laser-Induced Fluorescence Imaging in Free-Piston Shock Tunnels*. Ph.D. thesis, Australian National University.

Palma, P.C. (1998-1999). *LINUS: Nitric Oxide (NO) Spectroscopy and LIF Line Selection Program (Version 3.0.0)*, Australian National University, Canberra.

Palmer, J.L., B.K. McMillin, and R.K. Hanson (24-26 June 1991). "Planar Laser-Induced Fluorescence Imaging of Underexpanded Free Jet Flow in a Shock Tunnel Facility," *22nd AIAA Fluid Dynamics, Plasma Dynamics and Lasers Conference*, Honolulu, HI. AIAA 91-1687.

Palmer, J.L., and R.K. Hanson (1995). "Shock tunnel flow visualization using planar laser-induced fluorescence imaging of NO and OH," *Shock Waves* **4**: 313-323.

Panda, J., and R.G. Seasholtz (1999). "Measurements of shock structure and shock-vortex interaction in underexpanded jets using Rayleigh scattering," *Phys. Fluids* **11**: 3761-3777.

267

Paul, P.H., M.P. Lee, and R.K. Hanson (1 May 1989). "Molecular velocity imaging of supersonic flows using pulsed planar laser-induced fluorescence of NO," *Optics Letters* **14** (9): 417-419.

Paul, P.H., J. A. Gray, and J. L. Durant, Jr. (Aug 1994). "Collisional quenching corrections for laser-induced fluorescence measurements of NO $A^2\Sigma^+$," *AIAA Journal* **32** (8): 1670-1675.

Peters, C.E., and W.J. Phares (19-21 Jan 1970). "The structure of plumes from moderately underexpanded supersonic nozzles," *8th AIAA Aerospace Sciences Meeting*, New York, NY. AIAA 70-229.

Pope, Stephen B. (2000). *Turbulent Flows*. Cambridge University Press, Cambridge, U.K.

Princeton Instruments/Acton (7 Mar 2006). *PI-MAX / PI-MAX2 System User Manual*. Version 5.0. Princeton Instruments, a division of Roper Scientific, Inc. Trenton, NJ.

Ritzert, Frank J. (2005). "Flexible Metallic Overwrap Concept Developed for On-Orbit Repair of Space Shuttle Orbiter Leading Edges," NASA Glenn Research Center, Cleveland, OH. Research and Technology Technical Memorandum NASA/TM-2005-213419.

Ruyten, W.M., W.D. Williams, and F.L. Heltsley (20-23 June 1994). "Computational Flow Imaging for Planar Laser-Induced Fluorescence Applications (CFI-PLIF)," *18th AIAA Aerospace Ground Testing Conference*, Colorado Springs, CO. AIAA 94-2621.

Seitzman, J. M., F. Kychakoff, and R.K. Hanson (Sep 1985). "Instantaneous temperature field measurements using planar laser-induced fluorescence," *Optics Letters* **10** (9): 439-441.

Seitzman, J.M. and R.K. Hanson (1991). "Planar Fluorescence Imaging: Basic Concepts for Scalar and Velocity Measurements," Chapter 14 in *Combusting-Flow Diagnostics*, eds. D. Durano, M. Heitor, J. Whitelaw and P. Witze, Kluwer Academic Publishers, NATO/ASI Series E.

Siegman, Anthony E. (1986). *Lasers*, University Science Books, Mill Valley, CA.

Smith, E. Brian (2004). *Basic Chemical Thermodynamics*, 5th ed. Imperial College Press.

Stephenson, J.C. (1974). "Vibrational relaxation of NO $X^2\Pi(v = 1)$ in the temperature range 100-300 K," *Journal of Chemical Physics* **60**: 4289-4294.

Stitt, Leonard E. (Dec 1961). "Interaction of Highly Underexpanded Jets with Simulated Lunar Surfaces," Lewis Research Center, Cleveland, OH. NASA Technical Note D-1095.

Tabor, M. (1989). "Chaos and Integrability in Nonlinear Dynamics: An Introduction." New York: Wiley.

Tipler, P.A. (1990). *Physics for Scientists and Engineers*, 3rd ed. Worth Publishers, New York.

Thurber, M.C., F.Grisch, and R.K. Hanson (1-3 July 1996). "Temperature imaging with single- and dual-wavelength acetone PLIF," *32nd AIAA/ASME/SAE/ASEE Joint Propulsion Conference and Exhibit*, Buena Vista, FL.

Thurow, B., M. Samimy, and W. Lempert (24-26 June 2002). "Structure of a Supersonic Rectangular Impinging Jet via Real-Time Optical Diagnostics," *32nd AIAA Fluid Dynamics Conference*, St. Louis, MO. AIAA 2002-2865.

van Cruyningen, Ike (Sep 1990). *Quantitative Imaging of Turbulent Gaseous Jets Using Planar Laser-Induced Fluorescence*. M.S. thesis, High Temperature Gasdynamics Laboratory (HTGL), Stanford University, Stanford, CA. HTGL Report No. T-267.

White, F. M. (1991). *Viscous Fluid Flow*, 2nd ed., McGraw-Hill, Inc., New York.

Wilkes, J.A., D.W. Alderfer, S.B. Jones, and P.M. Danehy (1-5 Dec 2003). "Portable Fluorescence imaging system for hypersonic flow facilities," *JANNAF Interagency Propulsion Committee Meeting*, Colorado Springs, CO.

Wilkes, J.A., P.M. Danehy, R.J. and Nowak (29 Aug-1 Sep 2005). "Fluorescence Imaging Study of Transition in Underexpanded Free Jets," *Proceedings of the 21st International Congress on Instrumentation in Aerospace Simulation Facilities (ICIASF)*[CD-ROM], Sendai, Japan: pp. 1-8.

Wilkes, J.A., C.E. Glass, P.M. Danehy, and R.J. Nowak (9-12 Jan 2006). "Fluorescence Imaging of Underexpanded Jets and Comparison with CFD," *44th AIAA Aerospace Sciences Meeting and Exhibit*, Reno, NV. AIAA 2006-910.

Wu, J., L. Tang, E.A. Luke, X-L. Tong, and P. Cinnella (8-11 Jan 2001). "A Comprehensive Numerical Study of Jet Flow Impingement over Flat Plates at Varied Angles," *39th AIAA Aerospace Sciences Meeting and Exhibit*, Reno, NV. AIAA-2001-0745.

Yüceil, K. Bülent, and M. Volkan Ötügen (Dec 2002). "Scaling parameters for underexpanded supersonic jets," *Physics of Fluids* **14**, (12): 4206-4215.

Zapryagaev, V., V. Pickalov, N. Kiselev, and A. Nepomnyashchiy (November 2004). "Combination interaction of Taylor-Goertler vortices in a curved shear layer of supersonic jet," *Theoretical and Computational Fluid Dynamics* **18** (2-4): 301-308.